ISSN 2367-7570

Workshop
"Solar Influences on the Magnetosphere, Ionosphere and Atmosphere"

Book
of
Proceedings

Seventeenth Workshop
June, 2025

Organized by:
Space Research and Technologies Institute
Bulgarian Academy of Sciences

Editorial Board

Katya Georgieva (Space Research and Technology Institute, Sofia, Bulgaria) - Editor-in-Chief
Atila Özgüc (Bogazici Univ. Kandilli Observatory, Istanbul, Turkey)
Crisan Demetrescu (Institute of Geodynamics, Romanian Academy)
Dragan Roša (Zagreb Astrronomical Observatory, Croatia)
Jean-Pierre Rozelot (Université Côte d’Azur)
Mykhailo Riabov (Odessa observatory "URAN-4" Radio Astronomical Institute NAS Ukraine)
Nat Gopalswamy (NASA Goddard Space Flight Center)
Olga Malandraki (IAASARS, National Observatory of Athens, Greece)
Petra Koucká-Knižová (Institute of Atmospheric Physics, Czech Republic)
Vladimir Obridko (IZMIRAN, Moscow, Russian Federation)

Editors: **Katya Georgieva, Boian Kirov, Simeon Asenovski**

Acknowledgements

The Workshop’s organizers acknowledge the support by the Bulgarian National Science Fund, Grant No КП-06-МНФ/53, and the Bulgarian Academy of Sciences.

Scientific Organizing Committee

Katya Georgieva (Space Research and Technology Institute, Sofia, Bulgaria) – *Chair*
Atila Özgüc (Bogazici Univ. Kandilli Observatory, Istanbul, Turkey)
Crisan Demetrescu (Institute of Geodynamics, Romanian Academy)
Dragan Roša (Zagreb Astrronomical Observatory, Croatia)
Jean-Pierre Rozelot (Université Côte d'Azur)
Nat Gopalswamy (NASA Goddard Space Flight Center)
Olga Malandraki (IAASARS, National Observatory of Athens, Greece)
Petra Koucká-Knižová (Institute of Atmospheric Physics, Czech Republic)
Vladimir Obridko (IZMIRAN, Moscow, Russian Federation)

Preface

The Seventeenth International Workshop "Solar Influences on the Magnetosphere, Ionosphere and Atmosphere" was held on June 2–6, 2025 in Primorsko, Bulgaria.

In total, 68 participants from 19 countries attended. The scientific program featured 37 oral presentations and 51 posters.

These Proceedings include peer-reviewed contributions selected from the works presented at the Workshop. The Scientific Organizing Committee and the Editors of the Proceedings thank all participants for their contributions and lively discussions, and the session chairs for their dedication in shaping a stimulating program.

We are grateful to our hosts in Primorsko and to all colleagues who assisted in organizing the meeting.

DOI: 10.31401/WS.2025.proc

CONTENT

Sun and Solar Activity

Solar Wind-Magnetosphere-Ionosphere Interactions

Instrumentation for Space Weather Monitoring

Solar Influences on the Lower Atmosphere and Climate

Data Processing and Modelling

Solar Effects in the Biosphere and Lithosphere

DOI: 10.31401/WS.2025.proc.01

Proceedings of
the Seventeenth Workshop "Solar Influences on the Magnetosphere, Ionosphere and Atmosphere"
June, 2025

Variations of Umbral Magnetic Field Strength with Umbral Area, Brightness, and Sunspot Number

Calisir M.[1], *Yurchyshyn V.*[2]

[1]Department of Space Science and Technologies, Akdeniz University Faculty of Science, 07058 Antalya, Turkey
muhammed.calisirr@gmail.com; alikilcik@akdeniz.edu.tr
[2]Big Bear Solar Observatory, New Jersey Institute of Technology, Big Bear City, USA
vasyl.yurchyshyn@njit.edu.

Abstract

Sunspots are regions on the Sun where the magnetic field is highly concentrated. The magnetic field drives the physical conditions within and around sunspots. The study of the relationship between the magnetic field strength in the sunspot umbra and the umbral area, umbral brightness and sunspot number (SSN) provides important information about the physical properties of sunspots and the overall structure of the Sun. In this study, we analyzed high-resolution sunspot images obtained from the Big Bear Solar Observatory (BBSO)/Goode Solar Telescope (GST) for 2015 - 2022 time intervals. The corresponding daily sunspot number (SSN) data were taken from the Solar Influences Data Analysis Center (SIDC) website, and the magnetic field measurements were obtained from the GST/Near InfraRed Imaging Spectropolarimeter (NIRIS). The variations of the mean umbral magnetic field intensity with respect to the umbral area, umbral brightness, and SSN were investigated, and Pearson correlation analysis was performed to explore the relationships between them. Our analysis revealed the following results: i) There is a power-law relationship between the mean umbral area and the magnetic field strength and the magnetic field strength increases with increasing umbral area. ii) The magnetic field strength decreases with increasing mean umbral brightness. iii) A weak relationship was found between the umbral magnetic field strength and the SSN.

Keywords: sunspot; umbral area; umbral magnetic field; sunspot number

1. Introduction

Solar magnetic fields are generated by the motion of electrically charged ions and electrons within the solar plasma (Hale 1908; Hale et al. 1919). These magnetic fields play a crucial role in the formation of sunspots and are directly linked to the operation of the solar dynamo (Hale et al. 1919; Charbonneau 2020; Fan 2021). Therefore, studying the magnetic field of sunspots provides valuable insights into the underlying physical processes driving solar activity.

Sunspots are temporary dark areas on the surface of the Sun due to their low temperature compared to their surroundings. Sunspots have very strong magnetic fields and the magnetic field in these structures is on average on the order of 1000 G (Gauss). The surface of the Sun outside the spots has a magnetic field of about a few Gauss (Bhowmik et al. 2023). Sunspots are believed to result from the interaction between the Sun's magnetic field and turbulent convection near the surface: in regions with strong magnetic fields, convection is significantly suppressed, leading to inefficient heat transfer and consequently the formation of locally cooler and darker sunspots (Stein, 2012). They are strongly related to active solar events such as solar flares, coronal mass ejections etc. Sunspots are usually observed in groups and each group consists of different spots. A well-developed sunspot is fundamentally composed of two main parts: the umbra, situated at the center of the spot and characterized by its pronounced darkness, and the penumbra, which surrounds the umbra and appears brighter compared to the umbra.

Sunspots are generally observed in the ± 35 degrees latitude zone, called the active zone. The active events we observe on the Sun increase and decrease approximately every 11 years called the solar cycle. At the start of a solar cycle, very few sunspots, mostly small in size (Mandal et al., 2017), appear on the solar disc. Especially at the beginning of the solar cycle, sunspots observed in the latitude belt of 40-45 degrees move towards lower latitudes as the cycle progresses. Although the duration of the solar cycle is not constant, sunspots continuously form and dissipate over time. These dynamic patterns are accompanied by significant changes in sunspot properties, including umbral intensity and size, which have been linked to different phases of the solar cycle. Albregtsen and Maltby, (1978, 1981) reported the sunspot intensity varies approximately linearly with the phase of the solar cycle. Albregtsen, Joras, and Maltby (1984) analyzed the solar cycle variation of umbral intensities. Their study is based on broadband pinhole photometer intensity observations of 22 large sunspots, covering approximately 600 days during 15.5 years. They observed that the umbra/photosphere intensity ratio to be a linear function of the phase of the solar cycle. Norton and Gilman (2004) used brightness ratios and magnetic field data from the Advanced Stokes Polarimeter and the Michelson Doppler Imager (MDI) for 10 sunspot umbrae of various sizes observed between May 1998 and June 2003. They reported that the mean umbral intensity decreased in the northern hemisphere through the solar cycle. Such findings not only enhance our understanding of solar activity mechanisms but also provide observational evidence supporting the dynamo theory, which explains the Sun’s magnetic field generation.

Magnetic fields can cause significant changes in the dynamics in and around the spot. The region where the magnetic field is most concentrated is the umbra of sunspots. Watanabe (2014), used Hinode data to analyze umbral dots (UDs), which are fine structures observed in the umbra. As noted by Watanabe (2014), statistical correlations offer a useful perspective on the evolution of internal sunspot structures. The author pointed out that the umbral magnetic field is not uniform during sunspot development, since the umbra forms through the aggregation of pores with varying magnetic field strengths. The strength of the magnetic field varies depending on the size and shape of the spot. Pevtsov et al. 2014 used observations made at the Mount Wilson Observatory (MWO) between May 1920 and December 1958 to investigate the properties of sunspot magnetic fields. They stated magnetic field strength increases as the sunspot area increases. A sunspot umbra typically has a vertical magnetic field, while toward the penumbra, the field lines become inclined and become largely horizontal in this region (Rempel et al., 2009; Borrero & Ichimoto, 2011). Yurchyshyn et al. (2020) used data obtained with the Visible Imaging Spectrometer on the Goode Solar Telescope (GST) to detect the origin of umbral flashes (UFs) and umbral waves (UWs). In their study, it is reported that the dark umbra center has a strong magnetic field strength on the sunspot-center side of the enhanced magnetic fields. They showed that the magnetic field in the sunspot umbra is more dynamic, and its relationship with the Sun's magnetic activity cannot be ignored. Therefore, understanding the magnetic activity of sunspots is crucial for predicting solar activity, space weather conditions, and their effects on Earth. This highlights the need for a deeper understanding of sunspot properties.

In the present study, we analyzed 16 sunspot umbrae observed in 13 different ARs with the GST broadband imager between 2015 and 2022. We obtained variations of umbral magnetic field strength with umbral area, brightness, and sunspot number. We performed regression and Pearson correlation analyses to investigate the relationships between mean umbral field strength and other parameters. The outline of the article is as follows: In Section 3, we present the data and methods used. In Section 4, we present the analysis results. In Section 5, our conclusions are presented.

2. Data and Method

2.1.Data

In this study 13 sunspot data were selected from Big Bear Solar Observatory (BBSO)/Goode Solar Telescope (GST) archive data (Figure 1). The used data set covers the 2015 – 2022 time interval (Table 1). For the analysis the Titanium Oxide (TiO) filter (7057 Å) images of each sunspot were selected. The TiO spectral band is highly sensitive to temperature, making it well-suited for observations of dark and cool regions, even inside the umbra. The resolution of TiO data per pixel is 0.034”. Also, the GST allows simultaneous TiO and Near-Infrared Imaging Spectropolarimeter (NIRIS) measurements to be taken. We used simultaneously one TiO and one NIRIS image for the analysis. The TiO filter was used to determine the umbral area and brightness, and the NIRIS filter was used to obtain the magnetic field strength. The resolution of NIRIS data per pixel is 0.083”.

Table 1. *List of the analyzed sunspots*

Number	NOAA Active Region Number	Observation Time	Sunspot Location	TIO Time (UT)	NIRIS Time (UT)	Daily Sunspot Number
1	AR12384	14/07/2015	S18W19	17:52:02	17:52:09	43
2	AR12411	08/09/2015	N14E13	16:30:38	16:30:45	42
3	AR12565 **(dual umbra)**	14/07/2016	N04E30	16:41:25	16:41:24	58
4	AR12717	01/08/2018	S07E15	16:48:46	16:48:48	12
5	AR12720	25/08/2018	N08W38	17:04:47	17:04:48	32
6	AR12767	28/07/2020	S20W18	16:23:56	16:24:00	20
7	AR12770 **(dual umbra)**	08/08/2020	N23E11	17:18:02	17:18:09	12
8	AR12776	20/10/2020	S13W17	18:01:06	18:01:03	14
9	AR12902	30/11/2021	N18W03	16:35:57	16:35:52	59
10	AR12934	24/01/2022	S25E16	17:43:37	17:43:33	33
11	AR13046	06/07/2022	N18W05	18:32:03	18:32:10	82
12	AR13053	12/07/2022	N16W20	20:02:43	20:02:50	114
13	AR13147 **(dual umbra)**	20/11//2022	S12E20	17:50:28	17:50:26	84

The umbra and penumbra were separated by applying a binary filter based on intensity threshold (Calisir et al, 2023). The threshold value selected as 0.65 for developed penumbra, while it has been used to be 0.70 for sunspots with undeveloped or poorly developed penumbra (see Figure 2). The threshold value was determined as a multiple of the mean intensity of the entire sunspot, including the quiet sun area around the sunspot.

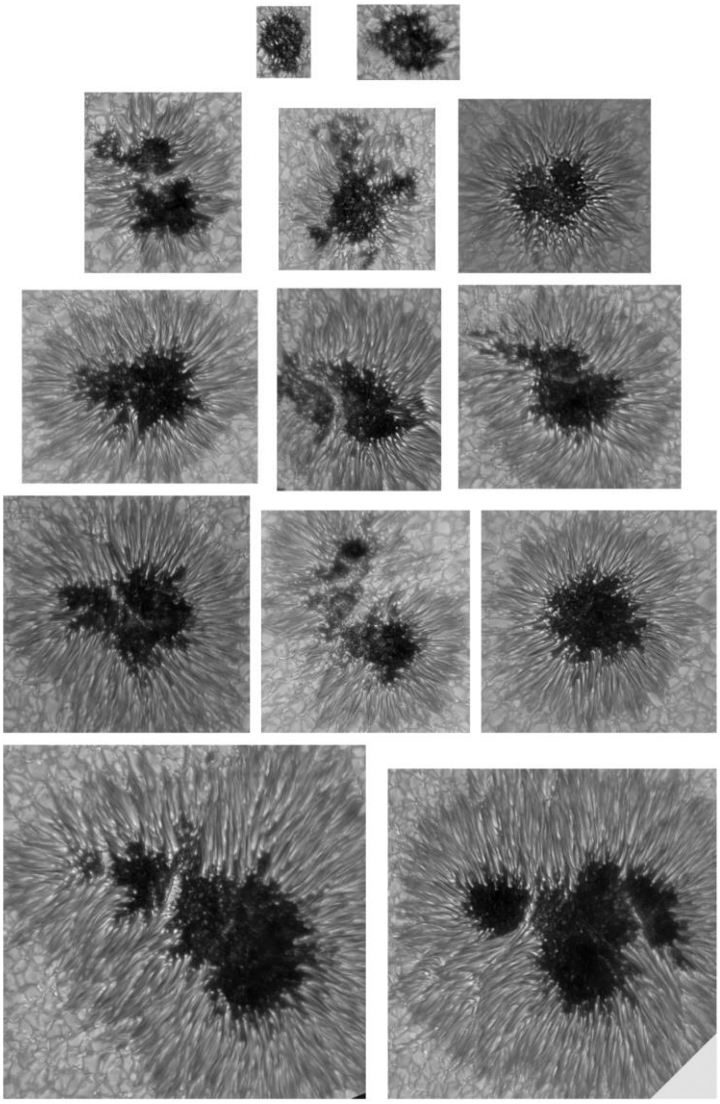

Figure 1. *Images of all sunspots used in the study.*

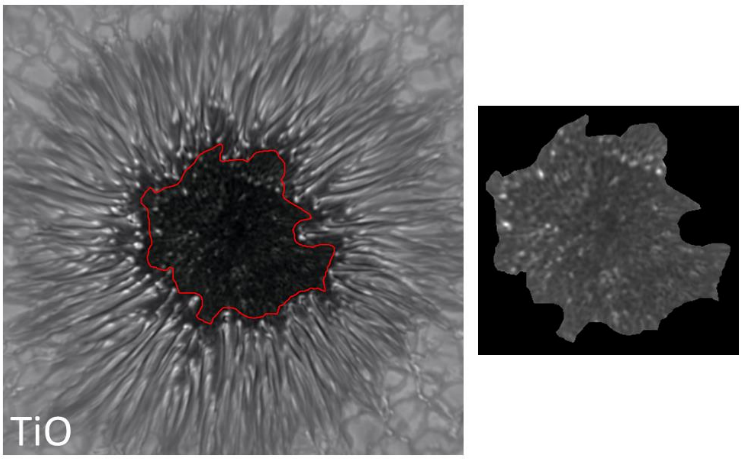

Figure 2. *Left panel: TiO image (AR 12384). Red contour: Detection of the umbra. Right Panel: The zoomed in extracted umbral core.*

2.2.Calculation of Umbral Parameters

Umbral Area: To calculate the umbral area, the umbra was separated from the penumbra, and the area of the remaining image was calculated in terms of the total number of pixels and it was converted to Mm².

Umbral Brightness: The mean pixel value within the umbral area was calculated for each image.

Umbral Magnetic Field: For the umbral magnetic field we selected the exactly the same region from the TiO data (Figure 3). To calculate the intensity (strength) of the umbral magnetic field; similarly, the pixel values within the field were averaged.

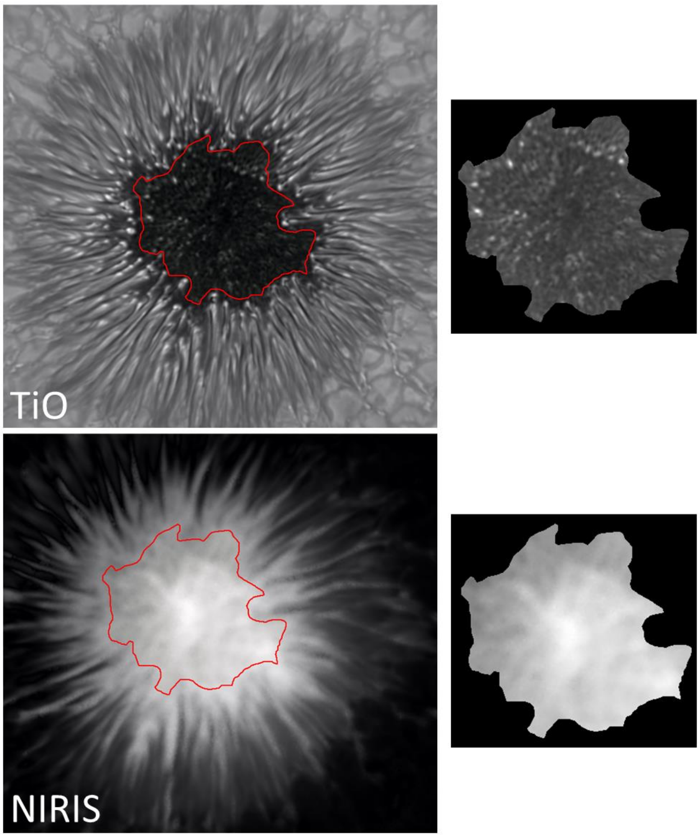

Figure 3. *Left panel: TiO and NIRIS images (AR 12384). Right Panel: The zoomed in extracted umbral cores.*

2.3.Sunspot Number (SSN)

To investigate the solar cycle dependency of the obtained mean umbral magnetic field strength, we compared it with the daily sunspot number data available at SIDC (https://www.sidc.be/silso/datafiles). We added the daily sunspot numbers for the corresponding dates. (It is shown as a yellow column in Table 1.)

3. Results

We used almost simultaneously 13 images from NIRIS and TiO filters. Since some sunspots contain double umbra (AR 12565, AR 12770 and AR 13147), a total of 16 umbra were analyzed. We obtained the mean umbral magnetic field strength, umbral area, and umbral brightness for each sunspot (Table 2).

Table 2. *Mean physical parameters of analyzed sunspots.*

Umbra	Mean Umbral Magnetic Field (Gauss)	Mean Umbral Area (Mm2)	Mean Umbral Brightness (Relative Intensity)
20150714	1494.2	47.54	0.37
20150908	1531.72	28.06	0.43
20160714 **Large Umbra**	1892.09	136.48	0.33
20160714 **Small Umbra**	1532.2	25.09	0.28
20180801	1367.21	12.99	0.56
20180825	1655.65	25.33	0.50
20200728	1974.78	44.71	0.32
20200808 **Large Umbra**	1849.61	19.80	0.34
20200808 **Small Umbra**	989.99	11.69	0.42
20201020	1938.02	44.90	0.35
20211130	1748.68	25.10	0.50
20220124	1954.99	54.98	0.35
20220706	1746.24	19.91	0.43
20220712	1177.14	24.71	0.35
20221120 **Large Umbra**	2098.64	121.80	0.30
20221120 **Small Umbra**	1766.36	18.77	0.33

Relationship between umbral magnetic field and umbral area, brightness, sunspot number

We performed regression and Pearson correlation analyses to investigate the relationships between mean umbral field strength and other parameters (mean umbral area, mean umbral brightness and sunspot number) (Figure 4). Their error of correlations coefficients were calculated by using the standard error calculation method. The results are presented in Table 3.

Table 3. *Summary of the obtained correlation coefficients (r).*

	Mean Umbral Area (Mm^2)	Mean Umbral Brightness (Intensity)	Sunspot Number
Mean Umbral Magnetic Field Intensity (Gauss)	**+0.64 ± 0.21**	**-0.39 ± 0.25**	**0.33 ± 0.26**

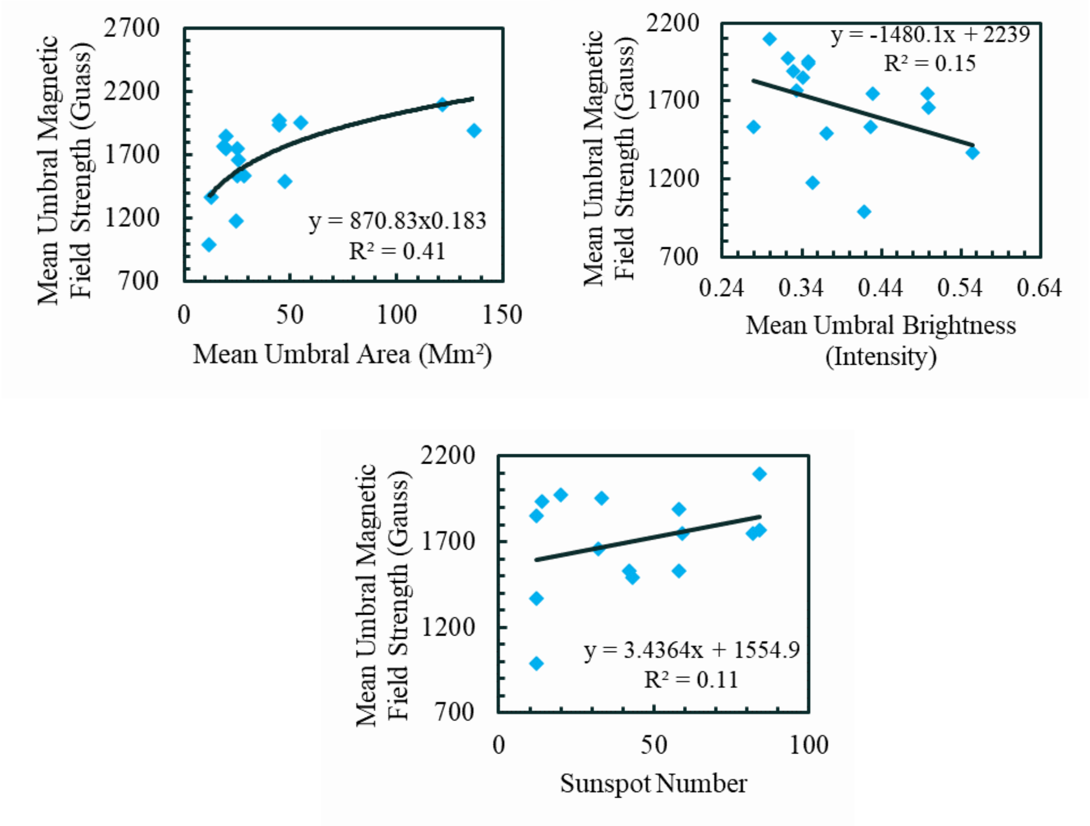

Figure 4. *Relationships between umbral magnetic field and umbral area, brightness, sunspot number in the analyzed on all 16 sunspot umbra.*

Pearson correlation analyses were carried out to reveal the relationship between umbral magnetic field intensity and above parameters (sunspot area, brightness and sunspot number). An examination of Table 3 and Figure 4 clearly shows that there are significant and systematic relationships between umbral magnetic field strength and these parameters. According to the analysis results, a positive correlation was found between umbral magnetic field strength and both umbral area and sunspot number. In contrast, as umbral brightness increases, the magnetic field strength decreases, indicating an inverse relationship. This suggests that brighter umbrae are generally associated with weaker magnetic fields. A comparison of the correlation coefficients revealed that the strongest correlation with umbral magnetic field strength was found with umbral area, while the weakest correlation was with sunspot number. All correlation coefficients were found to be statistically significant, and these results strongly support the idea that magnetic field strength in sunspot umbrae is related to observed local structures and overall solar activity.

4. Conclusions and Discussions

We analyzed 16 sunspot umbrae observed in 13 different ARs with the GST broadband imager. We obtained variations of umbral magnetic field strength with umbral area, brightness, and sunspot number. Our main results are as follows:

- The mean umbral magnetic field strength increases exponentially as the mean umbral area increases.

- The mean umbral magnetic field strength decreases linearly with the mean umbral brightness. On the contrary, it increases linearly with the sunspot number.

- We found that all obtained correlation coefficients are meaningful.

The magnetic field strength varies with the size of the sunspot; it is higher in larger spots, while it is lower in spots with smaller umbrae. This result confirms the findings of Pevtsov et al. (2014) and clearly emphasizes that the relationship between sunspot size and magnetic field strength should not be overlooked. Watanabe (2014) stated that the umbral magnetic field is not homogeneous during the evolution of sunspots and that the umbra is formed by the merging of dynamics with varying magnetic field strengths. Yurchyshyn et al. (2020) reported that the dark umbra at the center of the sunspot has a strong magnetic field. In this study, we found that the magnetic field strength decreases linearly as the umbral brightness increases. Observations have also shown that the darker region in the center of the umbra has strong magnetic fields. This finding shows that the homogeneity of the umbra is related to the magnetic field. The change in spot dynamics with increasing magnetic field strength and the corresponding decrease in spot brightness indicate that there are significant differences in the energy transport and observed structures inside the umbra.

Previous studies reported that umbral brightness is linked to different phases of the solar cycle and are associated with significant changes in sunspot characteristics (Albregtsen and Maltby, 1978, 1981; Albregtsen, Joras, and Maltby, 1984; Norton and Gilman, 2004). Albregtsen, Joras, and Maltby (1984), have confirmed the earlier finding (Albregtsen and Maltby, 1978, 1981) the sunspot intensity varies linearly with the phase of the solar cycle. They reported the high correlation between the intensities of the umbra and the penumbra of the same spot suggests that the mechanism which is responsible for the solar cycle intensity variations acts on the whole sunspot, and not only locally on the umbra. Norton and Gilman (2004), found that the mean umbral intensity in the northern hemisphere decreased during the solar cycle, reaching a minimum around the time of sunspot maximum. They reported this may be possible evidence of the toroidal field strength peaking at solar maximum. Such findings not only improve our understanding of solar activity mechanisms but also provide observational evidence supporting the dynamo theory that explains the formation of the Sun's magnetic field. On the other hand, the linear relationship observed between umbral magnetic field strength and sunspot number indicates that even the magnetic properties of a single sunspot are not independent of the Sun's large-scale magnetic activity, but rather are related to the solar cycle. This suggests that the magnetic field structures of umbrae are driven not only by local morphological conditions, but also by the global magnetic dynamics of the Sun. Taken together, these findings emphasize that the magnetic field structures of sunspots are shaped in a complex manner and that these structures can be linked to the solar cycle.

Acknowledgments

This study was supported by Project 122F004 awarded by the Scientific and Technological Research Council of Türkiye.

References

Albregtsen, F., Maltby, P. (1978). New light on sunspot darkness and the solar cycle, *Nature*, Vol. 274, pp. 41–43, DOI: 10.1038/274041a0.

Albregtsen, F., Maltby, P. (1981). Solar cycle variation of sunspot intensity, *Solar Physics*, Vol. 71, pp. 269–283, DOI: 10.1007/BF00167551.

Albregtsen, F., Joras, P.B., Maltby, P. (1984). Limb darkening and solar cycle variation of sunspot intensities, *Solar Physics*, Vol. 90, pp. 17–28, DOI: 10.1007/BF00153781.

Borrero, J.M., Ichimoto, K. (2011). Magnetic structure of sunspots, *Living Reviews in Solar Physics*, Vol. 8, No. 4, 98 pp., DOI: 10.12942/lrsp-2011-4.

Bhowmik, P., Jiang, J., Upton, L., Lemerle, A., Nandy, D. (2023). Physical models for solar cycle predictions, *Space Science Reviews*, Vol. 219, No. 40, DOI: 10.1007/s11214-023-00983-x.

Calisir, M.A., Yazici, H.T., Kilcik, A., Yurchyshyn, V. (2023). Relationships between physical parameters of umbral dots measured for 12 sunspot umbras with the Goode Solar Telescope, *Solar Physics*, Vol. 298, No. 103, DOI: 10.1007/s11207-023-02198-3.

Charbonneau, P. (2020). Dynamo models of the solar cycle, *Living Reviews in Solar Physics*, Vol. 17, No. 4, DOI: 10.1007/s41116-020-00025-6.

Fan, Y. (2021). Magnetic fields in the solar convection zone, *Living Reviews in Solar Physics*, Vol. 18, No. 5, DOI: 10.1007/s41116-021-00031-2.

Hale, G.E. (1908a). On the probable existence of a magnetic field in sun-spots, *Astrophysical Journal*, Vol. 28, pp. 315–319, DOI: 10.1086/141602.

Hale, G.E. (1908b). The Zeeman effect in the Sun, *Publications of the Astronomical Society of the Pacific*, Vol. 20, No. 123, pp. 287–290, DOI: 10.1086/121847.

Hale, G.E., Ellerman, F., Nicholson, S.B. (1919). The magnetic polarity of sun-spots, *Astrophysical Journal*, Vol. 49, pp. 153–158, DOI: 10.1086/142452.

Mandal, S., Hegde, M., Samanta, T., Hazra, G., Banerjee, D., Ravindra, B. (2017). Kodaikanal digitized white-light data archive (1921–2011): Analysis of various solar cycle features, *Astronomy & Astrophysics*, Vol. 601, A106, DOI: 10.1051/0004-6361/201628651.

Norton, A.A., Gilman, P.A. (2004). Magnetic field–minimum intensity correlation in sunspots: A tool for solar dynamo diagnostics, *Astrophysical Journal*, Vol. 603, pp. 348–357, DOI: 10.1086/381362.

Pevtsov, A.A., Bertello, L., Tlatov, A.G., Kilcik, A., Nagovitsyn, Y.A., Cliver, E.W. (2014). Cyclic and long-term variation of sunspot magnetic fields, *Solar Physics*, Vol. 289, No. 2, pp. 593–602, DOI: 10.1007/s11207-012-0220-5.

Rempel, M., Schüssler, M., Knölker, M. (2009). Radiative magnetohydrodynamic simulation of sunspot structure, *Astrophysical Journal*, Vol. 691, No. 1, pp. 640–649, DOI: 10.1088/0004-637X/691/1/640.

Stein, R.F. (2012). Solar surface magneto-convection, *Living Reviews in Solar Physics*, Vol. 9, No. 4, DOI: 10.12942/lrsp-2012-4.

Watanabe, H. (2014). Observations of umbral dots and their physical models, *Publications of the Astronomical Society of Japan*, Vol. 66, S1, DOI: 10.1093/pasj/psu102.

Yurchyshyn, V., Kilcik, A., Şahin, S., Abramenko, V., Lim, E.-K. (2020). Spatial distribution of the origin of umbral waves in a sunspot umbra, *Astrophysical Journal*, Vol. 896, No. 2, Art. 150, DOI: 10.3847/1538-4357/ab91b8.

DOI: 10.31401/WS.2025.proc.02

Proceedings of
the Seventeenth Workshop "Solar Influences on the Magnetosphere, Ionosphere and Atmosphere"
June, 2025

Hemispheric Asymmetry of the Solar Dynamo

Georgieva K., Kirov B., Asenovski S.

Space Research and Technology Institute, Bulgarian Academy of Sciences, Sofia, Bulgaria.
kgeorgieva@space.bas.bg

Abstract

The solar dynamo transforms the poloidal solar magnetic field prevailing during sunspot minimum into toroidal field which gives rise to sunspots, and back. The transition of poloidal into toroidal field is due to the differential rotation at the base of the convection zone which stretches the North-South magnetic field lines into East-West direction. Two mechanisms are responsible for the recreation of the poloidal from the toroidal field: turbulent diffusion, and large-scale meridional circulation. The dynamo's regime of operation depends of the relative importance of these two mechanisms. If both are operational, the sunspot number has two maxima during the solar cycle: one diffusion-generated, the other one advection-generated.

Earlier we found that, averaged over the two solar hemispheres, the diffusion-generated peak seems to appear earlier and at higher heliolatitudes than the advection-generated one in all sunspot cycles from 15 to 19. The order is reversed in cycles 12-14 and 20-23.

Here we repeat this study separately for the two solar hemispheres, and compare the two Gleissberg cycles minima between the 19th and 20th centuries, and between the 20th and 21st centuries. We find that the solar dynamo did not operate in different regimes during the last two Gleissberg minima. Moreover, it does not operate in different regimes during these secular minima and the cycles between them. An unexpected result is that the evolution of sunspot activity generated by diffusion and advection is different in the Southern and Northern hemispheres. The pattern is the same in all studied cycles with the exception of cycle 19 – the cycle of the secular sunspot maximum, which is quite peculiar.

Keywords: solar dynamo; Gnevyshev gap; hemispheric asymmetry

1. Introduction

Solar cycles are fundamental to our understanding of solar activity and have a direct impact on all aspects of solar-terrestrial interactions. Each of these periods is characterized by a systematic increase and decrease in the number of sunspots, which corresponds to changes in the Sun's magnetic field. Understanding solar cycles is crucial not only for solar science but also for predicting space weather, which can have direct effects on satellite communications, navigation, space travel, and Earth's energy infrastructure. Therefore, they are of interest not only academically but also as a practical necessity for contemporary society.

Sunspots are visible indicators of solar activity and magnetism. Their number and distribution change over each cycle and are associated with various solar phenomena, including solar flares which can disrupt communications, and the eruptions of solar plasma known as coronal mass ejections (CMEs), which can significantly affect space weather and Earth's technological systems.

The most prominent cyclicity of solar activity is the ~11-year ("Schwabe") sunspot cycle. The Schwabe cycles are not all the same, but vary in both amplitude and duration, modulated by a secular cycle known as the "Gleissberg cycle" (Gleissberg, 1930).

Some ~11-year sunspot cycles feature a single maximum, while others have two maxima. Long ago it was found that all cycles are double peaked (Gnevyshev, 1963; Antalova and Gnevyshev, 1965), with the two peaks observed at different latitudes and supposedly caused by different physical mechanisms. Moreover, even if the solar activity progresses differently in the two hemispheres which leads to two peaks in global averages, two separate peaks are also observed in each of the hemispheres. Using the superposed method analysis for all eight sunspot cycles from 1874 to 1962, Antalova and Gnevyshev (1965) concluded that in all cycles the first peak appears simultaneously at all latitudes, and the second one only at low latitudes. Their relative amplitude and the time between them vary, therefore in some cycles they can be seen as a single peak in time averages, in other cycles the gap between them known as "Gnevyshev gap" is clearly seen.

Georgieva (2011) proposed an explanation of the two peaks. As is well known, in the course of the solar cycle sunspots appear in bipolar pairs at lower and lower heliolatitudes with the leading (in the direction of solar rotation) sunspot at lower heliolatitudes and with the polarity of the respective pole, and the trailing sunspot at higher heliolatitudes and with the opposite polarity. According to the flux-transport solar dynamo mechanism (Babkock, 1961; Leighton, 1964; Wang, 1991), late in the sunspot cycle when the sunspot pairs appear close to the equator, the leading polarity spots in each hemisphere diffuse across the equator and cancel with the opposite polarity spots of the other hemisphere. The trailing polarity spots of these sunspot pairs and the remaining complete pairs are carried poleward where they first cancel the polar field of the old cycle and then accumulate to form the opposite polarity field of the new cycle.

Two processes are responsible for this transport: supergranular diffusion, and large-scale meridional circulation, poleward at the surface and equatorward at the base of the convection zone where it carries like a conveyor belt the poloidal field which is there transformed by the differential rotation into toroidal field and emerges at lower and lower latitudes as sunspots of the new cycle. The regime of operation of the solar dynamo depends on their relative importance in carrying the flux to the pole. If the time scale of the meridional circulation is much shorter than the diffusion time scale (advection dominated regime), all of the flux will pass the whole way on the surface to the pole where it will reverse the polar field and then sink to the base of the convection zone. If the diffusion time scale is much shorter (diffusion dominated regime), all of the toroidal field is generated from the flux which has diffused to the base of the convection zone, shortcircuiting the merifional circulation. Only a small part of the trailing polarity flux reaches high latitudes before being diffused, and reverses the polar field there. In the intermediate case when neither of the two mechanisms is much more efficient than the other, some of the magnetic flux shortcuts the meridional circulation and diffuses directly to the bottom of the convection zone at mid-latitudes. Another part of the flux follows the path all the way to the poles, down to the base of the convection zone, and then equatorward to latitudes where sunspots tend to form (Figure 1). Estimations of the diffusivity and meridional circulation (Georgieva and Kirov, 2011) show that this is the regime in which solar dynamo has been recently operating. This leads to two surges of toroidal field: one generated by the flux shortcircuiting the meridional circulation due to diffusion, and one generated by the flux making the full circle poleward at the surface, down to the bottom of the convection zone at high latitudes, and equatorward from there. The diffusion-related peak appears simultaneously at a broad range of latitudes, while the advection-related one moves equatorward with time (Yeates et al., 2008). The order in which these two peaks appear, the time between them, and their relative amplitudes depend on the relative importance of diffusion and advection.

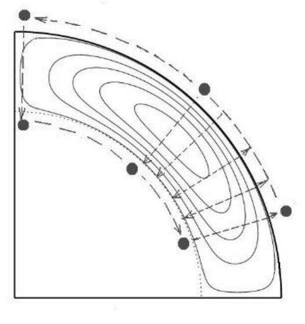

Figure 1. *Intermediate regime: a part of the flux diffuses through the convection zone, “short-circuiting” the meridional circulation, another part makes a full circle to the poles, down to the base of the convection zone and equatorward to sunspot latitudes.*

2. Data

For quantifying sunspot activity we use the sunspot area in 50 latitude bins distributed uniformly in Sine (latitude) for each Carrington rotation since 1874. This is the well known “Butterfly diagram” provided by Dr. David Hathaway from Stanford University (http://SolarCycleScience.com/).

3. Results

A comparison of cycle 12/14, and cycles 23/24 shows that both cycles 23 and 24 during the recent Gleissberg minimum have well expressed doule sunspot maxima, while the cycles during the previous Gleissberg minimum are almost all (with the exception of cycle 12) characterizes by single maxima (Figure 2).

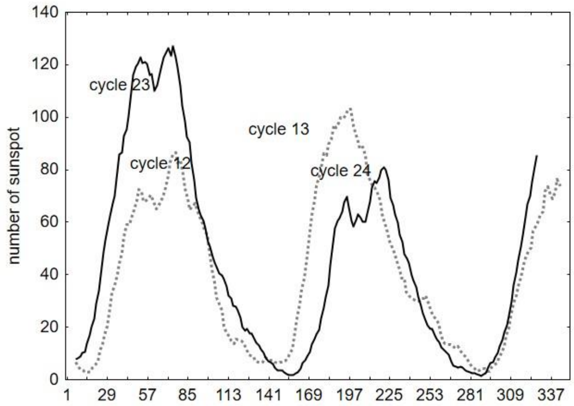

***Figure 2**. A comparison between cycles 12-14 during the 19-20th century Gleissberg minimum (dotted line) and cycles 23-25 during the 20-21st century Gleissberg minimum (solid line). X-axis: months since the beginning of the period studied; Y-axis: sunspot number (V1.0)*

To elucidate the temporal variation in sunspot activity, Figures 4 and 5 demonstrate the evolution of the latitude-time variations of the sunspot areas in the two hemispheres (upper panels), of global latitude-time sunspot areas (middle panels), and of the respective global averages for cycles 12-14 and 23-24, respectively.

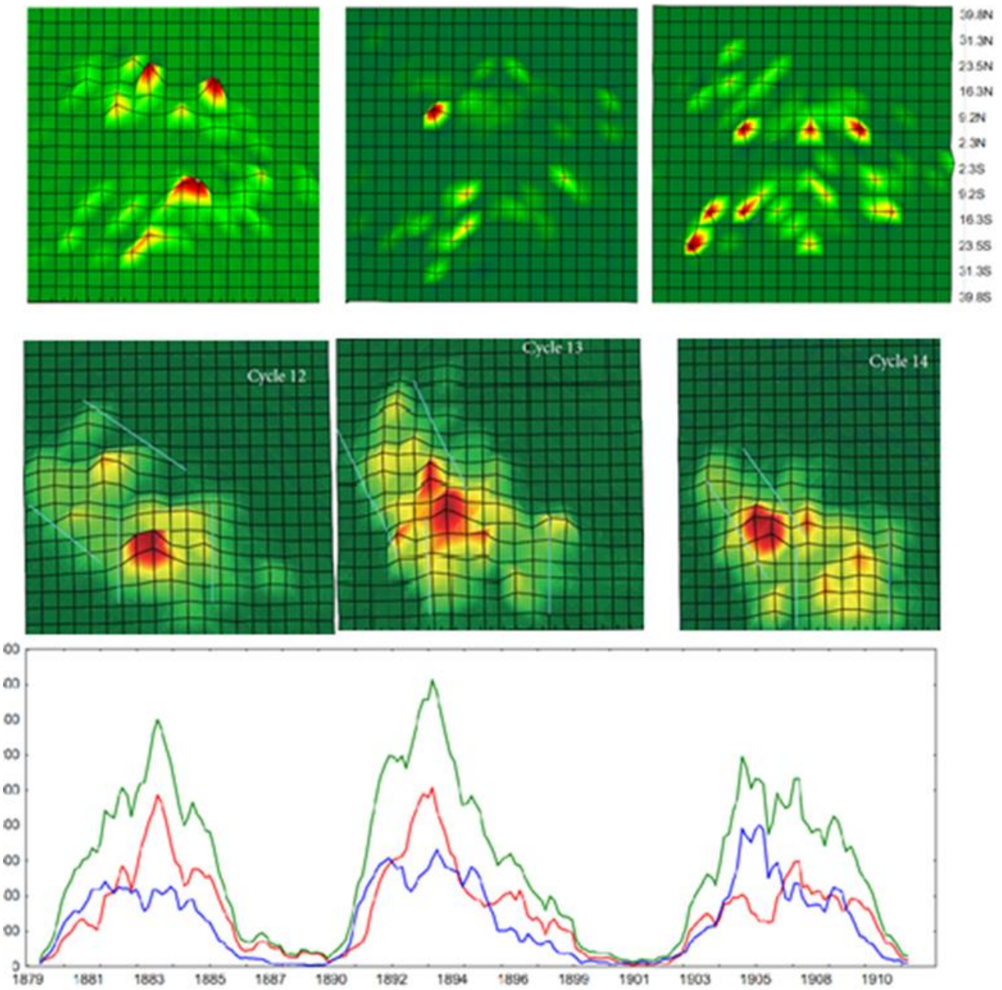

Figure 3. *Latitude-time evolution of sunspot area for sunspot cycles 12 – 14. Upper panel: in the two hemispheres; middle panel: averaged over the whole disk; bottom panel: green line – total sunspot area; red line – Southern hemisphere sunspot area; blue line – Northern hemisphere sunspot area.*

In cycle 12, the first surge (or rather a number of surges) of sunspots in the Southern hemisphere appeared at about 30o and moved equatorward. We identify this as the advection-generated sunspot activity region (Yeates et al., 2008). This region then merged with a second surge which appeared later in a wide range of latitudes with a peak at about 9^o, and persisted between 2^o and 26^o, slowly moving to the equator. We identify it as the diffusion-generated sunspot activity region. In the Nortern hemisphere, the sunspots first emerged in a broad latitudinal region between about 9 and 25^o with a maximum around 16^o, and persisted there (diffusion-generated), and the second surge started later at about 20^o and moved equatorward (advection-generated). The situation is similar in the following two cycles: first an advection-related peak followed by a diffusion-related peak in the Southern hemisphere, first a diffusion-related followed by an advection-relaated peak in the Northern hemisphere. In cycle 12 there is some time between the two surges in both hemispheres, so in global averages a clear Gnevyshev gap is observed. In cycles 13 and 14 the surges of sunspot appearance overlap, and distinctly separated maxima are not observed in global averages. In all three cycles the diffusion-generated peak is higher than the advection-generated one, and it determines the peak in global average.

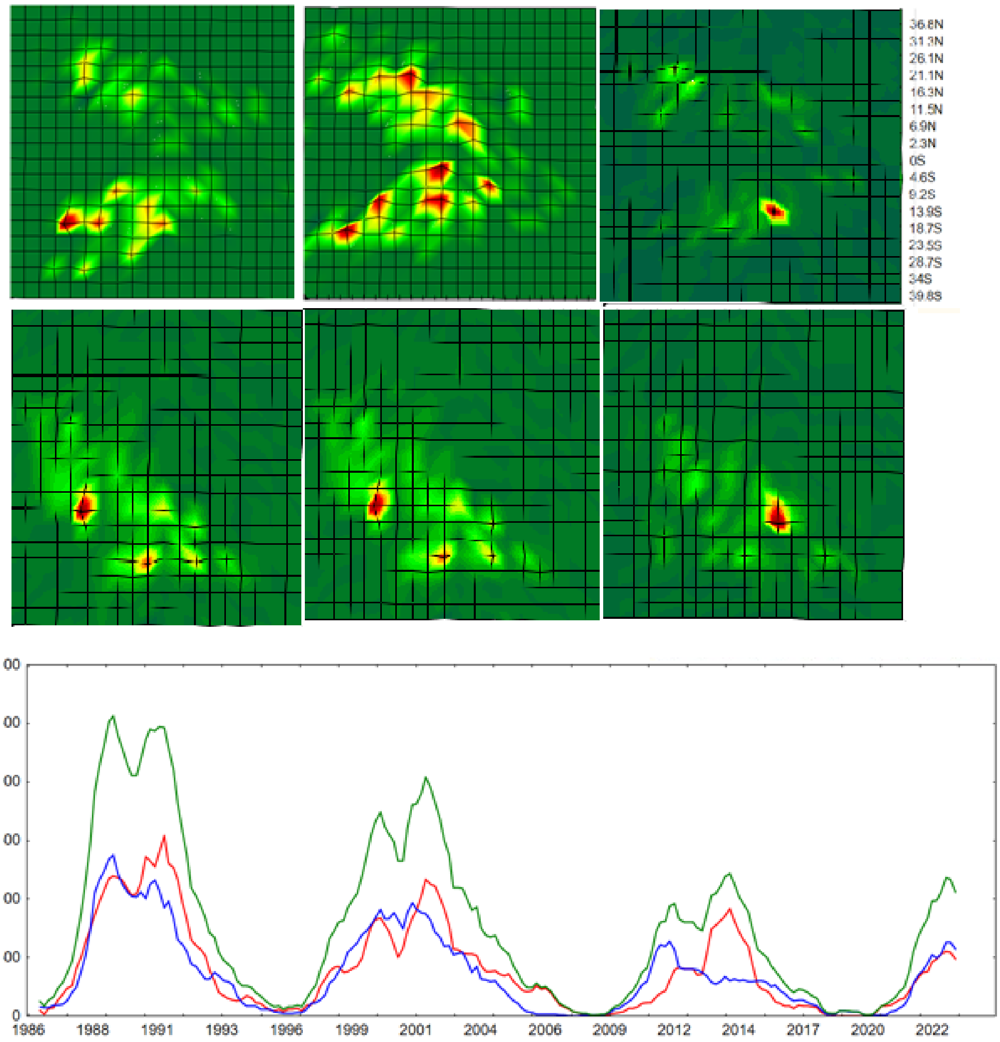

Figure 4. *The same as Figure 2 for cycles 22-24.*

In cycle 23 (Figure 4), the first sunspot surge in the Southern hemisphere was again advection-related. It started at about 30o and moved to the equator, on the way merging with the diffusion-related peak which emerged later between 28° and 2°. In the Northern hemisphere, the diffusion-generated surge started first at about 26° and expanded to about 2°, followed by a couple of advection-generated surges which continued for about 50 rotations. In the global average, the first sunspot peak was due to the superposition of the Southern hemisphere advection-generated maximum and the Northern hemisphere diffusion-generated maximum, while the second and higher one – mostly due to the Southern hemisphere advection-generated maximum.

In cycle 24 the advection-generated peak in the Southern hemisphere started at 24°, moved slowly almost to the equator, to 11°. At about 11° this advection-generated peak merged with the much stronger diffusion-generated peak spanning from 30° to 7° and persisting for many rotations until the end of 2018, a year before the start of the following cycle. The first, diffusion-generated peak, in the Northern hemisphere was also much stronger than the subsequent two advection-generated peaks. As a result, the global picture was dominated by the diffusion-generated peaks in the two hemispheres which were well separated in time, so a clear Gnevyshev gap was observed. It was in this case due not to the two distinct peaks in each of the hemispheres, but to the superposition of the dominant peaks in the two of them.

Also shown in Figure 4 for comparison is cycle 22 (1986-1996) where the first global sunspot maximim is due to the superposition of the advection-generated Southern hemisphere maximum and the diffusion-generated Northern hemisphere maximum, while the second global sunspot maximim is due to the superposition of the diffusion-generated Southern hemisphere maximum and the advection-generated Northern hemisphere maximum.

In summary, in both 19/20 and 20/21 century Gleissberg minima, each sunspot cycle began with an advection-generated followed by a diffusion-generated peak in the Southern hemisphere, and by a diffusion-generated followed by an advection-generated peak in the Northern hemisphere.

We have also checked the evolution of the sunspot activity in the two solar hemispheres for all cycles for which data are available (since 1874 up to present time, (http://SolarCycleScience.com/). We have found that the same pattern is observed in all sunspot cycles (not shown) with the exception of cycle 19 – the cycle of the secular sunspot maximum, which is quite a peculiar cycle.

4. Discussion

Some sunspot cycles have a single maximum in the number and area of sunspots, as well as in other manifestations of solar activity, while others are double peaked. Gnevyshev (1963) used the intensity of the coronal line 5303 Å at different heliolatitudes from 1954 to 1962 (sunspot cycle 19) and found that though the cycle featured a single maximum when averaged over all latitudes, the coronal intensity had actually two maxima: a first one at all latitudes, and then a second one only at low latitudes. Similar temporal distribution was found also in the data on sunspots and prominrnces, which led to the conclusion that these two maxima in the 11-year sunspot cycle are characteristic not only of the solar corona but of all layers in the solar atmosphere (Gnevyshev, 1963).

The 5303 Å coronal emission has been measured since 1939. To study the evolution of the sunspot cycles on a longer time-scale, Antalova and Gnevyshev (1965) used the sunspot areas published in the Greenwich Data Catalog from 1874 to 1958, and in the Pulkovo Solar Acrivity Catalog from 1959 until 1962, and found that actually all cycles are double peaked when looked at different latitudes. If the time between the peaks is short, they appear as a single peak in the time/latitude averages. If the peaks are well separated in time, the gap between them known as "Gnevyshev gap" is clearly seen. Using the superposed method analysis for all cycles from 12 to 19 at different latitudes, Antalova and Gnevyshev (1965) concluded that in all studied cycles the first peak appears simultaneously at all latitudes, and the second one only at low latitudes.

Gnevyshev (1963) speculated that the two peaks may be caused by different physical mechanisms. At that time the possible physical mechanisms causing peaks in sunspot acyivity were not identified. As mentioned in the Introduction, according to the Babkock-Leighton flux-transport solar dynamo mechanism (Babkock, 1961; Leighton, 1964), when the leading polarity spots in each hemisphere diffuse across the equator and cancel with the opposite polarity leading spots of the other hemisphere, the trailing polarity spots of these sunspot pairs and the remaining complete pairs are carried poleward by turbulent diffusion to first cancel the polar field of the old cycle and then accumulate to form the opposite polarity field of the new cycle. In the Babkock-Leighton flux-transport solar dynamo mechanism, turbulent diffusion was originally considered the only factor to transfer the toroidal field of a cycle into opposite-polarity poloidal field of the next cycle. Later Wang et al. (1991) proposed the large-scale meridional circulation as another important factor with a surface flow toward the poles where the poloidal field of the next cycle is generated with polarity opposite to the one in the preceding cycle, then the flow sinks to the base of the convection zone, and is carried equatorward by the counterflow there, on the way generating the toroidal field of the next cycle. The regime of operation of solar dynamo depends on the relative importance of diffusion and advection (meridional transport). If both factors are at work, the sunspot activity will have two peaks in the course of the solar cycle: diffusion-generated and afvection-generated (Georgieva, 2011). The diffusion-generated peak appears nearly simultaneously at all latitudes, and the afvection-generated one moves with time to the equator (Yeates et al., 2008).

The observation of Antalova and Gnevyshev (1965) that in all cycles the first peak (diffusion-generated) appears simultaneously at all latitudes, and the second one (advection-generated) only at low latitudes, was based on data averaged over the whole solar disk and over all cycles from 12 to 19 (superposed analysis). In the present study we looked at the sunspot activity evolution separately in the two solar hemispheres based on sunspot area data since 1874, and found that since cycle 12, in all cycles there is a well expressed hemispheric asymmetry: first an advection-related peak followed by a diffusion-related peak in the Southern hemisphere, first a diffusion-related followed by an advection-related one in the Northerm hemisphere. This pattern is the same during the last two Gleissberg minima (cycles 12-14, and 22-24, respectively), and the cycles between them, with the exception of cycle 19 in the secular solar maximum, which is anomalous in several respects and has long been recognized as peculiar. This means that there is no evidence that the global dynamo switched operating regimes between those secular minima.

Helioseismology further supports a hemispheric pathway to asymmetry. Long-term measurements reveal persistent north–south asymmetries in torsional oscillations that precede and correlate with hemispheric asymmetries in surface activity; the velocity asymmetry leads flux/sunspot asymmetry, suggesting a causal link (Lekshmi, Nandy & Antia, 2018; 2019). Such flow asymmetries provide a plausible physical conduit by which modest, early-cycle differences in deep-seated dynamics are amplified into measurable hemispheric phasing and amplitude differences at the surface—consistent with our finding that the diffusion-first versus advection-first sequencing can differ by hemisphere.

References

Antalová, A., Gnevyshev, M.N. (1965). Principal characteristics of the 11-year solar activity cycle, *Soviet Astronomy*, Vol. 9, No. 2, pp. 198–203.

Babcock, H.W. (1961). The topology of the Sun's magnetic field and the 22-year cycle, *Astrophysical Journal*, Vol. 133, pp. 572–580.

Georgieva, K. (2011). Why the sunspot cycle is double peaked, *ISRN Astronomy and Astrophysics*, Article ID 437838, DOI: 10.5402/2011/437838.

Georgieva, K., Kirov, B. (2011). Solar dynamo and geomagnetic activity, *Journal of Atmospheric and Solar–Terrestrial Physics*, Vol. 73, pp. 207–222.

Gleissberg, W. (1939). The 88-year cycle in solar activity, *The Observatory*, Vol. 62, pp. 158–159.

Gnevyshev, M.N. (1963). The corona and the 11-year cycle of solar activity, *Soviet Astronomy*, Vol. 7, pp. 311–318.

Leighton, R.B. (1964). Transport of magnetic fields on the Sun, *Astrophysical Journal*, Vol. 140, pp. 1547–1562, DOI: 10.1086/148058.

Lekshmi, B., Nandy, D., Antia, H.M. (2018). North–south asymmetry in torsional oscillations, *Astrophysical Journal*, Vol. 861, Art. 121, DOI: 10.3847/1538-4357/aacbd5.

Lekshmi, B., Nandy, D., Antia, H.M. (2019). Hemispheric precursors of solar cycle asymmetry, *Monthly Notices of the Royal Astronomical Society*, Vol. 489, pp. 714–722, DOI: 10.1093/mnras/stz2168.

Wang, Y.-M., Sheeley, N.R. Jr., Nash, A.G. (1991). A new solar cycle model including meridional circulation, *Astrophysical Journal*, Vol. 383, pp. 431–442, DOI: 10.1086/170800.

Yeates, A.R., Nandy, D., Mackay, D.H. (2008). Exploring the physical basis of solar cycle predictions: Flux transport dynamics and predictability, *Astrophysical Journal*, Vol. 673, pp. 544–556, DOI: 10.1086/524352.

DOI: 10.31401/WS.2025.proc.03

Proceedings of
the Seventeenth Workshop “Solar Influences on the Magnetosphere, Ionosphere and Atmosphere”
June, 2025

Daily and Monthly Predictions of the Maximum CME Speed Index for Solar Cycle 25 Using Simplex Projection Method

Gerçeker K., Kilcik A.

Department of Space Sciences and Technologies, Akdeniz University Faculty of Science, 07058, Antalya, Türkiye
kemalhangerceker@gmail.com , alikilcik@akdeniz.edu.tr

Abstract

Coronal Mass Ejections (CMEs) and their speed are not only important indicators of solar activity, but also for geomagnetic activity. In this study, we present daily and monthly predictions for Solar Cycle 25 using the Maximum CME Speed Index (MCMESI) and the Simplex Projection method. By generating both short-term (daily) and long-term (monthly) predictions for MCMESI, we demonstrate the predictability of this parameter. The monthly mean data set was derived from daily values, and predictions for the continuation of Solar Cycle 25 produced using monthly mean MCMESI. Both datasets cover the period from May 1999 to January 2025. Predictions generated from the monthly mean data suggest that Solar Cycle 25 is expected to complete in the mid-2030s. Solar Cycle 25 appears to be stronger than Solar Cycle 24 in terms of amplitude. For the daily predictions, we successfully postcasted (re-predicted) the last week of December 2024 and the first week of January 2025 on a daily basis.

Keywords: Coronal Mass Ejection; Linear Speed; Nonlinear Prediction

1. Introduction

Solar activity drives space weather, which can disturb satellites, radio links, navigation, and even power grids. Coronal mass ejections (CMEs) play an important role in space weather; the fast CMEs and the southward interplanetary magnetic field are closely linked to powerful geomagnetic storms (Gonzalez et al., 1999; Nitta & Mulligan 2021).

The Maximum CME Speed Index (MCMESI) is the speed of the fastest CME in a given day. Studies show that MCMESI tracks solar and geospace conditions and is related to geomagnetic indices such as Ap and Dst (Kilcik et al., 2011; Kilcik et al., 2020). Therefore, prediction of the MCMESI leads to geomagnetic activity prediction and helps protect against the effects of geomagnetic storms. For the prediction, we used Empirical Dynamic Modeling (EDM) and its Simplex Projection method, which learns system behavior directly from data using time-delay embeddings and nearest-neighbor projections, without assuming fixed equations. These types of methods have repeatedly shown strong short-term predictive skills in complex, partially chaotic systems (Sugihara & May 1990; Sugihara et al., 2012; Ye et al., 2015).

Recent daily/near-daily prediction efforts in space weather focus mainly on geomagnetic indices driven by upstream solar-wind/IMF data, with machine learning and nonlinear models achieving multi-hour to day-ahead skill (e.g., Dst and Kp). Examples include LSTM/GP hybrids for multi-hour Dst, recurrent models for day-ahead Kp from solar wind inputs, operational Dst models, and image-aided day-ahead Dst predictions (Gruet et al., 2018; Wang et al., 2023). However, daily predictions built directly on CME-based indices such as MCMESI remain rare, leaving an opportunity for targeted nonlinear modeling.

In this study, the MCMESI is evaluated as a predictive driver and Simplex Projection is applied to produce monthly and daily predictions for Solar Cycle 25. Short-horizon behavior (e.g., 3–4 days), where nonlinear methods typically perform best, is also bench-marked using

CME information compiled by the SOHO/LASCO CDAW catalog (Yashiro et al., 2004; Gopalswamy et al., 2009).

2. Data and Methods

The CME data were taken from the SOHO/LASCO CDAW CME Catalog (https://cdaw.gsfc.nasa.gov/CME_list/). Then we selected the fastest CME for each day. The monthly mean MCMESI was obtained as the arithmetic mean of the daily speed of this CME for the time period of May 1999–January 2025. The temporal variations of the daily and monthly MCMESI data sets are presented in Figure 1.

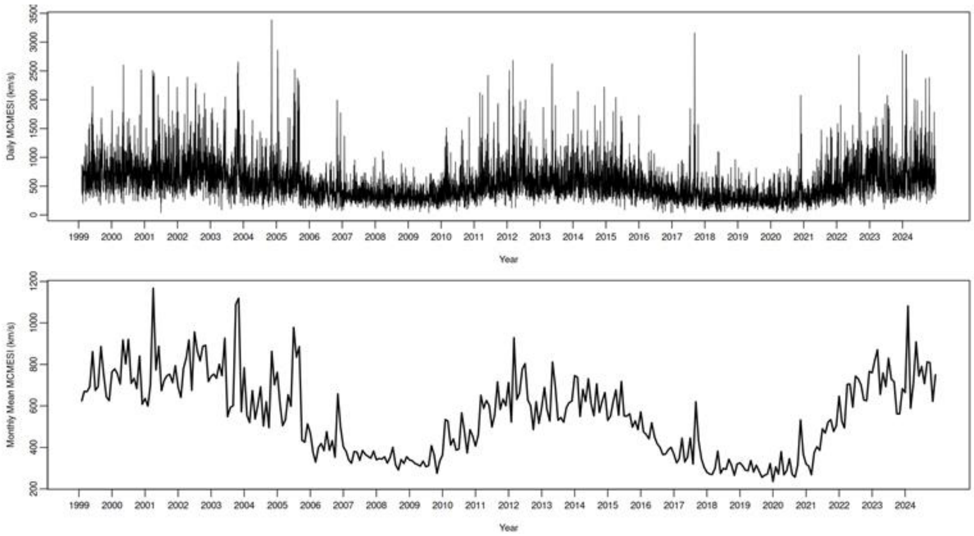

Figure 1. *Daily (top panel) and monthly mean (bottom panel) variations of the Maximum CME Speed Index (MCMESI).*

Following Takens' theorem (Takens 1981), the delay embedding

$$X(t) = [x(t), x(t-\tau), \dots, x(t-(E-1)\tau)], \qquad (1)$$

was formed, where $X(t)$ is the state vector, $x(t)$ the scalar observation, τ the time delay, and E the embedding dimension. Proper choices of E and τ allow the reconstructed attractor to preserve the relevant geometry of the original system and thus support prediction.

For a current state vector $X(t)$, the $E+1$ nearest neighbors $X_1, X_2, \dots, X_{E+1}$ are identified. Let ν_n denote the current state and ν_i a neighbor with Euclidean distance $\|\nu_n - \nu_i\|$. Using the provided notation, the predictions for horizons $1,2,\dots,T_a$ are computed as

$$Pred_{[1,2,\dots,T_a]} = \sum_{i=1}^{E+1} \omega_i \, \nu^1_{(i+[1,2,\dots,T_a])}, \qquad (2)$$

with exponential distance weights

$$\omega_i = \frac{exp(-\|\nu_n - \nu_i\|/\omega_{avg})}{\sum_{j=1}^{E+1} exp\left(-\|\nu_n - \nu_j\|/\omega_{avg}\right)}, \qquad (3)$$

where ω_{avg} is the average scaling factor. Multi-step predictions are obtained by iterating $Pred_{[1,2,\dots,T_a]}$. This equation-free, state-dependent procedure is standard in EDM and is well supported in nonlinear prediction (Sugihara 1990; Sugihara 2012; Ye 2015).

For the monthly data, the last 12 months were excluded from the data, and the first 12 predicted points were compared with the known excluded observations. For the daily series, the last 9 days data were excluded; the first 2 of these were used only for model selection, while the remaining 7 days were kept strictly unobserved and predicted forward. The selection was based on two complementary skill criteria; the Mean Absolute Error (MAE),

$$MAE = \frac{1}{N}\sum_{i=1}^{N}|x_i - \bar{x}|, \tag{4}$$

measure the average amplitude error in km/s and the Pearson correlation coefficient ρ,

$$\rho = \frac{\sum_{i=1}^{N}(x_i - \bar{x})(y_i - \bar{y})}{\sqrt{\sum_{i=1}^{N}(x_i - \bar{x})^2}\sqrt{\sum_{i=1}^{N}(y_i - \bar{y})^2}}, \tag{5}$$

Short-term behavior is emphasized on 3–4 day predictions. This is consistent with the general expectation that predictive ability in chaotic systems decreases with predefined time.

Possible values for E and τ were specified in advance $(E = 2 - 10, \tau = 1 - 30)$. The split points defining the end of the library set and the beginning of the prediction set were sequentially scanned across a large portion of the data set, and all (E, τ) combinations were tested at each split point. Predictions for each scenario were generated based on ρ and MAE calculations. The best configurations were taken to be those yielding the highest ρ and lowest MAE values. The selected combinations were then used to generate the final predictions.

Simplex Projection method reconstructs the state space from a single time series and predicts by using the nearest past states and a distance-weighted average of their futures; no fixed equations are assumed, and only the embedding dimension E, time delay τ, and split point must be set. This equation-free, geometry-based design makes the approach data-efficient, easy to update as new values arrive, and appropriate when records are limited. In practice, short horizons are favored: daily predictions performed best for about 3–4 days, while longer (e.g., 7-day) horizons can still be produced with the expected loss of skill. These properties make Simplex Projection a natural choice for MCMESI and for other solar/geomagnetic indices that exhibit state-dependent behavior.

3. Results

The monthly MCMESI series was produced by averaging the daily MCMESI from May 1999 to January 2025. To test true out-of-sample skill, the last 12 months data (January–December 2024) were excluded from the data as a validation block. For Simplex Projection parameter combinations, candidate (E, τ) and split point values were predetermined within a certain range; a continuation model was created for each candidate starting from January 2024. The first 12 predicted points were then compared with the held-out observations using ρ and MAE, and the settings giving highest ρ and lowest MAE were retained. The selected configuration was finally used to produce the monthly cycle continuation presented in Figure 2.

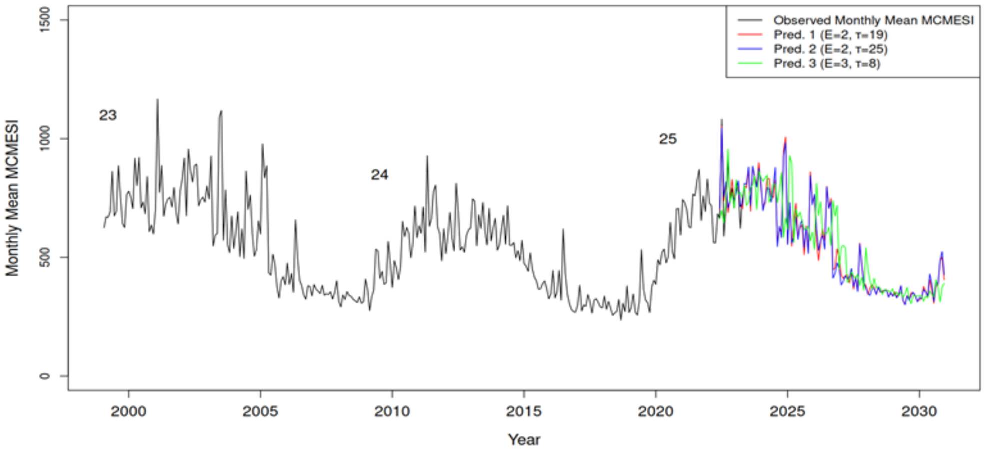

Figure 2. *Predictions for the continuation of Solar Cycle 25 produced using monthly mean MCMESI.*

A total of 90 monthly predictions were generated for the monthly data (12 held-out months of 2024 plus a 78-month period). The best-performing settings were determined by comparing the first 12 prediction points with the 12 held-out observations using MAE and ρ; the configuration with the highest ρ and lowest MAE value was ranked highest. The three best-performing configurations were retained, and their cycle continuations are shown in Figure 2. These continuations indicate that Solar Cycle 25 is stronger than Solar Cycle 24 in terms of the amplitude of the MCMESI, but slightly weaker or similar to Solar Cycle 23. The trajectories show a steady decline after 2025, with the cycle completing in the early to mid-2030s. High activity is also projected between 2024 and 2027, indicating the period of most intense geoeffective conditions in this cycle.

The daily MCMESI series was analyzed with the same Simplex Projection framework. To evaluate true short-horizon skill, 9 end-of-record values were withheld (the last week of 2024: 2 points used only for model selection and 7 points kept strictly unseen for prediction). Candidate (E, τ) and split point sets were pre-specified; three best combinations were retained based on the highest ρ and lowest MAE, and used to generate the 7-day forward predictions as shown in Figure 3.

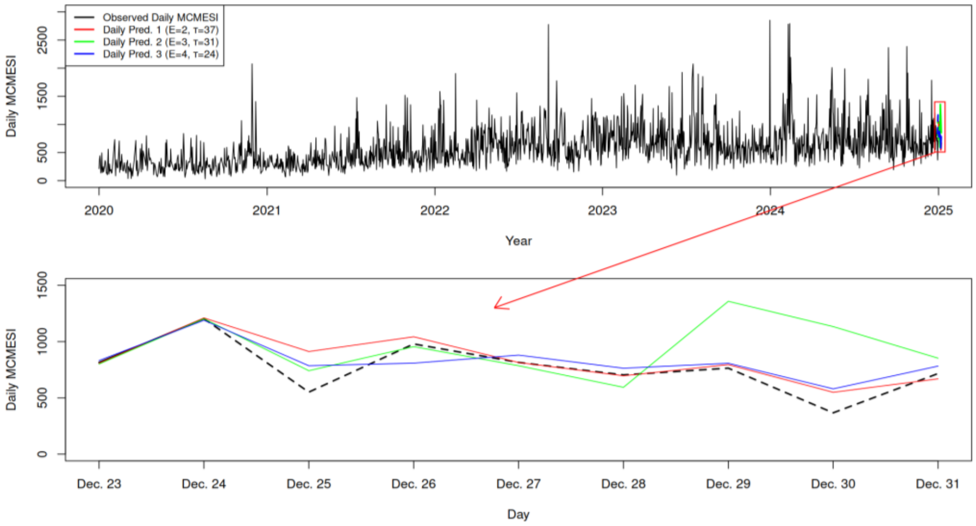

Figure 3. *Predictions for the last 9 days (2 observed + 7 considered unobserved) of 2024 generated using daily MCMESI values.*

As a first step, the three most successful predictions selected are closely aligned with the 2 observed points, indicating that the current situation is well captured. Over the next 7 days, the predicted trajectories reproduce the week's development in both shape and amplitude quite well, indicating good short-term prediction performance for the daily MCMESI.

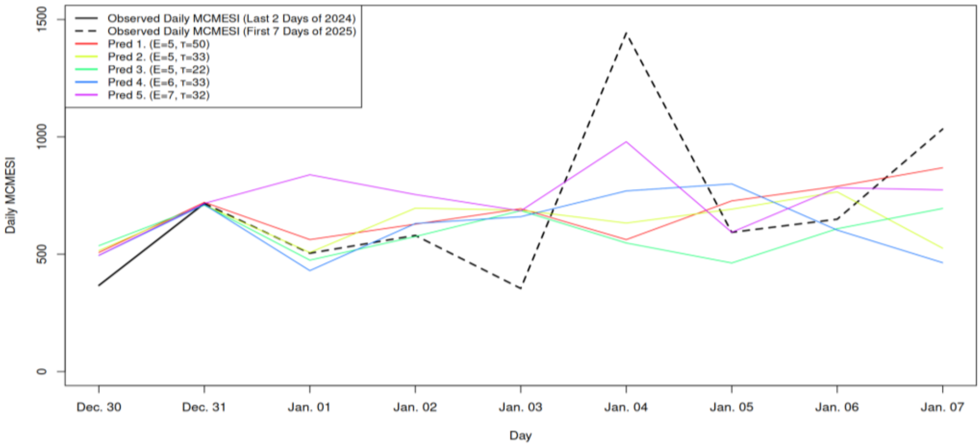

Figure 4. *Daily MCMESI predictions across the 2024→2025 boundary using a 2+7 setup. Predictions were initialized with the last 2 observed days of 2024 (Dec 30–31) and extended over 7 unobserved days (Jan 1–7, 2025); the subsequently published Jan 1–7 observations are overplotted as a dashed black line for validation.*

As shown in Figure 4, 9 days were analyzed using the 2+7 design as we entered 2025: the last 2 days of 2024 were used for parameter selection, and the following 7 days were predicted. Five predictions from the retained (E, τ) combinations are displayed in the figure. The most successful settings involved higher embedding dimensions E than in the previous week, suggesting a more complex state-space in the first week of 2025. The predictions and observations made during the first three days (January 1-3) showed good agreement, but in subsequent stages, performance declined as expected with increasing time. If the prediction had been initialized on Jan 3 (i.e., using three observed points for selection), the Jan 4 peak would likely have been captured more accurately. Overall, week-long predictions are feasible, but for precision and operational use, 3–4 day horizons are generally preferable.

From the monthly predictions, Solar Cycle 25 was predicted to exceed Cycle 24 in maximum CME-speed amplitude and to be slightly weaker or comparable to Cycle 23; activity was projected to decline after ~2025, with cycle completion in the early–mid 2030s. The 2024–2027 interval was identified as the most active part of the cycle, implying the highest geoeffectivity. In the daily analysis, the 2+7 design produced close agreement for the first 3–4 days, while skill decreased at longer times; in some weeks, higher embedding dimensions (E) were selected, indicating temporally varying complexity in the dynamics. Overall, Simplex Projection was applicable and efficient method for MCMESI prediction. While 3–4-day time intervals are recommended for predictions, a one-week prediction can be published with appropriate precautions.

4. Conclusion and Discussion

In this study, MCMESI-based predictions were performed on a monthly and daily basis using the Simplex Projection method. The findings of the study are as follows:

1. Solar Cycle 25 is stronger than Solar Cycle 24 in MCMESI amplitude and slightly weaker or comparable to Solar Cycle 23.

2. 2024–2027 is indicated as the most geo-effective interval of Solar Cycle 25. MCMESI activity declines after ~2025; cycle completion is predicted for early–mid 2030s.
3. For daily predictions, best agreement occurs over ~3–4 days; week-long predictions are feasible but show the expected loss of skill with time.
4. It has been proven that the Simplex Projection method can be applied to monthly and especially daily MCMESI data.

Based on monthly data, our MCMESI predictions indicate that Solar Cycle 25 (SC25) has exceeded SC24 and is slightly weaker than or comparable to SC23, with activity declining after ~2025 and reaching a minimum in the early to mid-2030s. This picture is broadly consistent with prediction-oriented cycle studies that anticipated SC25 to be similar to or somewhat stronger than SC24 and peaking near 2024 (e.g., Bhowmik & Nandy 2018), while remaining well below the most optimistic “very strong SC25” scenarios inferred from terminator-based arguments (McIntosh et al., 2020). It also sits between competing physics-based predictions that predicted either a weaker-than-SC24 (Upton & Hathaway 2018) or a substantially stronger one (McIntosh et al., 2020), and is consistent with review assessments of SC25 predictions that emphasized the spread across methods (Petrovay 2020).

On a daily basis, the 2+7-day design provided the highest compatibility for ~3–4 days, followed by the expected skill loss over longer periods. This short-horizon character aligns with operational geomagnetic-index prediction results: data-driven/ML and hybrid models for Dst and Kp typically achieve multi-hour to day-ahead skill but degrade with time (e.g., Temerin & Li 2006; Gruet et al., 2018; Hu et al., 2023). Our CME-based prediction tool, which relies on a single series, provides useful predictions for 3–4 days without upstream solar wind inputs, but shares the same fundamental limitation of decreasing accuracy over time.

Relative to event-level CME arrival time prediction, our approach plays a complementary role. Physics-based and drag-based systems (e.g., WSA–ENLIL+Cone, DBM/DBEM) generally report typical absolute arrival-time errors of order 10–15 hours and are strongest when detailed CME parameters are available; ensemble variants quantify uncertainty. In contrast, MCMESI-Simplex, rather than predicting the arrival time of individual CMEs, provides continuous predictions at the index level regarding amplitude and short-term evolution, indicating periods of high activity. Combining event timing models for specific CME events with MCMESI's index-level predictions can provide perspectives on both when and how they will be active (e.g., Mays et al., 2015; Napoletano et al., 2022).

Finally, higher embedding dimensions likely reflect temporally varying state complexity. This behavior has also been observed in studies where model skill depends on prevailing solar-wind/CME conditions.

Acknowledgements

This study was supported by Project 124N011 awarded by the Scientific and Technological Research Council of Türkiye (TÜBİTAK). We would also like to thank the Bulgarian Academy of Sciences (BAS) for their partial support.

References

Bhowmik, P., Nandy, D. (2018). Prediction of the strength and timing of sunspot cycle 25 reveal decadal-scale space environmental conditions, *Nature Communications*, Vol. 9, 5209, DOI: 10.1038/s41467-018-07690-0.

Gonzalez, W.D., Tsurutani, B.T., Clúa de Gonzalez, A.L. (1999). Interplanetary origin of geomagnetic storms, *Space Science Reviews*, Vol. 88, No. 3, pp. 529–562, DOI: 10.1023/A:1005160129098.

Gopalswamy, N., Yashiro, S., Michalek, G., Stenborg, G., Vourlidas, A., Freeland, S., Howard, R. (2009). The SOHO/LASCO CME catalog, *Earth, Moon, and Planets*, Vol. 104, No. 1, pp. 295–313, DOI: 10.1007/s11038-008-9282-7.

Gruet, M.A., Chandorkar, M., Sicard, A., Camporeale, E. (2018). Multiple-hour-ahead forecast of the Dst index using a combination of long short-term memory neural network and Gaussian process, *Space Weather*, Vol. 16, No. 11, pp. 1882–1896, DOI: 10.1029/2018SW001898.

Hu, A., Camporeale, E., Swiger, B. (2023). Multi-hour-ahead Dst index prediction using multi-fidelity boosted neural networks, *Space Weather*, Vol. 21, No. 4, e2022SW003286, DOI: 10.1029/2022SW003286.

Kilcik, A., Chowdhury, P., Sarp, V., Yurchyshyn, V., Donmez, B., Rozelot, J.P., Ozguc, A. (2020). Temporal and periodic variation of the MCMESI for the last two solar cycles; comparison with the number of different class X-ray solar flares, *Solar Physics*, Vol. 295, No. 11, 159, DOI: 10.1007/s11207-020-01711-2.

Kilcik, A., Yurchyshyn, V.B., Abramenko, V., Goode, P.R., Ozguc, A., Rozelot, J.P., Cao, W. (2011). Time distributions of large and small sunspot groups over four solar cycles, *Astrophysical Journal*, Vol. 731, No. 1, 30, DOI: 10.1088/0004-637X/731/1/30.

Mays, M.L., Taktakishvili, A., Pulkkinen, A., MacNeice, P.J., Rastätter, L., Odstrčil, D., Kuznetsova, M.M. (2015). Ensemble modeling of CMEs using the WSA–ENLIL+ Cone model, *Solar Physics*, Vol. 290, No. 6, pp. 1775–1814, DOI: 10.1007/s11207-015-0692-1.

McIntosh, S.W., Chapman, S., Leamon, R.J., Egeland, R., Watkins, N.W. (2020). Overlapping magnetic activity cycles and the sunspot number: Forecasting sunspot cycle 25 amplitude, *Solar Physics*, Vol. 295, No. 12, 163, DOI: 10.1007/s11207-020-01723-y.

Napoletano, G., Foldes, R., Camporeale, E., de Gasperis, G., Giovannelli, L., Paouris, E., Del Moro, D. (2022). Parameter distributions for the drag-based modeling of CME propagation, *Space Weather*, Vol. 20, No. 9, e2021SW002925, DOI: 10.1029/2021SW002925.

Nitta, N.V., Mulligan, T., Kilpua, E.K., Lynch, B.J., Mierla, M., O'Kane, J., Zhukov, A.N. (2021). Understanding the origins of problem geomagnetic storms associated with "stealth" coronal mass ejections, *Space Science Reviews*, Vol. 217, No. 8, 82, DOI: 10.1007/s11214-021-00857-0.

Petrovay, K. (2020). Solar cycle prediction, *Living Reviews in Solar Physics*, Vol. 17, No. 1, 2, DOI: 10.1007/s41116-020-0022-z.

Sugihara, G., May, R., Ye, H., Hsieh, C.-H., Deyle, E., Fogarty, M., Munch, S. (2012). Detecting causality in complex ecosystems, *Science*, Vol. 338, No. 6106, pp. 496–500, DOI: 10.1126/science.1227079.

Sugihara, G., May, R.M. (1990). Nonlinear forecasting as a way of distinguishing chaos from measurement error in time series, *Nature*, Vol. 344, No. 6268, pp. 734–741, DOI: 10.1038/344734a0.

Takens, F. (1981). Detecting strange attractors in turbulence, in: Rand, D., Young, L.-S. (eds), *Dynamical Systems and Turbulence, Warwick 1980*, *Lecture Notes in Mathematics*, Vol. 898, Springer, Berlin, Heidelberg, DOI: 10.1007/BFb0091924.

Temerin, M., Li, X. (2006). Dst model for 1995–2002, *Journal of Geophysical Research: Space Physics*, Vol. 111, A4, DOI: 10.1029/2005JA011257.

Upton, L.A., Hathaway, D.H. (2018). An updated solar cycle 25 prediction with AFT: The modern minimum, *Geophysical Research Letters*, Vol. 45, No. 16, pp. 8091–8095, DOI: 10.1029/2018GL078387.

Wang, J., Luo, B., Liu, S., Shi, L. (2023). A machine learning-based model for the next 3-day geomagnetic index (Kp) forecast, *Frontiers in Astronomy and Space Sciences*, Vol. 10, 1082737, DOI: 10.3389/fspas.2023.1082737.

Yashiro, S., Gopalswamy, N., Michalek, G., St. Cyr, O.C., Plunkett, S.P., Rich, N.B., Howard, R.A. (2004). A catalog of white light coronal mass ejections observed by the SOHO spacecraft, *Journal of Geophysical Research: Space Physics*, Vol. 109, A7, DOI: 10.1029/2003JA010282.

Ye, H., Beamish, R.J., Glaser, S.M., Grant, S.C., Hsieh, C.-H., Richards, L.J., Sugihara, G. (2015). Equation-free mechanistic ecosystem forecasting using empirical dynamic modeling, *Proceedings of the National Academy of Sciences*, Vol. 112, No. 13, pp. E1569–E1576, DOI: 10.1073/pnas.1417063112.

DOI: 10.31401/WS.2025.proc.04

Solar Cycle Variation of Sustained Gamma-ray Emission Events from the Sun and Related Energetic Events

Gopalswamy N.[1], *Mäkelä P.A.*[1,2], *Akiyama S.*[1,2], *Yashiro S.*[1,2], *Xie H.*[1,2]

[1]NASA Goddard Space Flight Center, Greenbelt, MD 20771, USA
nat.gopalswamy@nasa.gov
[2]The Catholic University of America, Washington DC 20064

Abstract

The sustained gamma-ray emission (SGRE) from the Sun is one of the fascinating high-energy phenomena closely related to the acceleration of protons to energies >300 MeV. Here we report on the solar cycle variation of SGRE events based on observations from Fermi's Large Area Telescope (LAT). This report covers solar cycles (SCs) 24 and 25 during which Fermi has been operating. Since SGRE events are closely related to solar energetic particle (SEP) events and interplanetary type II radio bursts caused by fast and wide coronal mass ejections (CMEs), we consider these phenomena as well. Many studies have shown that SC 25 is similar or slightly stronger than SC 24. The number of SEP events, GLE events, IP type II bursts, and fast and wide CMEs confirm this conclusion. However, the number of SGRE events observed by Fermi/LAT has diminished significantly in SC 25 relative to SC 24. One of the issues has been the reduced coverage of the Sun since 2018 due to a mechanical problem with a solar array of the Fermi mission. By identifying the Fermi/LAT gaps and the number of energetic events (fast and wide CMEs, interplanetary type II bursts) we conclude that about three times more SGRE events must have occurred than the 15 events observed by Fermi.

Keywords: sustained gamma-ray emission; solar cycle; solar energetic particle events.

1. Introduction

The sustained gamma-ray emission (SGRE) from the Sun lasts well beyond the impulsive phase of the associated solar flare. The emission is due to the decay of neutral pions suggesting that the underlying >300 MeV particles might have the same origin as large solar energetic particle (SEP) events [Forrest et al. 1985]. For more than two decades since their discovery, only a handful SGRE events were detected by various instruments [see Chupp and Ryan 2009]. The situation changed when the Fermi satellite was launched in 2008. Fermi's Large Area Telescope (LAT, Atwood et al. [2009]) detected dozens of events in solar cycles (SCs) 24 and 25 [Share et al. 2018; Allafort 2018; Ajello et al. 2021]. These observations show a close relation among SGRE events, interplanetary (IP) type II bursts, SEP events, and energetic (fast and wide) coronal mass ejections (CMEs). The physical connection can be understood as follows: energetic CMEs drive strong shocks that accelerate electrons and protons. The accelerated electrons give rise to type II radio bursts, while the >300 MeV protons propagate to the Sun from the shock downstream, interact with the dense atmosphere, and produce neutral pions that decay into gamma-rays. Energetic particles from the shock upstream escape into space to be detected as SEP events by spacecraft. CMEs underlying SGRE events possess properties similar to CMEs producing ground level enhancement (GLE) in SEP events [Gopalswamy et al. 2018]. Many shocks continue to accelerate particles until Earth and even beyond and thus are capable of supplying energetic particles over a long period of time to sustain the gamma-ray emission. This is also indicated by the ending frequency of the associated IP type II bursts indicating shocks efficiently accelerating electrons survive for long distances from the Sun. One of the implications for the shock source of >300 MeV protons is that the SGRE source needs to be extended – tens of degrees – around the eruption site. The occurrence of SGRE in association with eruptions occurring tens of degrees behind the limb strongly support the shock paradigm [Pesce-Rollins et al. 2015; Plotnikov et al. 2017; Jin et al. 2017; Gopalswamy et al. 2020; 2025]. Another potential source of >300 MeV protons is the flare reconnection region. Particles accelerated in the reconnection region can get trapped into post-eruption arcade (PEA) loops and can precipitate to the photosphere causing impulsive gamma-rays [Ryan and Lee 1991; de Nolfo et al. 2019]. These sources are necessarily compact (a maximum extent of ~15 degrees). Sustaining energetic protons in such loops to account of the long-duration SGRE requires unusual turbulence conditions [Kanbach et al. 1993]. In this paper, we take CME-driven shocks as the source of energetic particles responsible for SGRE.

In section 3, we compare the SGRE and associated events occurring during the first 61 months of SCs 24 (December 2008 to December 2013) and 25 (December 2019 to December 2024). These epochs roughly include the rise and maximum phases of the two cycles. In section 4, we estimate the number of SGRE events, considering the sunspot number, SEP events, fast and wide (FW) CMEs, and IP type II bursts identified during Fermi/LAT data gaps that started in March 2018. In section 5, we provide our summary and conclusions.

2. Observations

Fermi/LAT observations are available at https://hesperia.gsfc.nasa.gov/fermi_solar/ up to date and in the published catalogs for SC 24 [Share et al. 2018, Allafort 2018, and Ajello et al. 2021]. CME, SEP, and type II burst data are from the CDAW data center [https://cdaw.gsfc.nasa.gov, Yashiro et al. 2004; Gopalswamy et al. 2009; 2010; 2019; Gopalswamy et al. 2024]. Details on the solar array drive anomaly (SODA) including various observing modes employed are available in the Fermi web site (https://fermi.gsfc.nasa.gov/ssc/observations/types/post_anomaly/). In order to extract the times of Sun exposure, we make use of the information provided in the Fermi Timeline web site: https://fermi.gsfc.nasa.gov/ssc/observations/timeline/posting/. For solar cycle reference, we use the sunspot number (SSN) V2.0 available from the Sunspot Index and Long-term Solar Observations (SILSO) maintained at https://wwwbis.sidc.be/silso/infosnmtot. Solar wind data to characterize the solar cycle variation of the heliospheric state are obtained from NASA's OMNI database (https://omniweb.gsfc.nasa.gov/).

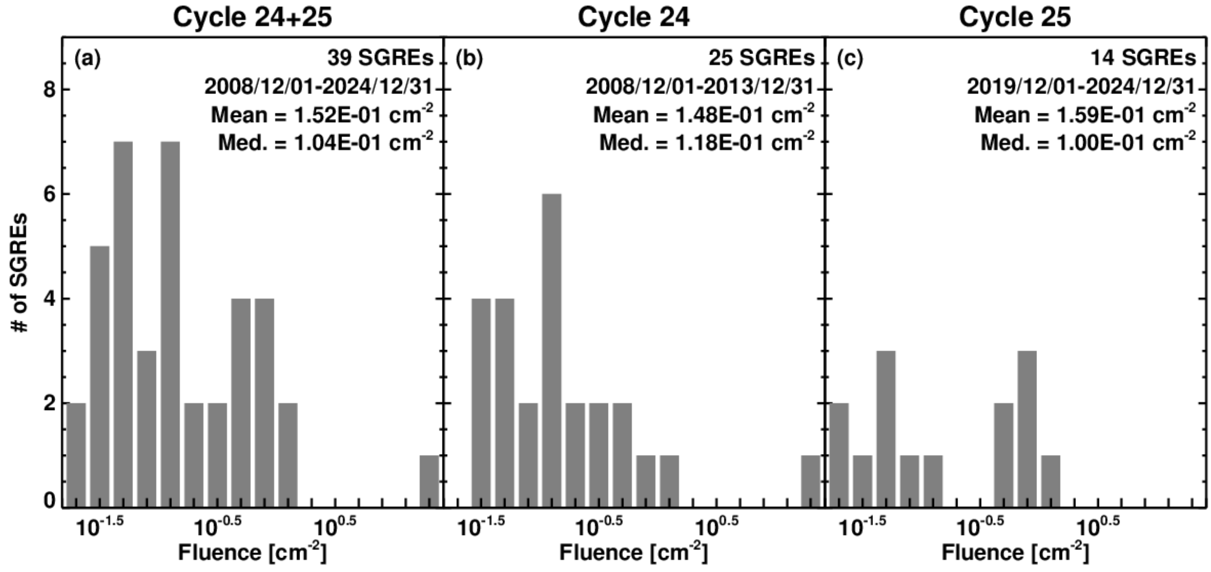

Figure 1. *Histograms of SGRE fluence in SCs 24 and 25 (a), SC 24 (b), and SC 25 (c).*

Figure 1 shows fluence distributions of SGRE events that occurred during the first 61 months in SCs 24 and 25. The number of SGRE events in SC 24 is much higher in SC 25. The mean values are very similar in the two cycles, but smaller than the mean value (0.49 cm^{-2}) over the whole of SC 24 [Gopalswamy et al. 2019]. Thus, the primary difference seem to be the number of events between the two cycles. Figure 2 shows the histograms of the SGRE durations over the first 61 months in SCs 24 and 25. The duration distributions are similar, although the mean values are slightly smaller in SC 25. Over the whole of cycle 24, the average duration is larger by a factor of 2. The duration comparison is probably influenced by the large SODA-related data gaps in Fermi/LAT observations since March 2018 (see later).

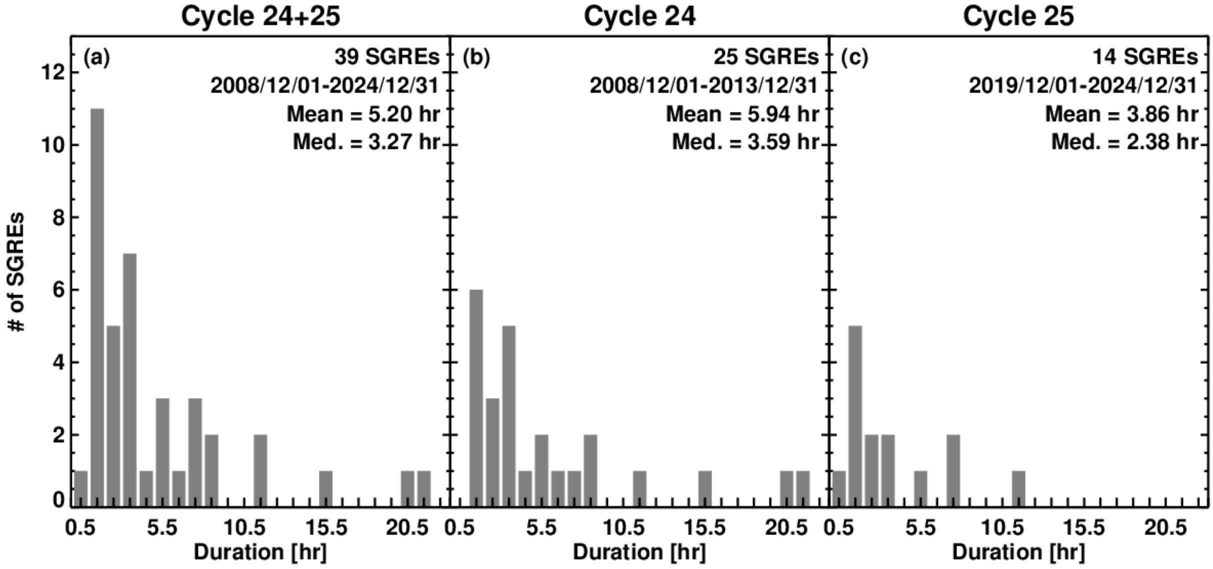

***Figure 2**. Histograms of SGRE durations in SCs 24 and 25 (a), SC 24 (b), and SC 25 (c).*

2.1. Overview of SGRE Events

Table 1 compares the number of energetic events related to SGRE between SCs 24 and 25 over the first 61 months in each cycle: CMEs, SEPs, geomagnetic storms, decameter-hectometric (DH) type II bursts, and solar wind properties. The solar wind properties are listed because they can influence the properties of CMEs and their interaction with the solar wind medium and hence their ability in causing SEPs and geomagnetic storms. The SILSO sunspot number (SSN) averaged over the first 61 months are 56.9 and 79.0, respectively, indicating that SC 25 is ~39% stronger than SC 24, opposite of what happened between SCs 23 and 24 [Gopalswamy et al. 2014; 2015a]. The number of SGRE events shows a decline of ~44% in SC 25 with a similar decline (~40%) when normalized to SSN. SC 25 has been very active at the maximum phase, with a significantly larger number of halo CMEs observed in SC 25. However, the halo CME abundance normalized to the SSN decreased by ~7%, which is consistent with the fact that weaker cycles have a higher halo CME abundance [Gopalswamy et al. 2015b]. The number of FW (speed $V \geq 900$ km/s and width $W \geq 60^o$) CMEs and DH type II bursts normalized to the SSN increased by 29% and 33%, respectively in SC 25. The number of major flares (soft X-ray flare class M1.0 or higher) normalized to the SSN increased by 182%. The number of large SEP events (proton intensity ≥10 pfu) in SC 25 decreased by 17% when normalized to SSN. However, the number of GLE events in SC 25 quadrupled compared to SC 24, indicating that normalized number shows an increase of 150%. The number of intense geomagnetic storms (Dst ≤ -100 nT) in SC 25 increased by 50%, although when normalized to SSN, the increase is ~ 6%. Halo CMEs, FW CMEs, SEPs, GLEs, and DH type II bursts are also closely associated with SGREs. Of these halo CMEs are influenced by heliospheric pressure, while SEPs are affected by the magnetic connectivity of the eruption region to GOES. The remaining ones, viz., FW CMEs and DH type II bursts have similar solar cycle variation because DH type II bursts are produced by FW CMEs [Gopalswamy et al. 2001]. While all the energetic events indicate a stronger cycle 25, the SGRE events has the opposite trend. We expect the number of SGREs roughly follow the solar cycle variation of FW CMEs and DH type II bursts. The number of SGRE events normalized to the number of DH type II bursts is 0.25 in SC 24, whereas it drops to 0.08 in SC 25. This is clearly abnormal, which we analyze in detail in the following subsections.

Table 1. *Number (#) of energetic event and solar wind properties in Solar Cycles 24 and 25*

Property	SC 24	SC 25	Ratio
Averaged SSN	56.9	79.0	1.39
#SGRE events	25 (0.44)	14 (0.18)	0.56 (0.4)
#Halo CMEs	192 (3.37)[a]	247 (3.12)	1.29 (0.93)
# FW CMEs V≥900 km/s & W≥60^{o}	149 (2.62)	268 (3.39)	1.80 (1.29)
#DH Type II bursts	99 (1.74)	183 (2.32)	1.85 (1.33)
#≥M1.0 flares	389 (6.84)	1525 (19.30)	3.92 (2.82)
#≥10 pfu SEP events	30 (0.53)	35 (0.44)	1.17 (0.83)
# GLE events	1 (0.02)	4 (0.05)	4.0 (2.50)
# Intense storms (Dst ≤ -100 nT)	12 (0.21)	18 (0.23)	1.5 (1.06)
#SGRE/#FW CMEs	0.17	0.05	0.31
#SGRE/#DH type II	0.25	0.08	0.30
#SGRE/#SEP events	0.83	0.40	0.48
Total Pressure (pPa)	27.1	32.6	1.20
Magnetic field strength B (nT)	4.92	5.50	1.12
Bulk speed V km/s	399	410	1.03
Proton density N (cm^{-3})	5.07	5.62	1.11
Proton temperature T (10^5 K)	0.75	0.88	1.18
Alfven Speed V_A (km/s)	47.9	50.9	1.06

[a] The numbers within parentheses are normalized to the average SSN

2.2. Solar Wind Parameters

The number of energetic events such as GLEs and intense geomagnetic storms is known to decrease more drastically than SSN when the heliospheric state is weak [Gopalswamy et al. 2014; 2015a]. The heliospheric state is discerned from in-situ observations made by spacecraft at Sun-Earth L1. The dominant factor that characterizes the heliospheric state is the total pressure (magnetic + gas) in the heliosphere. We made use of OMNI data to derive the total pressure from the observations of magnetic field strength, solar wind plasma density, and temperature. The monthly averages of the derived/measured quantities are plotted in Figure 3: solar wind bulk speed, total pressure, magnetic field, density, temperature, and Alfven speed. We see that the total pressure averaged over the first 61 months in SC 25 increased by 20% compared to SC 24, somewhat smaller than the increase in SSN. The combined increases of solar wind magnetic field, density and temperature can readily account for the increase in total pressure. With higher heliospheric pressure, one does not expect energetic events to decline in SC 25. In fact, we see an increase in the number of energetic events such as GLEs and intense geomagnetic storms (Table 1). The reduction in the halo CME abundance normalized to SSN in SC 25 is consistent with the increased heliospheric pressure [Gopalswamy et al. 2014; 2015b]. While the solar wind speed did not change significantly, the Alfven speed increased by ~6%. If the higher Alfven speed measured at 1 au applies to the near-Sun ambient medium, one expects that it is harder to form shocks and hence might have contributed partially to the reduction in the normalized number of large SEP events in SC 25.

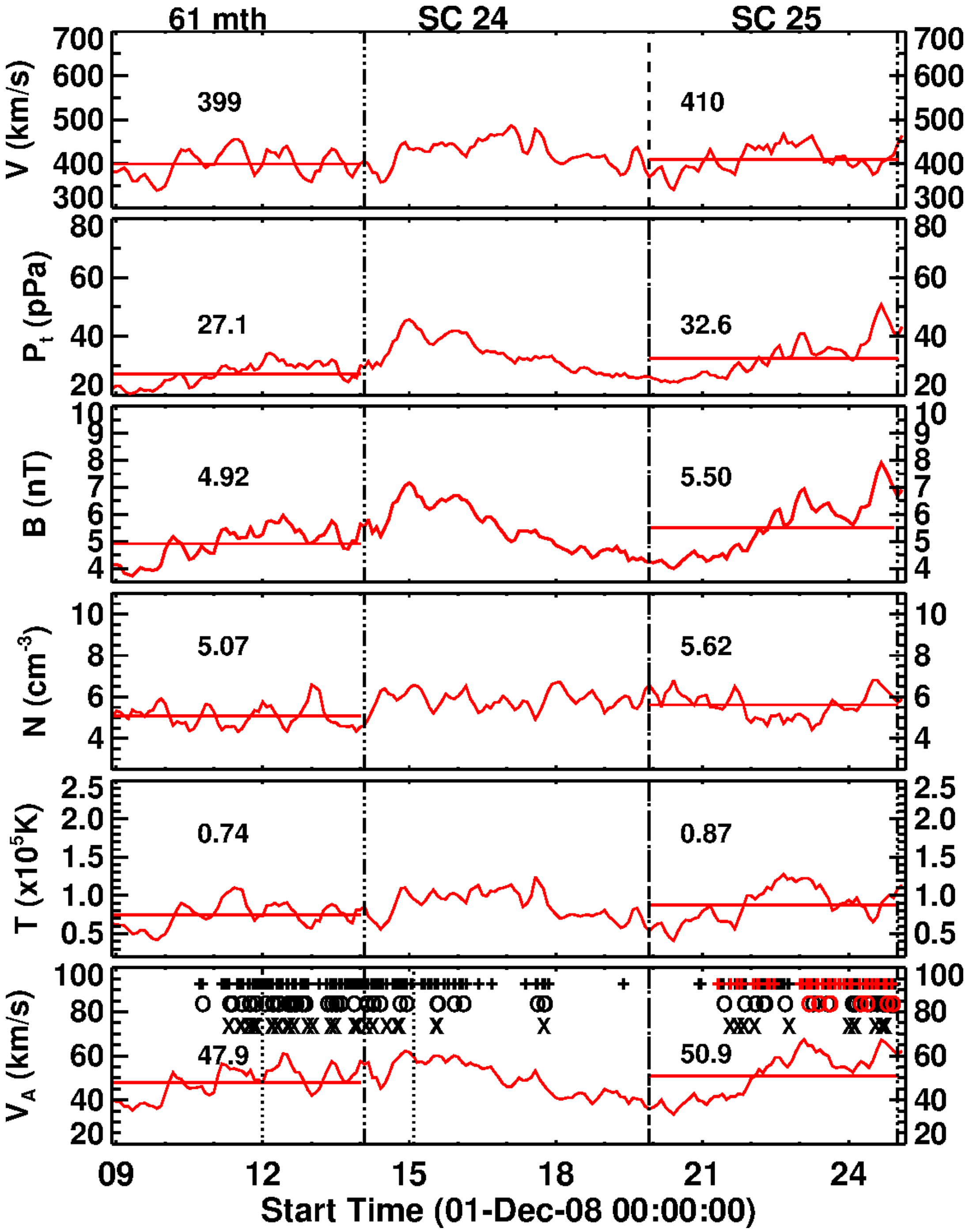

Figure 3*. Solar wind parameters from 2009 to 2024: bulk speed (V), total pressure (Pt), magnetic field strength (B), density (N), temperature (T), Alfven speed (V_A). The corresponding epochs (first 61 months) in the two cycles are indicated by the horizontal red lines and the average value of each parameter over the epochs is noted and listed in Table 1. For example, the average V_A is 48.2 km/s in SC 24 and 51.1 km/s in SC 25. The three rows of symbols in the bottom (V_A) panel mark occurrence dates of DH type II bursts (+), SEP events (O) and SGRE events (X). The symbols in red denote events occurring during Fermi/LAT data gaps. The vertical dashed lines in the bottom panel mark the maximum phase in SC 24.*

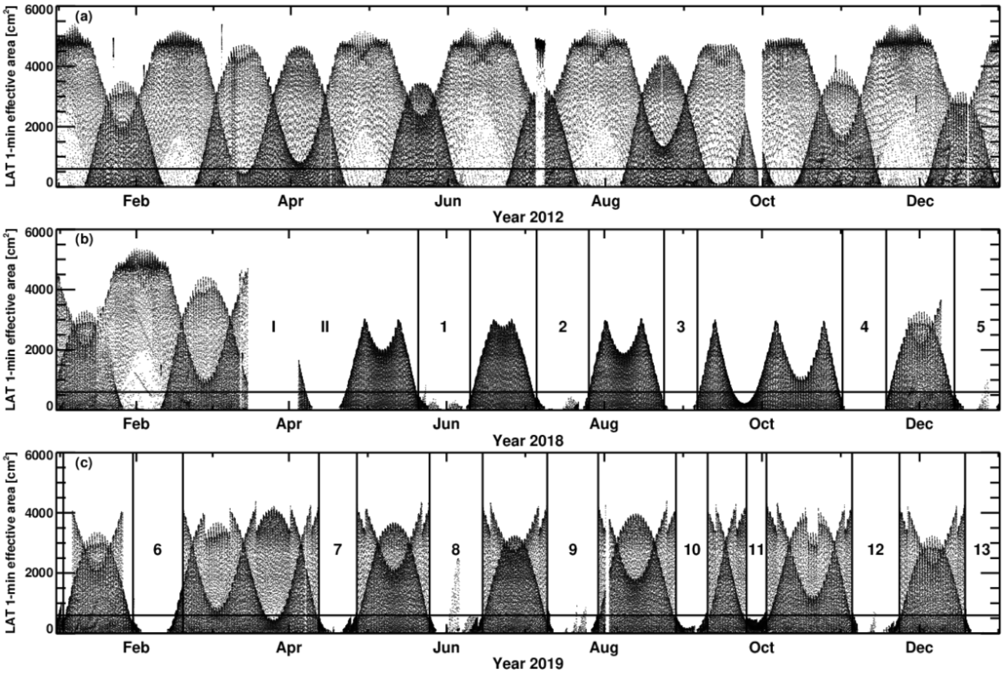

Figure 4. *Plots of solar exposures during the years 2012 (a), 2018 (b), and 2019 (c). The horizontal lines in each panel at a 1-min exposure area of 650 cm^2 represents the cutoff value. Note that the exposure gaps start in 2018 March. Gaps (I) and (II) in March and April 2018 represent the transition period before new observing modes are established. Gaps 1-13 represent the lack of solar exposure in the remaining months of 2018 and the whole of 2019. The complicated exposure profile is due to Fermi using different survey modes (two-sided rocking (+/- 50 deg survey or 50/60 deg asymmetric survey) against the rate for modified sine observations) interleaved throughout the year depending on the position of the Sun relative to the orbit plane. During the exposure gaps, the modified sine is used.*

2.3. *Fermi/LAT Data Coverage in SC 25*

In this section we examine Fermi/LAT timeline of observations to investigate the SODA-related reduction in solar coverage that started in 2018. Although the solar array is fully functional, the solar array in question got stuck at an angle to the LAT boresight because the drive assembly is not able to rotate the array. In order for the stuck array to be illuminated, the Sun is kept toward the edge of the LAT field of view resulting in a reduced exposure with LAT. After identifying the intervals of SODA-related data gaps, we also identify energetic events such as FW CMEs, DH type II bursts, and large SEP events.

Figure 4 illustrates the reduction in solar exposure using plots for the pre-anomaly year 2012, the anomaly year 2018, and the year 2019 that is fully under the reduced capability. Comparing the plots for the year 2012 (panel a) and 2019 (panel c) in Fig. 4, we see two important changes. (i) there are SODA-related large gaps (1-3 weeks at a time) in the Sun exposure, and (ii) the maximum LAT effective area is reduced to below 4000 cm^2 in 2019 and later years compared to a maximum of 5500 cm^2 in the pre-anomaly period. The gaps are substantial, so any SGRE event occurring during these gaps will not be counted. We also manually examined the Fermi/LAT 4-day quick look plots (https://hesperia.gsfc.nasa.gov/fermi_solar/) to identify extended intervals with no Sun exposure. We see that there are 8 intervals of large data gap in the year 2019. These intervals are consistent with the modified sine observations during which there was no Sun exposure. For example, the gap marked 6 in panel Fig. 4c started at 19:44 UT on 23 January 2019 and ended at 03:52 UT on 16 February 2019, amounting a gap of ~24 days.

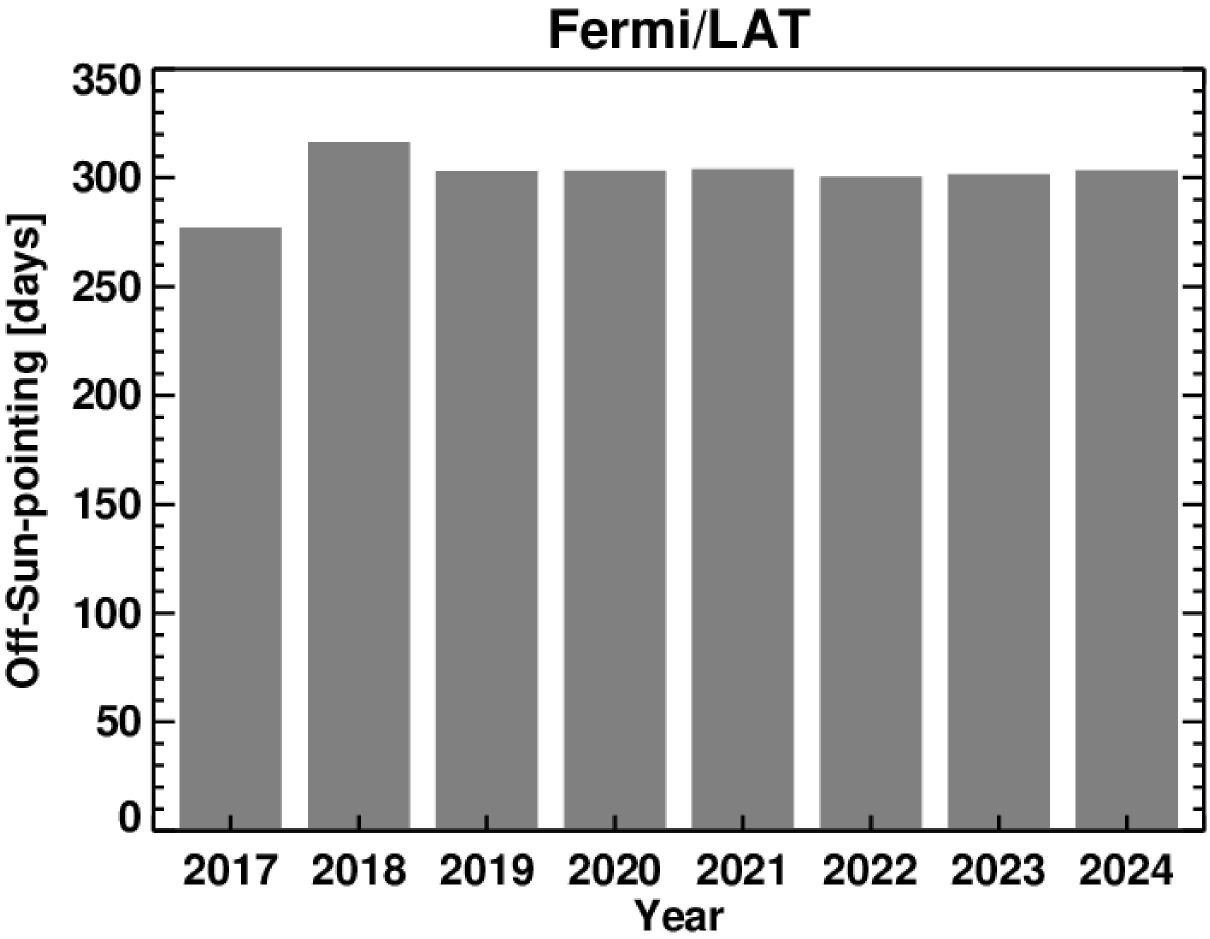

Figure 5. *Effective number of days per year during which the Sun had no Fermi/LAT exposure. As before, the data for the pre-anomaly year 2017 is compared with the post-anomaly years. In 2017, there was no Sun exposure for ~275 days. In 2018, new observing mode was being established, so there was no Sun exposure for ~315 days. During later years (2019-2024), there were no Sun exposures for ~305 days. Note that the normal level of Sun exposure during the pre-anomaly years is ~90 days per year because of the 96 min orbit (only 48 min on the dayside) during which the Sun exposure is typically for ~30 min. This is the reason for Fermi/LAT having no Sun exposure for 275 days in the pre-anomaly years. In other words, the effective number of days that Fermi/LAT had Sun exposure decreased from ~90 days per year to ~60 days per year because of the SODA incident.*

Counting all the gaps, we have plotted in Fig. 5 the effective number of days during which Fermi/LAT was not pointed to the Sun. For the pre-anomaly period, we have taken 2017 as the representative year for reference. In the pre-anomaly years, the total Sun exposure per year is only ~90 days, counting all the Sun exposures (typically ~30 min per 96-min orbit) with effective LAT area ≥ 600 cm^2. The anomaly year 2018 had a larger reduction because of the planning activities for new observing modes suitable for the SODA situation (the total annual Sun exposure was ~50 days). In the years after 2018, the Sun exposure was between 60 and 65 days, which corresponds to a reduction of ~ 30% compared to pre-anomaly years.

During each of the gap intervals, we identified and counted the number of energetic events FW CMEs, DH type II bursts, and large SEP events in the appropriate catalogs available at the CDAW data center (https://cdaw.gsfc.nasa.gov). The DH type II bursts and SEP events identified in the gaps are marked with red symbols in the bottom panel of Fig. 3, while the black symbols denote events occurring outside of LAT gaps. We can see a large number of DH type II bursts and SEP events in SC 25 as was also listed in Table 1. During the entire year 2023, there was only one SGRE event (2023 December 31 event that extended to 2024 January 1), although there were many DH type II bursts and SEP events. There were 9 LAT gaps in this year, and each gap had at least one DH type II burst with a total number of 28. On the other hand, we counted only 7 large SEP events during 3 gaps; 6 gaps did not have any SEP event, although some occurred during high background from previous events. There were 55 DH type II bursts and 12 SEP events that occurred outside of the gaps in 2023. The number of LAT gaps is similar in the year 2024, the year of second SSN peak. However, there were several SGRE events in 2024 when LAT had Sun exposure. Table 2 lists the number of FW CMEs, DH type II bursts, and large SEP events that occurred during the gaps and outside the gaps. We see that most of the energetic events occurred during the solar maximum years (2022-2024). Therefore, we expect more SGRE events during these maximum years.

Table 2. *Number of LAT data gaps and energetic events in solar cycle 25*

Year	#SGRE	#LAT DG	#FW CMEs	#IP Type II	#SEP Events
2018	0	7	0 (0)	0 (0)	0 (0)
2019	0	8	0 (0)	1 (0)	0 (0)
2020	0	8	2 (0)	2 (0)	0 (0)
2021	2	8	11 (1)	15 (4)	2 (0)
2022	4	8	61 (19)	34 (8)	5 (0)
2023	1	9	86 (30)	55 (28)	12 (7)
2024	8	9	108 (35)	77 (39)	16 (6)

3. Estimating the number of SGRE events in SC 25

We now estimate the total number of SGRE events in SC 25 including those observed during and outside of the LAT data gaps. (i) Let us look at the 30% overall reduction in Sun exposure in SC 25. If we assume that SGRE events in SC 25 occurred with the same rate as in SC 24, we expect about 30% more events in SC 25, viz., ~33 events. (ii) The estimate in (i) does not take in to account the fact that solar activity is stronger in SC 25. From Table 1, we see that the SSN increased by 39%. One can argue that the number of SGRE events must be proportionately higher in SC 25 based on the fact that energetic CMEs generally originate from active regions. The normalized number of SGRE events SC 24 is 0.44. Multiplying this by 1.39, we get the normalized number of SGRE events in SC 25 as 0.61. This gives the total number of SGRE events in SC 25 to be ~48 (0.61 × 79.0). This indicates that ~33 events must have occurred during LAT gaps in SC 25. (iii) One of the main CME properties relevant to SGRE is that the underlying CMEs are energetic (FW). In SC 24, 17% of FW CMEs were associated with SGRE. If the association rate remains the same in SC 25, out of the 268 FW CMEs observed in SC 25, ~46 should have resulted in SGRE. This number is not too different from the estimate using SSN increase. (iv) DH type II bursts have been shown to have a quantitative relationship with SGRE events in terms of their duration and ending frequency [Gopalswamy et al. 2018]. The number of DH type II bursts in SC 25 nearly doubled (183) compared to that (99) in SC 24. If the 25% association rate of DH type II bursts with SGRE in SC 24 holds for SC 25, we expect ~46 SGRE events. This number is the same as that derived from FW CMEs because FW CMEs and DH type II bursts are closely related.

If we apply the rates in (iii) and (iv) to the number of FW CMEs and DH type II bursts in the LAT gaps, we get only ~15 and ~20 SGRE events, respectively in the gaps. Combining these numbers with the 15 observed SGRE events, we get 30 and 35 events based on the FW CME and DH type II observations. Interestingly, these numbers agree with the estimate based on the reduction in Sun exposure (i). We must point out that we have not examined other smaller (non-

SODA) Fermi/LAT data gaps that are not part of the SODA-related data gaps. Therefore, the estimates from the SODA-related gaps alone are likely underestimated. There are other ways to characterize the SGRE association rate based on DH type II bursts. For example, Share et al. [2018] reported that almost all SGRE events are associated with >100 keV hard X-ray bursts during the eruption. Results of such an investigation will be reported elsewhere.

4. Summary and Conclusions

We investigated the solar cycle variation of the number of SGRE events during the first 61 months in SC 25 as compared to a corresponding epoch in SC 24. We attribute the primary reason for the reduction to the reduced solar coverage by Fermi/LAT following the solar array drive anomaly that started in March 2018. We estimated that the solar coverage decreased by ~30% after the anomaly. We identified 8-9 Fermi/LAT data gaps per year related to the drive anomaly. The gap intervals typically lasted for 1-3 weeks until the end of 2024 during which fermi/LAT did not observe the Sun. However, 85 FW CMEs and 79 DH type II bursts occurred during these gaps, mostly during the maximum years 2021-2024 suggesting that more SGRE events must have occurred during these gaps. The lowest estimate of the total number of SGRE events (33) was obtained based on the reduction in Sun exposure. Estimates based on the increase in SSN, FW CMEs, and DH type II bursts are 48, 46, and 46, respectively. All these estimates do indicate that SC 25 is stronger than SC 24 from the SGRE point of view as well.

Acknowledgments

This work was supported by NASA's STEREO project, the Living with a Star program, and the Internal Science Funding Model project. HX, SA, and SY are partially supported by NSF grant AGS-2228967. We thank Elizabeth Hays, Fermi Project Scientist, for discussion on the 2018 solar array drive anomaly.

References

Atwood, W.B., Abdo, A.A., Ackermann, M., Althouse, W., Anderson, B., Axelsson, M., et al. (2009). The Large Area Telescope on the Fermi Gamma-Ray Space Telescope mission, *Astrophysical Journal*, 697, 1071, https://doi.org/10.1088/0004-637X/697/2/1071.

Ajello, M., Baldini, L., Bastieri, D., et al. (2021). First Fermi-LAT Solar Flare Catalog, *Astrophysical Journal Supplement Series*, 252, 13, https://doi.org/10.3847/1538-4365/abd32e.

Allafort, A.J. (2018). High-energy gamma-ray observations of solar flares with the Fermi Large Area Telescope, *PhD Thesis*, Stanford University.

Chupp, E.L., Ryan, J.M. (2009). High energy neutron and pion-decay gamma-ray emissions from solar flares, *Research in Astronomy and Astrophysics*, 9, 11, https://doi.org/10.1088/1674-4527/9/1/003.

de Nolfo, G.A., Bruno, A., Ryan, J.M., et al. (2019). Comparing long-duration gamma-ray flares and high-energy solar energetic particles, *Astrophysical Journal*, 879, 90, https://doi.org/10.3847/1538-4357/ab258f.

Forrest, D.J., Vestrand, W.T., Chupp, E.L., et al. (1985). Neutral pion production in solar flares, *Proceedings of the 19th International Cosmic Ray Conference (ICRC19)*, 4, 146.

Gopalswamy, N., Yashiro, S., Kaiser, M.L., Howard, R.A., Bougeret, J.-L. (2001). Characteristics of coronal mass ejections associated with long-wavelength type II radio bursts, *Journal of Geophysical Research*, 106(A12), 29219, https://doi.org/10.1029/2001JA000234.

Gopalswamy, N., Yashiro, S., Michalek, G., Stenborg, G., Vourlidas, A., Freeland, S., Howard, R. (2009). The SOHO/LASCO CME catalog, *Earth, Moon, and Planets*, 104, 295, https://doi.org/10.1007/s11038-008-9282-7.

Gopalswamy, N., Yashiro, S., Michalek, G., et al. (2010). A catalog of halo coronal mass ejections from SOHO, *Sun and Geosphere*, 5, 7.

Gopalswamy, N., Akiyama, S., Yashiro, S. (2014). Anomalous expansion of coronal mass ejections during solar cycle 24 and its space weather implications, *Geophysical Research Letters*, 41, 2673, https://doi.org/10.1002/2014GL059858.

Gopalswamy, N., Yashiro, S., Xie, H., Akiyama, S., Mäkelä, P. (2015a). Properties and geoeffectiveness of magnetic clouds, *Journal of Geophysical Research*, 120, 9221, https://doi.org/10.1002/2015JA021446.

Gopalswamy, N., Xie, H., Akiyama, S., Mäkelä, P., Yashiro, S., Michalek, G. (2015b). The peculiar behavior of halo coronal mass ejections in solar cycle 24, *Astrophysical Journal Letters*, 804, L23, https://doi.org/10.1088/2041-8205/804/1/L23.

Gopalswamy, N., Mäkelä, P., Yashiro, S., Lara, A., Xie, H., Akiyama, S., MacDowall, R.J. (2018). Interplanetary type II radio bursts from Wind/WAVES and sustained gamma-ray emission from Fermi/LAT: Evidence for shock source, *Astrophysical Journal Letters*, 868, L19, https://doi.org/10.3847/2041-8213/aaef36.

Gopalswamy, N., Mäkelä, P., Yashiro, S. (2019a). A catalog of type II radio bursts observed by Wind/WAVES and their statistical properties, *Sun and Geosphere*, 14, 111.

Gopalswamy, N., Mäkelä, P., Yashiro, S., Lara, A., Akiyama, S., Xie, H. (2019b). On the shock source of sustained gamma-ray emission from the Sun, *Journal of Physics: Conference Series*, 1332(1), 012004, https://doi.org/10.1088/1742-6596/1332/1/012004.

Gopalswamy, N., Mäkelä, P., Yashiro, S., et al. (2020). Source of energetic protons in the 2014 September 1 sustained gamma-ray emission event, *Solar Physics*, 295, 18, https://doi.org/10.1007/s11207-020-1590-8.

Gopalswamy, N., Michalek, G., Yashiro, S., et al. (2024). The SOHO LASCO CME catalog – Version 2, *Proceedings of IAU Symposium 388*, https://arxiv.org/abs/2407.04165.

Gopalswamy, N., Mäkelä, P., Akiyama, S., et al. (2025). Multispacecraft observations of the 2024 September 9 backside solar eruption that resulted in a sustained gamma-ray emission event, *Solar Physics*, 300, 120, https://doi.org/10.1007/s11207-025-02526-9.

Jin, M., Petrosian, V., Liu, W., et al. (2018). Probing the puzzle of behind-the-limb gamma-ray flares: Data-driven simulations of magnetic connectivity and CME-driven shock evolution, *Astrophysical Journal*, 867, 122, https://doi.org/10.3847/1538-4357/aae1fd.

Kanbach, G., Bertsch, D.L., Fichtel, C.E., et al. (1993). Detection of a long-duration solar gamma-ray flare on June 11, 1991 with EGRET on COMPTON-GRO, *Astronomy and Astrophysics Supplement Series*, 97, 349.

Pesce-Rollins, M., Omodei, N., Petrosian, V., et al. (2015). First detection of >100 MeV gamma rays associated with a behind-the-limb solar flare, *Astrophysical Journal Letters*, 805, L15, https://doi.org/10.1088/2041-8205/805/2/L15.

Plotnikov, I., Rouillard, A.P., Share, G.H. (2017). The magnetic connectivity of coronal shocks from behind-the-limb flares to the visible solar surface during gamma-ray events, *Astronomy and Astrophysics*, 608, A43, https://doi.org/10.1051/0004-6361/201730804.

Ryan, J.M., Lee, M.A. (1991). On the transport and acceleration of solar flare particles in a coronal loop, *Astrophysical Journal*, 368, 316, https://doi.org/10.1086/169695.

Share, G.H., Murphy, R.J., White, S.M., Tolbert, A.K., Dennis, B.R., Schwartz, R.A., Smart, D.F., Shea, M.A. (2018). Characteristics of late-phase >100 MeV gamma-ray emission in solar eruptive events, *Astrophysical Journal*, 869, 182, https://doi.org/10.3847/1538-4357/aaebf7.

Yashiro, S., Gopalswamy, N., Michalek, G., St. Cyr, O.C., Plunkett, S.P., Rich, N.B., Howard, R.A. (2004). A catalog of white light coronal mass ejections observed by the SOHO spacecraft, *Journal of Geophysical Research*, 109, A07105, https://doi.org/10.1029/2003JA010282.

DOI: 10.31401/WS.2025.proc.05

Proceedings of
the Seventeenth Workshop “Solar Influences on the Magnetosphere, Ionosphere and Atmosphere”
June, 2025

3D Speed Reconstruction of CME Events during Solar Cycle 24

Hedz S.[1], *Tsvetkov Ts.*[2]

[1]Independent Researcher
[2]Institute of Astronomy and National Astronomical Observatory, Bulgarian Academy of Sciences,
Sofia, Bulgaria
tstsvetkov@astro.bas.bg

Abstract

Coronal mass ejections (CMEs) are a form of solar activity that has a major influence on space weather and requires further investigation of its properties. Calculating their 3D velocities allows for better understanding of their origin and true structure. We analyzed the correlation between the 2D velocities measured by SOHO/LASCO observations and the 3D velocities of 14 events of solar cycle 24, reconstructed using the StereoCAT online tool that allows simultaneous multi-instrumental measurements. Despite our relatively small sample and that StereoCAT analysis is subject to limitations, including human selection of tie-points, varying spacecraft viewing geometries, and incomplete data coverage for some events, we found extremely strong relationship between projected and “true” velocity of explored CMEs.

Keywords: coronal mass ejections; corona; magnetic fields

1. Introduction

CMEs constitute sudden expulsions of dense clouds of plasma from the outer atmosphere of the Sun. The various origins of CMEs include solar flares (SFs), eruptive prominences and nonequilibrium magnetic field configurations [Wagner, 1984]. CMEs as a phenomenon were first observed in 1971, which makes them a relatively recent discovery. The projected onto the plane of sky speeds of CMEs can range from less than 100 km s^{-1} to 2000 km s^{-1} [Yurchyshyn et al., 2005]. Occasionally their speeds may reach values up to 3 500 km s-1 [Chen, 2011]. The mean CME speed varies between 300 km s^{-1} (near solar minimum) and 500 km s^{-1} (near maximum of the solar cycle) [Yashiro et al., 2004]. Early CME speed measurements revealed two general profiles: slow CMEs, usually linked to eruptive prominences, and fast CMEs, associated with ARs [Gosling et al., 1976]. Sheeley et al. (1999) later classified CMEs into two types: gradual CMEs (400–600 km s^{-1}), associated with prominences, and impulsive CMEs ($\geq$750 km s^{-1}), associated with SFs. However, CME speed-height profiles form a continuous distribution rather than two distinct groups [Low and Zhang, 2002].

CMEs occur at a varying rate throughout the solar cycle. NASA’s Coordinated Data Analysis Workshop (CDAW) CMEs frequency rate during solar cycle (SC) 23 was ~ 0.5 CMEs/day at solar minimum and ~ 6 CMEs/day near solar maximum [Chen, 2011]. During the solar cycles 23 and 24 the mean speed of CMEs as observed by LASCO was found to be 360 km s^{-1}.

Active regions (ARs) are generally known to power solar eruptions due to the quantity of magnetic energy stored in them and free energy accumulated in the photosphere [Kontogiannis, 2022]. Additionally, ARs are a crucial part of identifying the evolution of the solar magnetic field as the cause for all types of solar activity. ARs vary in sizes and occur as a result of local magnetic anomalies due to the processes related to the solar dynamo mechanism [Weber et al., 2023]. The size of ARs, along with complexity and strength do not correlate with the kinematic properties of CMEs. They do, however increase the ARs’ capability to produce active events, including CMEs. It has been proved for 84% of the 32 CME events investigated in a study by Subramanian and Dere (2001) to have an AR as their source. Another study carried out by

Wang and Zhang (2008) came to the conclusion that only 3% of ARs tend to produce fast CME events, regardless of using an alternative AR catalog based on SOHO/MDI synoptic charts.

The aim of this study is to evaluate the 3D parameters of CMEs and estimate if they can give us a better insight of their properties and propagation than the most commonly used 2D velocities. 3D reconstruction of CMEs is done using a variety of techniques, such as forward modeling, tie-pointing and triangulation, constraint on the mass calculation, polarization ratio, etc. [Mierla et al., 2010]. The 3D velocities of CMEs can be calculated by combining measurements provided by multiple spacecrafts. The correlation between the values of 3D and 2D speeds of CMEs is found to be high with the mean coefficient of determination being ~68% [Tsvetkov et al., 2019].

CMEs are known to alter space weather as their sub-structures can in many cases cause geomagnetic storms [Gopalswamy, 2016]. Upon CME events happening, the ejected substance from the solar corona interacts with planets including Earth. CMEs may impact the environment and human activity regarding technology and sometimes be dangerous to our planet. This makes the study of CMEs essential as it is needed to be able to predict space weather alternations most precisely in the future.

2. Instruments

For this study, observations done by the Solar Terrestrial Relation Observatory (STEREO) and the Solar and Heliospheric Observatory (SOHO) are used as the primary source of data for CME analysis.

STEREO mission includes two identical space-borne observatories, situated at different points of Earth's orbit ahead (STEREO A) and behind (STEREO B) our planet. COR1 and COR2 instruments are visible light Lyot coronagraphs and are part of the SECCHI instrument suite. The opportunities for CME research created by STEREO include accessing stereographic imagery of CMEs, exploring the magnetic origins of CMEs, investigating of their physical evolution, and observing geo-effective CMEs. In the study the data from STEREO COR2 is used, the field of view of the instrument being 15 solar radii with an inner limit of 2.5 solar radii [Howard et al., 2008].

The SOHO mission's primary objective is the investigation of the Sun's interior, as well as the solar wind and its acceleration. The SOHO spacecraft is equipped with helioseismology, coronal, and solar wind measurement instruments. The LASCO (Large Angle and Spectrometric Coronagraph) consists of three coronagraphs: C1, C2, and C3. For the purposes of the study, we are using the data from the C2 and C3 instruments. C2's field of view is 1.5 to 6 solar radii, and C3's is 3 to 30 solar radii [Domingo et al., 1995].

For combining and analyzing the data, as well as calculating CME kinematic properties, the Stereo CME Analysis Tool (StereoCAT) web app is utilized. For the initial selection of events as well as the comparison between the "projected" and the "true" velocities data from the SOHO/LASCO CME Catalog[1] are used.

3. Results

For this study, a total of 14 CME events was analyzed and their 3D velocities estimated using the StereoCAT tool. All of the utilized events took place during the Solar Cycle 24 (2008-2019), 50% (7/14 CMEs) of them being related to ARs, of which 4 CMEs can be associated with more than one AR. On the other hand, only 2/14 CMES (14%) are associated with SFs.

---

[1] https://cdaw.gsfc.nasa.gov/CME_list/

Our sample includes relatively low number of events with speeds mostly lying in the range between 200-600 km s^{-1}. The distribution of the 2D velocities, as measured by SOHO/LASCO CME Catalog is shown on Figure 1. According to Sheeley et al. (1999), most of the events included in our study (12/14) are gradual CMEs and only 2/14 are impulsive, despite one of the latter (2013/11/02) not being associated with SF.

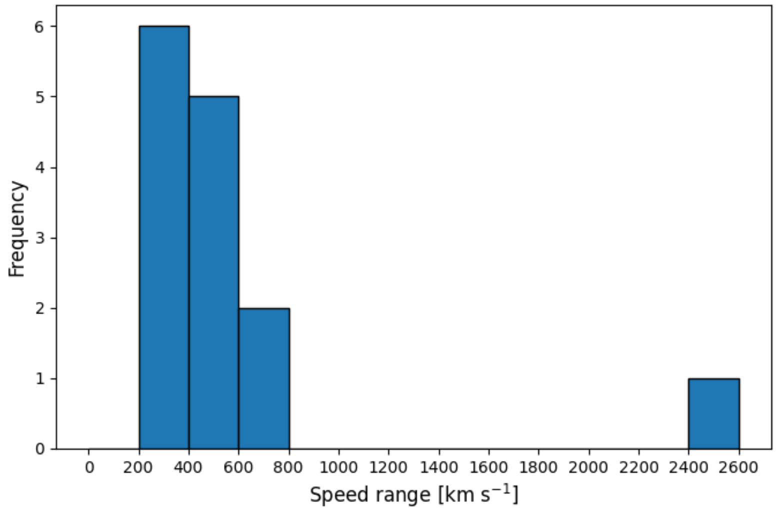

Figure 1. *The 2D "projected" in the plane of the sky velocity distribution of the CMEs included in this study.*

The 3D velocities were calculated upon measuring the CMEs using the images from 2 spacecraft simultaneously. Depending on the visibility of each event in the field of view of the spacecraft, we created combinations of instruments which allowed for the most precise measurements for the longest possible period. For 2/14 events the data from STEREO Behind was absent, and for 2/14 there were gaps in data from LASCO C2 and C3 instruments. The number of CMEs measured with different combination of instruments is listed in Table 1.

Table 1. *Number of the cases in which we chose to use each combination of instruments to measure the 3D velocity of a CME.*

Combination of instruments	No. of events
STEREO A + STEREO B	6
STEREO A + LASCO C2	1
STEREO A + LASCO C3	2
STEREO B + LASCO C2	2
STEREO B + LASCO C3	3

The "true" velocities obtained from different combinations of instruments are shown in Figure 2. At first glance, the distribution resembles that of the 2D velocities measured by the SOHO coronagraph observations. A slight shift towards higher velocities is noticeable, with no event with a velocity <200 km s^{-1}, and the largest number (6/14) of the CMEs having velocities in the range 400-600 km s^{-1}. The fastest ejection of matter is at a velocity of 2600-2800 km s^{-1} (instead of 2400-2600 km s^{-1} for the 2D velocities).

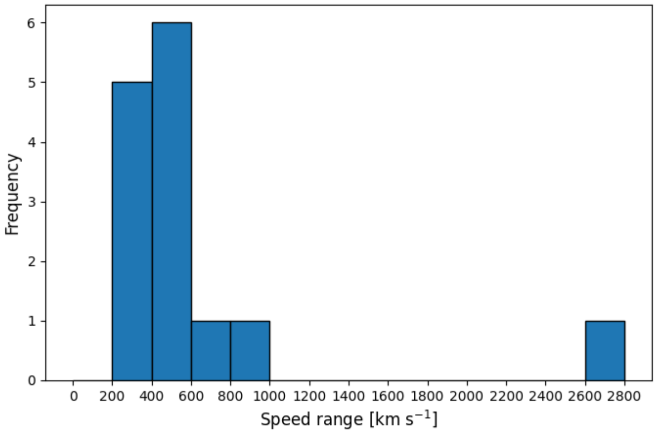

Figure 2. *Distribution of the "true" velocities of the explored sample of CMEs.*

To compare the results, we created a V_{2D} vs. V_{3D} scatter plot (Figure 3), showing a small deviation from y=x line. This indicates a near-linear relationship where the velocities tend to increase together, but not perfectly proportionally. In fact, the trend of the "true" velocities show that they tend to increase more sharply and show larger deviation as 2D speed increase. Events with lower speeds also show smaller deviations.

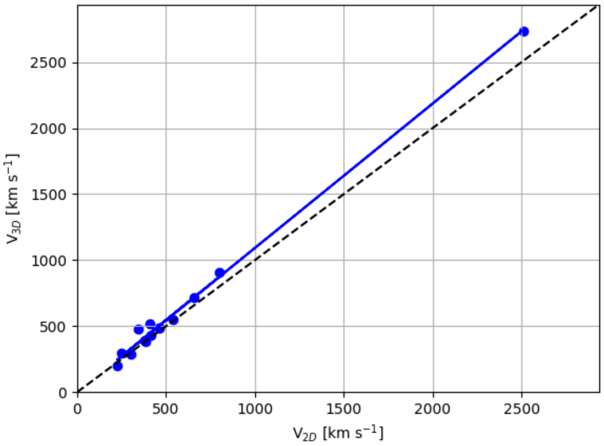

Figure 3. *Comparison between the plane-of-the-sky and "true" velocities of CMEs.*

Estimating Pearson correlation coefficient ($r = 1.0$) we found an extremely strong linear correlation between plane-of-sky (2D) and "true" (3D) CME speeds with 99.5% of the variance in the 3D speeds explained by the 2D measurements (coefficient of determination $r^2 = 0.995$). This indicates that 2D catalog values provide a really good first-order approximation of CME kinematics, but we should note that the low number of events studied probably also plays a significant role in this result. However, correlation does not imply identity: systematic differences remain between 2D and 3D values, reflecting projection effects. Therefore, while catalog speeds are a good proxy for relative variations in CME kinematics, absolute velocity estimates require 3D reconstruction.

To explore in depth, the differences between the speed of the CME (V_{3D}) and its projection (V_{2D}), we calculated the deviation for each measurement:

$$Deviation\ [\%] = \frac{V_{2D} - V_{3D}}{V_{3D}} \times 100. \tag{1}$$

The created histogram represents the percent of deviation of CMEs' 3D velocity from the linear one (Figure 4).

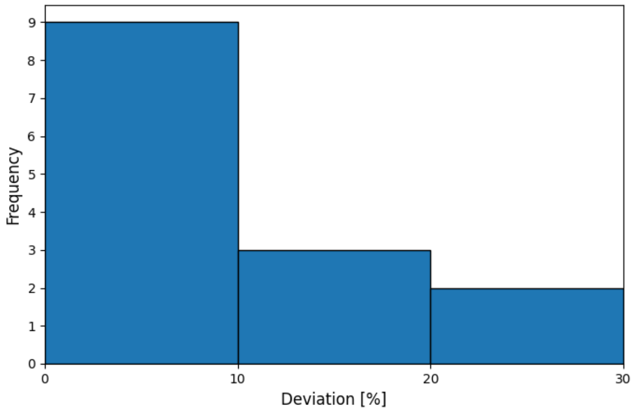

Figure 4. *Distribution of the deviation of the 3D velocities.*

The deviation for 9/14 events (64%) is under 10%, which is another example that the 2D velocities of CMEs are a good representation of the real ones. The two events that show a deviation higher than 20% are the ones from 2012 February 03 and 2013 November 01.

A comparison of CME speeds between events associated with active regions (AR-related) and those originating outside active regions (Non-AR-related) reveals some differences in their distributions. The box plot visualization (Figure 6) indicates that AR-related events exhibit a broader range, including one extreme high-speed outlier (the event from 2012 January 27), which raises their mean speed (803.3 km s^{-1}). In contrast, Non-AR-related CMEs form a more compact distribution, with a lower mean (405.8 km s^{-1}) that is close to their median (490 km s^{-1}). Despite the large difference in mean values, the medians are nearly identical (479 km s^{-1} vs. 490 km s^{-1}), suggesting that typical CME speeds are comparable across the two groups, while AR tend to occasionally produce exceptionally fast CMEs due to the strength and complexity of their magnetic fields.

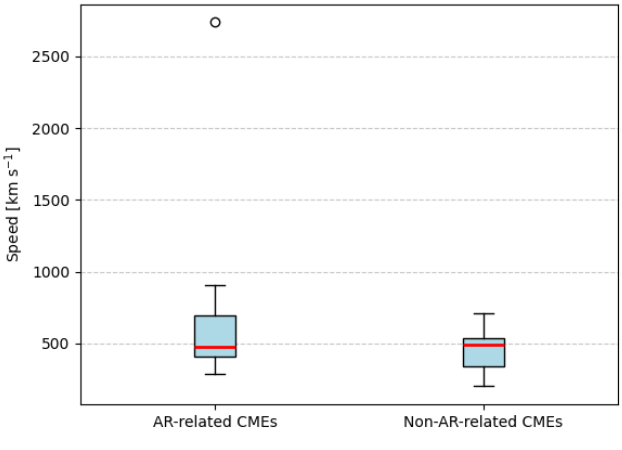

Figure 5. *Boxplot of CME 3D speeds by source type (active vs. non–active regions).*

To assess the agreement between two measurement techniques we obtained a Bland-Altman analysis of the two sets of data – 2D and 3D velocities of the CMEs in our sample (Figure 6). It shows that the catalog (2D) and reconstructed (3D) CME speeds are generally consistent, with most differences lying within ±200 km s^{-1}. The scatter is moderate, with some events exhibiting higher 2D than 3D speeds and others showing the opposite, but all within these bounds. The mean bias is -52.7 km s^{-1}, indicating that 2D speeds are on average ~53 km s^{-1}

lower than their 3D counterparts. Given that the absolute velocities range from several hundred to a few thousand km s^{-1}, this bias is relatively small, corresponding to only a few percent of the typical CME speed.

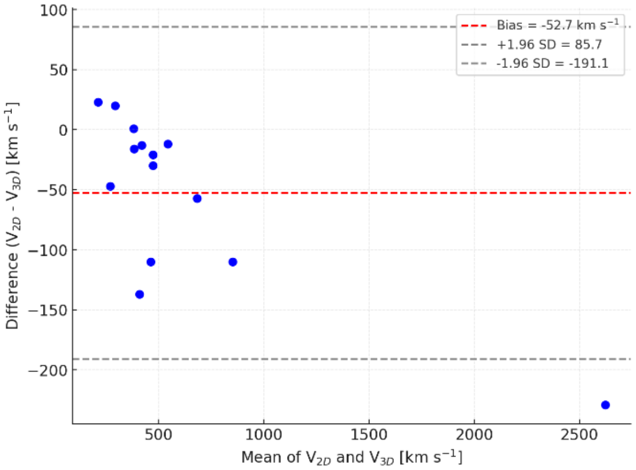

Figure 6. *Bland–Altman plot comparing CME speeds from SOHO/LASCO catalog (2D) and StereoCAT reconstructions (3D). The dashed lines indicate the mean bias (red) and the 95% limits of agreement (grey).*

4. Conclusions

In this work we compared CME plane-of-sky (2D) velocities from the SOHO/LASCO catalog with stereoscopically reconstructed (3D) velocities obtained using the StereoCAT tool for 14 events during Solar Cycle 24. Our results demonstrate that catalog speeds are strongly correlated with the reconstructed ones, indicating that 2D measurements provide a reliable first-order approximation of CME kinematics. Nonetheless, systematic differences persist due to projection effects, with a mean bias of –52.7 km s^{-1} (2D underestimation by only a few percent).

The comparison between AR-related and non-AR-related CMEs shows that while median velocities are similar, AR-associated eruptions occasionally produce extreme high-speed events, thereby elevating their mean values. This highlights the importance of active-region magnetic complexity in driving the fastest CMEs, even though typical velocities across different origins remain comparable.

Despite its usefulness, StereoCAT analysis is subject to limitations, including human selection of tie-points, varying spacecraft viewing geometries, and incomplete data coverage for some events. These factors, together with the relatively small sample size, must be considered when interpreting the results. In order to confirm or disapprove these results, in future we plan a far broader study including events for at least one solar cycle and/or estimating the efficiency of other modeling techniques for reconstruction of CMEs (such as graduated cylindrical shell).

Acknowledgment

This work is supported by the National Science Fund of Bulgaria with contracts No. KP-06-M78/1. We used data from SOHO/LASCO CME Catalog that is generated and maintained at the CDAW Data Center by NASA and The Catholic University of America in cooperation with the Naval Research Laboratory. SOHO is a project of international cooperation between ESA and NASA.

References

Chen, P.F. (2011). Coronal mass ejections: Models and their observational basis, *Living Reviews in Solar Physics*, Vol. 8, 1, DOI: 10.12942/lrsp-2011-1.

Domingo, V., Fleck, B., Poland, A.I. (1995). The SOHO mission: An overview, *Solar Physics*, Vol. 162, pp. 1–37, DOI: 10.1007/BF00733425.

Gopalswamy, N. (2016). History and development of coronal mass ejections as a key player in solar–terrestrial relationship, *Geoscience Letters*, Vol. 3, Art. 8, DOI: 10.1186/s40562-016-0039-2.

Gosling, J.T., Hildner, E., MacQueen, R.M., Munro, R.H., Poland, A.I., Ross, C.L. (1976). The speeds of coronal mass ejection events, *Solar Physics*, Vol. 48, pp. 389–397, DOI: 10.1007/BF00152004.

Howard, R.A., Moses, J.D., Vourlidas, A., et al. (2008). Sun–Earth Connection Coronal and Heliospheric Investigation (SECCHI), *Space Science Reviews*, Vol. 136, pp. 67–115, DOI: 10.1007/s11214-008-9341-4.

Kontogiannis, I. (2023). The characteristics of flare- and CME-productive solar active regions, *Advances in Space Research*, Vol. 71, pp. 2017–2037, DOI: 10.1016/j.asr.2022.10.008.

Low, B.C., Zhang, M. (2002). The hydromagnetic origin of the two dynamical types of solar coronal mass ejections, *Astrophysical Journal*, Vol. 564, L53, DOI: 10.1086/338798.

Mierla, M., Inhester, B., Antunes, A., et al. (2010). On the 3-D reconstruction of coronal mass ejections using coronagraph data, *Annales Geophysicae*, Vol. 28, pp. 203–215, DOI: 10.5194/angeo-28-203-2010.

Sheeley, N.R., Walters, J.H., Wang, Y.-M., Howard, R.A. (1999). Continuous tracking of coronal outflows: Two kinds of coronal mass ejections, *Journal of Geophysical Research: Space Physics*, Vol. 104, 24739, DOI: 10.1029/1999JA900308.

Subramanian, P., Dere, K.P. (2001). Source regions of coronal mass ejections, *Astrophysical Journal*, Vol. 561, No. 1, pp. 372–395, DOI: 10.1086/323213.

Tsvetkov, Ts., Miteva, R., Temmer, M., Petrov, N. (2019). STEREOCat speed de-projection of SEP-related CMEs, *Proceedings of the Eleventh Workshop “Solar Influences on the Magnetosphere, Ionosphere and Atmosphere”*, pp. 207–210, DOI: 10.31401/WS.2019.proc.

Wagner, W.J. (1984). Coronal mass ejections, *Annual Review of Astronomy and Astrophysics*, Vol. 22, No. 1, pp. 267–289, DOI: 10.1146/annurev.aa.22.090184.001411.

Wang, Y., Zhang, J. (2008). A statistical study of solar active regions that produce extremely fast coronal mass ejections, *Astrophysical Journal*, Vol. 680, No. 2, pp. 1516–1522, DOI: 10.1086/587619.

Weber, M.A., Schunker, H., Jouve, L., Işık, E. (2023). Understanding active region origins and emergence on the Sun and other cool stars, *Space Science Reviews*, Vol. 219, No. 8, Art. 63, DOI: 10.1007/s11214-023-01006-5.

Yashiro, S., Gopalswamy, N., Michalek, G., St. Cyr, O.C., Plunkett, S.P., Rich, N.B., Howard, R.A. (2004). A catalog of white light coronal mass ejections observed by the SOHO spacecraft, *Journal of Geophysical Research: Space Physics*, Vol. 109, A07105, DOI: 10.1029/2003JA010282.

Yurchyshyn, V., Yashiro, S., Abramenko, V., Wang, H., Gopalswamy, N. (2005). Statistical distributions of speeds of coronal mass ejections, *Astrophysical Journal*, Vol. 619, 599, DOI: 10.1086/426129.

Appendix

Detailed information about the explored CMEs and the results of the obtained 3D reconstruction is given below in Table 2.

Table 2. *Data for the main parameters of explored events (as given in SOHO LASCO CME Catalog), possible associated phenomena, interval and combination of POVs of instruments used for 3D reconstruction as well as the results and analysis of the obtained reconstruction.*

CME parameters				**Sources**		**Measurements**		**3D Reconstruction**				**Analysis**
Date	**Onset**	**Angular width**	**Linear speed**	**AR**	**SF**	**Instru-ments**	**Interval**	**Half-width**	**Speed**	**Long.**	**Lat.**	**Deviation**
YYYY-MM-DD	**[UT]**	**$[^0]$**	**[km/s]**					**$[^0]$**	**[km/s]**	**$[^0]$**	**$[^0]$**	**[%]**
2010-12-06	17:24	82	538			A+C3	19:24-00:24	36	550	-57	-34	-2.2
2011-12-15	4:12	96	304	11374		A+C2	05:30-08:36	25	284	43	-25	7.0
2012-01-27	18:27	360	2508	11402, 11401, 11405	X1.7(17:37) C5.5(06:24) C1.7(01:11)	A+B	18:40-19:39	76	2737	77	28	-8.4
2012-02-03	7:24	177	408			B+C3	09:06-12:09	26	518	-178	-32	-21.2
2012-02-04	18:12	122	656			A+B	19:52-21:54	24	713	-122	-33	-8.0
2012-11-10	14:12	191	460			A+B	16:24-21:39	34	490	131	-34	-6.1
2013-12-04	5:12	60	377	11907, 11906, 11913	C4.7(04:38)	B+C3	06:54-09:39	20	393	75	16	-4.1
2014-02-02	17:24	143	463	11965, 11966		B+C3	19:54-23:26	24	484	117	-43	-4.3
2013-11-01	15:48	184	342	11886		B+C2	16:09-18:39	27	479	146	21	-28.6
2013-11-02	8:24	177	798	11886		A+B	08:54-11:24	46	908	124	43	-12.1
2013-11-03	8:24	98	224			A+B	09:39-19:54	35	201	40	-70	11.4
2013-12-11	7:36	79	383			A+C3	09:18-15:09	33	382	2	-60	0.3
2013-12-27	2:48	77	247			A+B	06:24-14:24	27	294	-29	-62	-16.0
2013-12-29	5:48	215	415	11938, 11937		B+C2	07:24-09:36	39	428	-38	-29	-3.0

DOI: 10.31401/WS.2025.proc.06

Nonlinear and Causal Dynamics between Solar and Geomagnetic Activity Indices: Findings from Chaos and Causality Measures

Kilcik A., Gerçeker K.

Department of Space Sciences and Technologies, Akdeniz University Faculty of Science, 07058, Antalya, Türkiye.
alikilcik@akdeniz.edu.tr, kemalhangerceker@gmail.com

Abstract

This study aims to identify nonlinear/chaotic features and causal relationships among monthly SSN, F10.7, aa, and Dst indices over December 1963–March 2025. Phase-space is reconstructed via AMI-selected delay τ and FNN dimension E; we estimate the Hurst exponent H, the largest Lyapunov exponent λ, and the correlation dimension D_2; and apply CCM with SSN as reference. H spans $0.84 - 0.93$ ($SSN \approx 0.93$; $F10.7 \approx 0.93$; $aa \approx 0.88$; $Dst \approx 0.84$), indicating strong persistence. λ ranges from ≈ 0.010 to ≈ 0.040 (highest for Dst, lowest for aa), implying deterministic chaos with finite prediction horizons. D_2 varies between $3.37 - 3.86$, consistent with low–moderate dimensional structure. CCM analysis shows a strong linear relationship between SSN–F10.7, while indicating a non-linear causal relationship between SSN and other indices. In conclusion, sunspot variability affects global geomagnetic activity continuously and nonlinearly on a monthly scale; this effect is most pronounced for aa and weaker for Dst.

Keywords: Chaos; Nonlinear and Causality Analyses; Solar and Geomagnetic Activity

1. Introduction

Understanding how solar activity and geomagnetic variability co-evolve is essential for space weather predictions and its impacts on satellites, navigation and communication, aviation, etc., (Eastwood et al., 2017). At geospace scales, energy transfer is controlled by solar-wind/IMF coupling; sustained southward IMF and strong convection electric fields build the ring current and trigger geomagnetic storms (Dungey 1961; Echer et al., 2008).

Here, we analyzed monthly indices that together sample the driver and the response: the international sunspot number (SSN), the 10.7 cm solar radio flux (F10.7), the geomagnetic aa index, and the disturbance storm-time (Dst) index. SSN and F10.7 are tracers of solar magnetic activity and EUV variability (Hathaway 2015; Tapping 2013). The aa index provides a long-term global geomagnetic activity (Mayaud, 1972), while Dst tracks the storm-time low-latitude magnetic depression in short time primarily due to the ring current and is widely used as a standard storm metric (Gonzalez et al., 1994). Taken together, these series allow for a joint view of memory, nonlinearity, and possible Sun-geospace directionality on monthly scales.

We reconstruct dynamics with delay coordinates, choosing the time delay τ by Average Mutual Information and the embedding dimension E by False Nearest Neighbors (Fraser & Swinney 1986; Kennel et al., 1992). In these embeddings we estimate the Hurst exponent H for persistence (Hurst 1951), the largest Lyapunov exponent λ for sensitivity and prediction limits (Rosenstein et al., 1993),, and the correlation dimension D_2 for effective dimensionality (Grassberger & Procaccia 1983a). To go beyond correlation, we use Convergent Cross Mapping to test for directional/causality influence via library-size convergence and asymmetry of cross-map skill (Sugihara et al., 2012).

There is an ongoing debate as to whether the variability of the solar cycle is primarily low-dimensional deterministic or largely stochastic. Evidence exists on both sides, but recent reviews and data-driven models point to mixed dynamics and limited predictability horizons

(Petrovay 2020; Wang et al., 2025). In this study, we aim to quantify persistence and predictability, estimate dimensionality, and determine the directional connections between SSN, F10.7, aa, and Dst in order to establish a clear basis for future results.

2. Data and Methods

In this study, four indices were analyzed using monthly data for the time intervals December 1963—March 2025. The monthly sunspot number (SSN) was obtained from WDC—SILSO (Royal Observatory of Belgium, https://www.sidc.be/SILSO/). The 10.7 cm solar radio flux (F10.7, SFU) was obtained as daily values from NASA/OMNIWeb (https://omniweb.gsfc.nasa.gov/), and monthly averages were calculated. The Dst index (nT) was obtained as hourly values from the Geomagnetism WDC/Kyoto (https://wdc.kugi.kyoto-u.ac.jp/dstdir/), and monthly averages were calculated. The aa index (nT) was obtained as 3-hourly values from the International Service of Geomagnetic Indices (ISGI, https://isgi.unistra.fr/indices_aa.php) and similarly converted to monthly averages. All subsequent analyses were performed on these monthly series within the above time period.

For nonlinear analyses, each scalar series $x(t)$ was embedded via delay coordinates

$$X(t) = [x(t), x(t-\tau), \dots, x(t-(E-1)\tau)], \tag{1}$$

with delay τ chosen as the first local minimum of Average Mutual Information (AMI) (Fraser & Swinney 1986) and embedding dimension E by False Nearest Neighbors (FNN) (Kennel et al., 1992), following the embedding theorem of Takens' (Takens 1981). A Theiler window (Theiler 1986) was applied when selecting the nearest neighbors to suppress temporal autocorrelation effects. Also, the long-memory (persistence) of the data is estimated by using Hurst exponent (H) analysis. This analysis follows the standard convention: $H > 0.5$ persistent, $H = 0.5$ memory-less random walk, $H < 0.5$ anti-persistent (Hurst 1951; Mandelbrot & Wallis 1969). Sensitivity to initial conditions and practical predictability limits are quantified by calculating the largest Lyapunov exponent (λ). The largest Lyapunov exponent: $\lambda > 0$ indicates deterministic chaos, $\lambda \approx 0$ neutrality/periodicity, and $\lambda < 0$ convergence (Rosenstein et al., 1993). To calculate the predictability of the data set used the correlation dimension (D_2) analysis (Grassberger & Procaccia 1983a,b). Finally, to test directionality beyond co-variation, we used Convergent Cross Mapping CCM (Sugihara et al., 2012).

The chosen methods provide complementary views of the monthly SSN, F10.7, aa, and Dst series. By using these methods together, it is possible to (i) quantify persistence and prediction limits, (ii) estimate effective dimensionality, and (iii) identify directional connections between the Sun and space. This provides a clear and repeatable basis for subsequent results.

3. Results

Here, we analyzed the monthly average SSN, F10.7, aa, and Dst indices for the period between January 1957 and March 2025.

(1) Hurst Exponent (H)

Figure 1 shows Hurst exponent analysis ($log(R/S)$ versus $log(n)$ with fitted slopes) for all data sets. The fitted slopes give $H(SSN) = 0.9255$, $H(F10.7) = 0.9324$, $H(aa) = 0.8835$ and $H(Dst) = 0.8446$. All H values are well above 0.5, which means the series are positively autocorrelated and display strong persistence: increases (decreases) tend to be followed by increases (decreases) at monthly scales rather than reverting quickly to the mean. So trend continuity is a common feature across the system in a monthly period. All proxies are very close in magnitude consistent with its smoother month-to-month evolution and the fact that all indices are shaped by the solar cycle and its sub-annual modulation. In practical terms, these H values indicate that low-frequency variability dominates the monthly signal; short runs of oppositesigned fluctuations do occur, but the longer-range tendency is to continue the prevailing trend.

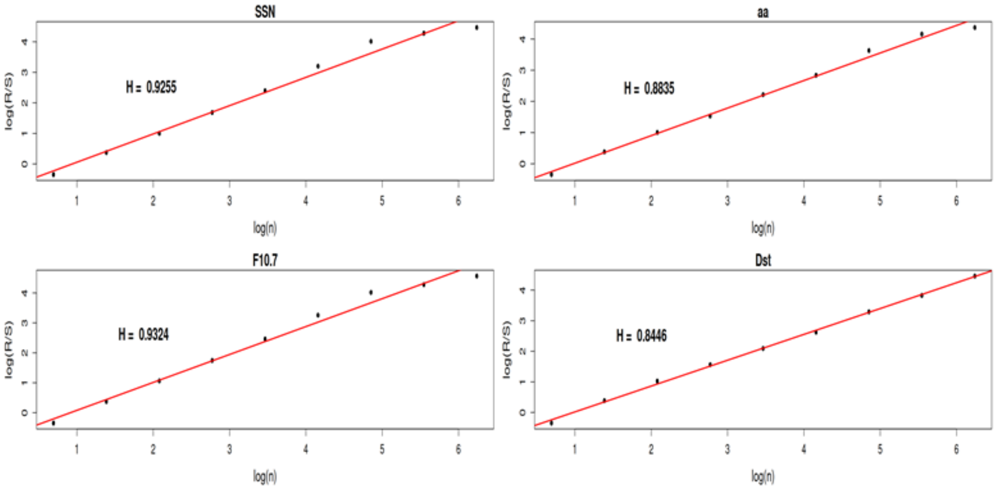

Figure 1. *Hurst exponent (H) analysis results for all data sets used in this study.*

(2) Largest Lyapunov Exponent (λ)

Figure 2 plots $S(t)$ versus evolution steps with the linear segment used to estimate the largest Lyapunov exponent for the used data sets. Linear segments of $S(t)$ yield $\lambda(SSN) = 0.02018$, $\lambda(F10.7) = 0.01433$. Since all are positive, the dynamics are chaotic in the deterministic sense and admit only a finite prediction horizon. The larger E means nearby trajectories diverge faster there than the smaller one, so short range predictions for data which has small λ decay a bit more quickly in skill. The gradual leveling of $S(t)$ at longer evolution steps is consistent with saturation once typical separations reach the attractor scale.

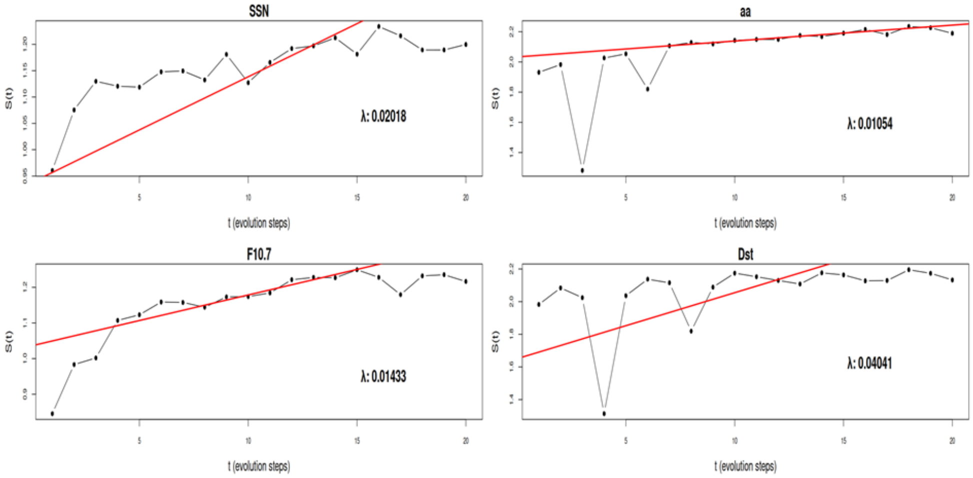

Figure 2. *Lyapunov exponent λ (growth of S(t)) and linear fits results for all data sets used in this study.*

The Dst value is the largest of the four, implying the shortest predictability window among these indices; conversely, aa has the smallest λ and thus the slowest divergence. In rank order of sensitivity to initial conditions we have $Dst > SSN > F10.7 > aa$. When combined with Hurst results, this means that the series can be both persistent and chaotic: trends continue on monthly scales, while fine-scale details can diverge quickly enough to limit deterministic predictions.

(3) Correlation Dimension (D_2)

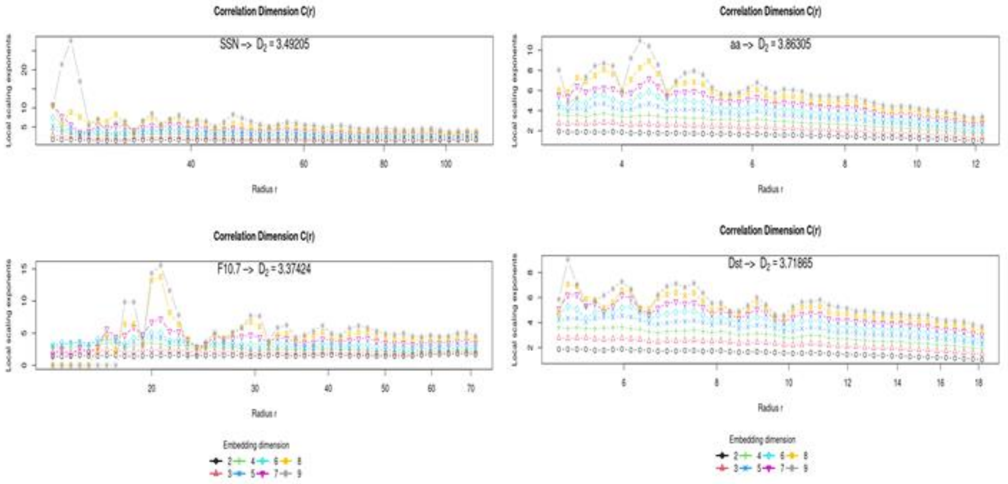

Figure 3. *Correlation Dimension D_2 (local scaling exponents and plateaus) results for the used data sets.*

Figure 3 displays local slopes of $logC(r)$ versus $logr$ and the plateau regions used to read off Correlation Dimension (D_2) for the used data sets. The plateau regions give $D_2(SSN) = 3.49205$, $D_2(F10.7) = 3.37424$, $D_2(aa) = 3.86305$ and $D_2(Dst) = 3.71865$. Dimensions in the $3 - 4$ range indicate low-to-moderate dimensional chaos: the dynamics are not purely random, but they also do not collapse to a near-periodic low-D structure. The closeness of the two values suggests that, despite different measurement bases, SSN and F10.7 share a similar effective number of active degrees of freedom on monthly scales.

(4) Convergent Cross Mapping (CCM)

Figure 7 plots cross-map skill $\rho(L)$ against library size L for each pair, with the dashed line showing the Pearson correlation. For SSN–F10.7, both directions rise and nearly coincide and they stay close to—but below—the Pearson correlation level (≈ 0.98). This points to very strong co-variation (linear relationship) dominated by the solar cycle, without a clear one-way driver at the monthly scale.

For SSN–aa, both curves increase with L and are above the Pearson correlation ($\rho \approx 0.41$), indicating nonlinear information beyond simple correlation. The curve that reconstructs SSN from aa is consistently higher and saturates (≈ 0.67) than the reverse reconstruct aa from SSN curve (≈ 0.57). By the CCM rule, this asymmetry supports the causal effect of SSN on aa (SSN → aa).

For SSN–Dst, both directions show a modest rise above the Pearson correlation level ($\rho \approx 0.38$). The reconstruct SSN from Dst curve is only slightly higher (≈ 0.454) than the reconstruct Dst from SSN curve (≈ 0.447), implying a weak SSN → Dst effect. Overall, CCM highlights clear SSN → aa causal relationship, weaker SSN → Dst causal relationship, and mainly linear relationship for SSN–F10.7.

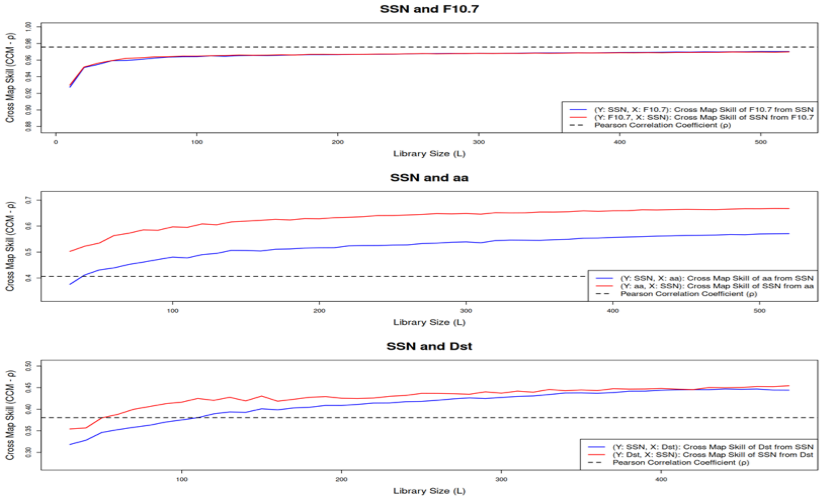

Figure 4. *Convergent Cross Mapping (Cross-map skill CCM-ρ(L) versus library size) results for the pairs SSN–F10.7, SSN–aa, and SSN–Dst (directions shown blue and red = CCM-ρ; black dashed line = Pearson ρ).*

4. Conclusion and Discussion

In this study, we analyzed monthly SSN, F10.7, aa, and Dst over January 1957–March 2025 using Hurst exponent (R/S), largest Lyapunov exponent, correlation dimension, and Convergent Cross Mapping (CCM). The findings of the study are as follows:

1. All indices have $H > 0.8$ ($SSN \approx 0.93$, $F10.7 \approx 0.93$, $aa \approx 0.88$, $Dst \approx 0.84$), indicating positive autocorrelation and trend continuity on monthly scales. The ordering $F10.7 \geq SSN > aa > Dst$ suggests that memory gradually weakens from solar to geomagnetic proxies.
2. The largest Lyapunov exponents (λ) are positive ($SSN \approx 0.020$, $F10.7 \approx 0.014$, $aa \approx 0.011$, $Dst \approx 0.040$). The sensitivity ranking $Dst > SSN > F10.7 > aa$ implies the shortest relative predictability for Dst and the longest for aa.
3. Correlation dimensions vary between $D_2 \approx 3–4$ ($SSN \approx 3.49$, $F10.7 \approx 3.37$, $aa \approx 3.86$, $Dst \approx 3.72$), consistent with low-to-moderate dimensional chaotic structure rather than pure randomness.
4. SSN–F10.7 shows a strong linear co-variation/relationship; SSN → aa and SSN → Dst indicate nonlinear causal relationships beyond simple correlation, with a clear driver role for SSN on aa and a weaker influence on Dst.

Our persistence results are consistent with the dominance of low-frequency variability linked to the solar cycle (Hathaway 2015) and with the long-memory behavior captured by R/S analysis (Hurst 1951; Mandelbrot & Wallis, 1969). Positive Lyapunov exponents indicate deterministic chaos and finite prediction horizons from the data themselves (Rosenstein et al., 1993). $D_2 \sim 3–4$ indicate a low-to-medium dimensional structure; this is not a completely random process, nor is it a system with a very low D_2 value that is nearly periodic (Grassberger & Procaccia, 1983a,b). These patterns align with current debates: while recent analyses have reported traces of low-dimensional dynamics in sunspot numbers, state-of-the-art investigations and dynamo modeling argue that the cycle behaves as a weak nonlinear, noise-perturbed limit cycle and is characterized by a mixture of deterministic-stochastic dynamics and inherently limited predictability (Cameron & Schüssler 2017, 2019; Petrovay 2020; Usoskin 2023; Huang

2025); observation-based iterative maps likewise indicate short cycle-to-cycle memory and prominent stochasticity (Wang et al., 2025).

The CCM results align with known physics of Sun–geospace relationship. The near-symmetric SSN–F10.7 curves reflect a common solar driver rather than a simple one-way causal chain. In contrast, SSN → aa is plausible because aa integrates global activity driven by solar-wind–magnetosphere coupling (Dungey 1961), and our asymmetric, saturating cross-map skills indicate information flow beyond static correlation (Sugihara et al., 2012). The weak SSN → Dst result is also reasonable: Dst strongly depends on the sustained southward IMF and enhanced convection (Gonzalez et al., 1994; Echer et al., 2008), that is, event-like conditions that monthly averaging can mute, reducing apparent directionality.

Acknowledgements

This study was supported by Project 124N011 awarded by the Scientific and Technological Research Council of Türkiye (TÜBİTAK). This study is also part of the Master of Science thesis of Kemalhan Gerçeker.

References

Cameron, R.H., Schüssler, M. (2017). Understanding solar cycle variability, *Astrophysical Journal*, Vol. 843, No. 2, 111, DOI: 10.3847/1538-4357/aa767a.

Cameron, R.H., Schuessler, M. (2019). Solar activity: Periodicities beyond 11 years are consistent with random forcing, *Astronomy and Astrophysics*, Vol. 625, A28, DOI: 10.1051/0004-6361/201935290.

Dungey, J.W. (1961). Interplanetary magnetic field and the auroral zones, *Physical Review Letters*, Vol. 6, No. 2, 47, DOI: 10.1103/PhysRevLett.6.47.

Eastwood, J.P., Biffis, E., Hapgood, M.A., Green, L., Bisi, M.M., Bentley, R.D., Burnett, C. (2017). The economic impact of space weather: Where do we stand?, *Risk Analysis*, Vol. 37, No. 2, pp. 206–218.

Echer, E., Gonzalez, W.D., Tsurutani, B.T., Gonzalez, A.C. (2008). Interplanetary conditions causing intense geomagnetic storms (Dst ≤ -100 nT) during solar cycle 23 (1996–2006), *Journal of Geophysical Research: Space Physics*, Vol. 113, A5, DOI: 10.1029/2007JA012744.

Fraser, A.M., Swinney, H.L. (1986). Independent coordinates for strange attractors from mutual information, *Physical Review A*, Vol. 33, No. 2, 1134, DOI: 10.1103/PhysRevA.33.1134.

Gonzalez, W.D., Joselyn, J.A., Kamide, Y., Kroehl, H.W., Rostoker, G., Tsurutani, B.T., Vasyliunas, V.M. (1994). What is a geomagnetic storm?, *Journal of Geophysical Research: Space Physics*, Vol. 99, No. A4, pp. 5771–5792, DOI: 10.1029/93JA02867.

Grassberger, P., Procaccia, I. (1983a). Characterization of strange attractors, *Physical Review Letters*, Vol. 50, No. 5, 346, DOI: 10.1103/PhysRevLett.50.346.

Grassberger, P., Procaccia, I. (1983b). Measuring the strangeness of strange attractors, *Physica D: Nonlinear Phenomena*, Vol. 9, No. 1–2, pp. 189–208, DOI: 10.1016/0167-2789(83)90298-1.

Hathaway, D.H. (2015). The solar cycle, *Living Reviews in Solar Physics*, Vol. 12, No. 1, 4, DOI: 10.1007/lrsp-2015-4.

Huang, L., Li, Q. (2025). Dynamical analysis of long-term solar activity based on ensemble empirical mode decomposition, *Monthly Notices of the Royal Astronomical Society*, Vol. 542, No. 1, pp. 136–150, DOI: 10.1093/mnras/staf1135.

Hurst, H.E. (1951). Long-term storage capacity of reservoirs, *Transactions of the American Society of Civil Engineers*, Vol. 116, No. 1, pp. 770–799, DOI: 10.1061/TACEAT.0006518.

Kennel, M.B., Brown, R., Abarbanel, H.D. (1992). Determining embedding dimension for phase-space reconstruction using a geometrical construction, *Physical Review A*, Vol. 45, No. 6, 3403, DOI: 10.1103/PhysRevA.45.3403.

Mandelbrot, B.B., Wallis, J.R. (1969). Robustness of the rescaled range R/S in the measurement of noncyclic long-run statistical dependence, *Water Resources Research*, Vol. 5, No. 5, pp. 967–988, DOI: 10.1029/WR005i005p00967.

Mayaud, P.N. (1972). The aa indices: A 100-year series characterizing the magnetic activity, *Journal of Geophysical Research*, Vol. 77, No. 34, pp. 6870–6874, DOI: 10.1029/JA077i034p06870.

Petrovay, K. (2020). Solar cycle prediction, *Living Reviews in Solar Physics*, Vol. 17, No. 1, 2, DOI: 10.1007/s41116-020-0022-z.

Rosenstein, M.T., Collins, J.J., De Luca, C.J. (1993). A practical method for calculating largest Lyapunov exponents from small data sets, *Physica D: Nonlinear Phenomena*, Vol. 65, No. 1–2, pp. 117–134, DOI: 10.1016/0167-2789(93)90009-P.

Sugihara, G., May, R., Ye, H., Hsieh, C.-H., Deyle, E., Fogarty, M., Munch, S. (2012). Detecting causality in complex ecosystems, *Science*, Vol. 338, No. 6106, pp. 496–500, DOI: 10.1126/science.1227079.

Takens, F. (1981). Detecting strange attractors in turbulence, in: Rand, D., Young, L.-S. (eds), *Dynamical Systems and Turbulence, Warwick 1980*, *Lecture Notes in Mathematics*, Vol. 898, Springer, Berlin, Heidelberg, DOI: 10.1007/BFb0091924.

Tapping, K.F. (2013). The 10.7 cm solar radio flux (F10.7), *Space Weather*, Vol. 11, No. 7, pp. 394–406, DOI: 10.1002/swe.20064.

Theiler, J. (1986). Spurious dimension from correlation algorithms applied to limited time-series data, *Physical Review A*, Vol. 34, No. 3, 2427, DOI: 10.1103/PhysRevA.34.2427.

Usoskin, I.G. (2023). A history of solar activity over millennia, *Living Reviews in Solar Physics*, Vol. 20, No. 1, 2, DOI: 10.1007/s41116-023-00036-z.

Wang, Z.F., Jiang, J., Wang, J.X. (2025). Observation-based iterative map for solar cycles. I. Nature of solar cycle variability, *Astrophysical Journal*, Vol. 984, No. 2, 183, DOI: 10.3847/1538-4357/adc72d.

DOI: 10.31401/WS.2025.proc.07

Two Interacting CMEs and Related Eruptions

Koleva K., Duchlev P.

Space Research and Technology Institute, Bulgarian Academy of Sciences
kkoleva@space.bas.bg

Abstract

We investigate the morphology and kinematic characteristics of prominence eruption, occurring in the east solar limb on 2010 June 20. The event was observed by the Atmospheric Imaging Assembly (AIA) on board the Solar Dynamics Observatory (SDO) and by the STEREO Observatory. Two successive CMEs were linked to the eruption. We examine the associated CMEs' kinematics. The observed eruptions showed a strong non-radial motions towards the equator. We study the non radial latitudinal offset of the prominence eruption and related CMEs.

Keywords: solar eruptions; coronal mass ejection; non-radial motion

1. Introduction

One of the most studied phenomena in the solar atmosphere is solar prominences, which are also called filaments when viewed against the solar disk. They are dense and cool structures that stretch outward into the hot and thin solar corona [Tandberg-Hanssen, 1995; Mackay et al.; 2010, Parenti, 2014]. The prominences may become unstable and erupt under certain conditions. It is known that prominence eruptions are part of a larger single eruption that can result in producing a coronal mass ejection (CME) and a solar flare [Forbes, 2000; Priest & Forbes, 2002]. White-light coronagraph images show the erupted prominence material as a bright core of the CME structure.

There are typically two stages to the filament/prominence eruption's kinematic evolution: a slow-rise phase, during which the filament gradually rises with very low acceleration, followed by a sudden transition to a fast-acceleration phase [Sterling et al., 2007].

Observations show that during their eruption, prominences and CMEs can occasionally deviate from the radial direction [Gopalswamy & Thompson, 2000; Koleva et al., 2024]. According to observations CMEs can deflect by ten or more degrees from the source location. Both the prominences and the CMEs show non-radial motions, and therefore, the CME deflects as a whole.

The propagation of CMEs is one of the primary factors affecting space weather on Earth. Changing the propagation's direction can seriously affect the CME's arrival time at 1 AU. Therefore, accurate space weather forecasting requires an understanding of the life cycle of CMEs, from their start at the Sun to their propagation through the heliosphere to their geoeffective consequences at Earth. It is essential to understand as well the CME-CME interactions, which can lead to complex ejecta with enhanced geoeffective signatures, often resulting in more intense geomagnetic storms.

2. Data and Method

The prominence eruption was observed at the east solar limb on 2010 June 20 by SDO/AIA. The eruption was observed from two different observation positions and was associated with two CMEs.

For the present study, we used images taken with 1 min cadence in the He II 304 Å and Fe IX 171 Å passbands of the Atmospheric Imaging Assembly [AIA; Lemen at al., 2012] onboard the Solar Dynamics Observatory [SDO; Pesnell et al., 2012]. The AIA consists of seven

Extreme Ultra-Violet (EUV) and three Ultra-Violet (UV) channels, which provide an unprecedented view of the solar corona with an average cadence of ∼12 s. The AIA image field-of-view reaches 1.3 solar radii with a spatial resolution of ∼ 1.5″.

We also analyzed data from the Extreme Ultra-violet Imager (EUVI) onboard the Solar Terrestrial Relations Observatory [STEREO; [29]] Behind (B) spacecraft to investigate the filament eruptions behind the limb. We used data in the He II 304 Å channel with 10 min cadence. Separation angle between STEREO B and Earth at the time of observation was 69.80 degrees.

Images obtained by the Large Angle and Spectrometric Coronagraph (LASCO) onboard the Solar and Heliospheric Observatory [SOHO; Brueckner, 1995] were examined to investigate the associated CME kinematics and related non-radial motion. LASCO has two working coronagraphs, namely, C2 and C3, that observe the Sun in white-light from 2.5 to 30 R⨀. The non-radial offsets of the related CMEs were analyzed by tracking the variations of their position angles (PAs) over time. The PAs are measured counterclockwise from the solar North in degrees. We used the PA of the leading edge of the CME during its propagation in the plane of the sky. For our purposes we used the online CME Catalog at the Coordinated Data Analysis Workshop (CDAW) Data Center [Yashiro at al., 2004], and the “measuring” tool therein. All the data analysis was performed by the solar software (SSWIDL).

3. Filament morphology

The eruption observed by AIA/SDO started on June 19, 2010, at 23:34 UT, at a central position angle (CPA) of 70°, and lasted until 03:00 UT on June 20, 2010, when the prominence material left the instrument's field-of-view (FOV). The prominence was shaped like a loop with two legs anchored in the solar surface. The eruption was of the full type, with no material falling back onto the surface detected. The evolution of the eruption is depicted in Figure 1 within the AIA 171 Å channel, with overplayed contour of the erupting prominence material. The last panel of the figure displays the eruption in a running difference image.

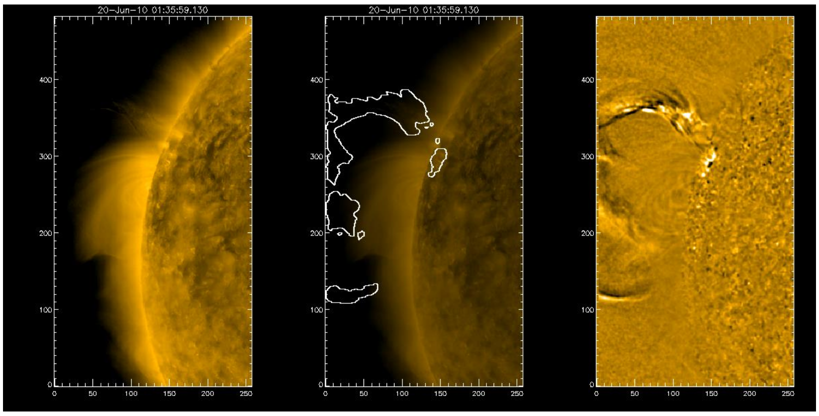

Figure 1. left: *AIA/SDO 171 Å image,* ***middle:****the same image with overlay contour of the erupting prominence, and* ***right:*** *the differential image (credit: http://eruptivesun.com/).*

In the in EUVI/STEREO–B 304 Å images the eruption was visible on the disk as a filament eruption (Figure 2). Comprising two sections, the filament spans half of the solar hemisphere from the northeast nearly to the equator. The filament began to rise at approximately 01:16 UT, and both components proceeded southward until 03:56 UT.

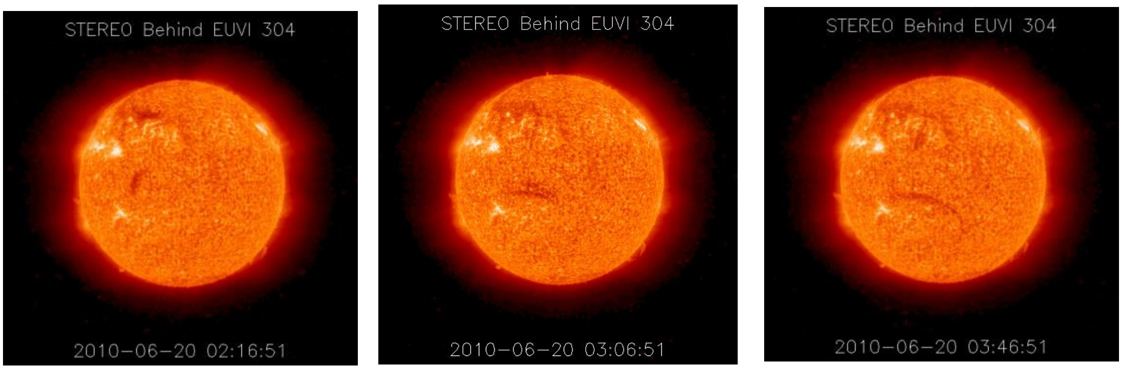

Figure 2. *Evolution of filament eruptions in the 304 Å channel as seen by EUVI/STEREO B.*

4. Eruption kinematic

To examine the event's kinematics, we performed a time-distance analysis. This technique is based on investigating how plasma material moves along an artificial slit. We traced the top of the prominence loop, using AIA/SDO 304 Å data. Figure 3 (left panel) displays the artificial slit that was chosen for the kinematics analysis in the 01:18 UT frame. The corresponding time–distance plot is presented in right panel of Figure 3.

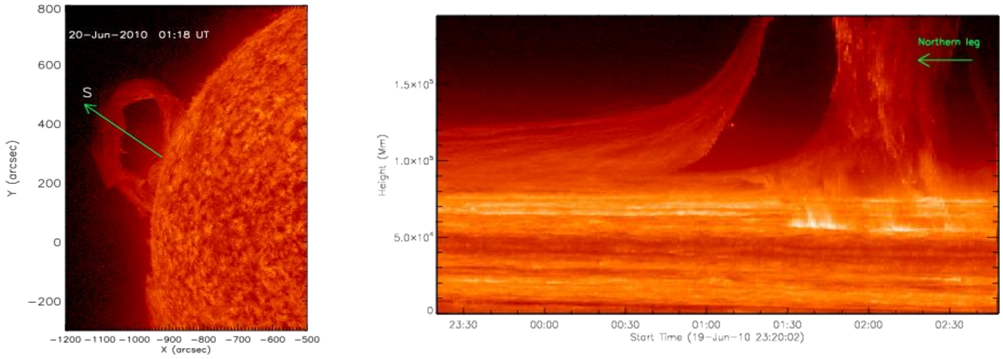

Figure 3. *AIA/SDO 304 Å image, showing the slice position and corresponding time-distance plot.*

From this time–distance plot, we obtained the distance–time data for the leading edge of the erupting prominence. Figure 4A illustrates how the height of the erupting prominence changes over time. The eruption started at 23:34 UT, when the prominence began to slowly rise. It is evident from the time-distance plot that the eruption contains two phases: the slow-rise phase, lasting until 01:30 UT, and the fast rise phase, between 01:30 UT and 03:00 UT, when the prominence material rises rapidly. At around 03:00 UT the top of the prominence loop reached a maximum height at the AIA FOV of 166 Mm above the limb.

The data points of the time-distance plot were fitted with second order polynomial function and the fitted function is plotted as red solid line in Figure 4A. From the first derivative of the polynomial fit of the height-time curve, we defined the speed of the prominence eruption. The velocity changes during the eruption are presented in Figure 4B. During the slow-rise phase the prominence rises with velocity between 0.9 km/s and 9 km/s.

The prominence rises at a speed between 0.9 and 9 km/s during the slow-rise phase, while during the fast-rise phase the velocity increases up to 62 km/s. The prominence loop reached heights of 165 Mm above the solar limb.

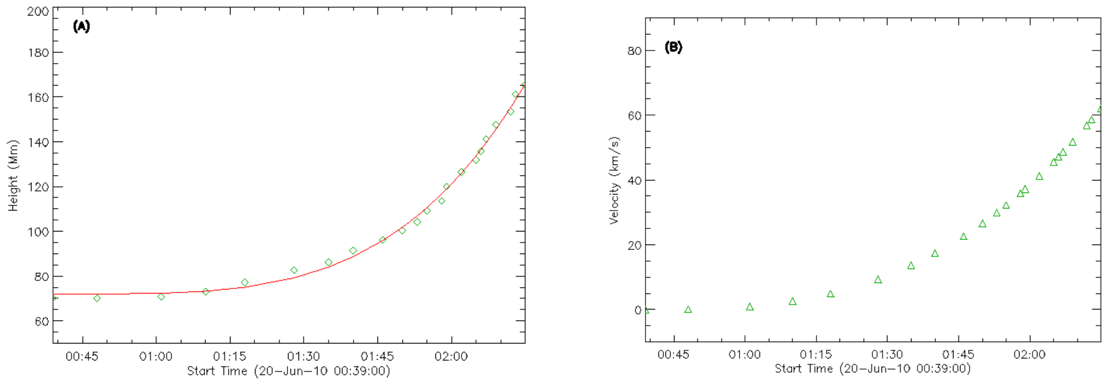

Figure 4. ***(A)*** *Time–distance plot of the prominence eruption. The red solid line is the fitting curve to the data points along the slice.* ***(B)*** *Velocity changes during the eruption.*

5. Associated CMEs evolution

The prominence eruption started at PA of 70° at 23:34 UT the previous day. Two successive CMEs were observed to be associated with the prominence eruption.

Morphology and kimematics

The first CME (CME1) appeared in LASCO/C2 FOV at 23:26 UT, at a CPA of 118°. CME 1 has an angular width of 33° and propagated with a linear speed of 210 km/s and acceleration of about 8 m/s^2. This CME propagated radially in the solar corona.

The second CME (CME 2) first appearance in the LASCO/C2 FOV was at 02:06 UT at a CPA of 108°.

CME2 had an angular width of 93° and propagated at a linear speed of 595 km/s with an acceleration of 6.4 m/s2. The Figure 5 displays the CME2 height-time plot and velocity changes.

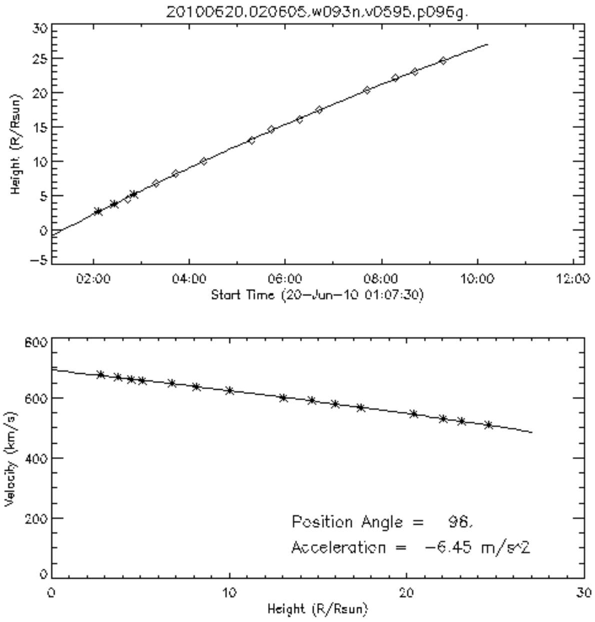

Figure 5. ***(top)*** *Time–distance plot for CME 2.* ***(bottom)*** *Linear velocity changes (image from: https://cdaw.gsfc.nasa.gov/CME_list/index.html).*

CME Deflection

The prominence eruption began at PA of 70°. During the next 4 hr, the CME2 nose and the prominence underwent a significant equatorward deflection to PA of ~97°. Figure 6 (a) shows the CME2 PA, marked with a red line, at 02:36 UT. At 04:20 UT the CME2 was observed in C3 FOV at PA ~97° and than continued its propagation without deflection. In Figure 6 (b), the CME2 is shown at 03:26 UT, before it left the LASCO/C2 field of view. The dashed red line points to the CME2 position angle at 03:26 UT, the red line marks the CME2 PA as measured at 02:26 UT, and the double dashed yellow line shows the direction of the initial PA of the PE. Thus the PA offset between the initial PE location and the CME2 nose was 27° towards the equator.

After 08:42 UT the two CMEs in LASCO/C3 look like one twisted common structure at PA ~ 123°. In LASCO/C3 running difference images, this event could be traced up to 26 solar radii and propagated in the solar corona without appearing to deviate from the radial direction (see Figure 6, c).

The time variations of the CME2 core and nose are shown in Figure 7(a). We also examined the variation of the PA with heliocentric distance and the result is presented in Figure 7(b). The non-radial motion stopped at about 9 $R_{\odot}$.

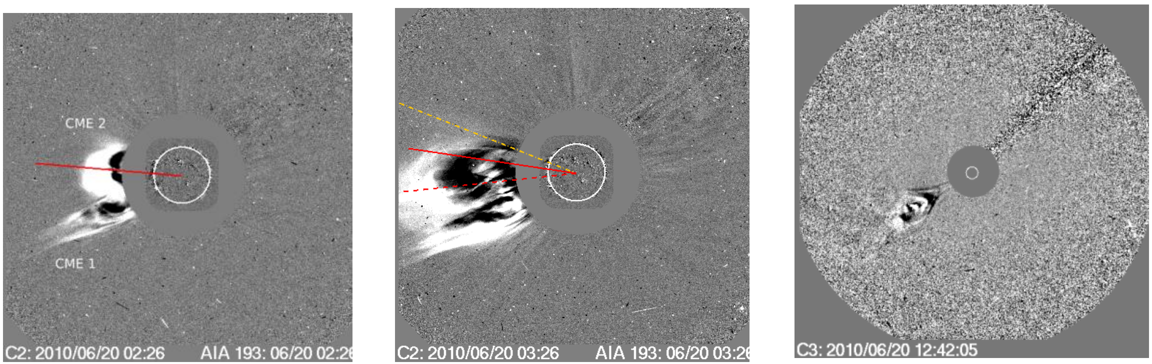

Figure 6. *(a) SOHO/LASCO/C2 and AIA/SDO 193 Å composite image at 02:26 UT. The red line denotes the CME2 PA (b). SOHO/LASCO/C2 and AIA/SDO 193 Å composite image at 03:26 UT. The CME2 PA for 02:26 UT and 03:26 UT and PE PA are shown by red, dashed red and double dashed yellow lines, respectively. (c) Running difference images from LASCO/C3 coronagraph at 12:42 UT.*

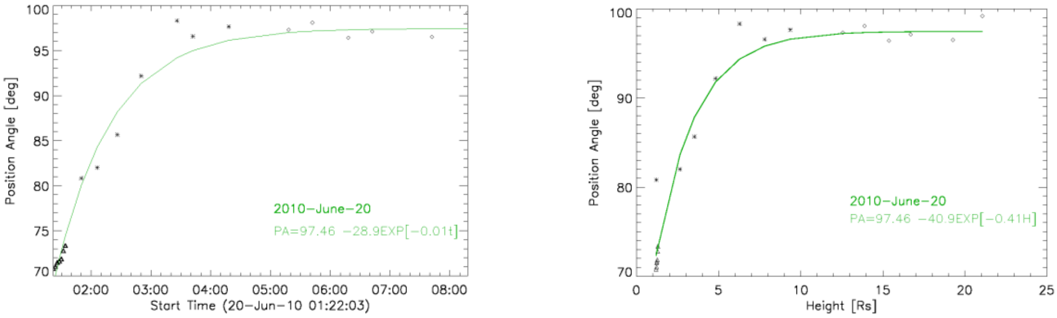

Figure 7. *(a) Variation of the position angle of CME core and nose as a function of time. Triangles, stars, and diamonds represent measurements, respectively in AIA FOV, from C2, and C3 coronagraph of SOHO/LASCO. (b) CME Position angle (PA) at various heliocentric distances. The solid line is the fit to the data points, showing that the non-radial motion stopped at about 9* $R_{\odot}$.

6. Results

We examine the morphology and kinematics of the June 20, 2010. The prominence eruption that took place in the east solar limb and was observed by AIA/SDO and STEREO B observatory. The eruption in the AIA FOV was followed by two successive CMEs, which we named CME 1 and CME 2.

The results from the study can be summarized as follows:

- ✓ The eruption observed by AIA/SDO started at CPA of 70° at 23:34 UT on the previous day and lasted until 03:00 UT on June 20, 2010. During this time period the images obtained by the EUVI/STEREO–B show a huge disk filament, consisting of two distinct parts. The eruption of the two components of that filament could be interpreted as the cause of the two observed CMEs.
- ✓ The kinematics characteristics of the prominence eruption, as observed by AIA/SDO, reveal two eruptive phases. During the slow-rise phase, between 23:34 UT and 01:30 UT, the prominence slow rises with velocity between 0.9 km/s and 9 km/s. This phase was followed by a fast-rise phase with velocity of 62 km/s. Before leaving the AIA FOV, the prominence loop reached a height of 165 Mm above the solar limb.
- ✓ The eruption was associated with two CMEs, namely, CME1 and CME 2. CME1 appeared at CPA of 118° and propagated radially in the solar corona with a linear speed of 210 km/s and acceleration of about 8 m/s^2.
- ✓ CME 2 started at CPA of 108°. It demonstrated substantial non-radial motions while propagating at a linear speed of 595 km/s with an acceleration of 6.4 m/s^2. The latitudinal offset between the initial PE location and the CME2 nose was 27° towards the equator. Such deflection can be attributed to the influence of a polar coronal hole (CH).
- ✓ The two CMEs seemed to be one twisted common structure around 08:42 UT, most likely due to their interaction. This structure spread radially in the solar corona and could be traced up to 26 $R_\odot$.

References

Brueckner, G.E. (1995). The Large Angle Spectroscopic Coronagraph (LASCO), *Solar Physics*, Vol. 162, pp. 357–402, DOI: 10.1007/BF00733434.

Forbes, T.G. (2000). A review on the genesis of coronal mass ejections, *Journal of Geophysical Research: Space Physics*, Vol. 105, No. A10, pp. 23153–23166, DOI: 10.1029/2000JA000005.

Gopalswamy, N., Thompson, B.J. (2000). Early life of coronal mass ejections, *Journal of Atmospheric and Solar–Terrestrial Physics*, Vol. 62, pp. 1457–1469, DOI: 10.1016/S1364-6826(00)00079-1.

Kaiser, M.L., Kucera, T.A., Davila, J.M., et al. (2008). The STEREO mission: An introduction, *Space Science Reviews*, Vol. 136, pp. 5–16, DOI: 10.1007/s11214-007-9277-0.

Koleva, K., Gopalswamy, N., Devi, P., Yashiro, S., Michalek, G. (2024). Spatial relationship between CMEs and prominence eruptions during solar cycles 24 and 25, *Astrophysical Journal*, Vol. 966, 22, DOI: 10.3847/1538-4357/ad2df3.

Lemen, J.R., Title, A.M., Akin, D.J., et al. (2012). The Atmospheric Imaging Assembly (AIA) on the Solar Dynamics Observatory (SDO), *Solar Physics*, Vol. 275, pp. 17–40, DOI: 10.1007/s11207-011-9776-8.

Mackay, D.H., Karpen, J.T., Ballester, J.L., Schmieder, B., Aulanier, G. (2010). Physics of solar prominences: II — Magnetic structure and dynamics, *Space Science Reviews*, Vol. 151, pp. 333–399, DOI: 10.1007/s11214-010-9628-0.

Parenti, S. (2014). Solar prominences: Observations, *Living Reviews in Solar Physics*, Vol. 11, pp. 1–89, DOI: 10.12942/lrsp-2014-1.

Pesnell, W.D., Thompson, B.J., Chamberlin, P.C. (2012). The Solar Dynamics Observatory (SDO), *Solar Physics*, Vol. 275, pp. 3–15, DOI: 10.1007/s11207-011-9841-3.

Priest, E.R., Forbes, T.G. (2002). The magnetic nature of solar flares, *Astronomy and Astrophysics Review*, Vol. 10, No. 4, pp. 313–377, DOI: 10.1007/s001590100013.

Sterling, A., Harra, L., Moore, R. (2007). New evidence for the role of emerging flux in a solar filament’s slow rise preceding its CME-producing fast eruption, *Astrophysical Journal*, Vol. 669, pp. 1359–1371, DOI: 10.1086/520829.

Tandberg-Hanssen, E. (1995). *The Nature of Solar Prominences*, *Astrophysics and Space Science Library*, Vol. 199, Kluwer Academic Publishers, Dordrecht, The Netherlands, DOI: 10.1007/978-94-017-3396-0.

Yashiro, S., Gopalswamy, N., Michalek, G., et al. (2004). A catalog of white light coronal mass ejections observed by the SOHO spacecraft, *Journal of Geophysical Research: Space Physics*, Vol. 109, A07105, DOI: 10.1029/2003JA010282.

DOI: 10.31401/WS.2025.proc.08

Application of Microwave Average Time Profile to Analysis of Flares with Long-Duration Energy Release

Motyk I.D., Kashapova L.K., Rozhkova, D.V.

Institute of solar-terrestrial physics, Siberian Branch of Russian Aacademy of Sciences
motykilya@iszf.irk.ru

Abstract

We present results of study of a powerful solar flare using microwave average temporal profiles describing elementary processes of electron acceleration and precipitation. The average profile was reconstructed using simple single-peak profiles of solar flares observed in a wide range of frequencies (3-24 GHz) using the Siberian Radioheliograph. Analysis of these profiles confirms the dominance of non-thermal emission in their formation. The template for analysis includes both the average profile and an analytical approximation, which combines a fourth-order polynomial for the rising phase and two exponential functions for the decaying phase. Applying our method to the microwave temporal profile of the X1.8 long-duration flare on October 9, 2024, we revealed three secondary energy release events that occurred after the main impulsive phase and estimated their characteristics. Analysis of event characteristics reveals a gradual increase in event power - the first two events were not distinguishable in hard X-ray profiles due to low electron fluxes. The results demonstrate the effectiveness of microwave average temporal profiles in detecting secondary energy release, and their usefulness for studying long-duration flares.

Keywords: Solar flares; average time profile; microwave emission;

1. Introduction

The most of current solar flare models describe scenarios of “simple” or “classical” solar flares where the key element is single main act of energy release. However, many flares are more complex and cannot be described by these models. For example, long-duration events are not explained by these models and require a different approach. In these flares, the observed time for flare emission decay is longer than 2 hours, and explaining by plasma cooling only does not satisfy qualitative estimations based on theoretical predictions. Nowadays it can be explained by additional processes that occur during flare, such asadditional acts of energy release, which we are focused on. However, the role of these processes and their contribution to extending the flare cooling time is unclear. We can better understand this by presenting a complex flare as a set of multiple simple events that can be studied and evaluated separately. In order to separate the main flare from other events that follow it, we need to understand the general behavior of a "classical" flare and describe it using a template or an average time profile. Then, this average time profile can be applied to the flare and help us to reveal the parameters of each event of energy release. The method showed its usefulness in analysing white-light flares on M4 red-dwarf star in [Davenport et al., 2014]. The average time profiles were constructed for UV/EUV [Kashapova et al., 2021] and soft X-ray [Gryciuk et al. 2017] emission of solar flares. In this paper, we focus on an average microwave time profile, because the microwave emission provides useful information about the emission mechanism and parameters of flare plasma for both powerful and weak events. The aim of this paper is to show the application of an average microwave profile for analyzing events.

2. Data and processing techniques

The average temporal profile (hereinafter, the average profile) is a temporal profile, derived from a set of flares with simple shape of temporal profiles. We define the average profile as the temporal profile of a flare, which follows a classic scenario describing only one increase in flux and a slow decay.

As mentioned above, the microwave (MV) emission from solar flares is a sensitive indicator of the electron fluxes and their properties, as well as the mechanisms that generate this emission. Therefore, an analysis of the spectrum shape can reveal thermal or non-thermal mechanisms of emission generation. As it is better to create an average profile of emission from the same mechanism, there is a need for a wide range of observations with high spectral resolution in order to select flares with the shape of the spectrum typical for gyrosynchrotron emission of non-thermal electrons. The Siberian Radioheliograph (SRH) [Altyncev et al., 2020] provides data well suitable for these purposes. It is a radio interferometer operating on 48 frequencies within the 3–24 GHz range with high temporal resolution (~ 3.5 s.) and high flux sensitivity (~0.001 sfu). Except for radio images it also provides “sun-as-a-star” flux observations with high flux sensitivity.

For average profile reconstruction we used events selected by automatic event detection algorithm [Rozhkova et al., 2024]. Preliminary it was found ~600 candidates during the period of July–September 2023 and May 2024. We select events with simple temporal profiles from the candidates, applying the following criteria of a "classical" profile: there is only one emission maximum, a fast rise phase and a gradual decay phase. Fluctuations in the emission in a temporal profile must not exceed 30% of the maximum value.

As a result, we selected 116 dynamic spectra of the flares with “classical” temporal profiles and the shape of microwave spectrum that is characteristic of gyrosyncrotron emission of non-thermal electrons. The microwave spectrum of the flare consists of optically thin and thick emission sources which are formed in different regions of flare loop (footpoints and top). So, we have to separate the emission coming from them. One of the ways to separate them is using peak frequency of the spectrum [Dulk, 1985]. The emission at frequencies below the peak frequency are from optically thick emission source and the emission above peak frequency is from optically thin source.

Each time profile has different intensity and duration, and in order to reveal the general behaviour of both powerful and weak events we need normalize them by both intensity and time. We normalized the intensity (or flux) at each frequency and then scaled the time to the half-width of the time profile ($t_{1/2}$) at a half-intensity as it was done in [Davenport et al., 2014]. Then, we derived normalized temporal profiles for optically thick and optically thin sources for each event. At the final step of average profile construction, we interpolated all profiles onto a grid with 0.001 $t_{1/2}$ time bins. The median values in each time bin formed the average profiles presented in fig. 1. As can be seen, the average profiles of emission from both optically thin and thick sources are very similar. The correlation coefficient between these profiles is 0.99, which means that they are identical. Usually, differences between the temporal profiles originating at different levels of a flare loop occur in cases of process related with thermal plasma. One example is filling the top by hot plasma or chromospheric evaporation. Similarity indicates that the average profiles show the process of accelerated electron precipitation during a solar flare.

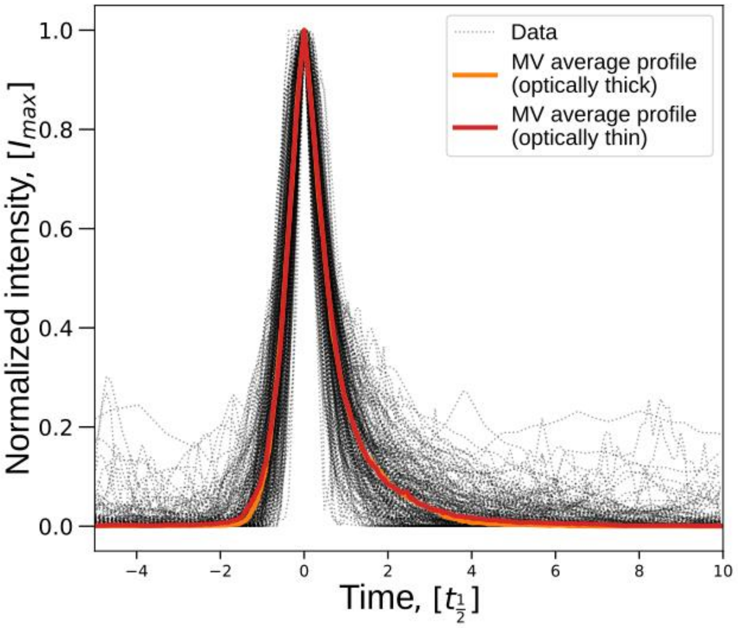

Figure 1. *Average time profiles of microwave emission of a solar flare for emission of different part of a flare loop.*

Based on constructed average profiles, we obtained analytical approximations, which consist of 4-order polynomial function for rise phase and two exponential functions for the decay phase. The found coefficients of the mentioned functions are presented in [Motyk et al., 2025]. By using analytical approximations, we developed a method that allows us to analyze flares for presence of accelerated electrons. We tested this method on the C1.2 class flare took place on Feburary 3, 2022. The analysis revealed two events of accelerated electron participation. One was due to a flare, and the other was due to an additional energy release event. Successful identification of weak events in small flare assumes the opportunity that we can apply our method to other more powerful events.

3. Application results and discussion

We applied our approach to the X1.8 flare that occurred on October 9, 2024. Its maximum was at about 01:56 UT. It lasted approximately 7 hours and was a long-duration event. The 1700 Å band images by SDO/AIA [Lemen et al., 2012] (fig. 2) show two ribbons located in the center of the solar disk. One of the ribbons was located within a sunspot, one of which was located in a sunspot. Usually, at first, we observe the maximum hard X-ray or microwave emission, and then the soft X-ray emission corresponds to the increasing density of heated plasma. Thus, the processes of acceleration and heating are going sequentially.

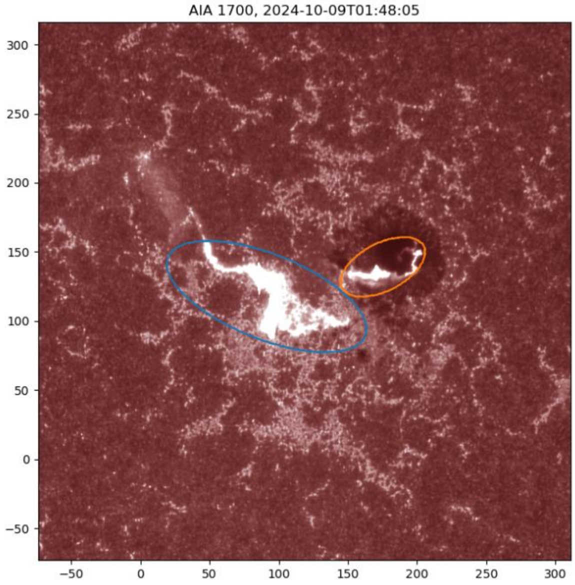

Figure 2. *Active region with highlighted ribbons of X1.8 flare at 01:48 UT which is approximately at the maximum of microwave emission. Blue and orange ovals indicate the regions used to get flux data in order to reconstruct the temporal profiles of ribbons 1 and 2, correspondingly.*

Analysis of the MV spectrum of the flare at its temporal profile maximum (UT 01:47) reveals that the emission mechanism was gyrosynchrotron, and the peak frequency separating the emission from optically thick and optically thin sources was at about 7 GHz. It means that the temporal profiles at frequencies higher than the trace processes of acceleration and precipitation of electrons. Figure 3 (left panel) presents the temporal profiles of 12.2 GHz MV emission and non-thermal X-ray emission in the 50-100 keV band by FERMI/GBM [Meegan et al., 2009]. The application of the average profile (AP) reveals that the flux after the temporal profile maximum at 12.2 GHz is significantly higher than predicted. After subtracting the average profile from the flare profile, three bursts of the decay phase in MV emission became more pronounced. In the subtracted MV time profile. We found three small bursts at 01:48 UT, 01:50 UT, and 01:55 UT that were well described by average profiles (APs). The properties of these APs, such as half-width and flux, are presented in Table 1.

Table 1. *Half-widths $t_{1/2}$ and maximum flux of average profiles (APs) of the flare and bursts on decay phase of microwave emission.*

	Half-width $t_{1/2}$, s	**Maximum flux, sfu**
Flare	137.5	834.31
Burst 1	23.0	133.18
Burst 2	52.5	286.27
Burst 3	121.0	392.80

As can be seen from Fig. 3 and Table 1, the main impulsive peak of the flare was accompanied by two fast and relatively small bursts associated with accelerated electron precipitation (bursts 1 and 2), which were not visible in the temporal profiles of hard X-ray emission. The last burst can be seen in both MV and hard X-ray temporal profiles. It has almost the same half-width as the main impulse burst, and the flare was more powerful than the previous two bursts. The reason why the first two bursts are not visible in hard X-rays may be due to the higher sensitivity of MV emission to electron fluxes. Therefore, we see a gradual increase in the power of non-thermal energy release after the main impulsive phase. We note that this process occurred simultaneously with the passing of the maximum temperature and reaching of the emission measure maximum.

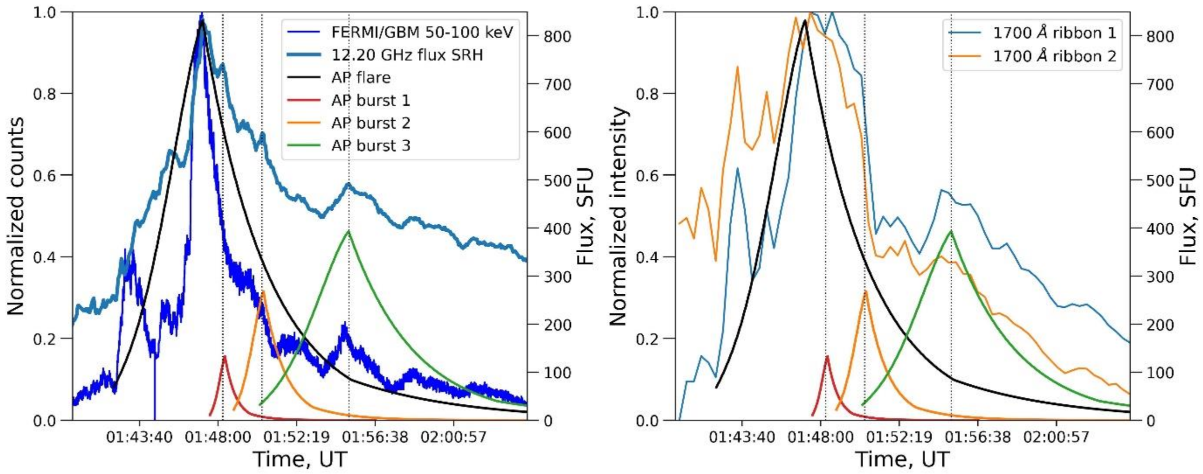

Figure 3. *Left panel: Microwave, hard X-ray temporal profiles and templates of flare and three bursts. The vertical lines show time of the maximum of each burst template. Right panel: Comparison of the evolution of emission flare ribbons at 1700 Å in the SDO/AIA band and templates of flares and three bursts. The temporal profiles of flare ribbon 1 and 2 are shown by the same color as they are marked on fig 2.*

The temporal profiles taken from the flare ribbon regions using 1700 Å AIA/SDO band images are presented in the left panel of Figure 3. The profile of ribbon 1 shows the evolution of the left ribbon intensity (see Fig. 2). The profile of ribbon 2 presents the intensity of the right flare ribbon located in the sunspot area. As one can see, that despite of low temporal resolution of the data (24 seconds), the flux of the temporal profile of ribbon 2 precedes the bursts seen in the profile of ribbon 1 during the impulse phase. This behavior changed after 1:50 UT, when the heating process began to dominate. This may be explained by the fact that ribbon 2 is closely associated with the site of initial energy release during the impulse phase. It is possible that the location of the energy release moved, and we began to detect a first response to these events through the emission of ribbon 1.

We note that the revealed MW bursts 1 and 2 precede the bursts seen in the temporal profiles of the 1700 Å band, while the hard X-ray profile did not show pronounced bursts at that moment. As can be seen, the temporal profile of region 1 has a small but pronounced peak around the same time as MW burst 3 (AP3). On the other hand, the temporal profile of ribbon 2 continues to decrease gradually. The difference in behaviour between the profiles indicates that the location of the burst 3 is closely related to the ribbon 1.

4. Conclusions

We applied the reconstructed microwave average temporal profile of a "classical" solar flare to the analysis of a powerful and long-lasting solar flare. The average temporal profile was obtained for gyrosynchrotron emission of non-thermal electrons and traced the process of acceleration and precipitation of electrons. As a comparison of the average temporal profiles formed at different levels of flare loop for the ideal case of gyro-synchrotron emission generation by accelerated electrons revealed that they were identical, we neglected thermal plasma effects in the interpretation of the results. As it was shown in the example of a weak solar flare on February 3, 2022, analysis of temporal profiles can be done by fitting them with a combination of average profiles or analytical functions or templates describing the behavior of the microwave temporal profile. The application of the suggested technique to study the temporal profiles of microwave emission from powerful flares on October 9, 2024 revealed that three additional energy release events occurred between the main impulsive peak in maximum soft X-rays and the flare. The presence of these bursts and their separation by the average profile indicates several events of electron acceleration occurring after the main impulse phase. The two first additional bursts are not seen in hard X-rays, which can be explained by the low sensitivity of this kind of emission to electron fluxes. Analysis of the average profiles obtained for each event allowed getting characteristics such as time duration, half-width at half intensity, and flux level at 12.2 GHz frequency. The dynamics of these parameters show a steep decrease in the power and duration of the acceleration and precipitation processes. Then, the power of the process gradually increases over time towards the last extracted event. There were seen two flare ribbons in the 1700 Å SDO/AIA band images, one of which (ribbon 2) was located in the sunspot area. In addition, we conducted a comparison of the temporal profiles of emissions from flare ribbons observed in the SDO/AIA 1700 Å band and found that the latest revealed burst was more pronounced in the temporal profile of ribbon 1, which is located outside the sunspot. This can be an indicator of the movement of the initial energy release from a sunspot close to another ribbon.

Acknowledgements and funding

The authors thank the teams of the Siberian Radioheliograph (Institute of Solar-Terrestrial Physics SB RAS), GOES, SDO and FERMI for providing open access to observational data. This study was supported by the grant of the Russian Science Foundation No. 24-22-00315, https://rscf.ru/en/project/24-22-00315

References

Altyntsev, A.T., Lesovoi, S.V., Globa, M.V., et al. (2020). Multiwave Siberian Radioheliograph, *Solar–Terrestrial Physics*, Vol. 6, No. 2, pp. 30–40, DOI: 10.12737/stp-62202003.

Davenport, J.R.A., Hawley, S.L., Hebb, L., et al. (2014). Kepler flares. II. The temporal morphology of white-light flares on GJ 1243, *Astrophysical Journal*, Vol. 797, No. 2, pp. 122–133, DOI: 10.1088/0004-637X/797/2/122.

Dulk, G.A. (1985). Radio emission from the Sun and stars, *Annual Review of Astronomy and Astrophysics*, Vol. 23, pp. 169–224, DOI: 10.1146/annurev.aa.23.090185.001125.

Gryciuk, M., Siarkowski, M., Sylwester, J., et al. (2017). Flare characteristics from X-ray light curves, *Solar Physics*, Vol. 292, No. 6, 77, DOI: 10.1007/s11207-017-1101-8.

Kashapova, L.K., Broomhall, A.-M., Larionova, A.I., et al. (2021). The morphology of average solar flare time profiles from observations of the Sun's lower atmosphere, *Monthly Notices of the Royal Astronomical Society*, Vol. 502, No. 3, pp. 3922–3931, DOI: 10.1093/mnras/stab276.

Lemen, J.R., Title, A.M., Akin, D.J., et al. (2012). The Atmospheric Imaging Assembly (AIA) on the Solar Dynamics Observatory (SDO), *Solar Physics*, Vol. 275, No. 1–2, pp. 17–40, DOI: 10.1007/s11207-011-9776-8.

Meegan, C., Lichti, G., Bhat, P.N., et al. (2009). The FERMI gamma-ray burst monitor, *Astrophysical Journal*, Vol. 702, No. 1, pp. 791–804, DOI: 10.1088/0004-637X/702/1/791.

Motyk, I.D., Kashapova, L.K., Rozhkova, D.V. (2025). Average temporal profiles of solar flare microwave emission: Morphology and application, *Astronomy Reports*, Vol. 69, No. 6, pp. 519–531, DOI: 10.1134/S1063772925701860.

Rozhkova, D., Kashapova, L., Gubin, A. (2024). A method to reveal and catalog solar flares observed with the Siberian Radioheliograph: First results, in: *Modern Astronomy: From the Early Universe to Exoplanets and Black Holes (VAK-2024)*, pp. 1129–1133, DOI: 10.26119/VAK2024.181.

DOI: 10.31401/WS.2025.proc.09

Proceedings of
the Seventeenth Workshop “Solar Influences on the Magnetosphere, Ionosphere and Atmosphere”
June, 2025

Solar Activity Forecasting and North-South Asymmetry

Obridko V.N.[1], Shibalova A.S.[2], Sokoloff D.D.[1,2], Livshits I.M.[1]

[1]IZMIRAN, Kaluzhskoe Shosse 4, Troitsk, Moscow, 108840, Russia
obridko@mail.ru
[2]Department of Physics, Lomonosov Moscow State University, Leninskie Gory 1, Moscow,
119991, Russia

Abstract

According to the generally accepted theory, the field of local active regions is generated from the poloidal magnetic field. The field in the polar regions, which is measured directly by magnetographs, can be a proxy of the latter. It has been shown that the mean-field dynamo is undoubtedly the main mechanism generating solar activity and the 11-year cycle. However, the magnetic flux generated by the dynamo, being the genetic basis of solar activity, still does not allow unambiguously linking the characteristics of the magnetic field with other indices of solar activity, including the best-known one - the sunspot number. Magnetic fields of active regions and spots are formed from the mean magnetic flux. Its most important properties are the threshold character and the conservation of the total flux. Therefore, a completely reliable long-term forecast of SSN is possible after the occurrence of an equatorial wave approximately 18 months before the maximum. The processes in leptocline play a decisive role in this case.

Keywords: solar magnetic field; solar cycle; forecast

1. Introduction

The basic concept of the solar dynamo is the transformation of the poloidal field into a toroidal field with the emergence of activity in the equatorial zone of the Sun (primarily sunspots) and the reverse process of restoring the poloidal field. This basically correct concept gives rise to several widely held ideas that are in fact not entirely true.

1. The polar field is the main reliable index of the original poloidal field.
2. Since the poloidal field is a primary phenomenon, knowledge of the polar field is sufficient to describe the main properties of the upcoming cycle and, in particular, its height.
3. Solar activity is generally symmetric about the equator, regardless of the characteristic spatial and temporal scales.

2. Is the measured polar field a good predictor of the following cycle?

This view is based on the idea that there is a single mechanism generating solar activity and that once the poloidal field has been established, the sunspot cycle is completely predetermined. This is not the case, or at least not always the case. It is unclear to what extent the solar dynamo is determined by stochastic or deterministic processes (Mininni et al. 2002). Moreover, existing dynamo models deal with the mean-field dynamo. Therefore, the output of any theory is the field structure, not the sunspot number that must be predicted. As a result, attempts based on dynamo models have so far yielded contradictory results (Biswas et al., 2023; Bushby and Tobias, 2007; Kitiashvili and Kosovichev, 2008, 2011; Kitiashvili, 2016; Dikpati, de Toma, and Gilman, 2006; Dikpati and Gilman, 2006; Choudhuri et al., 2007a, b; Upton and Hathaway, Jiang et al., 2018; Bhowmik, and Nandy, 2018; Labonville et al, 2019; Guo et al, 2021; Jiang et al, 2023; Bhowmik et al, 2023). For a detailed review of these publications, see (Nandy, 2021). The current Cycle is indicative in this regard. According to polar field data, one would expect the cycle to be about the same as Cycle 24 or slightly higher.

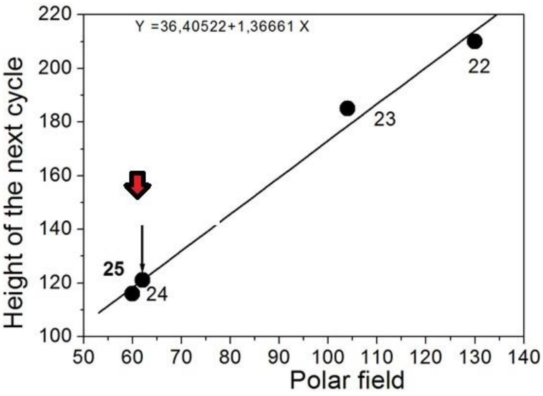

***Figure** 1. Relationship between the polar field measured in mT and the height of the upcoming sunspot cycle. For cycle 25, two values are shown: one is the predicted value based on the polar field (thin arrow), and the other is the value actually reached in October 2024 (thick red arrow).*

In May 2023, the smoothed SSN number reached 123.9 and continued to rise steadily. As shows the arrow in Figure 1, Cycle 25 promised to be at least 10% higher than Cycle 24 (Obridko et al., 2023a, b). But this forecast also turned out to be underestimated. A strong increase in activity in the second half of 2024 changed the course of the cycle, and the smoothed value for March 2024 was 141.3. Actually, the maximum was reached in October 2024 and its height was 160.8.

So, why didn't the forecast of the height of cycle 25 based on polar field data work? First of all, the data available on the WSO website (http://wso.stanford.edu/Polar.html) are not exactly the polar field. The WSO measures the strength of the Sun's polar field daily in the polar-most three-minute apertures. The polar-most aperture measures the line-of-sight field between the latitude of about 55° and the pole. In this case, the longitudinal component is measured directly, i.e. at these latitudes it is close to the meridional one. Even if we assume that the field on the photosphere is radial, at these latitudes it is multiplied by the cosine of the latitude, which is <0.5

In Figure 2, we compare the absolute values of the magnetic field at selected latitudes with the polar field and sunspot numbers.

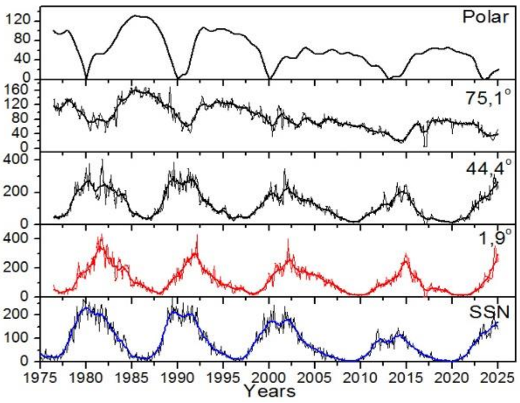

***Figure 2**. Comparison of the absolute values of the magnetic field at selected latitudes with the polar field and sunspot numbers.*

As seen on the top panel, the extrema of the polar field are in antiphase with the sunspot numbers, as it should be according to the basic dynamo model. The field maxima strictly correspond to the sunspot minima, and the dates of the field minima are close to the sunspot maxima. The situation changes starting from latitude ~50°. Now, the field extrema correspond to those of the sunspot numbers. A wave independent of the polar zone appears, moving to the equator.

In the period from 2004 to 2008, the mean-field maximum corresponding to the prolonged decline phase of Cycle 23 is scarcely noticeable. Many observers note an unusual character and a long duration of this phase. The field maximum at mid-latitudes and directly at the equator agrees with the secondary maximum of sunspot numbers. Note that even directly at the equatorial latitudes the mean magnetic field does not fully correspond to the sunspot curve.

The mean field and the sunspots are closely related but not identical phenomena. The general idea is that the mean-field dynamo creates a mean-field toroidal flow, which disintegrates into separate tubes by means of some additional mechanism. The mean magnetic flux forms magnetic fields of active regions and spots. We should emphasize that it is not part of the dynamo process, and no new total flux is generated. This is a fairly complex process, the initial impulse of which is an increase in the magnetic field to a certain threshold value. At this value, the heat influx from below becomes weaker, and thermodynamic processes begin to act. If the region of the increased field is large enough compared to the horizontal optical thickness, a dark feature (a sunspot) appears at the photosphere level.

3. What about NS asymmetry?

The development of the cycles is not synchronous in different hemispheres. In Cycles 12-13 and (less pronounced) in Cycles 14-15, the northern hemisphere was in the lead. In Cycles 16-19, the southern hemisphere was in the lead, and in the last cycles the northern hemisphere was leading again (Figure 3).

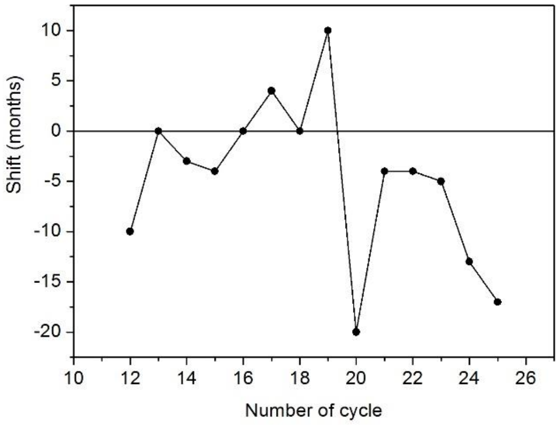

Figure 3. *Shift of thr cycles maxima (Data max N – Data max S).*

Here, we are facing an awkward question: Does the symmetry of the hemispheres indeed exist, or do we see only independent waves of activity in each hemisphere?

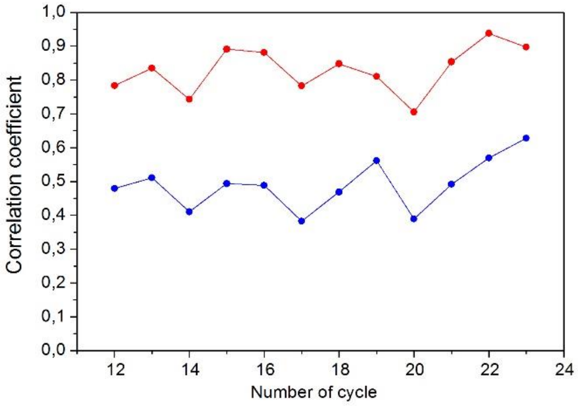

Figure 4. *Correlation coefficient r0 between North and South in sunspot areas (blue line r_0 for unsmoothed data, red line r_0 for smoothed data)*

Figure 4 shows the correlation coefficients separately for the unsmoothed values of the spot areas (blue curve) and the smoothed values (red curve). It turns out that the correlation of the unsmoothed values is quite low, the correlation coefficient for the entire data array is r0=0.526±0.850.

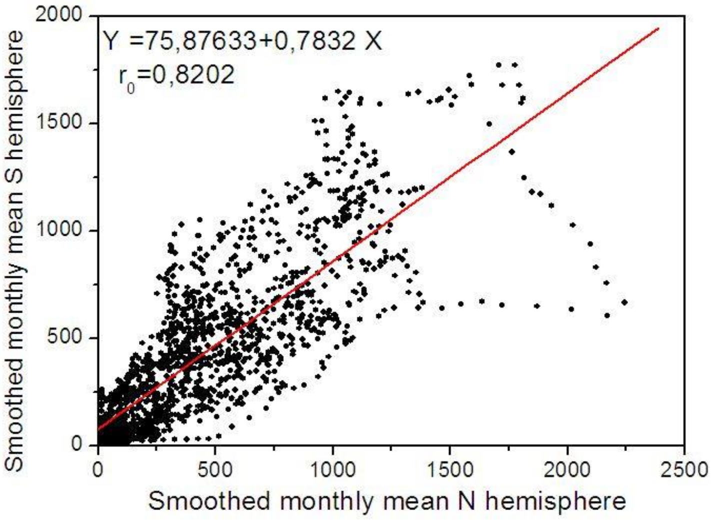

Figure 5*. Correlation of smoothed monthly means data.*

However, if we look at the values smoothed over a one-year window, the correlation improves significantly, r0=0.8202±0.572, (see Figures 4 – red line and Figure 5), and the improvement is achieved mainly due to larger values. It is interesting that in the region of large values, an excess of areas in the northern hemisphere becomes noticeable.

Symmetry of the smoothed data exists!! We have arrived at the conclusion that the 11-year cycles in both hemispheres are virtually identical in their spectral shape. The 11-year oscillations may be slightly offset in time in one hemisphere relative to the other. Other differences in shape have time scales of less than a year and can be considered to be due to processes other than the mean-field dynamo responsible for the main cycle.

Thus, in a fairly average magnetic field, the asymmetry of the hemispheres is not observed. Only the 11-year cycle is clearly visible. Thus, we come to the conclusion that the 11-year cycle is determined for structures of large time scales (more than a year) and is determined by large-scale magnetic fields. Accordingly, as a result, the 11-year cycle is stable and although there is a large shift between the maxima, it never exceeds 10-20 months.

4. What about small-scale structures?

Now, let us turn to the small-scale structures in the data under discussion. We quantify them in terms of the differences between the measured total sunspot areas in the northern (N) and southern (S) hemispheres and their smoothed values (labeled NSM and SSM, respectively).

$$\Delta N = S_N - S_{NSM} \tag{1}$$

$$\Delta S = S_S - S_{SSM} \tag{2}$$

We plotted the data for 1697 Carrington rotations. The difference ΔN changed sign 678 times, i.e. on average each 2.502 rotation. ΔS changed sign 715 times, i.e. on average each 2.364 rotations.

Here we come to a very important understanding of fractality and self-organization of solar plasma. The magnetic field as a whole is not described by mean characteristics, and the mean field dynamo reflects only general long-term characteristics. The magnetic field is a not random noise, but it is not a smooth quasi-constant function either.

The statistics of the distribution of positive and negative deviations from the smoothed curve over a time interval of up to one year are shown in Figure. 5. The amplitude of the deviations does not exceed 500 mph.

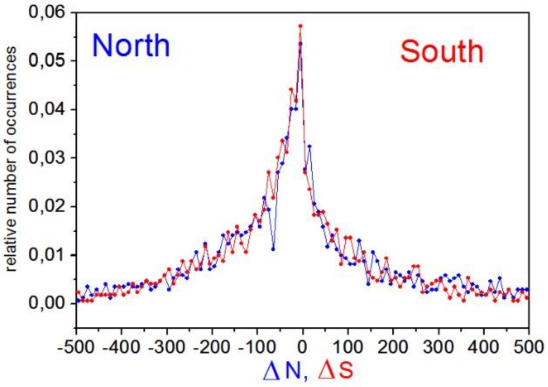

***Figure 5**. Distribution of small-scale features, the probability histogram (the abscissa is ΔN –blue, and ΔS (red), the ordinate is the relative number of occurrences.*

We see from this figure 5 that the positive and negative deviations from the smoothed data have a similar probability distribution; however, the positive and negative deviations look independent of each other.

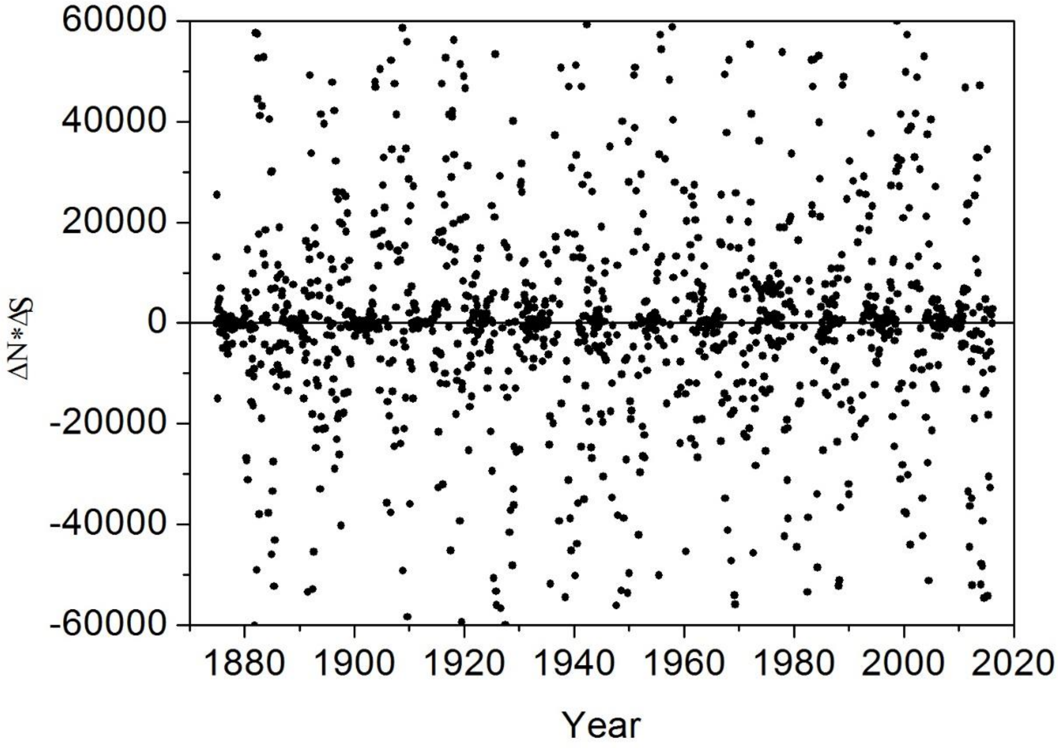

Figure 6. *The dependence of the coincidence index on time.*

To check the degree of coincidence of deviations in the northern and southern hemispheres by sign, the index C (coincidence) = ΔN * ΔS was calculated. Its dependence on time is shown in Figure 6. Obviously, in cases of coincidence of deviations by sign, the value of C is positive and all points should lie above the zero line, in cases of non-coincidence, the points should be below 0. It turned out that out of 1697 points, 881 (51.9%) coincided, and 816 (48.1%) did not coincide, i.e. the number of coincidences was almost equal to the number of non-coincidences, as it should be in the case of independence of two random processes.

Note that such an assessment takes into account only the coincidence or non-coincidence of the signs of the monochrome deviations. Neither the magnitude of the deviation nor its duration are taken into account. To take into account the magnitude and duration, the correlation coefficient of the ΔN and ΔS arrays was calculated. As expected, it turned out to be extremely small and amounted to r0 = –0.0482, which confirms the statistical independence in the northern and southern hemispheres for elements of activity with a lifetime of 2-4 rotations.

5. Conclusions

In summary, we demonstrate that surface magnetic field features such as sunspots and the structure of the mean surface magnetic field behave fundamentally differently in two time intervals, i.e. on time scales shorter and longer than a year. Short-term structures are distributed independently in the northern and southern hemispheres. In contrast, long-term structures are (anti)symmetric about the solar equator and follow the 11-year periodicity. The symmetry is not perfect, but is clearly visible in all data considered.

Thus, the nature of the north-south asymmetry is that it is determined by different processes. In general, the magnetic flux is generated by the global magnetic dynamo and acts equally in both hemispheres, ensuring synchronization of the 11-year cycles. But the spots and groups of spots themselves are created from this flux by a random process that has the same statistical properties in both hemispheres, but acts independently, and therefore the appearance of groups of spots in each hemisphere is not synchronized.

Both observational data and the dynamo model indicate that the immediate subphotospheric layer near the surface plays a key role in the formation of the magnetic butterfly diagram. The role of the leptocline in the solar dynamo has not yet been established. However, this shallow subsurface region is crucial for the formation of sunspots and active regions.

References

Biswas, A., Karak, B.B., Kumar, P. (2023). Exploring the reliability of polar field rise rate as a precursor for an early prediction of the solar cycle, *Monthly Notices of the Royal Astronomical Society*, Vol. 526, No. 3, pp. 3994–4003, DOI: 10.1093/mnras/stad2966.

Bhowmik, P., Nandy, D. (2018). Prediction of the strength and timing of sunspot cycle 25 reveal decadal-scale space environmental conditions, *Nature Communications*, Vol. 9, 5209, DOI: 10.1038/s41467-018-07690-0.

Bhowmik, P., Jiang, J., Upton, L., et al. (2023). Physical models for solar cycle predictions, *Space Science Reviews*, Vol. 219, No. 5, 40, DOI: 10.1007/s11214-023-00983-x.

Bushby, P.J., Tobias, S.M. (2007). On predicting the solar cycle using mean field models, *Astrophysical Journal*, Vol. 661, No. 2, pp. 1289–1296, DOI: 10.1086/516628.

Choudhuri, A.R., Chatterjee, P., Jiang, J. (2007). Predicting solar cycle 24 with a solar dynamo model, *Physical Review Letters*, Vol. 98, No. 13, 131103, DOI: 10.1103/PhysRevLett.98.131103.

Dikpati, M., Gilman, P.A. (2006). Simulating and predicting solar cycles using a flux transport dynamo, *Astrophysical Journal*, Vol. 649, No. 1, pp. 498–514, DOI: 10.1086/506314.

Dikpati, M., de Toma, G., Gilman, P.A. (2006). Predicting the strength of solar cycle 24 using a flux-transport dynamo-based tool, *Geophysical Research Letters*, Vol. 33, No. 5, L05102, DOI: 10.1029/2005GL025221.

Guo, W., Jiang, J., Wang, J.X. (2021). A dynamo-based prediction of solar cycle 25, *Solar Physics*, Vol. 296, No. 9, 136, DOI: 10.1007/s11207-021-01878-2.

Jiang, J., Wang, J.X., Jiao, Q.R., et al. (2018). Predictability of the solar cycle over one cycle, *Astrophysical Journal*, Vol. 863, No. 2, 159, DOI: 10.3847/1538-4357/aad197.

Jiang, J., Zhang, Z., Petrovay, K. (2023). Comparison of physics-based prediction models of solar cycle 25, *Journal of Atmospheric and Solar–Terrestrial Physics*, Vol. 243, 106018, DOI: 10.1016/j.jastp.2023.106018.

Kitiashvili, I., Kosovichev, A. (2011). Structure and dynamics of the Sun’s interior revealed by the helioseismic and magnetic imager, *Lecture Notes in Physics*, Vol. 832, pp. 121–140.

Kitiashvili, I., Kosovichev, A.G. (2008). Application of data assimilation method for predicting solar cycles, *Astrophysical Journal Letters*, Vol. 688, No. 1, L49–L52, DOI: 10.1086/594999.

Kitiashvili, I.N. (2016). Data assimilation approach for forecast of solar activity cycles, *Astrophysical Journal*, Vol. 831, No. 1, 15, DOI: 10.3847/0004-637X/831/1/15.

Labonville, F., Charbonneau, P., Lemerle, A. (2019). A dynamo-based forecast of solar cycle 25, *Solar Physics*, Vol. 294, No. 6, 82, DOI: 10.1007/s11207-019-1480-0.

Nandy, D. (2021). Progress in solar cycle predictions: Sunspot cycles 24–25 in perspective, *Solar Physics*, Vol. 296, No. 3, 54, DOI: 10.1007/s11207-021-01797-2.

Obridko, V., Shibalova, A., Sokoloff, D. (2023a). The extended solar cycle and asymmetry of the large-scale magnetic field, *Monthly Notices of the Royal Astronomical Society*, Vol. 523, 982–991.

Obridko, V., Sokoloff, D., Katsova, M. (2023b). Estimates of the height and date of the 25th cycle of solar activity, *Astronomicheskii Tsirkulyar*, No. 1658, pp. 1–3.

Upton, L.A., Hathaway, D.H. (2018). An updated solar cycle 25 prediction with AFT: The modern minimum, *Geophysical Research Letters*, Vol. 45, No. 16, pp. 8091–8095, DOI: 10.1029/2018GL078387.

DOI: 10.31401/WS.2025.proc.10

Proceedings of
the Seventeenth Workshop “Solar Influences on the Magnetosphere, Ionosphere and Atmosphere”
June, 2025

Solar Flare Location on the Extended Arc of Magnetic Lines with Increased Current Density, Obtained by Analyzing the Results of MHD Simulation

Podgorny A.I.[1], *Podgorny I.M.*[2]

[1]Lebedev Physical Institute RAS, Moscow, Russia
podgorny@lebedev.ru
[2]Institute of Astronomy RAS, Moscow, Russia

Abstract

The appearance of extended surface of magnetic lines with increased current density (extended current sheet) in solar corona can solve the problem of the coincidence of the positions of flares found from the results of MHD simulation with the observed positions of flares. The compare of magnetic configuration near such a surface with observed flare emission show that flare energy release can occur not in the position of current density maximum, but in the place, were the current density is rather large and where the magnetic field configuration promote the flare instability development. For more convenient search of flare positions to study the solar flare mechanism, it will be better to modernize the existing graphical system for searching for flare positions taking into account obtained results about location of flare instability.

Keywords: Solar flare; current sheet; magnetohydrodynamic simulation, singular line.

1. Introduction

Primordial energy release of the solar flare takes place in the solar corona at the altitude 15 000 km - 70 000 km (1/40 - 1/70 of the Solar radius), which is proofed by appearance of a source of flare thermal X-ray emission on the limb [Lin et al., 2003] and other numerous observations. The slow accumulation of energy for a solar flare in a stable magnetic field configuration in the corona, and then its transition to an unstable state, explains the physical mechanism, based on the accumulation of energy in the magnetic field of the current sheet formed in the vicinity of a singular line of magnetic field due to appropriate directions of magnetic forces $j \times B$ [S. I. Syrovatsky 1966; Bratenahl and Hirsch 1966]. During the process of quasi-stationary evolution, the current sheet transfers into an unstable state.

The fast release of magnetic energy of the current sheet leads to the observed manifestations of a flare, which are explained by the electrodynamic model of a solar flare proposed by I. M. Podgorny [Podgorny et. al 2010]. The occurrence of hard X-ray radiation on the solar surface during a flare is explained by the acceleration of electrons in field-aligned currents caused by the Hall electric field in the current sheet, directed along magnetic lines exiting from the current sheet in the direction of the solar surface. The electrodynamic model of solar flare uses analogies with the electrodynamic model of substorm, previously proposed by its author based on measurements on the ”Intercosmos-Bulgaria-1300” spacecraft [Podgorny et. al 1988].

Since it is impossible to obtain the configuration of the magnetic field in the corona from observations, to study the flare situation it is necessary to carry out MHD simulations in the solar corona. The magnetic field measured at the solar surface was used for setting the boundary condition. When setting the problem, no assumptions were made about the mechanism of the solar flare. To study the physical mechanism of a solar flare, calculations must begin several days before the flare, when magnetic energy for the flare has not yet accumulated in the corona. Setting of problem and developed methods including stabilization of numerical instability, which appears in first turn near the boundary of computational domain, are described in [Podgorny and Podgorny 2023].

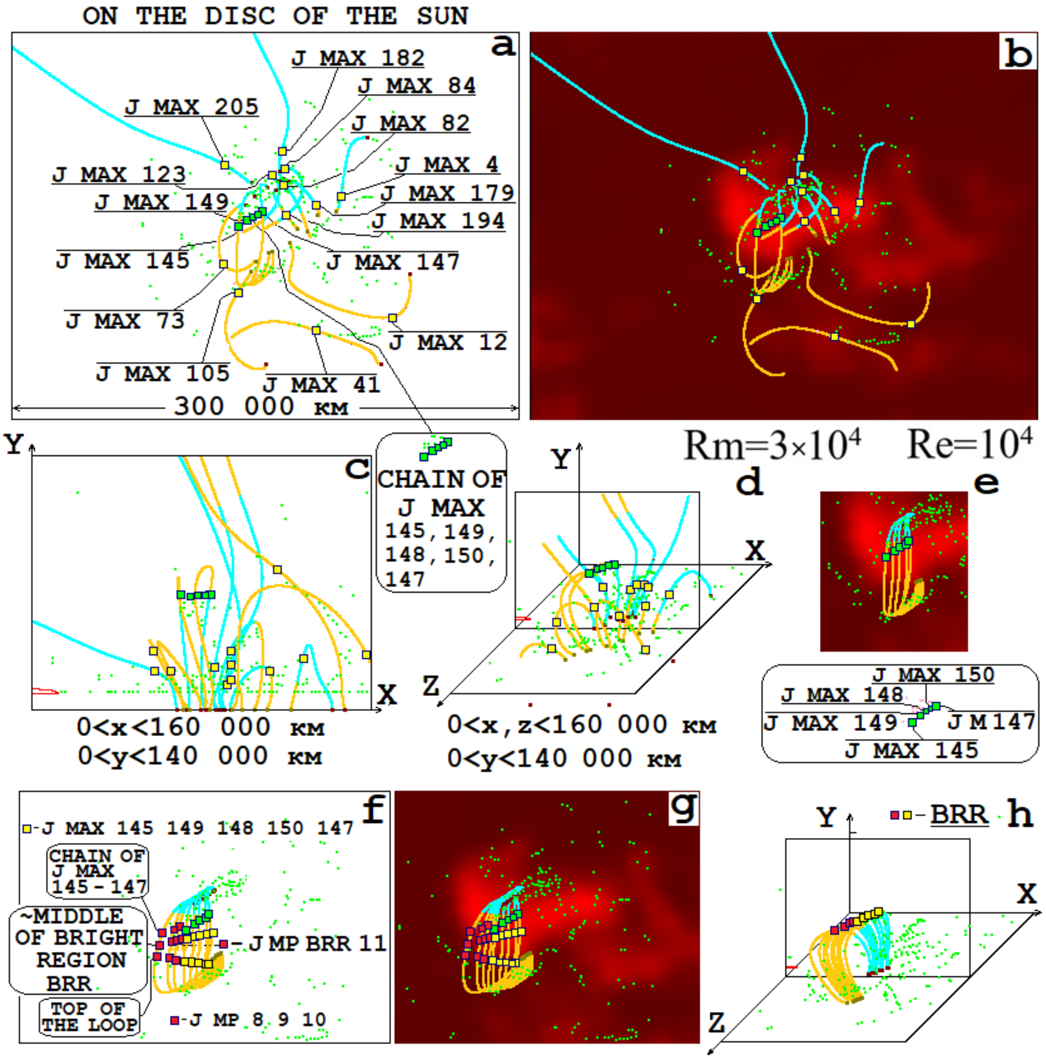

Figure 1. *The magnetic field configuration is represented by magnetic lines passing through the selected current density maxima. The projections of lines onto the picture plane perpendicular to the line of sight (a) with superposed distribution of microwave radio emission at a frequency of 17 GHz, obtained on the solar disk using the Nobeyama radioheliograph (b), onto the central plane of the computation domain (c), in 3D space (d). Arcade of lines (f, g, h) passing through the chain of maxima shown by green points. In (e, f, g, h) the lines passing through plane maxima in plane normal to magnetic field vector on the top of the loop are added.*

The magnetic field configuration obtained by MHD simulation is so complex that it is often impossible to determine the positions of singular lines and the current sheets appearing near them. For this purpose, a graphical search system [Podgorny and Podgorny 2013] was developed, based on determining the positions of the current density maxima, which are assumed to be achieved in the centers of the current sheets (according to presented here results this assumption is not always fulfilled, so the graphical search system should be corrected). The current density maxima are located on singular lines of the magnetic field. Magnetic forces **j**×**B**, creating a current sheet configuration, are determined by the current component along the singular line and the magnetic field components in the plane perpendicular to the singular line (the current sheet configuration plane, in which field

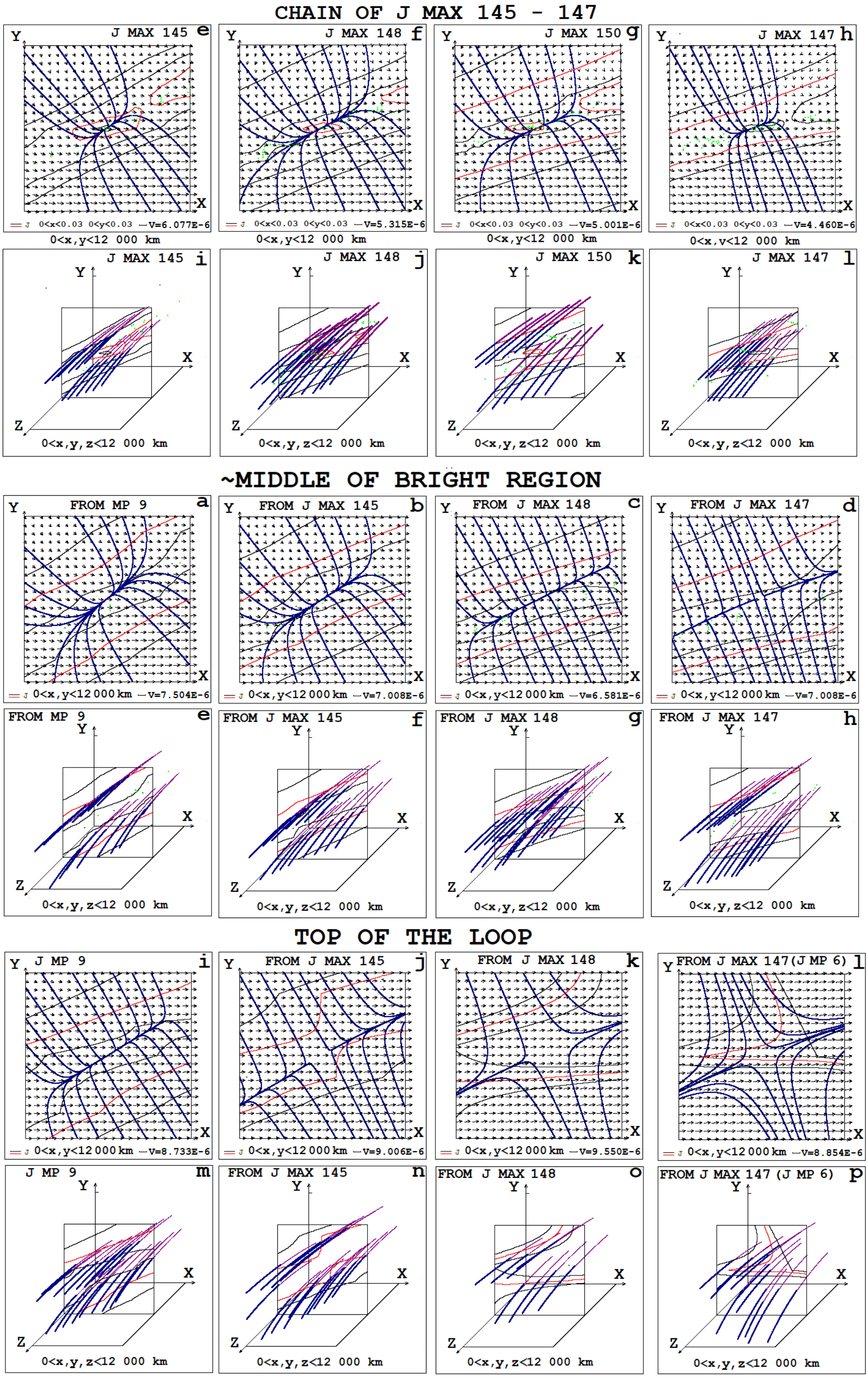

Figure 2. *Magnetic field configurations in small regions of 12 Mm.*

configuration of the current sheet is mostly pronounced). Therefore, the main role in the formation of current sheets is played by plane magnetic field configurations, i.e. lines tangent to the projections of the magnetic field vectors onto the configuration plane.

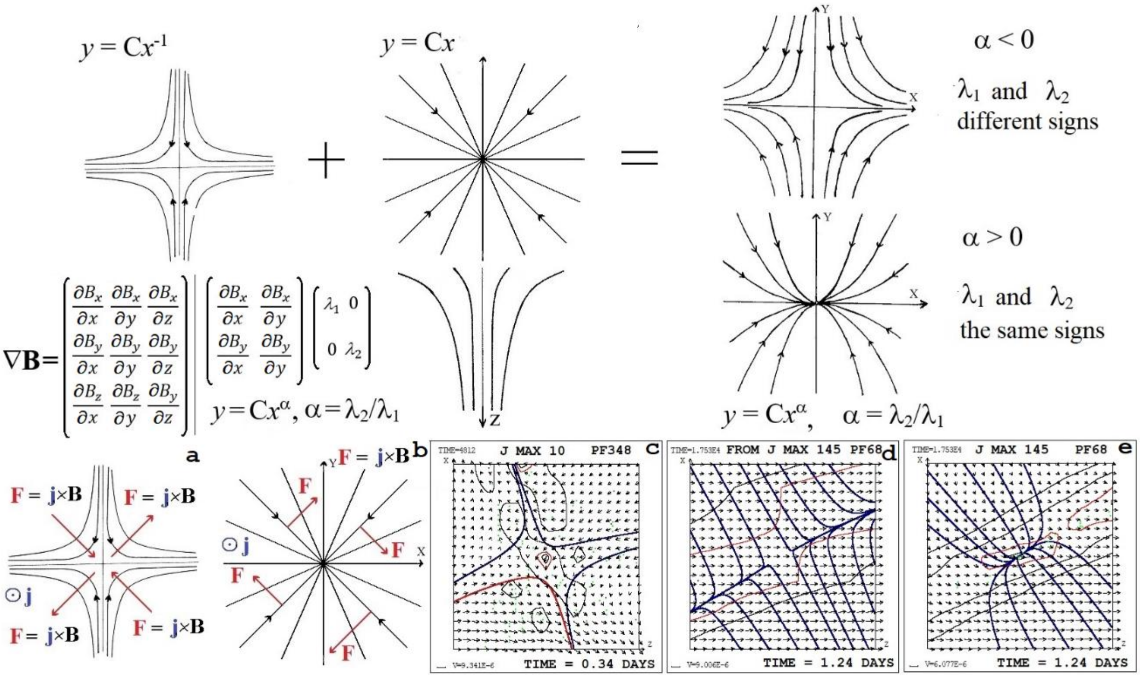

Figure 3. *Overlay of a diverging magnetic field on an X-type field near a singular line.*

2. Magnetic configuration near extended surface with increased current density

An analysis of the positions of current density maxima and magnetic field configurations in their vicinity, carried out for a number of flare and pre-flare situations [Podgorny et. al 2022, 2023; Podgorny and Podgorny 2023], showed the location of some maxima with magnetic field configurations promotable for the occurrence of a flare in the region of bright flare radiation. However, at the same time, maxima with such properties also occur outside the bright region of flare emission, and in the bright region there are not very many such maxima compared to their total number. To solve this problem, the pre-flare configuration of the magnetic field above the active region AR 10365 on May 26, 2003 at 02:32:05, three hours before the M 1.9 flare, was studied. In this moment the energy for solar flare is accumulated in the magnetic field and plasma of solar corona is heated by currents which creates this magnetic field. The results of MHD simulation were compared with observations of microwave radio emission at 17 GHz obtained from the Nobeyama Radioheliograph (NoRH). Magnetic field configuration is represented in Figure 1 by lines passing through maxima of current density with the numbers 145, 147, 194, 179, 4, 73, 105, 41, 12, 205, 123, 82, 84, 182. All current density maxima found by the graphical search system for flare positions are numbered in descending order of the current density value at the maximum. The current density maxima with numbers 145, 149, 148, 150 and 147 marked by green present the chain of maxima in the picture plane perpendicular to the line of sight which is situated near the bright region of pre-flare emission. To understand occurrence of bright region with intensive pre-flare energy release the magnetic lines passing through maxima of the chain are presented by their projections on the picture plane (Figure 1 e-g), which are situated mostly into the bright region, and by arcade in 3D space (Figure 1 h).

Figures 2a-h shows the plane (Fig. 2a-d) and three-dimensional (Fig. 2e-h) configurations near the chain maxima in a square and in a cube of 12,000 km. The two-dimensional region is a square of 12,000 km in size with the center at the point of the selected current density maximum, with the plane of the square located perpendicular to the magnetic field vector at the point of the selected maximum (plane of the current sheet configuration perpendicular to the magnetic line passing through the point of the selected maximum). The three-dimensional region is a cube 12,000 km in size centered at the point of the selected maximum of current density, so that the two-dimensional region is the central plane of this cube, i.e. a plane passing through the center of the cube parallel to two faces of the cube.

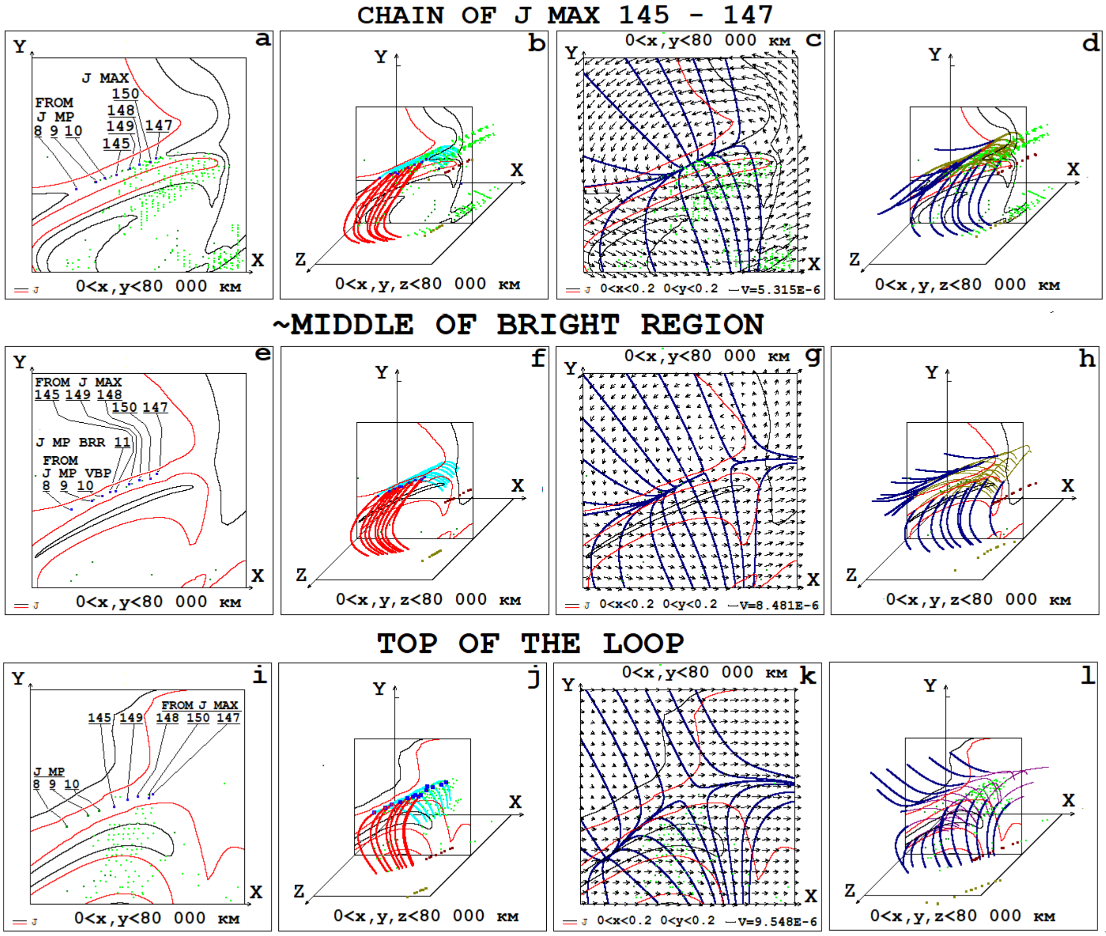

Figure 4. *Magnetic field configurations in large regions of 80 Mm.*

In Figures 2a-d the magnetic field strongly divergent in the plane of current sheet configuration (field appearing in magnetic traps of the mirror cell type) is superimposed on the X-type magnetic field. Variants of such superposition in which the X-type field or divergent magnetic field is dominated are shown in Figure 3. For configurations in Fig. 2a-d similar to Fig. 3e the magnetic forces cause plasma rotation around singular line (Fig. 3a), hindering the formation of current sheet and appearance of flare instability in formed current sheet. In three-dimensional configurations (Fig. 2e-h), the field lines do not diverge much along the singular line, which means a comparatively large longitudinal component of the magnetic field stabilizing the explosive instability. Therefore, these configurations in vicinities of chain maxima (Figures 2a-h) do not have properties that could significantly promote the flare release of energy. It became clear why chain of maxima is situated near the boundary.

The chain maxima are located close to each other (Fig. 1) and the field configurations in their vicinity are very similar (Fig. 2a-d и Fig. 2e-f), so that an assumption arises that all the chain maxima belong to the same current sheet of considerable width (~50,000 km), i.e. an extended surface with an increased current density. This assumption is confirmed by the study of plane and three-dimensional configurations in a square and in a cube with a larger size of

80,000 km with the center at the 148th maximum (Fig. 4a-d). The square is the central plane of the cube. In the square of a large size the intersection points of the magnetic lines passing through the chain maxima with the plane and also lines of equal current density are shown (Fig. 4a). Magnetic lines in a cube passing through the chain maxima form an arcade (Fig. 4b). The plane and three-dimensional configurations in large areas are shown in Figures 4c, d.

Configurations in small regions of 12 Mm in size with centers at the points of the arcade above the middle of bright region (Fig. 2 i-p) and at the top of the arcade (Fig. 2 q-x), as well as in large regions of 80 Mm in size with centers at the points above the bright region (Fig. 4e-h) and at the top of the arcade (Fig. 4i-l), were constructed similarly. The intersection points of the arcade magnetic lines with the central planes of large regions of 80 Mm in size were chosen as the centers of small regions of 12 Mm in size. To the magnetic lines of the arcade passing through the maxima of the chain, magnetic lines (Fig. 1f-h) passing through the plane maxima of the current density located in the central planes of the large-size regions of 80 Mm in the middle of the bright region and at the top of the arcade are added. The results presented in Figures 2, 4 show that the configurations in both the small 12 Mm and large 80 Mm regions in the middle of the bright pre-flare region and at the top of the arcade are more promotable for the occurrence of flare instability than in the chain of current density maxima.

3. Discussion and conclusion

The performed analysis of magnetic configurations provides an explanation for the heating of the plasma in the bright pre-flare region, despite the absence of a chain of current density maxima near the middle of this bright region. In the future, these results will need to be refined by performing more accurate calculations and analysis, and then used to modernize the graphical system for searching for the positions of solar flares.

References

Bratenahl, A., Hirsch, W. (1966). An experimental study of a neutral point in a plasma, *Proceedings of the AIAA Plasmadynamics Conference*, Monterey, CA, USA, 2–4 March 1966, Paper No. 66–152, DOI: 10.2514/6.1966-152.

Lin, R.P., Krucker, S., Hurford, G.J., et al. (2003). RHESSI observations of particle acceleration and energy release in an intense gamma-ray line flare, *Astrophysical Journal*, Vol. 595, L69–L76, DOI: 10.1086/378932.

Podgorny, I.M., Dubinin, E.M., Israilevich, P.L., Nikolaeva, N.S. (1988). Large-scale structure of the electric field and field-aligned currents in the auroral oval from Intercosmos–Bulgaria satellite data, *Geophysical Research Letters*, Vol. 15, pp. 1538–1540, DOI: 10.1029/GL015i013p01538.

Podgorny, I.M., Balabin, Y.V., Vashenyuk, E.V., Podgorny, A.I. (2010). The generation of hard X-rays and relativistic protons observed during solar flares, *Astronomy Reports*, Vol. 54, pp. 645–656, DOI: 10.1134/S1063772910070085.

Podgorny, A.I., Podgorny, I.M. (2013). MHD simulation of solar flare current sheet position and comparison with X-ray observations in active region NOAA 10365, *Sun and Geosphere*, Vol. 8, pp. 71–76.

Podgorny, A.I., Podgorny, I.M., Borisenko, A.V. (2022). Investigation of the mechanism of a solar flare by means of MHD simulations above the active region in real scale of time: The choice of parameters and the appearance of a flare situation, *Open Astronomy*, Vol. 31, pp. 27–37, DOI: 10.1515/astro-2022-0006.

Podgorny, A.I., Podgorny, I.M. (2023). Problems arising in studying the mechanism of a solar flare by comparing the results of MHD simulations above the real active region with observations, *Proceedings of the 15th Workshop "Solar Influences on the Magnetosphere, Ionosphere and Atmosphere"*, Primorsko, Bulgaria, June 2023, pp. 123–128, DOI: 10.31401/WS.2023.proc.

Podgorny, A.I., Podgorny, I.M., Borisenko, A.V. (2023). MHD simulations of the solar corona to determine the conditions for large solar flares and the acceleration of cosmic rays during them, *Physics*, Vol. 5, No. 3, pp. 895–910, DOI: 10.3390/physics5030058.

Syrovatskii, S.I. (1966). Dynamic dissipation of energy in the vicinity of the magnetic field neutral line, *Soviet Physics JETP*, Vol. 23, pp. 754–762. Available online: http://jetp.ras.ru/cgi-bin/e/index/e/23/4/p754?a=list

DOI: 10.31401/WS.2025.proc.11

Proceedings of
the Seventeenth Workshop "Solar Influences on the Magnetosphere, Ionosphere and Atmosphere"
June, 2025

On Modified Yukava Screening in Dense Hydrogen Plasma

Sakan N.M.[1]*, Simić.Z.*[2]*, Srećković V.A.*[1]*, Traparić I.*[1]*, Dechev M.*[3]

[1]University of Belgrade, Institute of Physics, PO Box 57, 11001 Belgrade, Serbia
nsakan@ipb.ac.rs
[2]Astronomical Observatory, Volgina 7, 11060 Belgrade, Serbia
[3]Institute of Astronomy and National Astronomical Observatory, Bulgarian Academy of Sciences,
72, Tsarigradsko chaussee Blvd. Sofia, Bulgaria

Abstract

The plasma of low and moderate non-ideality is of interest in solar and stellar plasma. The previous research of modeling a collective plasma influence onto the emitter in plasma was conducted with the modeling of electron screening influence by the usage of Debye screening mechanism. Although this was a known erroneous presumption a preliminary results has shown a expected behavior in respect to particles in plasma densities as well as temperatures that was present in modeled plasma. The more thorough research has shown that the modified Yukava type screening is more applicable. Here are presented preliminary results of plasma influence onto the emitter potential in pure hydrogen plasma. This is the further step in development of more detailed analysis of collective phenomena in area of moderate to dense plasma influence.

Keywords: hydrogen dense plasma; Solar plasma; plasma microfield;

1. Theoretical remarks

In dense plasma, the inter-particle Coulomb interaction becomes dominant over the thermal kinetic energy [Fortov et al., 2006.]. Under such conditions, the coupled system of particles exhibits behavior reminiscent of a crystalline solid. For the case of hydrogen, a simplified form of the non-ideality parameter Γ and Wigner-Seitz radius are given by

$$\Gamma=\frac{E_p}{E_k}=\frac{e^2}{\mathrm{kT}r_{\mathrm{WS}}}\sim \mathrm{e}^2 N_e^{1/3}\beta, \quad \beta=1/\mathrm{kT}, \ \text{and} \ r_{\mathrm{WS}}=\left(\frac{3}{4\pi \mathrm{N}_e}\right)^{1/3}. \tag{1}$$

At high Γ values ($\Gamma>1$), the ions arrange themselves in a structured, nearly crystalline configuration to minimize Coulomb energy. In particular, the system tends toward a locally ordered state resembling a face-centered cubic (FCC) lattice, which is one of the most efficient packing arrangements for spheres in three dimensions. The FCC structure, found in many solid metals, maximizes the nearest-neighbor distance while minimizing the free energy of the system. Similarly, in strongly coupled plasmas, the ions adopt configurations where their mutual repulsion is optimized, leading to short-range order analogous to that of an FCC crystal.

Inside such a dense-packed, crystal-like structure, screening mechanisms become crucial in determining the effective local pseudo-potential. The electron cloud surrounding ions modifies the bare Coulomb interaction, leading to screened potentials such as the Yukawa or Debye-Hückel form, which significantly influence the stability and dynamics of the ion lattice. This screening effect must be accounted for when describing the thermodynamic and transport properties of strongly coupled plasmas.

The interaction in plasma has been successfully modeled using a cut-off Coulomb potential in previous studies, as demonstrated in [Dimitrijević et al., 2018.], [Ignjatović et al., 2009.], [Mihajlov et al., 2015.], and [Salpeter. 1954.]. While plasma effects are typically expected to dominate at distances far from the ionic core (compared to its characteristic radius), they can also significantly influence the form of ab initio-derived pseudo potentials.

For hydrogen, the range $0.1 \leq \Gamma \leq 1.5$ represents a particularly important regime where the system transitions from weakly coupled ($\Gamma<1$) to moderately coupled ($\Gamma\geq1$) plasma. In this interval:

Near $\Gamma\leq0.1$, the system begins to show noticeable deviations from ideal plasma behavior.

At $\Gamma\geq1$, the potential energy becomes comparable to the kinetic one (the definition of Γ).

Approaching $\Gamma\geq1.5$, short-range order starts to emerge while maintaining fluid-like properties.

This transition region is crucial for understanding hydrogen plasmas in many astrophysical and laboratory conditions. For other ion species with different charge states and masses, the model's behavior needs more comprehensive examination, as the relevant ranges and coupling effects may differ substantially.

Yukawa-like Screening in Coupled Plasmas

The screening behavior in plasmas undergoes significant changes across different coupling regimes:

Weak Coupling Regime

In the Debye-Hückel limit, the screening is characterized by the Debye length in SI as well as atomic units:

$$\lambda_D = \sqrt{\frac{k_B T}{4\pi \mathrm{n}_e e^2}} = \sqrt{\frac{T}{4\pi \mathrm{n}_e}}, \tag{2}$$

where the screened potential follows the classical Yukawa form.

Intermediate Coupling Regime ($0.3<\Gamma\leq3.0$)

As coupling increases, nonlinear effects become important. We implement a modified Yukawa screening where:

$$\lambda_{\mathrm{eff}} = \frac{\lambda_D}{1+\alpha\Gamma^{3/2}}, \alpha \approx 0.2, \tag{3}$$

with the corresponding screened potential:

$$V(r) = -\frac{Z}{r} e^{-r/\lambda_{\mathrm{eff}}}. \tag{4}$$

Generalized Screening Approach

For arbitrary base potentials $V_{\mathrm{base}}(r)$, the screening can be incorporated through:

$$V_{\mathrm{screen}}(r) = \mathrm{V}_{\mathrm{base}}(r) e^{-r/\lambda_{\mathrm{eff}}}, \tag{5}$$

where λ_{eff} may be determined self-consistently . This approach maintains consistency with the OCP (One-Component Plasma) limit while allowing for more complex interactions.

2. Results and Discussion

The screening behavior in moderately coupled plasmas exhibits characteristic features that depend on both the number of ionic layer shells considered in calculation, the system temperature, as well as the inter ionic distance related to Wiegner-Seitz radius r_{WS} from the Eq. (1). For the purpose of the simplified analysis on all figures a behavior of the ratio of the calculated potential over a Coulomb potential, $V_{\mathrm{avg}}(r)/V_{\mathrm{Coul}}(r)$, is considered. Figures 1-4 demonstrate these effects. The number of shells indicate how many shells with ions on roughly another distance layer are taken into account. They roughly assemble a shell like structure, like onion shells around a emitter, central ion, considered into calculation.

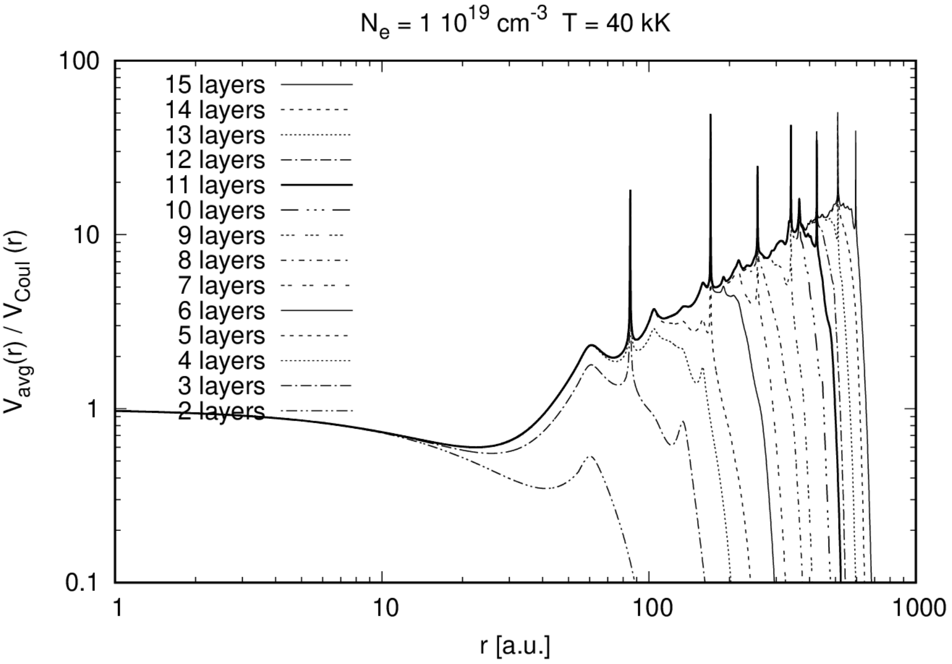

Figure 1. *Convergence of the averaged potential with increasing number of ionic shells (N = 1-15). The calculations are done for* $N_e = 1 \cdot 10^{19} cm^{-3}$*, T=40kK.*

Figure 1 shows the systematic convergence of the potential towards the long range averaged plasma potential as more ion shells are included. The number of layers reflects onto the number of ions in a surrounding of considered, a middle one, that are influencing its potential. With the increasing of layers a ions count in a calculation of a averaged potential arises rapidly, so it was needed to estimate a optimal one. The characteristic slope change at $r \approx 50$ a.u. marks the transition from local ionic structure to collective plasma screening. It could be seen that no more than couple of layers should not be considered. As a figure of merit for hydrogen case we have used 8 layers. Further enlargement of considered ionic layers did not reflect on the quality of the results but only on wasted computing power. The rapid fall of the potential ratio at highest radii values is related to the size of the considered system and screening effect. It has only physical meaning that reflects only our finite size of considered ions like perturbers.

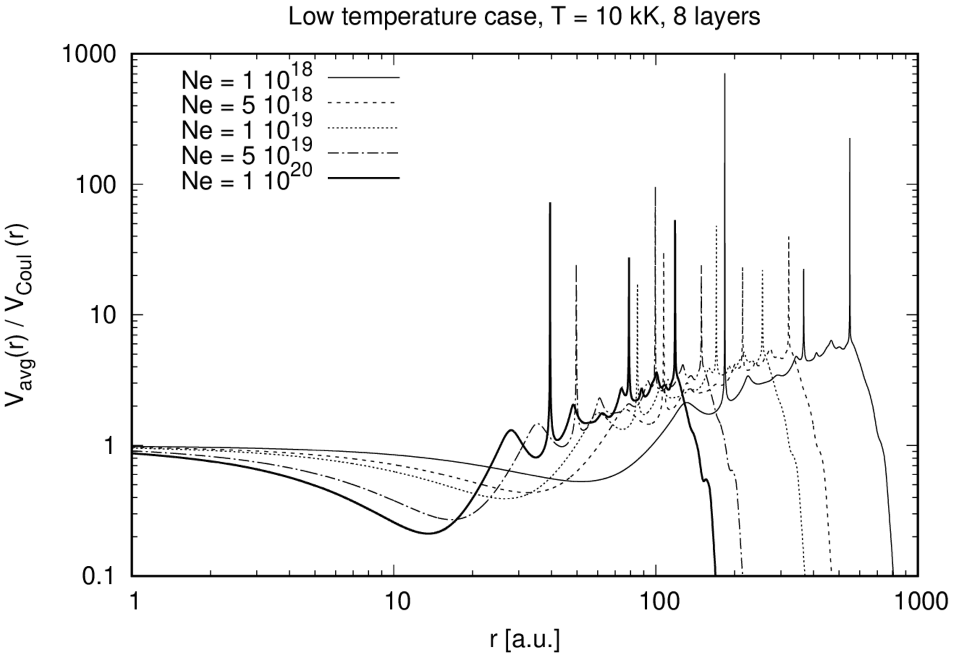

Figure 2. *Low temperature case, T=10kK.*

At lower temperatures (Fig. 2), shows the behavior of the calculated pseudo potential for low temperature T=10kK. The peak positions agree well with the expected FCC lattice positions (inset shows the radial distribution function).

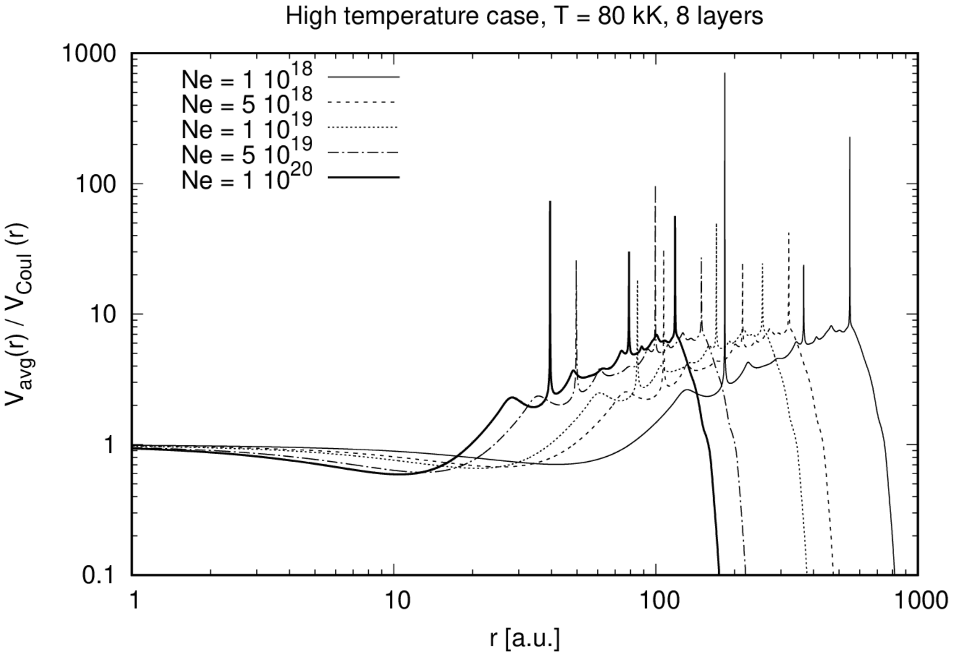

Figure 3. *High-temperature case T=80kK, considered shells influence is a significantly broadened if compare with Fig. 2.*

The high-temperature results (Fig. 3) differs from low temperature case, Fig. 2, solely by the electron screening. From here it could be denoted that the modified Yukawa potential screening has influence that may reflect onto the solution of the Schrodinger equation for the calculated potential.

3. Conclusions

Our analysis of screening in moderately coupled plasmas ($0.3 \leq \Gamma \leq 3$) yields three principal findings.

As first the modified Yukawa screening represents a improvement over conventional approaches in matching ab initio potentials with pure Debye screening, particularly for $1 \leq \Gamma \leq 2$ where correlation effects are strongest.

These results validate the pseudo crystalline approximation for solar chromosphere conditions (typically $\Gamma \approx 1.5$), while suggesting necessary modifications for photospheric applications ($\Gamma \approx 0.8$). The method’s accuracy could be further improved by incorporating temperature effect of the ions, anisotropic screening at high Γ, adding quantum corrections for T<5 kK, extending to multi-component plasmas.

This method is promising in obtaining a calculation intensity relaxed model that is capable producing a pseudo potential for describing a plasma behavior by the means od optical as well as transport cross sections

Acknowledgment

This research was supported by the Ministry of Science, Technological Development and Innovation of the Republic of Serbia (MSTDIRS) through 2025. contract with Astronomical Observatory (Belgrade), and with Institute of physics and with the support from the Bulgarian Academy of Sciences ans Serbian Academy of Science and Arts (Bilateral grant agreement between Institute of Astronomy and National Astronomical Observatory Sofia, Bulgaria, and Astronomical Observatory, Belgrade, Serbia), that is gratefully acknowledged.

References

Fortov, V., Iakubov, I., Khrapak, A. (2006). *Physics of Strongly Coupled Plasma*, International Series of Monographs on Physics, Oxford University Press, Oxford, ISBN: 0199299803, 9780199299805.

Dimitrijević, M.S., Srećković, V.A., Sakan, N.M., Bezuglov, N.N., Klyucharev, A.N. (2018). Geomagnetism and aeronomy, *Geomagnetism and Aeronomy*, Vol. 58, No. 8, pp. 1067–1072, DOI: 10.1134/S0016793218080054.

Ignjatović, Lj.M., Mihajlov, A.A., Sakan, N.M., Dimitrijević, M.S., Metropoulos, A. (2009). *Monthly Notices of the Royal Astronomical Society*, Vol. 396, No. 4, pp. 2201–2210, DOI: 10.1111/j.1365-2966.2009.14870.x.

Mihajlov, A.A., Srećković, V.A., Sakan, N.M. (2015). *Journal of Astrophysics and Astronomy*, Vol. 36, No. 4, 0, DOI: 10.1007/s12036-015-9344-y.

Salpeter, E.E. (1954). Electron screening and thermonuclear reactions, *Astrophysical Journal*, Vol. 120, p. 161, DOI: 10.1071/PH540373.

DOI: 10.31401/WS.2025.proc.12

Research on Solar Corona during Total Solar Eclipses

Tsvetkov Ts., Petrov N., Minev M.

Institute of Astronomy and National Astronomical Observatory, Bulgarian Academy of Sciences,
Sofia, Bulgaria
tstsvetkov@astro.bas.bg

Abstract

Total solar eclipse observations have played a pivotal role in unveiling numerous secrets of the solar corona. From its initial identification in the 17th century to groundbreaking revelations about its million-degree temperatures in later centuries, eclipses have continued to provide key insights into the corona's dynamics and its dependence on solar activity cycles. Despite advancements in instrumentation and theoretical models, eclipses remain unparalleled opportunities for coronal research. Notably, the region of the corona most effectively observed from the ground during these events is inaccessible to any current space-based coronagraphs.

Our team have yet organized 7 scientific expeditions to observe total solar eclipses for the last 26 years. In the current paper we share our experience on the obtained research and conducted experiments underlining the point of continuing such observations today.

Keywords: expedition; eclipse; corona;

1. Introduction

The solar corona, the Sun's outermost atmospheric layer, presents a dynamic and captivating region of plasma with temperatures reaching millions of degrees Kelvin. Understanding its intricate structure and behavior remains one of the most compelling challenges in solar physics. Despite extensive research, fundamental questions persist –including the mechanisms behind coronal heating and the drivers of solar wind acceleration.

One of the rare opportunities to directly observe the solar corona in its full grandeur arises during total solar eclipses (TSEs). During these fleeting moments, the bright solar disk is obscured, revealing the fainter and more extended features of the corona. Such observations are crucial for gaining insights into the complex magnetic field structures and plasma flows that define this enigmatic region. Despite the remarkable advancements in coronagraph technology, eclipse observations remain indispensable. Space-based instruments often face limitations such as stray light contamination and constrained fields of view, which hinder the ability to capture the full extent of coronal structures close to the solar limb [Boe et al., 2021]. Furthermore, eclipses offer the unique advantage of capturing a broad spatial and spectral view of the corona under natural conditions, unaltered by instrumental limitations inherent to ground-based or spaceborne coronagraphs.

Unlike regular solar observations, TSEs allow the study of the corona from its innermost regions near the solar limb to its far-reaching outer extensions up to about 7 solar radii. This continuous view provides critical data for understanding the interactions between closed and open magnetic field lines, which influence the formation of different activity events as well as the solar wind. The highly dynamic environment of the corona also exhibits complex density and temperature variations, including loop structures, streamers, and polar plumes. Investigating these features is essential for unraveling the mechanisms behind the corona's extremely high temperatures and transient events.

Scientific expeditions during TSEs have long played an important role in probing the corona's mysteries. Usually, they are meticulously planned to optimize the collection of high-quality data. Researchers deploy specialized instruments to capture detailed information about the corona's composition, magnetic fields, and plasma dynamics. These expeditions often target remote locations along the narrow eclipse path, where weather conditions and atmospheric clarity are favorable. The data gathered during these brief but invaluable opportunities have led to numerous breakthroughs, including improved models of solar wind generation and advancements in space weather forecasting [Boe et al, 2021; Filipov et al., 2020; Pasachoff, 2017].

This paper explores the scientific significance of TSE observations and their indispensable role in advancing our understanding of the solar corona. By highlighting observational techniques, data acquisition strategies, and key findings, we aim to underscore the critical insights these unique events offer into the Sun’s complex and dynamic outer atmosphere.

2. Total Solar Eclipse Expeditions

Our research focuses on leveraging these eclipse events to investigate the coronal structure, its dynamic properties, topology, and energetic processes. We employ an interdisciplinary approach that combines high-resolution imaging and detection of atmospheric changes by recording various meteorological parameters. By synthesizing observational data with theoretical insights, we aim to address key questions concerning both coronal properties and the Sun’s influence on the heliosphere and, therefore, on our planet [Nikolov and Petrov, 2014].

The first scientific observations of TSE ever made by Bulgarian astronomers dates back to 1961, when the lunar shadow passes through the northern part of our country. Unfortunately, no member of our team participated in the observations then, but we are provided with the original observations of this eclipse [Tsvetkov and Petrov, 2022]. Still, 38 years later - in 1999 the totality path crossed our territory once again. It was our first expedition for TSE observations, out of seven organized so far (Figure 1).

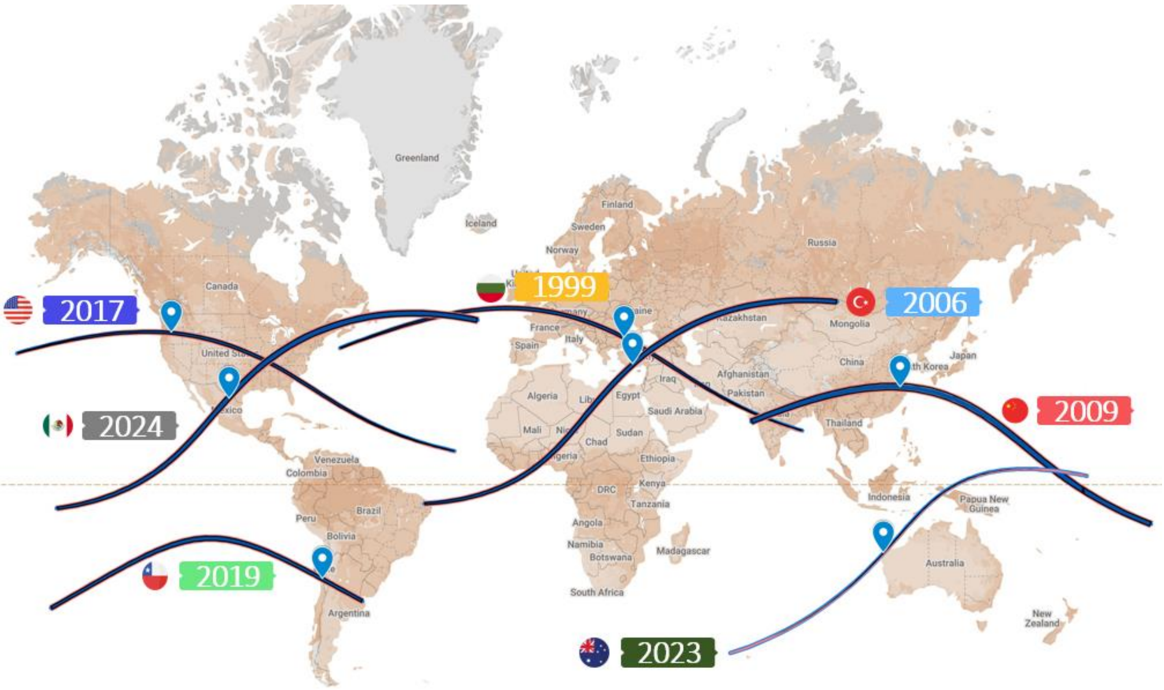

Figure 1. *Map of totality paths of all TSEs observed by our team with labels of observational site locations.*

Organizing TSE expeditions is a complex and demanding endeavor. Selecting an appropriate observation site requires careful consideration of multiple factors, including weather patterns, accessibility, and the path of totality. Often, this involves targeting remote locations where weather conditions are most favorable, necessitating extensive logistical planning to transport personnel and sensitive instruments. The challenges are compounded by the narrow time window of totality. Researchers must meticulously synchronize instrument setups and operational tasks to ensure that all planned measurements are successfully executed within this brief period.

Different solar eclipses provide diverse observational opportunities, contributing to a more comprehensive understanding of the solar corona. Variability in elevation, solar altitude, and atmospheric conditions during each event offers distinct perspectives on coronal structures and dynamics (Table 1). This has always been a priority when planning our next expedition. For example, in Chile (2019) the Sun was setting at the end of the partial phase of the eclipse, while in Mexico (2024) it reached 70^o during the totality. To achieve statistically significant results, it is essential to gather data from multiple eclipses, allowing researchers to analyse variations and correlations across different conditions (different phases of the solar cycle, different locations and environment, etc.). Also, the eclipses in 1999 and 2017 (and the ones from 2006 and 2024, respectively) are identical since they are separated by one saros. This cumulative approach not only enhances the robustness of scientific findings but also provides more accurate and nuanced understanding of the Sun’s outer atmosphere.

Table 1. *Details for the observational sites during the TSE expeditions of our team (1999 –2025).*

Date of the TSE	Location	Coordinates	Elevation [m]	Duration of totality [s]	Sun’s altitude [^{o}]
11 August 1999	Bulgaria	43^o 32’ 34.1” N 28^o 36’ 16.0” E	0	142	59
29 March 2006	Turkiye	36^o 47’ 10.1” N 31^o 23’ 21.6” E	38	225	54
22 July 2009	China	30^o 28’ 20.3” N 119^o 35’ 31.1” E	1200	338	54
21 August 2017	USA	44^o 42’ 11.6” N 120^o 47’ 52.2” W	1200	124	42
2 July 2019	Chile	29^o 47’ 32.1” S 70^o 53’ 06.0” W	1450	135	13
20 April 2023	Australia	22^o 07’ 21.9” S 114^o 05’ 08.1” E	10	58	54
8 April 2024	Mexico	27^o 13’ 15.2” N 101^o 43’ 52.2” W	660	249	70

On the other hand, during more than 25 years of research during TSEs now, we have witnessed significant technological advancements that have greatly enhanced the accuracy and quality of data collected. Early expeditions relied on analog imaging systems and less sensitive detectors, which limited the resolution and scope of observations. However, with the advent of high-resolution digital imaging and modern instruments, we now capture more detailed measurements of coronal structures and dynamics, we can precisely track the meteorological parameters during the eclipse and try new approaches to previously obtained experiments. On our expedition to Australia (2023) we tested for the first time during an eclipse the capabilities of a digital polarization camera for the purposes of polarization studies of the corona [Zinkova et al., 2022]. All these improvements have had a profoundly positive impact on our research, allowing for deeper insights into the corona's behavior.

3. Scientific Research

Solar corona as being a part of the solar atmosphere is a dynamic layer [Pasachoff et al., 2007]. Its shape and structure changes depending on the phase of the solar cycle, the height above the solar limb and heliogrpahic coordinates we are observing it at [Priest, 2014]. White-light observations of the corona during TSEs provide invaluable insights into the Sun's outer atmosphere, having a long-standing history in solar research. The first photograph of a total solar eclipse in the middle of the 19th century provided unprecedented views of the corona, laying the foundation for modern solar physics [Rue, 1863]. Nowadays they may reveal detailed structures in the corona [Pasachoff and Rusin, 2022]. During the eclipses observed near solar minimum – from Turkiye (2006), China (2009), USA (2017) and Chile (2019), streamers at lower latitudes and polar plumes are clearly visible (Figure 2). Getting closer to periods of solar maximum, the shape of the corona becomes asymmetrical due to the influence of strong magnetic fields, but meanwhile more coronal formations appear. Although we have registered the presence of prominences in the corona on all expeditions, in 1999 (2 years before reaching the 23-rd solar maximum) they were the most numerous – 12. New digital cameras and image-processing techniques developed before the TSEs in 2017 and 2019 (also near the solar maximum) allowed revealing details about the connection between the prominences and surrounding cavities. Usually, these features are captured on composite images, which are result of combining lots of high-quality photos of the corona, taken with a variety of instruments and settings. Lenses with different focal length and diversified exposure times reveal different parts of the corona, enhancing our comprehension of its morphology and its variations with solar activity (Figure 2).

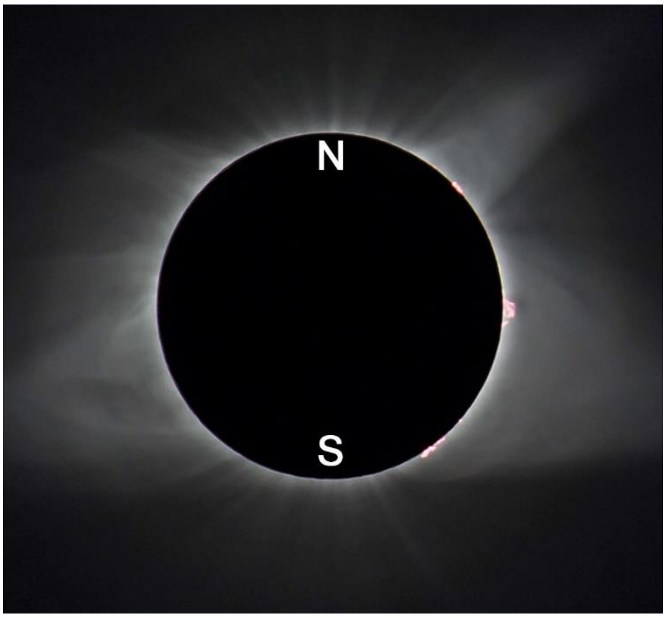

Figure 2. *A composite image of the corona from the TSE on 2017 August 21 (USA).*

Eclipse observations remain the sole method for capturing white-light data from the crucial lower and middle coronal regions as they host the formation of the solar wind and encompass the lower sections of coronal structures at least until coronal observations become feasible from the Moon or through tandem spacecraft equipped with a distant occulter [Pasachoff, 2017].

Polarimetric observations in white light allow scientists to separate the K-corona (arising from Thomson scattering by free electrons) from the F-corona (resulting from sunlight scattering by interplanetary dust). The intensity of the polarized light directly correlates with the number of free electrons along the line of sight, which enables mapping electron density distributions in the corona. Understanding how electron density varies across different regions of the corona is essential for pinpointing the sources of solar wind streams [Liang et al., 2023]. Electron density data, when combined with temperature and magnetic field measurements, help refine models of coronal heating mechanisms. Eclipse-based polarimetric observations often capture the inner corona, which is difficult to observe even with advanced spaceborne coronagraphs [Boe et al., 2021]. This provides unique, high-resolution data to improve and validate findings from space missions.

We obtain the polarimetric experiment during every expedition [Merzlyakov et al., 2019] collecting sufficient data that is about to be summarized. On Figure 3 we show the result of polarimetric observations of the corona during the eclipse in 2023 (Australia). Our data allowed separation of the polarized light or the so-called K-corona (right) from the total coronal white-light emission (left).

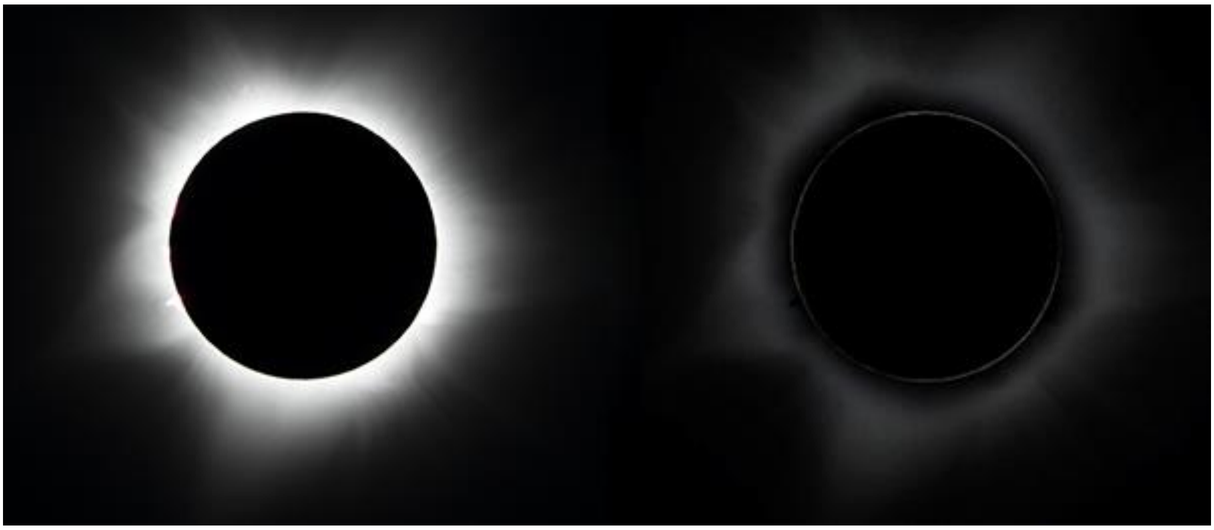

Figure 3. *White-light (left) vs. polarized (right) solar corona from the TSE on 20 April 2023 (Australia). Original images are taken with 600 mm lens and exposure time of 1/100 s.*

TSEs are not only interesting for the scientist studying the Sun, since they also have a noticeable impact on Earth's environment, particularly in terms of meteorological changes. During an eclipse, rapid fluctuations in solar radiation can lead to a temporary drop in temperature, changes in wind speed and direction, and variations in atmospheric pressure [Harrison and Hanna, 2016]. These phenomena often create localized cooling effects, providing valuable opportunities for studying atmospheric dynamics and the interplay between solar radiation and weather systems.

We tracked atmospheric conditions during every TSE, but since 2017 we included not only a temperature and humidity data logger, but also an anemometer measuring the wind velocity and direction. The biggest temperature drop we recorded during a totality happened in 2024 (Mexico) – 5.3 ^{o}C. A year earlier in 2023 (Australia) the temperature dropped 3.5 ^{o}C, while in 2019 (Chile) – only 1.6 ^{o}C.

On the other hand, by taking into account the meteorological parameters during the eclipse and comparing them to the shadow bands before and after the totality, we check the hypothesis about the role of the near-ground atmosphere on the shadow bands' patterns we observe. Since in this paper we are focused on the coronal research, more about our other experiments can be found in Zlatev et al. [2020].

In the future, we plan to continue working on the listed experiments in order to accumulate additional data that will help to obtain better quality results, as well as to add some new studies. For our next expedition, we plan to make a new attempt to register the outer boundary of the dust-free zone in the solar corona by detecting resonant emission of atoms and low-charged ions as a sign of the sublimation process of solid neutral particles from the S-corona.

4. Conclusions

TSEs remain invaluable events for advancing our understanding of the solar corona. Despite the significant progress made with spaceborne instruments, these natural phenomena still offer opportunities for observing regions of the corona that are otherwise inaccessible. The combination of high-resolution imaging, polarimetric data, and comprehensive observational campaigns during eclipses has contributed to refining our understanding of coronal structures, plasma dynamics and underlying physical processes. Additionally, eclipse observations continue to provide complementary data that enhance and validate findings from both theoretical models and space-based missions.

For more than quarter a century now our team organized 7 expeditions for observations of TSEs collecting in overall more than 20 minutes of totality for revealing the mysteries of the eclipsed Sun. In the near future our eyes are on the upcoming eclipse on 12 August 2026. This event will be particularly significant for mainland Europe, as it will be the first TSE visible there in the 21st century. The maximum duration of totality is expected to be approximately 2 minutes and 18 seconds with the point of greatest eclipse located between the coasts of Greenland and Iceland. We already started working on the organization of this expedition, since we consider the study of TSEs as a cornerstone of solar research, yielding crucial insights into one of the most dynamic and complex regions of the solar atmosphere.

Acknowledgment

This work is supported by the National Science Fund of Bulgaria with contracts No. KP-06-M78/1 and KP-06-N64/3.

References

Boe, B., Yamashiro, B., Druckmüller, M., Habbal, S. (2021). The double-bubble coronal mass ejection of the 2020 December 14 total solar eclipse, *Astrophysical Journal*, Vol. 914, No. 2, L39, DOI: 10.3847/2041-8213/ac05ca.

Filipov, B., Koutchmy, S., Lefaudeux, N. (2020). Solar total eclipse of 21 August 2017: Study of the inner corona dynamical events leading to a CME, *Solar Physics*, Vol. 295, 24, DOI: 10.1007/s11207-020-01586-4.

Harrison, R.G., Hanna, A. (2016). The solar eclipse: a natural meteorological experiment, *Philosophical Transactions of the Royal Society A*, Vol. 374, DOI: 10.1098/rsta.2015.0225.

Liang, Y., Qu, Z., Hao, L., Xu, Z., Zhong, Y. (2023). Imaging-polarimetric properties of the white-light inner corona, *Monthly Notices of the Royal Astronomical Society*, Vol. 518, No. 2, pp. 1776–1786, DOI: 10.1093/mnras/stac3183.

Merzlyakov, V.L., Tsvetkov, Ts., Starkova, L.I., Petrov, N. (2019). Polarization of white-light solar corona and sky polarization effect during total solar eclipse on March 29, 2006, *Serbian Astronomical Journal*, Vol. 199, pp. 83–89, DOI: 10.2298/SAJ190620005M.

Nikolov, T., Petrov, N. (2014). Main factors influencing climate change: A review, *Comptes Rendus de l’Académie Bulgare des Sciences*, Vol. 67, No. 11, EID: 2-s2.0-84916598222.

Pasachoff, J.M., Rusin, V., Druckmüller, M., Saniga, M. (2007). Fine structures in the white-light solar corona at the 2006 eclipse, *Astrophysical Journal*, Vol. 665, No. 1, pp. 824–829, DOI: 10.1086/519680.

Pasachoff, J.M. (2017). Heliophysics at total solar eclipses, *Nature Astronomy*, Vol. 1, 0190, DOI: 10.1038/s41550-017-0190.

Pasachoff, J.M., Rusin, V. (2022). White-light coronal imaging at the 21 August 2017 total solar eclipse, *Solar Physics*, Vol. 297, 3, DOI: 10.1007/s11207-022-01964-z.

Priest, E.R. (2014). *Magnetohydrodynamics of the Sun*, University of St Andrews, Cambridge University Press, DOI: 10.1017/CBO9781139020732.

de la Rue, W. (1863). The Bakerian Lecture — On the total solar eclipse of July 18th, 1860, observed at Rivabellosa, near Miranda de Ebro, in Spain, *Philosophical Transactions of the Royal Society*, Vol. 12, DOI: 10.1098/rspl.1862.0010.

Tsvetkov, Ts., Petrov, N. (2022). Why total solar eclipses are important to science?, *Journal of Physics: Conference Series*, Vol. 2255, 012001, DOI: 10.1088/1742-6596/2255/1/012001.

Zinkova, Y., Tsvetkov, Ts., Zlatev, R., Petrov, N. (2022). Polarization of the daytime sky, *Proceedings of Science*, Vol. 427, 040, DOI: 10.22323/1.427.0040.

Zlatev, R., Petrov, N., Tsvetkov, Ts., Ivanov, E., Miteva, R., Popov, V., Nakeva, Y., Bojevski, L. (2020). Shadow bands and related atmospheric phenomena registered during total solar eclipses, *Publications of the Astronomical Society "Rudjer Boskovic"*, Vol. 20, pp. 79–84.

DOI: 10.31401/WS.2025.proc.13

Proceedings of
the Seventeenth Workshop "Solar Influences on the Magnetosphere, Ionosphere and Atmosphere"
June, 2025

MHD Instabilities in Shear Flow of Anisotropic Solar Wind Plasma

Dzhalilov N., Samadov J.

Shamakhy Astrophysical Observatory;
dnamig@gmail.com
jannat.samadov@gmail.com

Abstract

The study investigates the stability of anisotropic collisionless plasma layers subjected to shear flows within the magnetohydrodynamic (MHD) framework. Using moment equations derived from the Vlasov kinetic model and incorporating heat fluxes along the magnetic field, a generalized wave equation is obtained to describe small perturbations in shearing plasma. The boundary value problem for a smooth hyperbolic velocity profile is solved under the WKB approximation to determine the complex spectral parameter governing instability growth. The resulting integral dispersion relation encompasses both body and surface modes of plasma instabilities. Analysis reveals that spatial confinement significantly modifies classical instability behavior: reducing the layer width amplifies mirror instabilities while suppressing oblique fire-hose modes. However, increasing the flow velocity gradient enhances oblique fire-hose instability, with body modes transforming into surface Kelvin–Helmholtz-type modes at high gradients. These results highlight the critical role of finite shear-layer geometry and velocity gradients in regulating instability development and turbulence generation in anisotropic cosmic plasmas, such as the solar wind and astrophysical jets.

Keywords: Solar Wind; MHD shearing flows; WKB solution

1. Introduction

In collisionless cosmic plasmas, the dissipation of macroscopic flow energy into microscopic scales remains one of the key problems of plasma astrophysics [Cranmer et al., 2015]. Energy transfer occurs through turbulent cascades that channel large-scale kinetic energy toward smaller, kinetic scales, where it is converted into heat by wave–particle interactions and nonlinear effects [Marsch, 2006; Gary et al., 2016]. Such processes underlie the heating and acceleration of the solar corona and solar wind [Kiyani et al., 2015; Verdini et al., 2019].

The onset of turbulence is closely related to plasma instabilities, which arise when free energy is stored in anisotropic pressures or velocity gradients. Shear flows are among the most efficient sources of such energy and are widely observed in the solar wind, magnetospheric boundaries, and coronal mass ejection fronts [Kivelson and Chen, 1995; Hasegawa et al., 2004; Foullon et al., 2011]. In these regions, the Kelvin–Helmholtz (KH) instability may develop, leading to large-scale vortices and enhanced transport across magnetic boundaries [Sisti et al., 2019].

However, weakly collisional magnetized plasmas are typically anisotropic with respect to the magnetic field, giving rise to instabilities such as fire-hose and mirror modes, which regulate pressure balance and redistribute energy [Vedenov and Sagdeev, 1958; Hellinger et al., 2006]. The classical CGL model [Chew et al., 1956] captures basic anisotropy effects but neglects parallel heat fluxes important in collisionless conditions. A more complete description is provided by the 16-moment fluid formalism, which includes anisotropic pressures and parallel heat flux dynamics [Ramos, 2003; Dzhalilov and Kuznetsov, 2013].

Previous studies have shown that finite shear-layer width can substantially modify or enhance these instabilities [Dzhalilov et al., 2011]. The present work extends this analysis by investigating the evolution of oblique fire-hose modes in anisotropic plasma flows with velocity shear. Using the 16-moment MHD framework, we derive the corresponding wave equations and apply the WKB approach to determine the spectral parameters and growth rates for different shear and layer thicknesses. The obtained results help to clarify the transition from ordered shear flows to turbulence in space plasmas such as the solar wind and coronal structures.

2. Basic Equations in the Fluid Description

For the fluid description of a collisionless anisotropic plasma aligned with an external magnetic field, the extended fluid model provides a more complete system than the classical CGL (Chew–Goldberger–Low) approximation, as it includes the evolution of heat fluxes along the magnetic field [Oraevski et al., 1985; Ramos, 2003]. This formulation captures the effects of anisotropy and dispersion essential for describing collisionless plasma dynamics [Ramos, 2003; Dzhalilov and Samadov, 2024]. In the present analysis, a simplified version of the extended MHD system is employed, incorporating both ion and electron contributions. Because electron–ion coupling is weak in collisionless regimes $(m_e/m_i \ll 1)$, the large-scale dynamics are governed mainly by ions, while electrons maintain quasi-neutrality. The plasma flow is assumed plane-parallel and directed along the z-axis, with a velocity shear in the x-direction. The equilibrium velocity is given by $v_0 = (0,0,V_0(x))$, and the background magnetic field B_0 is uniform and parallel to z. The equilibrium parameters $\rho_0, p_{\perp 0}, p_{\parallel 0}, B_0, S_{\perp 0}, S_{\parallel 0}$ are taken to be constant.

The stability of this configuration is analyzed by introducing small perturbations to all physical quantities, $f = f_0 + f'(x,y,z,t)$, where $f'(x,y,z,t) \sim F(x)e^{i(k_y y + k_z z - \omega t)}$. This Fourier decomposition with respect to $y, z, t$is crucial because the coefficients of the resulting differential equations depend only on x. Consequently, this step transforms the coupled system of partial differential equations into a set of ordinary differential equations (ODEs) in x.

Here, ω is the wave frequency, and k_y, k_z are the wavenumber components in the plane perpendicular to the shear direction. After linearizing the 16-moment equations and substituting the perturbed quantities, the system reduces to a single second-order differential equation for the magnetic field perturbation $B_x(x)$:

$$\frac{\partial}{\partial x}\left(A(x)\frac{\partial B_x}{\partial x}\right) - \beta_A(x)B_x = 0. \qquad (1)$$

This is the fundamental wave equation governing the spatial evolution of the magnetic perturbation. Where;

$$A(x) = \frac{\beta_A \beta_*}{k_y^2 \beta_* + k_z^2 \beta_A}, \qquad (2)$$

$$\beta_A(\tau, \Omega_A) = \alpha + \beta - 1 - \xi(\tau, \Omega_A)^2, \qquad (3)$$

$$\beta_*(\tau, \Omega_A) = \beta + 2\alpha + \frac{2\alpha^2\,(\xi^4 + 2g\,\xi^3 + 2g^2\,\xi^2 - 5\xi^2 - 6g\,\xi + 3)}{(\xi^2 - 1)\,(\xi^4 - 6\xi^2 - 4g\,\xi + 3)}. \qquad (4)$$

$$\xi(x) = M[\Omega + \Delta\tanh(\sigma x)], M = \frac{\bar{V}_0}{c_\parallel}, \Delta = \frac{h-1}{h+1} \qquad (5)$$

$\Omega = \Omega_r + i\Omega_i$ is the complex spectral parameter to be determined from the boundary conditions, M is the Mach number and Δ characterizes the shear strength ($0 \le \Delta \le 1$).

The coefficients in the obtained second-order ordinary differential wave equation (1) are variable and appear as complex functions of the background velocity profile $V_0(x)$. Since $V_0(x)$is, in general, an arbitrary function of the spatial coordinate x, its specific form determines both the structure and stability properties of the plasma flow. When two distinct plasma streams are in contact, a finite transition region inevitably develops between them. The thickness of this transition layer is governed by the relative velocities and the physical parameters of the adjoining flows.

To model this configuration analytically, we adopt a smooth velocity profile expressed through a hyperbolic tangent–type function:

$$V_0(x) = \frac{V_{02}e^{\sigma x} + V_{01}e^{-\sigma x}}{e^{\sigma x} + e^{-\sigma x}}, \sigma \ge 0. \qquad (6)$$

Here, $V_0(-\infty) = V_{01}$and $V_0(+\infty) = V_{02}$represent the asymptotic flow velocities, while $h = V_{01}/V_{02} \ge 1$and $V_0(0) = (V_{01} + V_{02})/2 = \bar{V}_0$denote, respectively, the velocity ratio and the mean flow speed. The parameter σ characterizes the inverse thickness of the shear (transition) layer, denoted by L.

Figure 1 schematically illustrates several possible velocity profiles $V_0(x)$for different values of σ. As the dimensionless product σLincreases, the transition region between the two streams becomes narrower, and for $\sigma L \gg 1$, it effectively approaches a sharp velocity discontinuity separating $V_{01}$and V_{02}. Conversely, when $\sigma L \ll 1$, the transition region broadens considerably, corresponding to a smooth, gradual shear between the flows.

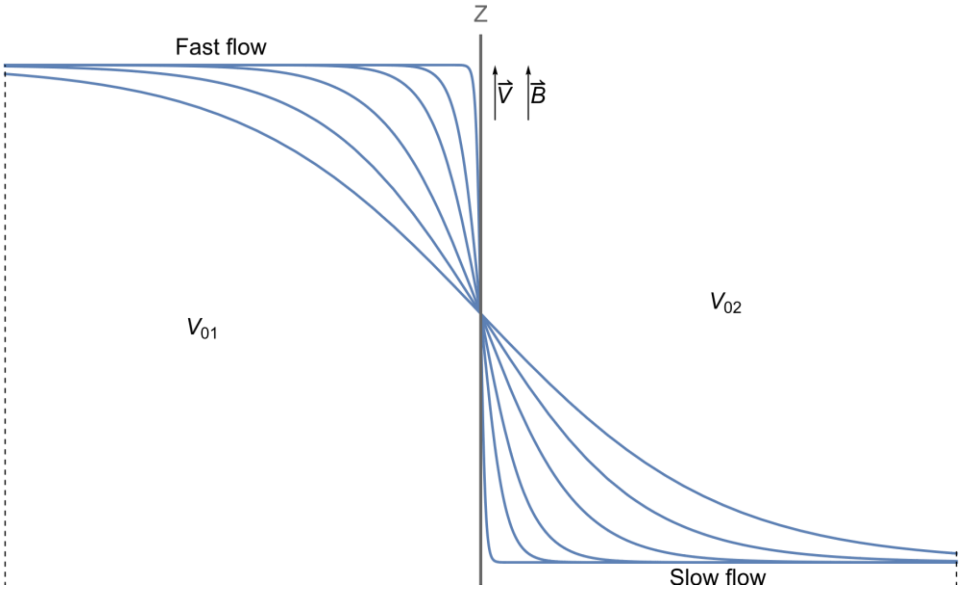

Figure 1. *Schematic representation of MHD plasma shearing flow. Different line profiles correspond to different values of* σL *in (6).*

3. WKB Approximation and Mathematica Solution

To solve the boundary value problem described above, the Wentzel–Kramers–Brillouin (WKB) approximation was applied, which allows analytical simplification of the second-order wave equation with slowly varying coefficients. As shown in [Dzhalilov and Samadov, 2024], the dispersion relation obtained from this approach can be expressed in the form

$$\int_0^1 (\sqrt{f(\xi_+)} + \sqrt{f(\xi_-)})\, d\tau = \lambda_n,$$

or equivalently,

$$\int_0^b \frac{\sqrt{f(\xi_+)} + \sqrt{f(\xi_-)}}{1 - z^2}\, dz = \sigma_L \lambda_n, \qquad (24)$$

where

$$f(\xi) = -\frac{(1-l)\beta_*(\xi) + l\beta_A(\xi)}{\beta_*(\xi)}, \lambda_n = \frac{n\pi}{kL} = \frac{\lambda_\perp n}{2L}. \qquad (25)$$

Here, $\lambda_n$represents the ratio between the wavelength $\lambda_\perp$in the (y, z)plane ($k^2 = k_y^2 + k_z^2$, $k = 2\pi/\lambda_\perp$) and the geometric width $2L$ of the plasma layer. The integer n denotes the number of nodes of the eigenfunction along the x-axis. If we define the longitudinal scale of the fluctuation structures as $\lambda_x = 2L/n$, then $\lambda_n = \lambda_\perp/\lambda_x$.

To determine the complex eigenfrequencies $\Omega = \Omega_r + i\Omega_i$ satisfying the dispersion equation (24), numerical computations were carried out in *Mathematica*. Specifically, the functions were integrated using NIntegrate, and the corresponding roots of the dispersion equation were obtained with the FindRoot command. This computational scheme provides discrete complex values of Ω whose imaginary parts determine the growth rates of unstable fire-hose modes in shear flows of anisotropic plasmas.

4. Results and Conclusions

The dispersion relation derived from the WKB approximation was solved numerically to obtain the complex frequency $\Omega = \Omega_r + i\Omega_i$, where the imaginary part $\Omega_i$characterizes the instability growth rate. The results are shown in Figs. 2–3 for different values of the shear parameter Δ, the layer thickness σ_L, and the structural parameter λ_n[Dzhalilov and Samadov, 2024].

Figure 2 shows the dependence of $\Omega_i$on the transverse scale parameter $\lambda_n$at fixed $M\Delta = 1.5$. The instability is strongest for small λ_n(few-node body modes) and decreases steeply as $\lambda_n$grows, demonstrating that modes with fine transverse structure couple more efficiently to the shear. Increasing $\sigma_L$shifts the instability onset to higher $\lambda_n$and increases its magnitude, confirming that narrower layers favor stronger growth.

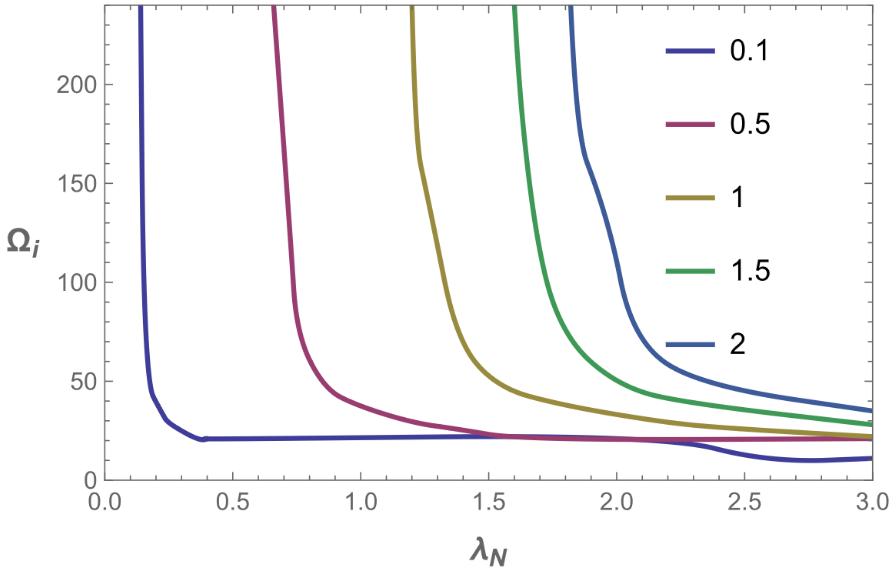

Figure 2. *The dependence of instability growing rate M Ωi of fire hose modes on the λn at different values of σL (numbers at the curves) when M Δ = 1.5.*

Figure 3 illustrates how the growth rate $\Omega_i$varies with the shear amplitude Δat fixed $\lambda_n = 1$. For weak shear ($\Delta \lesssim 0.1$), the instability is nearly suppressed. As Δincreases, $\Omega_i$rises sharply and reaches a maximum around $\Delta \simeq 0.2 - 0.3$, indicating efficient energy transfer from the mean flow to the perturbations. Beyond this range, the growth rate gradually decreases. The effect strengthens for larger σ_L, showing that a sharper velocity gradient enhances the instability by concentrating free kinetic energy in the transition layer.

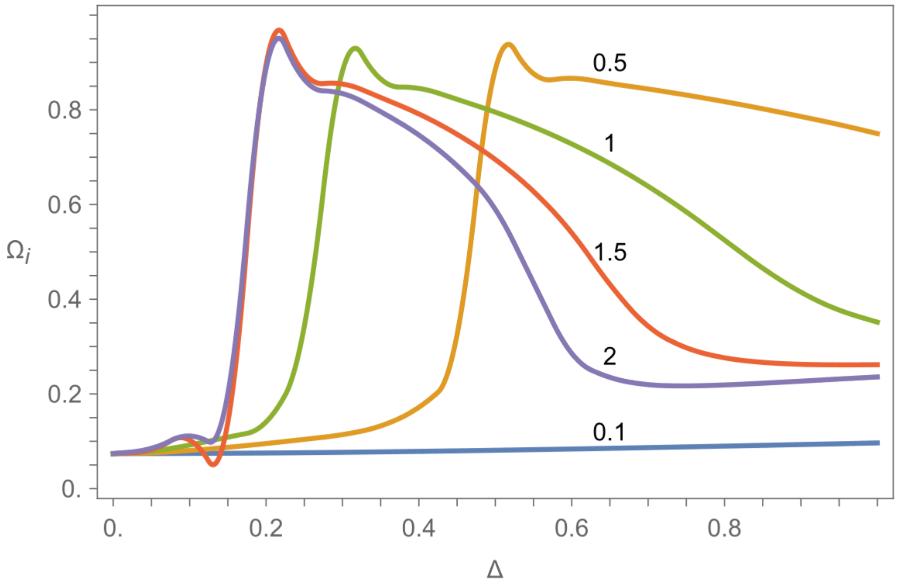

Figure 3. *The dependence of instability growing rate Ωi of fire-hose modes on the shearing rate of plasma supersonic flows Δ at different values of σL (numbers at curves) when λn = 1. Overall, the analysis shows that the fire-hose instability in anisotropic plasmas becomes highly sensitive to both the velocity-gradient scale and flow anisotropy. Sharper shear layers ($\sigma_L \gtrsim 1$) and moderate velocity contrasts ($\Delta \sim 0.2 - 0.4$) yield the largest Ω_i, while overly wide or weakly sheared flows remain stable. These results suggest that in space plasmas—such as solar-wind shear regions or CME boundaries—fine velocity gradients can efficiently trigger wave amplification and local turbulence, bridging the transition from bulk flow to chaotic magnetic structures.*

References

Bale, S.D., Kasper, J.C., Howes, G.G., Quataert, E., Salem, C., Sundkvist, D. (2009). Magnetic fluctuation power near proton temperature anisotropy instability thresholds in the solar wind, *Physical Review Letters*, 103, 211101, DOI: 10.1103/PhysRevLett.103.211101.

Bruno, R., Carbone, V. (2013). The solar wind as a turbulence laboratory, *Living Reviews in Solar Physics*, 10, 2, DOI: 10.12942/lrsp-2013-2.

Chew, G.F., Goldberger, M.L., Low, F.E. (1956). The Boltzmann equation and the one-fluid hydromagnetic equations in the absence of particle collisions, *Proceedings of the Royal Society of London A*, 236, 112–118, DOI: 10.1098/rspa.1956.0116.

Cranmer, S.R., Gibson, S.E., Riley, P. (2015). Origins of the ambient solar wind: Implications for space weather, *Space Science Reviews*, 188, 473–505, DOI: 10.1007/s11214-014-0106-6.

Dzhalilov, N.S., Kuznetsov, V.D. (2013). Low-frequency instabilities of collisionless plasma and the 16-moment approximation, *Plasma Physics Reports*, 39(12), 1026–1034.

Dzhalilov, N.S., Samadov, J.H. (2024). MHD instabilities in shear flows of anisotropic cosmic plasmas. I. Fire-hose modes, *Astronomical Journal of Azerbaijan*, 19(1), 25–36.

Hasegawa, H., Fujimoto, M., Phan, T.D., Rème, H., Balogh, A., et al. (2004). Transport of solar wind into Earth’s magnetosphere through rolled-up Kelvin–Helmholtz vortices, *Nature*, 430, 755–758, DOI: 10.1038/nature02799.

Hellinger, P., Matsumoto, H. (2000). New kinetic instability: Oblique Alfvén fire hose, *Journal of Geophysical Research*, 105, 10519–10526, DOI: 10.1029/1999JA000297.

Oraevski, V.N., Chodura, R., Feneberg, W. (1985). Stability of magnetized plasma with heat flux, *Physics of Fluids*, 28, 2769–2777, DOI: 10.1063/1.865341.

Ramos, J.J. (2003). Fluid equations, closures, and kinetic theory, *Physics of Plasmas*, 10, 3601–3612, DOI: 10.1063/1.1590983.

Vedenov, A.A., Sagdeev, R.Z. (1958). Some properties of plasma with an anisotropic distribution of velocities in a magnetic field, *Soviet Physics Doklady*, 3, 278–281.

DOI: 10.31401/WS.2025.proc.14

The Geomagnetic Midlatitude Effects of the Supersubstorms during May 10-12, 2024 Superstorm

Guineva V.H.[1], *Despirak I.V.*[2], *Werner R.*[1], *Lubchich A.A.*[2], *Raykova L.*[1], *Bojilova R.*[3]

[1]Space Research and Technology Institute (SRTI), Bulgarian Academy of Sciences, Stara Zagora Department, Bulgaria
v_guineva@yahoo.com
[2]Polar Geophysical Institute (PGI), Apatity, Russia
[3]National Institute of Geophysics, Geodesy and Geography (NIGGG) - Bulgarian Academy of Sciences, Sofia, Bulgaria

Abstract

The aim of this study is to conduct the detailed analysis of the geomagnetic auroral and midlatitude disturbances during the superstorm on 10–12 May 2024. It was the second-strongest geomagnetic storm of the space era (SYM/H ~ -518 nT). Storm main phase was observed from ~17:15 UT on May 10 to ~ 02:15 UT on May 11, the recovery phase was registered on May 11-13. Extremely intense geomagnetic disturbances, so-called “supersubstorms” (SSSs: SML < −2500 nT) were recorded during the superstorm. According to the SuperMAG data base, there were several SSS events: at ~19:20 and ~19:50 UT, ~22:35 and ~ 22:40 UT on 10 May, at ~09:00 and ~09:50 UT, at ~12:45, ~13:32 and ~13:43 UT on 11 May, 2024. The planetary space-time distribution of the magnetic disturbances during these SSS were studied using the data collected from the ground-based networks (SuperMAG, INTERMAGNET and IMAGE) as well as the magnetic registrations by the Iridium constellation of 66 satellites at 780 km altitude, distributed over six orbit planes spaced equally in longitude (AMPERE project). We studied the extremal geomagnetic disturbances during SSS by examining the morphology of the auroral electrojets, the corresponding positive magnetic bays at midlatitudes, and the solar wind driving conditions. Different features at mid-latitudes effects of these four SSS events are discussed.

Keywords: superstorm; supersubstorm; midlatitude positive bay

1. Introduction

Extreme geomagnetic storms provoked by geoeffective solar storms, has been recognized as a natural hazard [Weiler et al., 2025]. They may occasion widespread voltage control problems, power system collapse, transformer damage, pipeline damage, disruption of navigation by magnetic compass, satellite connection failures or change of satellite orbits. The geomagnetic storms are classified by two methods based on the k_p and Dst (SYM/H) geomagnetic indices. The NOAA geomagnetic storm scale includes five levels, by the storm effect on the different technologies. After this scale, the geomagnetic storms are classified from G1(k_p=5) to G5(k_p=9) [https://www.swpc.noaa.gov/noaa-scales-explanation]. The other type of classification is based on the Dst minimal value during the storm. The geomagnetic Dst index (Disturbance Storm Time) is a measure of the changes in the ring current flowing around the equator. The scale by Cander and Mihailovich (1998) offers 3 degrees of geomagnetic storm strength: moderate storm (-50 nT ≥ Dst ≥ -100 nT), intense storm (-100 nT ≥ Dst ≥ -250 nT), and super-storm (Dst ≤ -250 nT). Loewe and Prölss (1997) suggests a more detailed classification: weak storm (-30 nT ≥ Dst ≥ -50 nT), moderate storm (-50 nT ≥ Dst ≥ -100 nT), strong storm (-100 nT ≥ Dst ≥ -200 nT), severe storm (-200 nT ≥ Dst ≥ -250 nT), and great storm (Dst ≤ -350 nT). A geomagnetic storm may be classified as superstorm, if the Dst or SYM/H index reach values, lower from -450 nT or even -500 nT. Superstorms occur seldom. The recent superstorm on 10-12 May 2024 is the second by severity geomagnetic storm during the space era after the superstorm in 1989, and the only one for which simultaneous satellite data exist, together with the ground based data. This gives a unique opportunity to study different aspects of the reasons and conditions for the development of such phenomenon, to gain new knowledge, to verify and improve existing models, to plan new experiments in order to better predict such natural hazards. So, lots of papers concerning the superstorm on 10-12 May 2024 have been published [e.g. Haira et al., 2024; Wang et al., 2024; Lockwood et al., 2025; Weiler et al., 2025; Despirak et al., 2025; Kleimenova et al., 2025].

Another important element of the space weather is the magnetospheric substorms and their effects on the ionosphere and the ground magnetic field. Numerous studies have been devoted to this topic, starting with the classic work of Akasofu (1964). Magnetospheric substorms are associated with a series of processes in the magnetosphere and ionosphere, generalized by Akasofu (2004). Most of the substorm studies are related to the influence of substorms on the surface magnetic field, expressed in auroral latitude negative bays in X and positive bays, the so-called midlatitude positive bays (MPB) in the X magnetic component at midlatitudes [e.g., McPherron, 1972; McPherron and Chu, 2017)]. It was found that the strongest midlatitude positive bays occur during strong substorms, while strong geomagnetic storms develop [Guineva et al., 2024a; Guineva et al., 2024b].

The strength of the substorms is estimated by the global SML index, obtained by the SuperMAG magnetometers network. In the study of very strong magnetic substorms, a special class of substorms was identified, for which the name "supersubstorms" was introduced, and in which a number of phenomena are observed, distinguishing them from "ordinary" substorms. The so-called “supersubstorms” (SSS) are events during which the SML index reaches unusually low negative values (SML < -2500 nT) [Tsurutani et al., 2015]. Several of the most striking supersubstorm events have been examined in detail in detail by some authors of the present work [e.g. Despirak et al., 2022; Despirak et al., 2023; Lubchich et al., 2023].

During the superstorm on 10-12 May 2024 occured four supersubstorm events. These unique and rarely encountered extreme conditions allow for research and information to be gathered on the entire range of phenomena from the Sun to the Earth and on Earth that characterize extreme space weather.

The aim of this study is to conduct a detailed analysis of the geomagnetic auroral and midlatitude disturbances over Europe during the above-mentioned extremely disturbed conditions: the supersubstorms during the superstorm on 10–12 May 2024.

2. Data used

The interplanetary and geomagnetic conditions during the superstorm have been determined by data of OMNI database of the CDA Web (https://cdaweb.gsfc.nasa.gov/).

To obtain information about the ionospheric currents and consequently, about the western and eastern electrojet locations, we used data from AMPERE project (https://ampere.jhuapl.edu/products/) [Anderson et al. 2021; Waters et al. 2001]. It includes magnetic registrations by the Iridium constellation of 66 satellites at 780 km altitude, distributed over six orbit planes spaced equally in longitude and results from subsequent processing. Type 1 summary plots was used, which cover latitudes from 40° magnetic latitude (MLAT) to the pole to ensure coverage not only of the auroral reagon, but a considerable part of the midlatitudes, as well. All quantities are shown in Altitude Adjusted Corrected Geomagnetic Coordinates (AACGM). These summary plots display 10 minutes the input data, reduced magnetic perturbations showing the horizontal plane vectors (to the left), the horizontal vector from the spherical harmonic fit to the magnetic perturbation data (in the center), and the radial current density in μA/m2 (to the right). Upward currents are shown in red and downward currents in blue.

The supersubstorms have been identified by the SML index from SuperMAG (https://supermag.jhuapl.edu/) according to Tsurutani's definition [Tsurutani et al., 2015].

The magnetic field disturbances over Europe have been estimated by the regional IMAGE IL index for the PPN-NAL chain, wich is near the longitude of Panagjurishte. The PPN-NAL area covers longitudes from 12°÷27°E (96°-113° GMLon.). The IL index is available in the IMAGE database (https://space.fmi.fi/image/www/il_index_panel.php).

The midlatitude disturbances during the studied period have been taken from the Catalog of the magnetic variations at the Panagjurishte station (PAG), developed at the Space Research and Technology Institute of the Bulgarian Academy of Sciences, based on INTERMAGNET data (https://imag-data.bgs.ac.uk/GIN_V1/GINForms2). The catalog is available at: http://space.bas.bg/Catalog_MPB/. The Panagjurishte (PAG) coordinates are: 24.2°E, 42.5°N (96.8°GMLon., 37° GMLat.). For the study the processed X component at PAG representing the X variations (delta X) obtained based on 25 days period with the considered day in the center is used. The developed processing procedure includes removal of the main field, removal of gaps and peaks, subtraction of the solar quiet day variationsand elimination of days with strong disturbances [Werner et. al. 2021]. Graphs of the midlatitude positive bays, detected based on the created methodology, are used, as well [Guineva et al., 2024c].

To compare the substorm by the midlatitude positive bays (MPB's), registered at PAG, with general substorm development at the same time, the substorm list by Forsyth et al. (2015), has been used (https://supermag.jhuapl.edu/substorms/?tab=description), SML index from SuperMAG (https://supermag.jhuapl.edu/indices/) and IL index data from IMAGE database (https://space.fmi.fi/image/www/il_index_panel.php).

3. Interplanetary and geomagnetic conditions

3.1. The superstorm on 10-12 may 2024

The superstorm on 10-12 May 2024 appears a huge magnetic storm (superstorm) of class G5 (Kp = 9) and a minimal value of the hourly index Dst equal to -412 nT, at 02:00 UT on 11 May, 2024 (http://wdc.kugi.kyoto-u.ac.jp/), and the minimal value of the minute analogue of Dst, the Sym/H reached -518 nT at 02:14 UT on 11 May 2014. The most intensive superstorm in the space era was the superstorm on 13-14 March 1989, with minimal Dst=-589 nTat 00:02 UT on 14 March 1989, and minimal SYM/H= -720 nT at 00:46 UT on 14 March 1989. Such a strong magnetic storm as the superstorm on 10-12 May 2024 has not been observed for more than 20 years. In terms of intensity, it is comparable to the strongest magnetic storms observed since the beginning of the space era, namely the storms of September 1957 (Dstmin = −427 nT), February 1958 (Dstmin = −426 nT), July 1959 (Dstmin = −429 nT) and November 2003 (Dstmin = −422 nT, SYM/Hmin=490 nT) (Kleimenova et al., 2025). The superstorm on 10-12 May 2024 is the first one about which simultaneous satellite data alog with ground data have been registered. It was provoked by a solar storm in May 2024. A series of eruption events occurred in May 2024, which are associated with AR13664/8. This active region revealed the appearance of an extremely intense magnetic flux, lasted for 3 days, and gave rise to multiple flares of class M and 4 flares of class X. Each flare was accompanied by halo CME.

The source regions of seven halo CMEs were determined, apportioned mainly along two distinct polarity inversion lines, leading to two groups of homologous CMEs. The strong flux emergence was the reason to a complex magnetic field configuration in the region [Wang et al., 2024]. By combined satellite data five CMEs in the frame of 28 hours, interacting with each other were identified near Earth, thus creating an interplanetary magnetic field with a very complex structure [Weiler et al., 2025]. This intricate near-Earth solar wind and IMF structure aroused the superstorm in May 2024 with a complex structure, as well. The superstorm had a three-step storm main phase, from ~17:15 UT on May 10, lasted ~9 hours, with SYM/H intensity of -518 nT. Due to 3 MC during the superstorm recovery phase it was very structured and prolonged to 2.8 days. Strong field-aligned polar region currents, ~10 times intensified during the main phase, with equatorward expansion to ~50° Mlat. [Haira et al., 2024]. During the superstorm, lots of intense substorms and several supersubstorms occurred. In Figure 1, the interplanetary and geomagnetic conditions from 10 to 14 May 2024 are shown. From up to down, the IMF B, the N-S IMF component Bz, the solar wind parameters: velocity V, proton density Np, temperature T, pressure P, and the AL and SYM/H indices are presented.

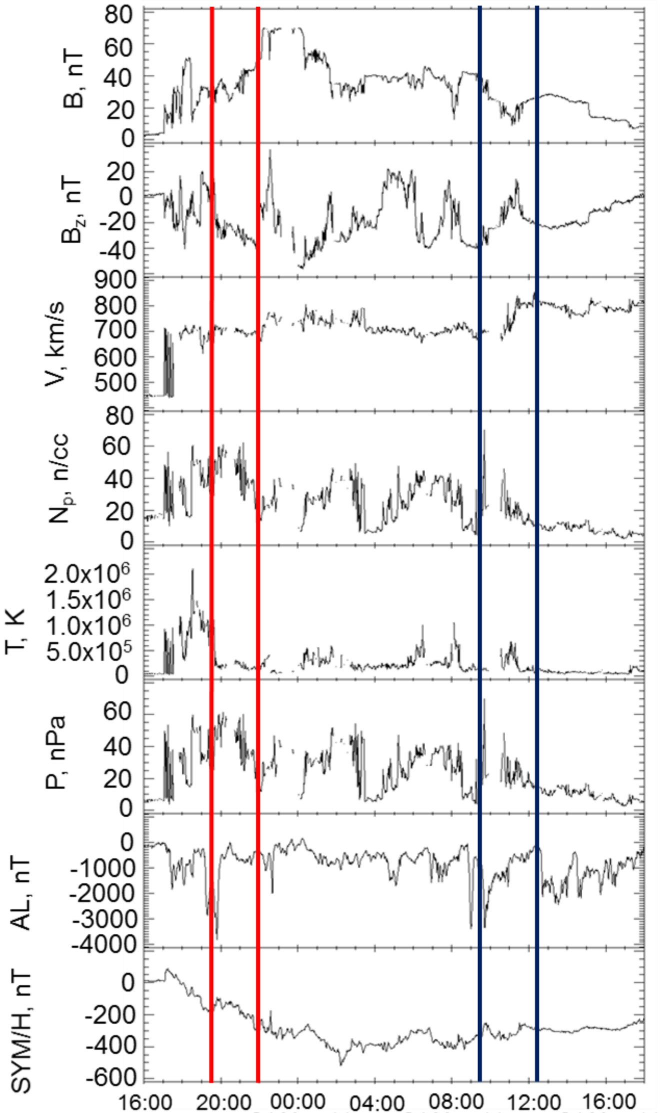

Figure 1. *Interplanetary and geomagnetic conditions during the superstorm on 10-12 May 2024. The red vertical lines indicate the beginnings of the midlatitude positive bays, observed at the midlatitude station Panagjurishte, associated with the first and second SSS event during the main phase of the superstorm, on 10 May 2024 (see sections 4.2, 5.3 and 6.3). The blue vertical lines mark the beginnigs of the negative bays, recoded at PAG, during the superstorm recovery phase, related to the third and fourth SSS events on 11 May 2024 (see sections 4.2, 7.3 and 8.3).*

3.2. The supersubstorms during the superstorm on 10-12 May 2024

We determined the onset and maximal development of the SSSs during the 10-12 May 2024 superstorm by the SML index from SuperMAG database and compared our results with the SuperMAG substorms lists (when available). In Figure 2 the SML course from 16 UT on 10 May 2024 to 24 UT on 11 May 2024 is given. Four SSS events were identified in this time interval, enumerated in Figure 2 and further in the text from (1) to (4). Two SSS events occurred on 10 May 2024, during the main storm phase, and two SSS events developed on 11 May 2024, in the recovery storm phase. Three of the SSS events, (1), (3) and (4), consist of two consecutive SSSs, which may partly overlap, so the precise onset time of the second SSS may be hard to determine. SSS event (2) represents one SSS.

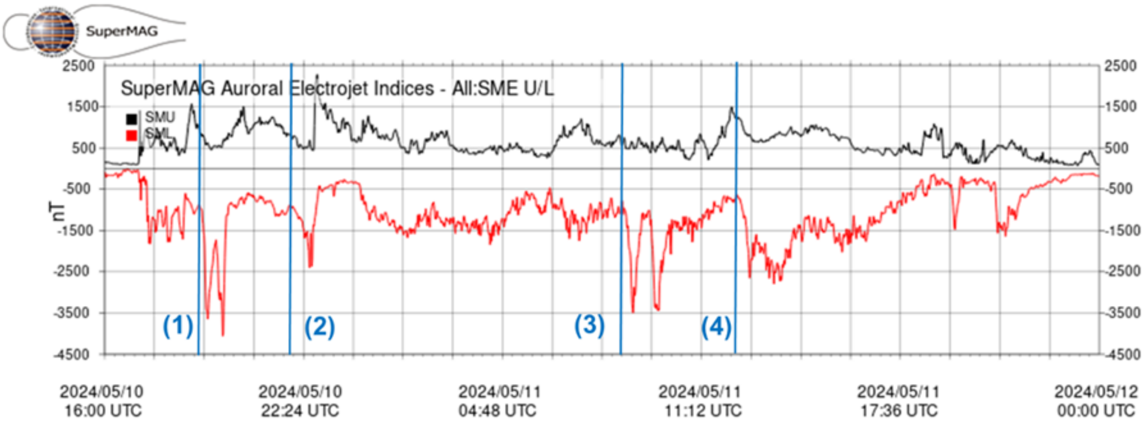

Figure 2. *SML and SMU indices by SuperMAG. The beginnings of the SSS events are marked by blue vertical lines and the SSS are enumerated by the time of occurrence.*

The onset times and the times of the maximal development and the intensity of the SSS events were determined as follows:

SSS event (1): The onset of the first SSS was at 19:03 UT on 10 May 2024, it reached maximal development at 19:19 UT with intensity -3649 nT. The onset of the second SSS was at 19:35 UT, and the maximal development - at 19:48 UT with intensity -4057 nT.

SSS event (2): The onset of the SSS (one for this event) was at 22:04 UT on 10 May 2024. At the maximal development, there are two close to each other minima: at 22:36 UT, with intensity -2404 nT, and at 22:40 UT, with intensity -2369 nT.

SSS event (3): The onset of the first SSS was at 08:39 UT on 11 May 2024, its maximal development was at 09:00 UT with intensity -3497 nT. The onset of the second SSS was at 09:25 UT, and the maximal development - at 09:50 UT with intensity -3433 nT.

SSS event (4): The onset of the first SSS was at 12:20 UT on 11 May 2024, it reached maximal development at 12:45 UT with intensity -2650 nT. The onset of the second SSS was at 13:04 UT. The SML curve is more disturbed, at the maximal development two close minima were obtained: at 13:32 UT with intensity -2797 nT, and at 13:43 UT with intensity -2722 nT.

4. First SSS event

4.1.AMPERE data

During the superstorm, the current systems are very strong and very complicated. [Haira et al., 2024] report, that there was obtained ~10 times increase of the upward- and downward-current components in both the northern and southern hemispheres during the storm period, compared to their pre-storm values. The high intensity and complex structure of the current systems are clearly visible in all figures for the moments of maximal development of the supersubstorms considered in our work.

In Figure 3, AMPERE data around the maximal SSS developments for the first SSS event are given. The maximal developments times are written in black frames below the data time interval. Here and in the following slides, the stars indicate the SSS onset location (taken from the Forsyth et al. substorms list [Forsyth et al. 2015]), and the ellipses – the region of the PPN-NAL and PAG stations. In this case, the SSS onsets are at a distance of about 200° from the PPN-NAL region (onset 1: 8.21 MLT, 60°GMLat; onset 2: 8.86 MLT, 67° GMLat). During the first SSS the current systems are concentrated above 55°-50° GMLat. It is seen, that the westward electrojet doesn't reach the European stations area (upper row of Figure 3). During the second SSS part of the westward electrojet is above the PPN-NAL region, namely over Spitsbergen archipelago.

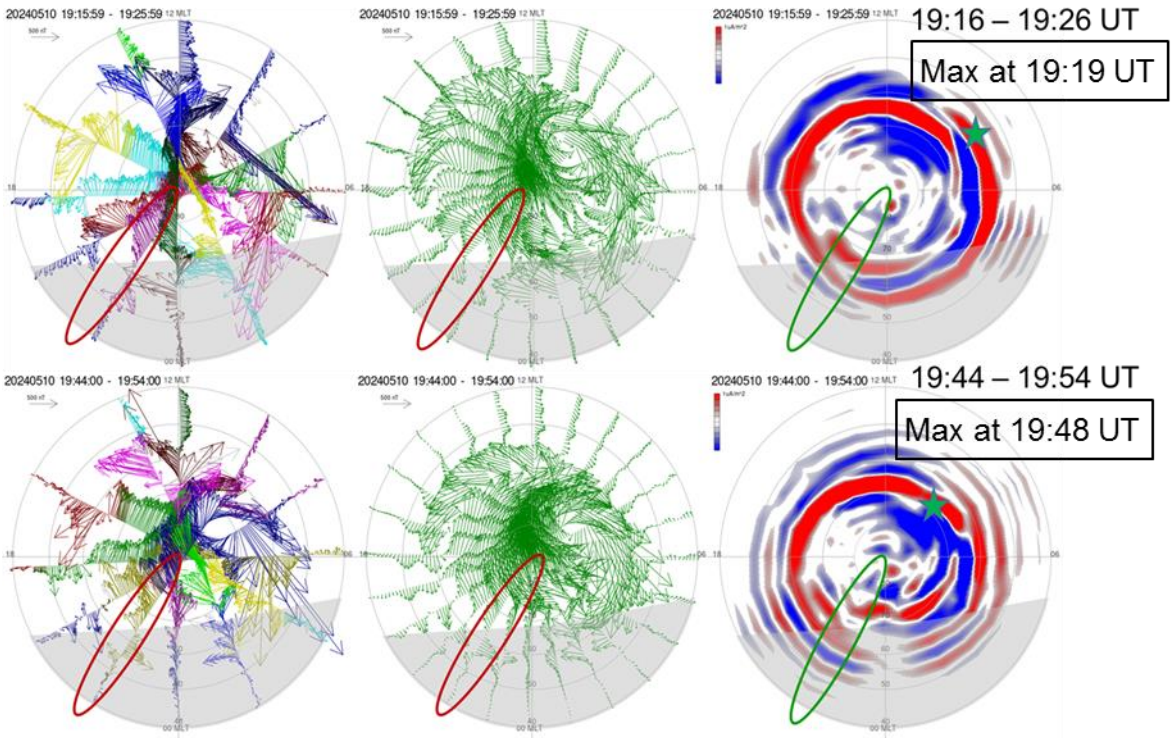

Figure 3. *AMPERE data around the SML minima times of the two SSSs of the first SSS event. The green stars indicate the SSS onsets (GMLat, MLT) and the ellipses – the location of the European magnetic stations at the same time.*

4.2.SuperMAG and IMAGE data

To study the magnitude and the overall distribution of the ground level magnetic field horizontal perturbations we used the polar plots from SuperMAG from 30° GMLat to the GM pole. The vectors are rotated 90° clockwise to show the ionospheric equivalent current direction. The uniformly gridded fitted vectors in an MLT-MLat grid rotated also 90° clockwise are drawn as well. The ground magnetic variations over Europe have been studied by data of the IMAGE stations.

In the left panel of Figure 4 the SuperMAG maps for the time of the first and second supersubstorm onsets and maximal developments are presented. It can be seen that the strongest magnetic disturbances are far from the PPN-NAL area. During the first SSS, only weak and chaotic disturbances are observed at European longitudes, and during the second SSS stronger disturbances can be seen only at very high latitudes.

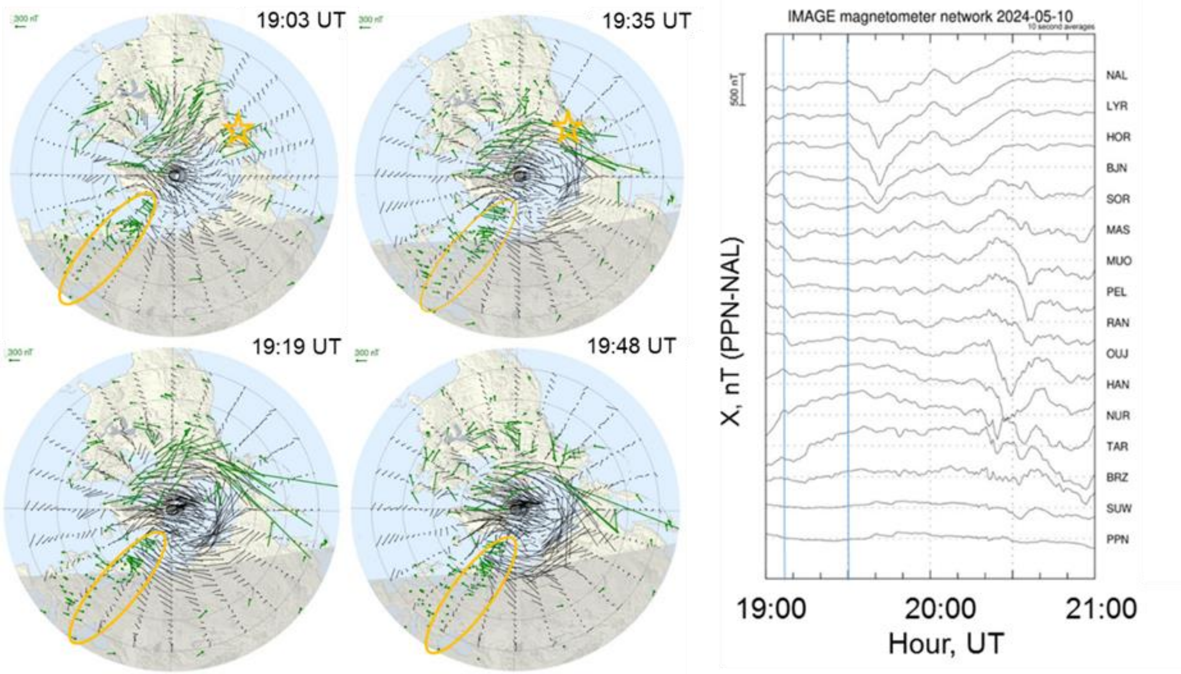

Figure 4. *Maps of the magnetic field vectors by SuperMAG for the onset and maximal development of the first SSS (left column) and of the second SSS during the first event (right column). The orange stars mark the supersubstorms onsets and the ellipses – the location of the IMAGE PPN-NAL stations and PAG. In the right panel, X magnetic component from the PPN-NAL chain stations is given from 19:00 to 21:00 UT on 10 May 2024. The blue vertical lines indicate the substorm onsets.*

From the right panel of Figure 4 it can be seen, that during the first disturbance, only weak X variations are observed in the auroral region, and during the second SSS a so-called “polar” substorm develops [Kleimenova et al., 2023; Despirak et al., 2025]. These results are in complete agreement with the ionospheric currents distribution by AMPERE (Figure 1), where part of the westward electrojet was just over the Spitsbergen archipelago.

4.3. First SSS event by SML, IL and magnetic X variations at PAG

In Figure 5 the global SML index and the auroral and midlatitudes disturbances of the regional IL PPN-NAL index and the variations of the X component of the magnetic field at PAG during the first SSS event are presented.

In the upper graph of Figure 5 the SML index is shown from 19 to 21 UT on 10.05.2024. The two SSS are clearly expressed. The SSS onsets are at a great distance from the PPN-NAL region, about 200° in longitude, in East direction. During the first SSS, with onset at 19:03 UT, the westward electrodjet didn’t reach European longitudes at the maximal SSS development, so there was no visible effect at auroral latitudes, as it is expressed by the IL graph for the same time interval (below SML graph in Figure 5). The X variations at PAG (the bottom panel of Figure 5) also do not reflect any influence of the first SSS at midlatitudes.

During the second SSS disturbances at high European latitudes were observed, by the IL index the disturbance began at 19:30 UT, somewhat earlier from the SML determined onset (19:35 UT), but such small discrepancy is not surprising, as the second SSS arose immediately after the first one, in already very disturbed conditions, which troubles the accurate determination of the SSS onset. At the maximal development at 19:42 UT IL= -1050 nT. This disturbance is comparatively small versus the global disturbance (-4057 nT), as the strongest disturbances happened to the East, in Asia. At PAG, the beginning of the disturbance provoked by the SSS was from 19:24 UT, and a strong midlatitude positive bay (MPB) formed, with maximal value of 74.6 nT.

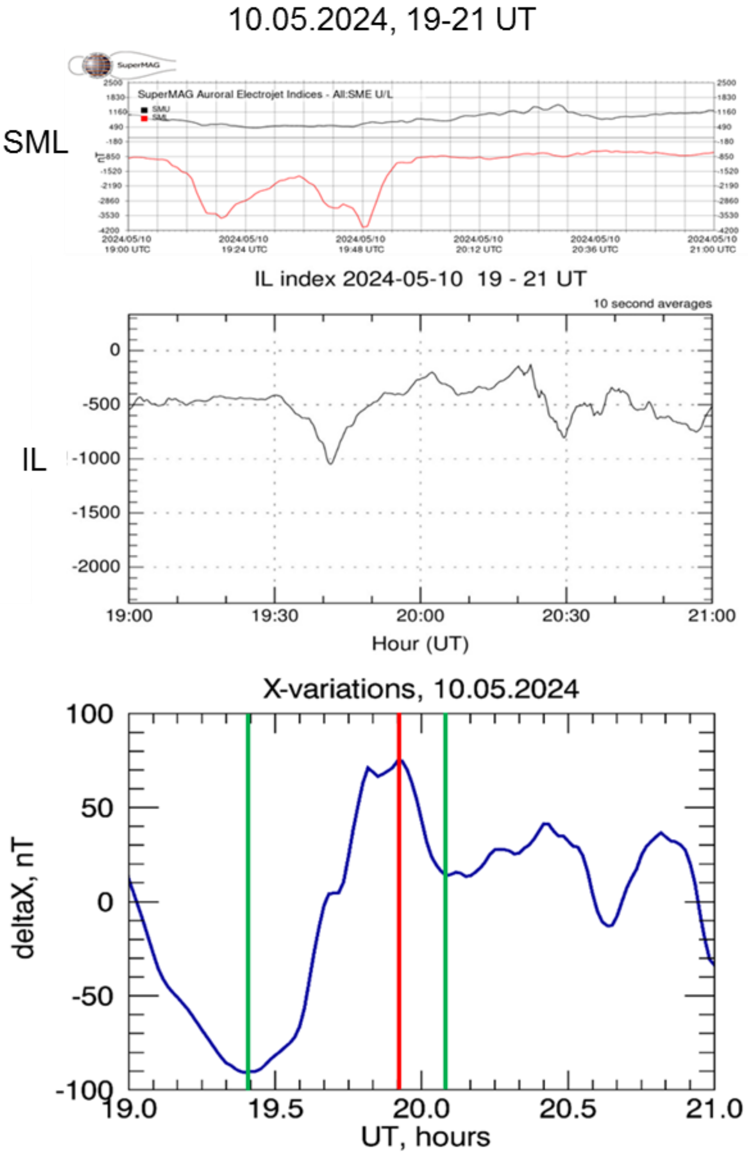

Figure 5. *SML index (up), IL index (down), and X variations at PAG (further down) from 19 UT to 21 UT on 10.05.2024. The green vertical lines in the bottom panel indicate the beginning and end of the MPB registered at PAG, and the red vertical line – the time of the MPB maximum.*

5. Second SSS event

5.1.Second SSS event by AMPERE data

The second SSS event consists from one supersubstorm, its onset was at 22:04 UT on 10 May 2024, and the onset location was at 8.21 MLT, 54° GMLat (Forsyth et al. substorms list [Forsyth et al. 2015]). In Figure 6 the distribution of the ionospheric currents near the time of maximal development, at 22:36 UT and 22:40 UT. It is seen that the area of the current systems expanded to lower latitudes and reached and maybe surpassed 40° GMLat. The PPN-NAL area falls under the westward electrojet.

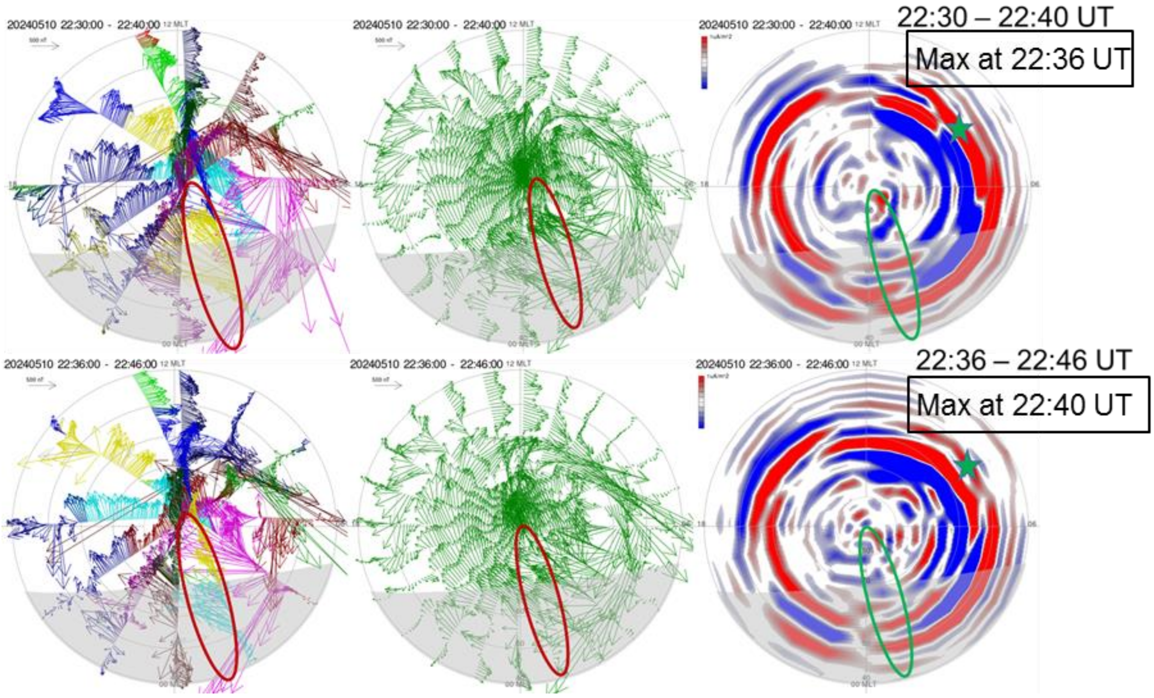

Figure 6. *Field aligned ionospheric currents at the time of the maximal development of the supersubstorm of the second SSS event. All designations are as in Figure 3.*

5.2.Second SSS event by SuperMAG and IMAGE data

In Figure 7 maps of the magnetic perturbations at the onset and near the maximal

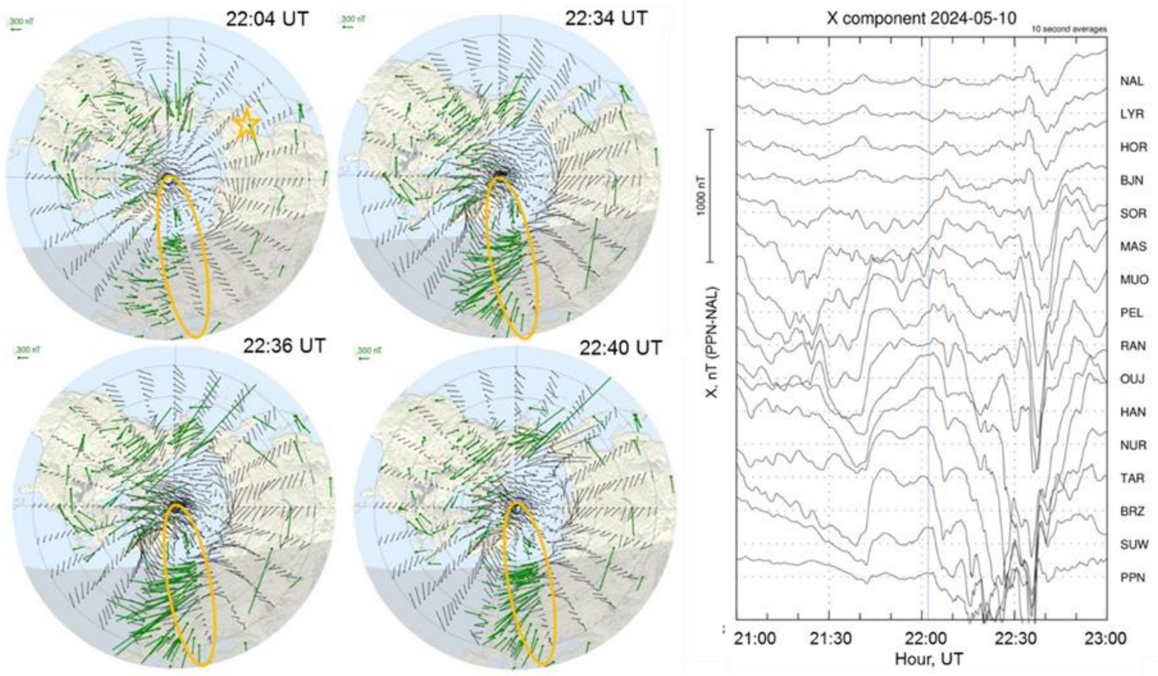

Figure 7. *Maps of the magnetic perturbations at the onset and near the maximal development of the second SSS event (left panels) and X components variations at the IMAGE PPN-NAL chain stations (right panel). All designations are as in Figure 4.*

development during the supersubstorm at 22:04 UT on 10.05.2024 (left panel) and the X magnetic component at the PPN-NAL chain stations from 21 UT to 23 UT (right panel) are shown.

From the maps it is seen, that magnetic disturbances are seen to span all longitudes and the strongest ones are over Europe, at subauroral and middle latitudes. During the second SSS event, IMAGE region is at about 1 MLT. In the X magnetograms the onset and further development of the SSS is evident.

5.3. Second SSS event by SML, IL and magnetic X variations at PAG

In Figure 8 the second SSS event is shown by the SML index (upper graph), by the IL PPN-NAL index (middle graph) and by the X variations at PAG (bottom graph).

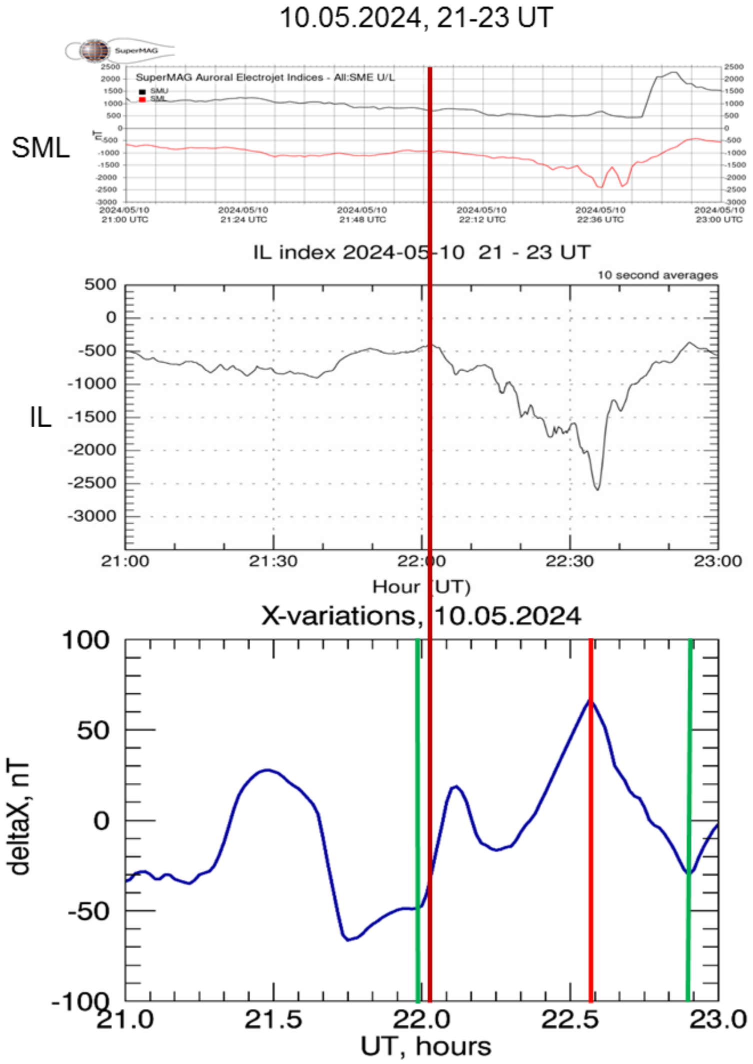

Figure 8. *SML index (up), IL index (down), and X variations at PAG (further down) from 21 UT to 23 UT on 10.05.2024. The dark red vertical line indicates the SSS onset, the green vertical lines in the bottom figure mark the beginning and end of the MPB at PAG, and the red vertical line – the maximum of the MPB.*

Although the defined onset of the SSS is at a distance of over 100° by longitude to the East from the IMAGE region (see Figure 6, 7), the beginning of the magnetic disturbance at European auroral latitudes at 22:04 UT coincides with the SSS onset (middle graph of Figure 8), and it is close in magnitude to the global disturbance determined by the SML. The SSS intensity by SML is -2404 nT, and by IL it is -2600 nT, both at 22:36 UT. The slightly higher regional SSS intensity value confirms that the strongest disturbances occurred over Europe.

A strong MPB at PAG is obtained, with beginning close to the SSS onset (at 21:58 UT, 6 min. earlier than the determined onset, see left green line in the bottom graph of Figure 8). The MPB maximal value was 66.8 nT.

6. Third SSS event

6.1.Third SSS event by AMPERE data

The third SSS event was observed during the recoveri phase of the superstorm, on 11.05.2024. It consists of two consecutive SSS with onsets at 8:39 UT (2.27 MLT, 54° GMLat) and 9:25 UT (1.98 MLT, 67° GMLat; Forsyth et al. sustorms list [Forsyth et al. 2015]). The SSS onsets are in the night sector, and the PPN-NAL area in this case is in the day sector. Usually at that time the PPN-NAL area should lie under the Eastward electrojet. In Figure 9 the AMPERE data near the maximal development of the two supersubstorms are given. All designations are as in Figure 3. By the current systems distribution it is seen, that at the first SSS maximal development the current configuration is rather complex, presenting several alternating slices of downward and upward currents with different intensity and boundaries (upper right image in Figure 9, the green ellipse). At the second SSS maximal development the PPN-NAL area lies under Eastward electrojet current structure (bottom right image in Figure 9, the green ellipse).

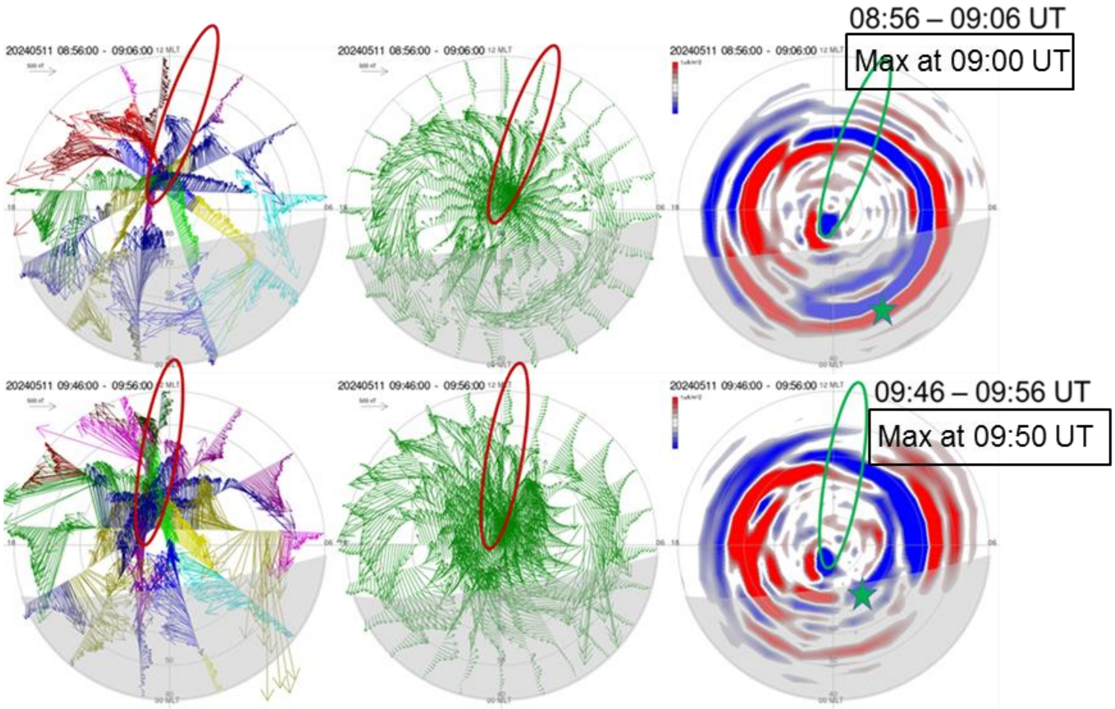

Figure 9. *AMPERE data at the time of the maximal development of the supersubstorms of the third SSS event during the superstorm. All designations are as in Figure 3.*

6.2.Third SSS event by SuperMAG and IMAGE data

The ground magnetic field variations during the third SSS event are presented in Figure 10. From the maps it is seen, that the main disturbances were in the night sector. The IMAGE stations get into the day sector. There are magnetic disturbances, but they seem rather chaotic. By the PPN-NAL graphs in the course of X, weak maxima can be observed in the auroral region after the onset of supersubstorms (blue vertical lines in the right panel), which spread to higher and lower latitudes, but do not stand out against the background of disturbances during the examined period.

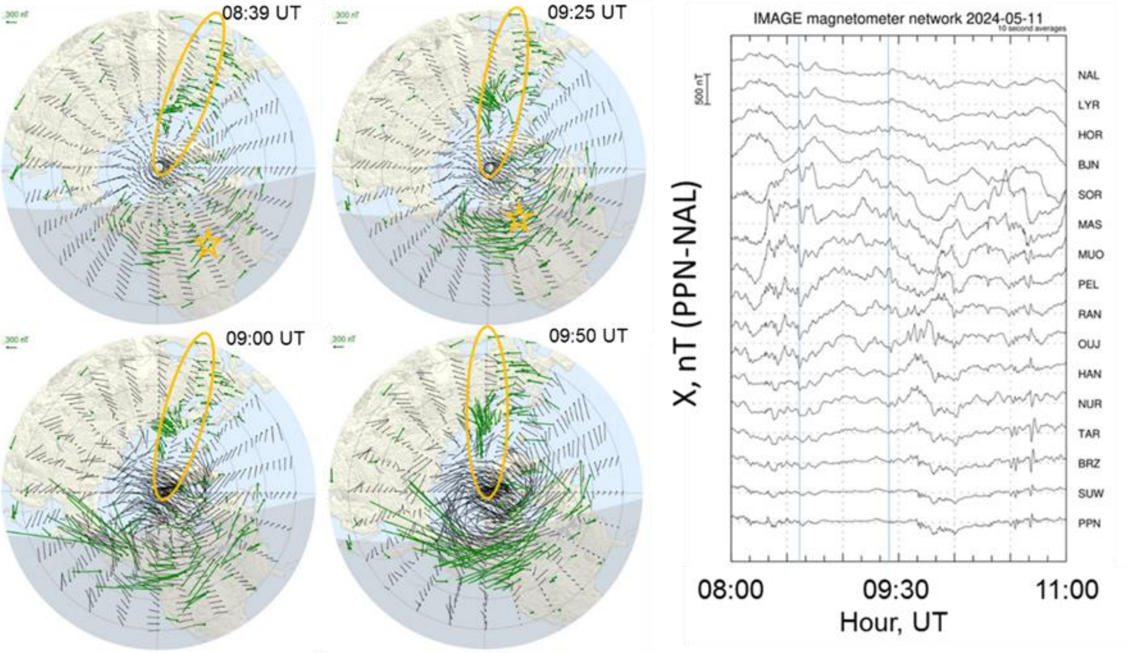

Figure 10. *Maps of the magnetic field vectors (left panel) at the onset (upper row) and maximal development (bottom row) times of the first SSS (left column) and second SSS (right column) of the third SSS event and X component variations at the IMAGE PPN-NAL stations from 08 UT to 11 UT on 11.05.2024 (right panel).*

6.3. Third SSS event by SML, AL, IL and magnetic X variations at PAG

The third SSS event and its effect at European auroral and midlatitudes are shown in Figure 11. From up to down the following quantities are presented: the global SML index, the global AL index, the regional IU and IL indices, and the X variations at the midlatitude station PAG. The two supersubstorms during the event are clearly expressed by the global indices. The SML and AL indices have the same shape and intensity. The behavior of the SML index is described in section 4.2. AL index also shows two-minima structure, with min at 09:00 UT and 09:44 UT, and corresponding values ~ -3400 nT and ~ -3380 nT, which is near the SML result.

By the IU index, near the maximal development of the first SSS a very small positive bay is observed, several times smaller than the neighboring positive disturbances. During the second SSS, a weak positive bay is obtained in the IU index, related to the eastward electrojet above the stations.

In addition, at Panagjurishte (PAG) (24.2°E, 42.5°N) there are no significant deviations in the X variations, either positive or negative, during the first SSS. But a negative bay is observed at ~09:50 – 10 UT, reaching -75 nT, which may be associated with the spreading current of the eastward electrojetde.

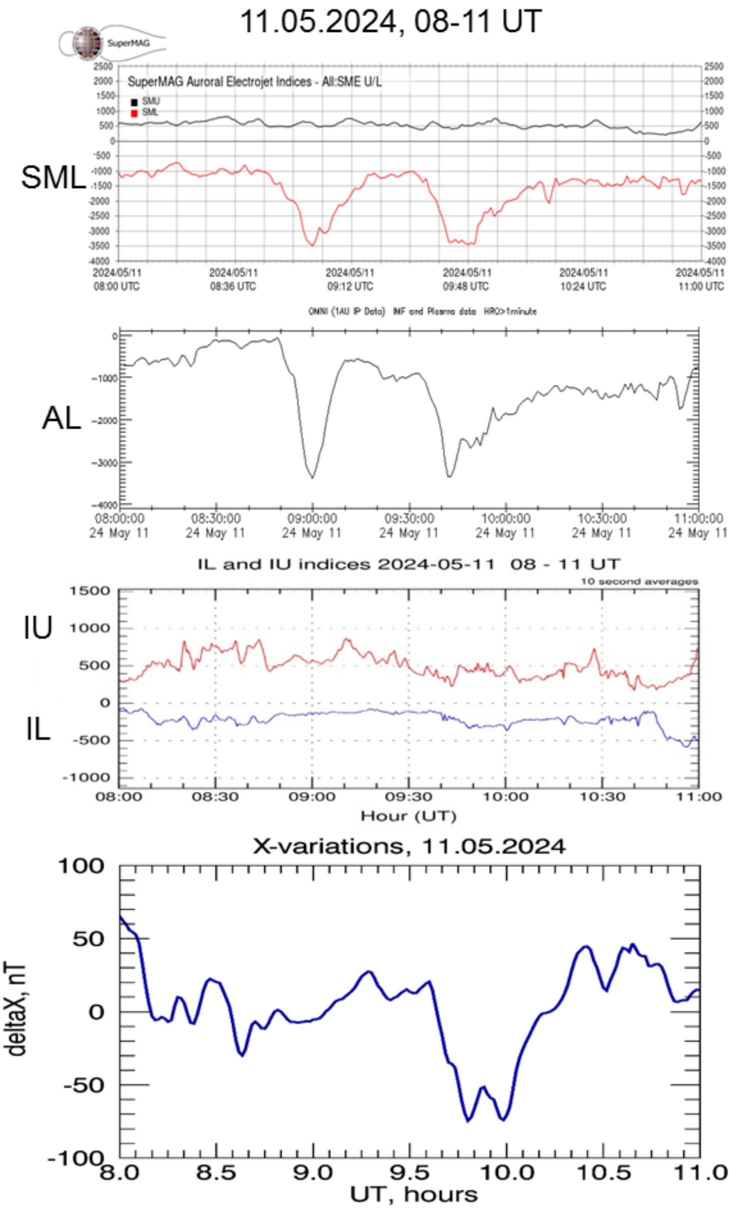

Figure 11. *From up to down: SML, AL, IU and IL indices, and X variations at PAG station from 8 UT to 11 UT on 11.05.2024.*

7. Fourth SSS event

7.1.Fourth SSS event by AMPERE data

The fourth SSS event occurred during the recovery phase of the superstorm, on 11.05.2024, and the European area lay in the evening MLT sector, under the eastward electrojet. The westward electrojet developed over America. In Figure 12 the AMPERE data near the maximal development of the two supersubstorms are presented. In the first row data about the first supersubstorm are given. The onset was at 3.48 MLT, 57° GMLat, and the maximal development at 12:45 UT. The second and third row show data near the maximal development of the second supersubstorm, for which two near SML minima were detected: at 13:32 UT (second row of Figure 12) and 13:43 UT (third row of Figure 12). The SSS onset was at 3.74 MLT, 67° GMLat. The field aligned currents were strong.

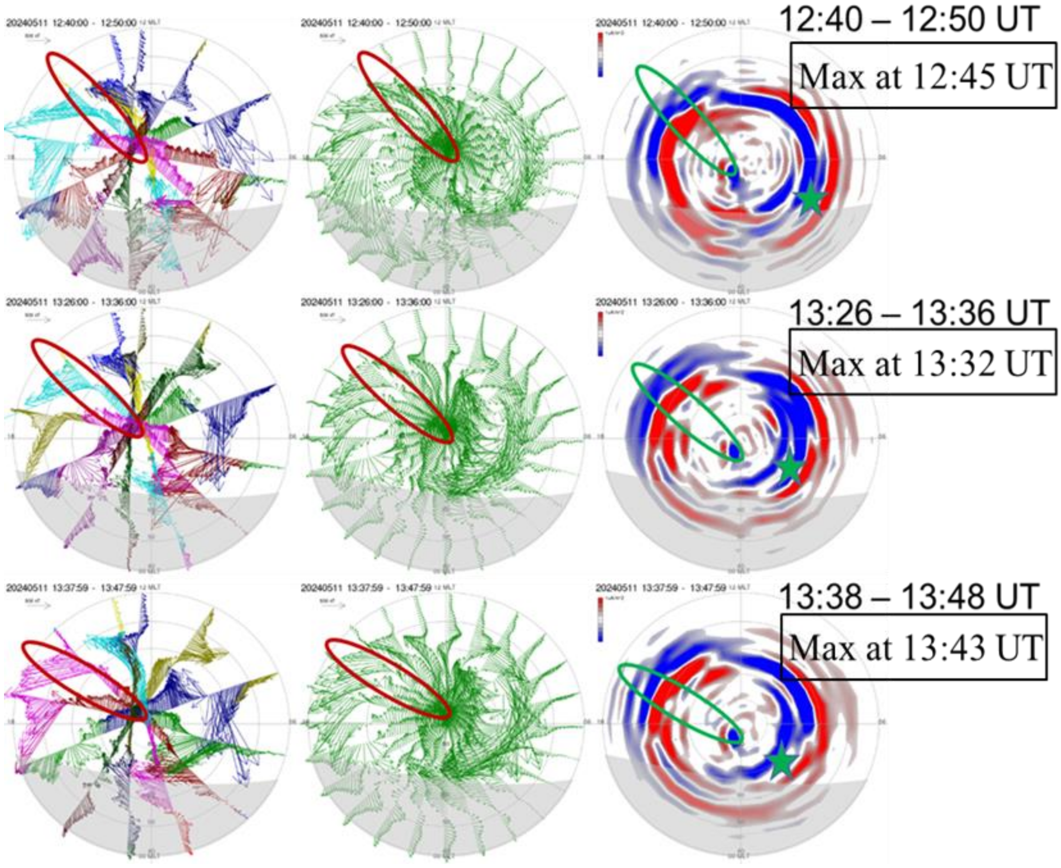

Figure 12. AMPERE data near the maximal developments of the first SSS (upper row) and second SSS (middle and bottom row) of the fourth SSS event on 11 May 2024. All designations are as in Figure 3.

7.2. Fourth SSS event by SuperMAG and IMAGE data

The ground magnetic variations during the fourth SSS event are shown in Figure 13. The left panel presents the maps of the magnetic vectors at the onsets (upper row) and maximal developments (bottom row) of the two supersubstorms. The right panel shows the X component of the magnetic field at the PPN-NAL chain stations from 11 UT to 16 UT on 11.05.2024.

During the first SSS IMAGE stations were under the eastward electrojet and positive bays in the X component at auroral latitudes were registered. During the second SSS, the magnetic vector orientation is more chaotic and some effect in X of the PPN-NAL chain did not appear.

7.3. Fourth SSS event by SML, AL, IL and magnetic X variations at PAG

The Fourth SSS event and its appearance at European auroral and midlatitudes are presented in Figure 14. In the panels from up to down the SML index, the AL index, the regional (for Europe) IU and IL indices, and the X variations at the midlatitude station PAG are presented. The two supersubstorms during the event are clearly seen by the course of the global indices.

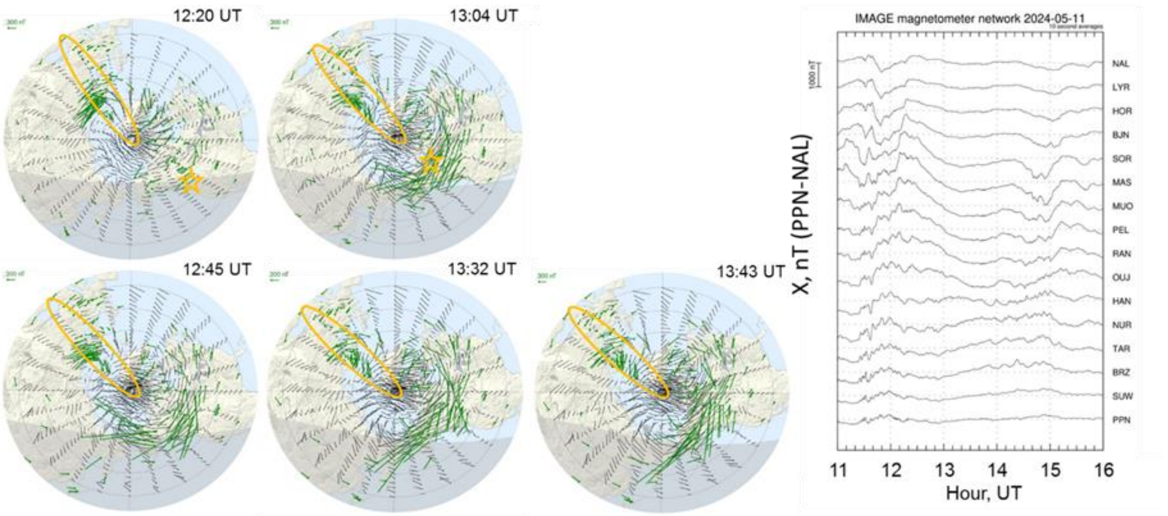

Figure 13. *SuperMAG maps of the magnetic perturbations (left panel) at the onset (upper row) and maximal development (bottom row) of the two SSSs from the fourth SSS event during the superstorm and X component of the magnetic field at the PPN-NAL stations from 11 to 16 UT (right panel).*

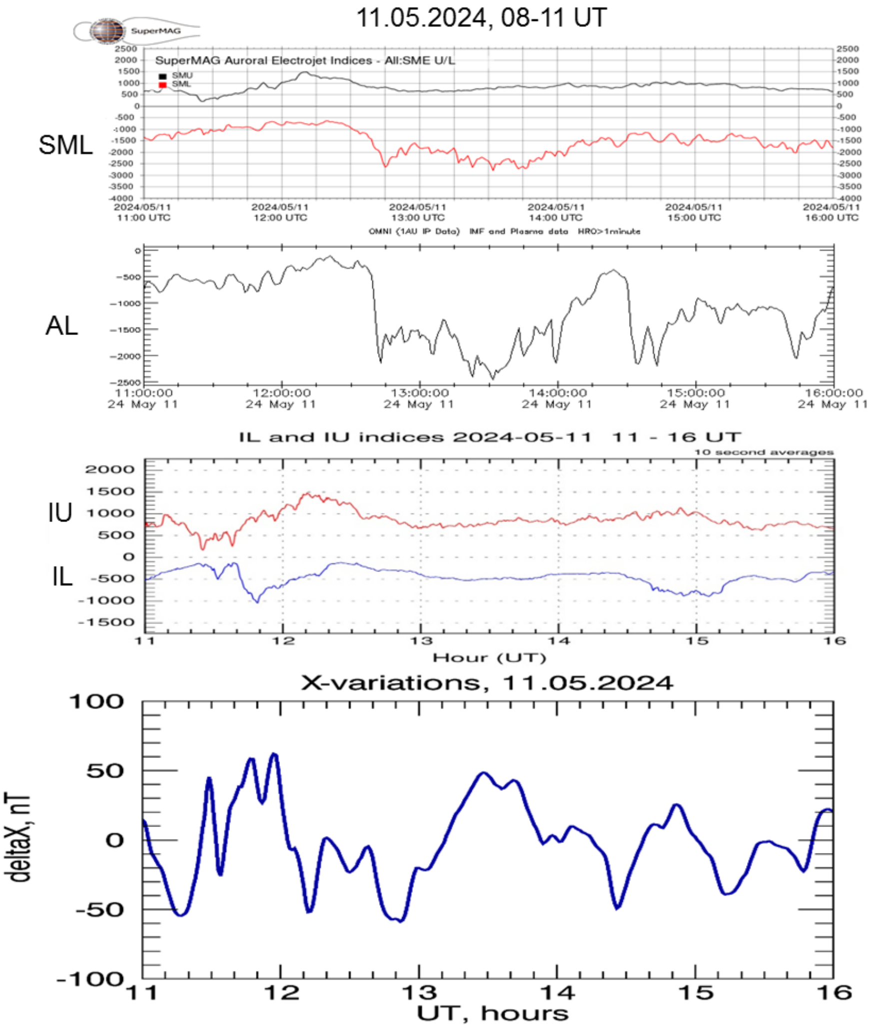

Figure 14. *SML (up), AL (down), IL and IU indices (further down), and X variations at PAG (bottom) from 11 UT to 16 UT on 11.05.2024.*

The SML and AL indices follow the same shape. The SSSs parameters by SML index are described above, in section 4.2. AL index shows a similar structure, with minima at 12:46 UT for the first SSS, 13:26 UT and 13:34 UT for the second SSS, and corresponding intensities ~ -2180 nT and ~ -2400 nT, and 2490 nT.

By IMAGE PPN-NAL IU index (96°-113° GMLon.) a positive peak is observed during the first SSS, related to the increasing of the eastward electrojet. Perhaps because the event is not isolated the increasing of the eastward electrojet was not recorded during the second SSS

At Panagjurishte (PAG) 24.2°E, 42.5°N) a minimum is observed during the first SSS, reaching -60 nT.

8. Summary

Auroral and midlaltitude disturbances observed by four supersubstorm events during the superstorm on 10-12 May 2024 have been examined. The planetary distribution of ionospheric currents, typical for SSS, confirmed the previous results: development of both westward and eastward electrojets on a global scale, encompassing the Earth from different sides was observed. During the main storm phase, the southern boundary of the field aligned currents reaches and maybe surpasses 40° GMLat. The field aligned currents manifest sometimes a very complicated structure, in most areas consisting of alternating slices of upward and downward currents.

The magnetic variations in the PPN-NAL and PAG longitudinal regions (12°-25°E; 96°-113° GMLon) have been considered.

When the PPN-NAL area is in the night MLT sector (the events on 10.05.2024) and the westward electrojet reaches it, negative bays in X are registered at auroral latitudes.

When the PPN-NAL area is in the day MLT sector, if the eastward electrojet is above the IMAGE stations, positive bays in X are observed.

Note that our study of midlaltitude positive bays (MPB) was confined to the analysis of data from only one station - PAG. It should be also noted that The MPB's during extremely disturbed conditions are typically of complicated form, in many cases they are composed of two or more maxima, sometimes with deep minima between them, which may bother the processing. Typically, data under highly disturbed conditions is highly noisy, both due to unusual rapid strong variations in the data and perhaps also due to ambient conditions. This sometimes requires additional specific processing and verification.

When the SSS is observed in the PPN-NAL area, in the night MLT sector, its effect is clearly expressed at midlatitudes (PAG), with a MPB beginning near the drop of IL index and high X_{max} values (above 50 nT).

When PAG was in the day MLT sector, no effect was observed when there is not a clearly expressed maximum in the IU index, and a significant decrease in X (of the range of -60÷ -70 nT) was obtained if the PPN-NAL region is below the eastward electrojet.

Acknowledgements: We acknowledge the substorm timing list identified by the Newell and Gjerloev technique, the SMU and SML indices (Newell and Gjerloev, 2011); and the SuperMAG collaboration (Gjerloev et al. 2012). The authors are grateful to the creators of the databases AMPERE (https://ampere.jhuapl.edu/), IMAGE (http://space.fmi.fi/image/), OMNI (https://cdaweb.gsfc.nasa.gov/), and INTERMAGNET (http://intermagnet.org/) for the opportunity to use them in this work.

References

Akasofu, S.-I. (1964). The development of the auroral substorm, *Planetary and Space Science*, Vol. 12, No. 4, pp. 273–282.

Akasofu, S.-I. (2004). Several 'controversial' issues on substorms, *Space Science Reviews*, Vol. 113, pp. 1–40, DOI: 10.1023/B:SPAC.0000042938.57710.fb.

Anderson, B.J., Angappan, R., Barik, A., Vines, S.K., Stanley, S., Bernasconi, P.N., Korth, H., Barnes, R.J. (2021). Iridium Communications Satellite Constellation data for study of Earth's magnetic field, *Geochemistry, Geophysics, Geosystems*, Vol. 22, e2020GC009515, DOI: 10.1029/2020GC009515.

Cander, L.R., Mihajlovic, S.J. (1998). Forecasting ionospheric structure during the great geomagnetic storms, *Journal of Geophysical Research: Space Physics*, Vol. 103, No. A1, pp. 391–398, DOI: 10.1029/97JA02418.

Despirak, I.V., Lubchich, A.A., Kleimenova, N.G., Setsko, P.V., Werner, R. (2022). Supersubstorm on 20 December 2015: Spatial geomagnetic effects, *Proceedings of the Fourteenth Workshop "Solar Influences on the Magnetosphere, Ionosphere and Atmosphere"*, pp. 10–15, DOI: 10.31401/WS.2022.proc.

Despirak, I.V., Lubchich, A.A., Kleimenova, N.G. (2023). Space weather conditions and non-storm supersubstorms observations, *Proceedings of the Fifteenth Workshop "Solar Influences on the Magnetosphere, Ionosphere and Atmosphere"*, pp. 35–40, DOI: 10.31401/WS.2023.proc.

Despirak, I.V., Kleimenova, N.G., Lubchich, A.A., Setsko, P.V., Malysheva, L.M. (2025). "Polar" substorms during slow solar wind, *Journal of Geophysical Research: Space Physics*, Vol. 130, e2024JA033555, DOI: 10.1029/2024JA033555.

Despirak, I.V., Setsko, P.V., Lubchich, A.A., Sakharov, Y., Selivanov, V. (2025). Geomagnetically induced currents (GICs) during the strong geomagnetic storm on 10–12 May 2024, *Advances in Space Research*, in press, DOI: 10.1016/j.asr.2025.06.081.

Forsyth, C., Rae, I.J., Coxon, J.C., Freeman, M.P., Jackman, C.M., Gjerloev, J., Fazakerley, A.N. (2015). A new technique for determining substorm onsets and phases from indices of the electrojet (SOPHIE), *Journal of Geophysical Research: Space Physics*, Vol. 120, No. 12, pp. 10592–10606, DOI: 10.1002/2015JA021343.

Gjerloev, J.W. (2012). The SuperMAG data processing technique, *Journal of Geophysical Research*, Vol. 117, A09213, DOI: 10.1029/2012JA017683.

Guineva, V., Werner, R., Bojilova, R., Raykova, L., Atanassov, A., Valev, D. (2024a). Analysis of substorms related to strong MPB at Panagyurishte station in 2022, *Proceedings of the Sixteenth Workshop "Solar Influences on the Magnetosphere, Ionosphere and Atmosphere"*, pp. 56–63, DOI: 10.31401/WS.2024.proc.

Guineva, V., Werner, R., Bojilova, R., Raykova, L., Atanassov, A., Valev, D. (2024b). Study of the midlatitude positive bays at the magnetic station Panagyurishte during the descending phase of Solar Cycle 24, *Proceedings of the Twentieth Anniversary International Scientific Conference SES2024*, pp. 48–54.

Guineva, V., Werner, R., Bojilova, R., Raykova, L., Atanassov, A., Valev, D. (2024c). A methodology to estimate the MPB parameters, *Proceedings of the 47th Annual Seminar "Physics of Auroral Phenomena"*, pp. 16–19, DOI: 10.51981/2588-0039.2024.47.003.

Hajra, R., Tsurutani, B.T., Lakhina, G.S., Lu, Q., Du, A. (2024). Interplanetary causes and impacts of the May 2024 superstorm on the geosphere: An overview, *Astrophysical Journal*, Vol. 974, pp. 264–276, DOI: 10.3847/1538-4357/ad7462.

Kleimenova, N.G., Despirak, I.V., Malysheva, L.M., Gromova, L.I., Lubchich, A.A., Roldugin, A.V., Gromov, S.V. (2023). Substorms on a contracted auroral oval, *Journal of Atmospheric and Solar-Terrestrial Physics*, Vol. 245, pp. 106049–106062, DOI: 10.1016/j.jastp.2023.106049.

Kleimenova, N.G., Gromova, L.I., Gromov, S.V., Malysheva, L.M. (2025). Ground-based geomagnetic disturbances and Pi2 pulsations in the main phase of the superstorm on May 10, 2024, *Advances in Space Research*, in press, DOI: 10.1016/j.asr.2025.04.025.

Loewe, C.A., Prolss, G.W. (1997). Classification of mean behavior of magnetic storms, *Journal of Geophysical Research*, Vol. 102, No. A7, pp. 14209–14213, DOI: 10.1029/96JA04020.

Lockwood, M., Owens, M.J., Brown, W., Vázquez, M. (2025). The May 2024 event in the context of auroral activity over the past 375 years, *Monthly Notices of the Royal Astronomical Society*, Vol. 540, No. 4, pp. 3596–3624, DOI: 10.1093/mnras/staf827.

Lubchich, A.A., Despirak, I.V., Werner, R. (2023). Intense mid-latitude magnetic disturbances and solar wind conditions, *Proceedings of the Fifteenth Workshop "Solar Influences on the Magnetosphere, Ionosphere and Atmosphere"*, pp. 61–66, DOI: 10.31401/WS.2023.proc.

McPherron, R.L. (1972). Substorm-related changes in the geomagnetic tail: The growth phase, *Planetary and Space Science*, Vol. 20, No. 9, pp. 1521–1539, DOI: 10.1016/0032-0633(72)90054-2.

McPherron, R.L., Chu, X. (2017). The midlatitude positive bay and the MPB index of substorm activity, *Space Science Reviews*, Vol. 206, pp. 91–122, DOI: 10.1007/s11214-016-0316-6.

Newell, P.T., Gjerloev, J.W. (2011a). Evaluation of SuperMAG auroral electrojet indices as indicators of substorms and auroral power, *Journal of Geophysical Research*, Vol. 116, A12211, DOI: 10.1029/2011JA016779.

Newell, P.T., Gjerloev, J.W. (2011b). Substorm and magnetosphere characteristic scales inferred from the SuperMAG auroral electrojet indices, *Journal of Geophysical Research*, Vol. 116, A12232, DOI: 10.1029/2011JA016936.

Tsurutani, B.T., Hajra, R., Echer, E., Gjerloev, J.W. (2015). Extremely intense (SML ≤ –2500 nT) substorms: Isolated events that are externally triggered?, *Annales Geophysicae*, Vol. 33, No. 5, pp. 519–524, DOI: 10.5194/angeo-33-519-2015.

Wang, R., Ying, D., Liu, Y.D., Zhao, X., Hu, H. (2024). Unveiling key factors in solar eruptions leading to the solar superstorm in May 2024, *Astronomy & Astrophysics*, Vol. 692, A112, DOI: 10.1051/0004-6361/202452008.

Waters, C.L., Anderson, B.J., Liou, K. (2001). Estimation of global field-aligned currents using the Iridium® system magnetometer data, *Geophysical Research Letters*, Vol. 28, pp. 2165–2168, DOI: 10.1029/2000GL012725.

Weiler, E., Möstl, C., Davies, E.E., Veronig, A.M., Amerstorfer, U.V., Amerstorfer, T., Le Louëdec, J., Bauer, M., Lugaz, N., Haberle, V., Rüdisser, H.T., Majumdar, S., Reiss, M. (2025). First observations of a geomagnetic superstorm with a sub-L1 monitor, *Space Weather*, Vol. 23, No. 3, e2024SW004260, DOI: 10.1029/2024SW004260.

Werner, R., Guineva, V., Atanassov, A., Bojilova, R., Raykova, L., Valev, D., Lubchich, A., Despirak, I. (2021). Calculation of the horizontal power perturbations of the Earth surface magnetic field, *Proceedings of the Thirteenth Workshop “Solar Influences on the Magnetosphere, Ionosphere and Atmosphere”*, pp. 159–164, DOI: 10.31401/WS.2021.proc.

DOI: 10.31401/WS.2025.proc.15

Proceedings of
the Seventeenth Workshop “Solar Influences on the Magnetosphere, Ionosphere and Atmosphere”
June, 2025

The Cyclicity of Radio Interference Manifestation in the Data of Cosmic Radio Sources Monitoring in the Decameter Wavelength Range

Lytvynenko O.A., Panishko S.K.

Institute of Radio Astronomy of NASU, spanishko@ukr.net

Abstracts

A special feature of radio astronomical observations in the decameter wave range is the high level of radio interference, the main sources of which are broadcast radio stations, various radio engineering systems, industrial and natural sources of radio emission. Due to ionospheric propagation, radio interference signals entering the receiving path of the radio telescope through the central and side lobes of the antenna pattern can come from radio sources located at a distance of hundreds and thousands of kilometers from the radio telescope. The interference level is determined by the power and operating mode of radio interference sources, radio range congestion, ionospheric propagation conditions, which change depending on the time of day, season of the year, and phase of the solar activity cycle. Different types of interference manifest themselves in observational data in different ways. This depends on the observation technology, equipment used, and data processing methods. In this paper, we consider the interference environment by analyzing the manifestation of radio interference in radiometer signal records obtained during long-term monitoring of a group of compact space radio sources on the URAN-4 radio telescope (Odessa region, Ukraine). The results obtained can be used to improve the efficiency of planning radio astronomical observations, and also allow us to track trends in the change in the intensity of radio interference affecting radio astronomical observations.

Key words: cosmic radio sources; decameter wavelength range: radio interferences.

1. Introduction

The quality of observation data of cosmic radio sources in low-frequency radio astronomy largely depends on the type and intensity of radio interference. The influence of radio interference is especially significant during measurements in the decameter range of radio waves. The level of interference is determined by the power and operating mode of radio interference sources, the load of the radio range with such sources, the conditions of ionospheric propagation, which change depending on the time of day, season of the year, and phase of the solar activity cycle. Information on how radio interference manifests itself at different time intervals from a day to several years can be used to improve the efficiency of planning radio astronomical observations, and will also allow us to track trends in the change in the intensity of radio interference affecting radio astronomical observations. The study of patterns in the occurrence of radio interference affecting the efficiency of radio astronomical observations in the decameter wavelength range, on the one hand, is of practical importance for radio telescopes of this range, in particular, such as the URAN and GURT radio telescope networks [Konovalenko et al., 2016], [Yerin et al., 2018]. On the other hand, given that the intensity of radio interference is largely determined by the state of the ionosphere, a change in the efficiency of radio astronomical observations in the decameter wavelength range can be an indirect factor characterizing changes in the state of the ionosphere and can be used in space weather studies, such as those carried out on the URAN radio telescope network [Shepeliev and Lytvynenko, 2021], [Kalinichenko et al., 2021].

The aim of the work is to study the cyclic manifestations of the appearance of radio interference based on observations of cosmic radio sources in the decameter range of radio waves.

2. Observation data and processing method

The cyclic variations of the radio interference manifestation were studied using materials of the monitoring observations of the power cosmic radio sources (3C 144, 3C 274, 3C 405, 3C 461) which carried out on the radio telescope URAN-4 (Figure 1) on frequencies 20 and 25 MHz and on two polarization A and B since 1987. The radio telescope is located in the Odessa region and is part of the URAN radio interferometer system, which is located at several points on the territory of Ukraine [Megn et al., 1997]. Since 1998, digital data recording has been used at the radio telescope [Derevyagin et al., 2019]. As a result, the paper considers time intervals under consideration when observations were carried out regularly: 1998-2007 and 2011-2024.

Figure 1. *Radio telescope URAN-4.*

Observations with the URAN-4 radio telescope are carried out in the form of recordings of several passes of each radio source through the direction pattern of the radio telescope during the day. Each record was processed separately and its characteristics were placed in a text file in the computer's memory [Lytvynenko et al., 2023]. During processing, a visual evaluation of each record was performed. The scores were also placed in the computer's memory along with other characteristics [Lytvynenko and Panishko, 2020]. Figure 2 shows records of radio sources with different levels of interference. Depending on how much the interference distorted the type of recording, the following estimates were applied:

0 – the recording was not processed due to high interference;
1 – good recording quality;
2 – interference in the form of short-period emissions is observed;
3 – interference is significant.

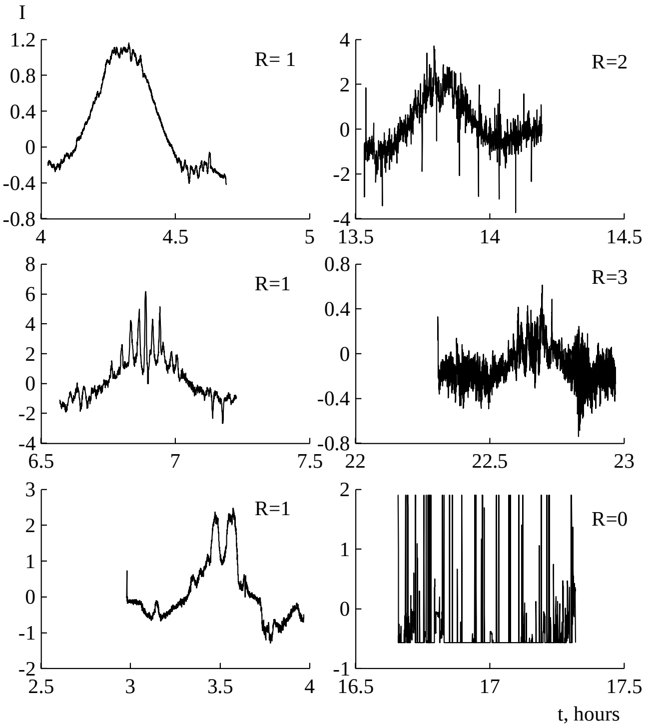

Figure 2. *Samples of the radio source records with different level of radio interferences.*

Table 1 shows the data on the number of records of radio sources obtained by the radio telescope URAN-4 during the intervals under consideration.

Table 1. *Statistics of the radio source records obtained on the radio telescope URAN-4.*

1. Time interval	**2. Number** **3. of observation** **4. records**	**5. Number** **6. of processed** **7. records**
	12. 528376	90762
14. Sum	15. 726716	24828

Table 2 shows the distribution of the number of observation records depending on the quality assessment. If we take into account that records with ratings 1 and 2 are mainly used for data analysis, then a significant part of the records (about 69%) is affected by radio interference.

Table 2. *Distribution PR of the observation record number N on dependence of the quality estimation R.*

17. R	**18. N**	**19. PR, %**
20.	21.	22.
		5.0
		28. 6.1
		31. 25.1

cycle of solar activity (May 1996 – January 2009), while the second period (2011-2024) coincides with the 24th cycle (January 2009 – December 2019) and the ascending branch of the

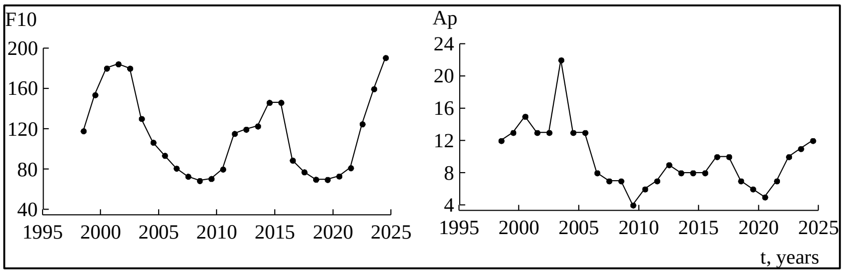

Figure 3. *Graphics of the solar flux F10 and geomagnetic index Ap for time intervals under consideration.*

3. Analysis of radio interference manifestation during time intervals from days to years

Further on the graphs the following curve colors are applied for data on different channels: 20 A – blue; 20 B – green; 25 A – red; 25 B – lilac. The left graphs show data for 1998–2007, and the right graphs show data for 2011–2024.

Figure 4 shows the hourly distribution of radio interference. From the figure it can be seen that in the case of high levels of interference (R = 0, R = 3), a similar distribution is observed with maximum values in the daytime, mainly from 08 to 20 hours local time (UT+2^{h}). In some graphs, you can see several peaks in the distribution, which are most likely related to the moments of sunrise and sunset. When there is no interference or its intensity is weak (R = 1, R = 2), the distributions are also similar. The minimum number of records of good quality is observed during the daytime from 08 to 20 hours local time. At night, their number is much higher. Thus, the effect of the daily distribution of the level of radio interference in the observation of cosmic radio sources can be considered significant. Measurements at night lead to a better result, and during the day, the intensity of radio interference increases, which affects the quality of the data obtained.

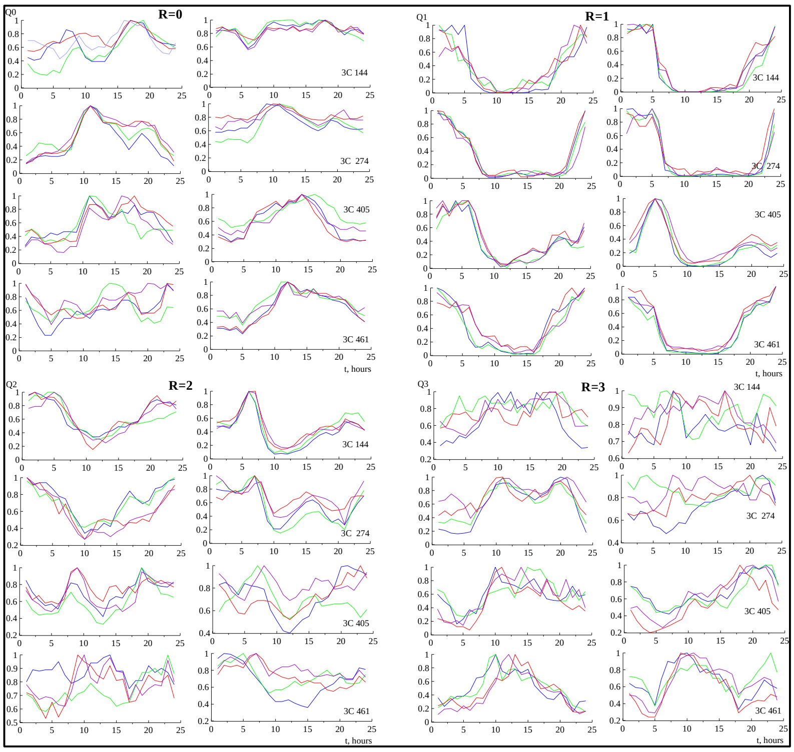

Figure 4. *Hourly distributions of record quality scores.*

Figure 5 shows the seasonal dependence of the recording quality estimates. Since radio sources 3C 144 and 3C 274 are observed at night in the winter months and during the day in the summer, and 3C 405 and 3C 461 are observed in the daytime during the winter months and at night in the summer, there is an interrelated seasonal-daily relationship. Thus, the seasonal dependence reflects the daily dependence for each radio source. This can also be seen from the Table 3 where are the times of the culmination of radio sources in the middle of the month during the year. The data for the months in which the maximum number of records of good quality was observed is underlined. Basically, these periods coincide with observations which obtained at night.

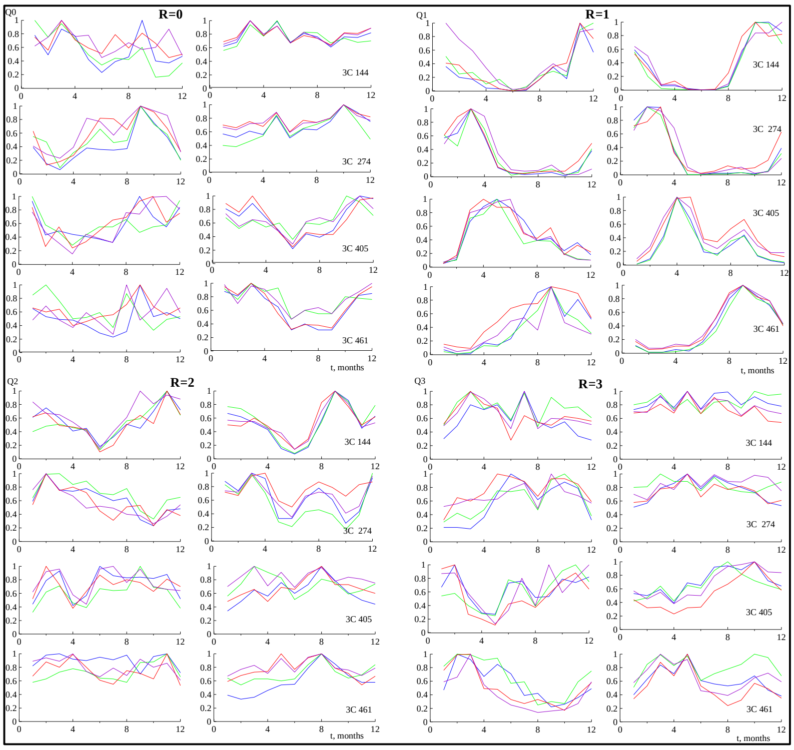

Figure 5. *Seasonal distributions of record quality scores.*

Table 3. *Culmination time of radio sources on months.*

35. M	**36. 3C 144**	**37. 3C 274**	**38. 3C 405**	**39. 3C461**
40.	41.	42.	43.	44.

Figure 6 shows the annual distributions of quality assessments of space radio source recordings. From the graphs, you can see that the data on different channels are quite correlated. It can also be noted that the distributions for the time intervals under consideration behave differently, although both cases are characterized by periodic variations with periods of about 3–4 years. For the 2011-2024 data, there is a trend of increasing radio interference since 2013, for the 1998-2007 data there are only periodic changes. Due to the presence of a periodic structure, it is quite difficult to determine how much the resulting distributions follow the cycles of solar activity and variations in geomagnetic data, although at the maxima of the F10 index there are maximums of radio interference. Thus, the data on annual distributions requires further research and interpretation.

Figure 6. *Annual distributions of record quality scores and a graph (at the bottom of the graph) of the behavior of the relative values of the F10 (black curve) and Ap (orange curve) indices during the time intervals under consideration*

4. Conclusions

Based on observations of radio source (3C 144, 3C 274, 3C 405, 3C 461) passes through direction pattern of radio telescope URAN-4 on frequencies 20 and 25 MHz and on two polarizations (A and B), the daily, seasonal and annual distributions of quality assessments of records were analyzed.

1. As expected, the daily distribution of quality assessments of radio source records shows that high-quality records are made at night. When observations were made during daylight hours, the amount of radio interferences increased significantly.

2. More likely, the seasonal distributions of values R also reflect the diurnal distribution, since radio sources 3C 144 and 3C 274 are observed at night in winter months and during daylight hours in summer. At the same time, the radio sources 3C 405 and 3C461 are observed during the daytime in the winter months, and at night in the summer. Thus, there is an interconnected seasonal-daily dependence.

3. The annual distributions of values R for the time intervals under consideration are quite complex. The first period (1998–2007) almost coincides with the 23th solar activity cycle, while the second (2011–2024) coincides with the 24th solar activity cycle and with ascending branch

of 25th cycle. In general, the amount of radio interferences increases with increasing of solar activity. There are periodic variations in the annual distributions that require further research and interpretation.

Acknowledgment

This study was supported by Science and technology center in Ukraine (Project No. 6435 "Features and interaction of phenomena in the solar corona and the interplanetary medium") and Special Program of NAS of Ukraine (project No4.1/25-П "Global monitoring of radio signals of natural and artificial origin of decameter-meter waves in the interests of cosmology and applied problems of defense capability").

References

Derevyagin, V.G., Kravetz, R.O., Lytvynenko, O.A., Panishko, S.K. (2019). Regular observations of the power cosmic radio sources on the radio telescope URAN-4: Processing method, results keeping system and their applying in ionosphere investigations, *Proceedings of the Eleventh Workshop “Solar Influences on the Magnetosphere, Ionosphere and Atmosphere”*, Primorsko, Bulgaria, June 3–7, pp. 84–88, DOI: 10.31401/WS.2019.proc.

Kalinichenko, M.M., et al. (2021). Statistical characteristics of radio source scintillations at decameter wavelengths, *Proceedings of the Thirteenth Workshop “Solar Influences on the Magnetosphere, Ionosphere and Atmosphere”*, Primorsko, Bulgaria, September 2021, pp. 28–33, DOI: 10.31401/WS.2021.proc.

Konovalenko, A., et al. (2016). The modern radio astronomy network in Ukraine: UTR-2, URAN and GURT, *Experimental Astronomy*, Vol. 41, pp. 1–38.

Lytvynenko, O.A., Panishko, S.K. (2020). Variations of the ionosphere scintillation parameters on the observations of the cosmic radio sources at the decameter wave range during two cycles of the solar activity, *Proceedings of the Twelfth Workshop “Solar Influences on the Magnetosphere, Ionosphere and Atmosphere”*, Primorsko, Bulgaria, September, pp. 77–80, DOI: 10.31401/WS.2020.proc.

Lytvynenko, O., Panishko, S., Derevyagin, V. (2022). Dependence of the ionospheric scintillation intensity of cosmic radio sources on their position in the sky, *Proceedings of the Fourteenth Workshop “Solar Influences on the Magnetosphere, Ionosphere and Atmosphere”*, Primorsko, Bulgaria, June, pp. 41–48, DOI: 10.31401/WS.2022.proc.

Lytvynenko, O.A., Panishko, S.K., Derevyagin, V.G. (2023). The long-term observations of the power cosmic radio sources on the radio telescope URAN-4 at the decameter wave range, *Odessa Astronomical Publications*, Vol. 36, pp. 118–121, DOI: 10.18524/1810-4215.2023.36.290139.

Megn, A., Braude, S.Ya., Rashkovskiy, S.L., et al. (1997). URAN system of the decameter interferometers (I), *Radiophysics and Radioastronomy*, Vol. 2, No. 4, pp. 385–401 (in Russian).

Shepeliev, V., Lytvynenko, O. (2021). Impact of space weather on ionospheric scintillation, *Proceedings of the Thirteenth Workshop “Solar Influences on the Magnetosphere, Ionosphere and Atmosphere”*, September 2021, pp. 147–152, DOI: 10.31401/WS.2021.proc.

Yerin, S., et al. (2018). Small-sized radio telescopes for monitoring and studies of solar radio emission at meter and decameter wavelengths, *Proceedings of the Tenth Workshop “Solar Influences on the Magnetosphere, Ionosphere and Atmosphere”*, Primorsko, Bulgaria, June 4–8, 2018, pp. 129–133, DOI: 10.31401/WS.2018.proc.

DOI: 10.31401/WS.2025.proc.16

Proceedings of
the Seventeenth Workshop “Solar Influences on the Magnetosphere, Ionosphere and Atmosphere”
June, 2025

Observation of Tropospheric Deep Convection in Mid-Latitudes with Potential Impact up to Ionospheric Heights

Potužníková K., Koucká Knížová P.

Institute of Atmospheric Physics, Czech Academy of Sciences, Prague, Czech Republic
kaca@ufa.cas.cz

Abstracts

Our case study investigates the coincidental occurrence of intense tropospheric convection and upper atmospheric variability. It focuses on the generation of gravity waves (GWs) at tropospheric heights and their potential impact on the ionosphere. Our analysis presents an organised mesoscale convective system (MCS) associated with a derecho event and air-mass severe thunderstorms with supercells occurring.

In both cases, sporadic ionospheric E layer was recorded. A significant reduction in electron density, which was expected after the passage of an extensive MCS, was also observed in the case of very intensive but spatially limited supercell thunderstorms.

1. Introduction

Sun and its changing activity are the most important factors influencing the state and variability of the neutral atmosphere and ionosphere. Changing solar flux and geomagnetic activity are reflected on broad time scales ranging from abrupt changes related for instance to geomagnetic storms up to secular solar variation. Apart from the solar and geomagnetic drivers, influence of the lower-lying atmospheric regions can contribute significantly to the resulting energy budget [Laštovička, 2006; Yigit et al., 2016; Koucká Knížová et al., 2018]. In the troposphere and lowermost stratosphere, convective storms represent important sources of atmospheric gravity waves (GWs), which can propagate upwards. Under favourable conditions defined by the neutral atmosphere dynamics, these waves may reach ionospheric heights and significantly influence the thermosphere and ionosphere up to the F2 layer.

In this study, we present ionospheric response on two different tropospheric convective sources of gravity waves over Central Europe and its: (i) a mesoscale convective system (MCS) with a derecho event, and (ii) a local-scale severe thunderstorms. Both meteorological cases emerged during periods of relatively quiet geomagnetic activity and stable solar forcing. Therefore, we further suppose that the observed disturbances in the ionosphere are primarily induced by GWs originated in the intense tropospheric convection.

2. Tropospheric observation

Strong updrafts in intense thunderstorms can penetrate the tropopause and extend a few kilometres into the lower stratosphere, where rising air parcels lose buoyancy, descend back to equilibrium level, and spread laterally to form extensive anvil clouds. These processes act as efficient sources of GWs that may propagate into the mesosphere and ionosphere. MCS is a cluster of storm cells with a roughly circular anvil several hundred kilometres across. MCSs typically form in the afternoon and may persist overnight due to radiative cooling of the anvil, which maintains sufficient lapse rate even without surface heating. With lifetimes often exceeding six hours, they represent long-lived sources of gravity waves comparable in cumulative impact to smaller tropical cyclones. In contrast, severe single-cell thunderstorms cover smaller areas. However, in some cases, they can develop into supercells with rotating updrafts whose intensity can locally equal or even exceed that of an MCS. In Central Europe, there are several mesoscale convective systems forming per year during the warm season (typically late May till early September). In addition, according to the European Severe Weather Database (ESWD), dozens of supercell thunderstorms occur annually in this region.

Figure 1 shows a MCS of the squall line type, formed in a very warm and humid air mass ahead of a cold front. The core of the storm, as indicated by both the overshooting tops visible on the satellite image (the sharp dark red spots) and the maximum reflectivity visible on the radar image, is arranged in a line along the German–Czech border. The southern part of the storm line is clearly bowed in the direction of its eastward movement. This indicates the intensification and subsequent acceleration of this part of the storm line. As the storm quickly moved across the Czech Republic, it was accompanied by destructive wind gusts at ground level that met the definition of a derecho (wind speeds greater than 25 m/s recorded over an area greater than 400 km).

At the end of May 2008, warm and moist air was advected northward into Germany from the Mediterranean region along large-scale upper-level trough, resulting in unstable atmospheric conditions favourable for deep convection. Figure 2 shows two independent supercells near the western border of the Czech Republic, each exhibiting cold rings and cold-U/V features ([Setvák, 2010] and summary of references herein), known as indirect indicators of potential storm severity. Throughout their existence, the storms generated a series of distinct overshooting tops that may have acted as sources of upward-propagating GWs. Compared to the previous MCS situation, the supercells have a smaller area of high reflectivity above 50 dBZ (an indicator of intense convection and dangerous phenomena such as hailstorms and torrential rain).

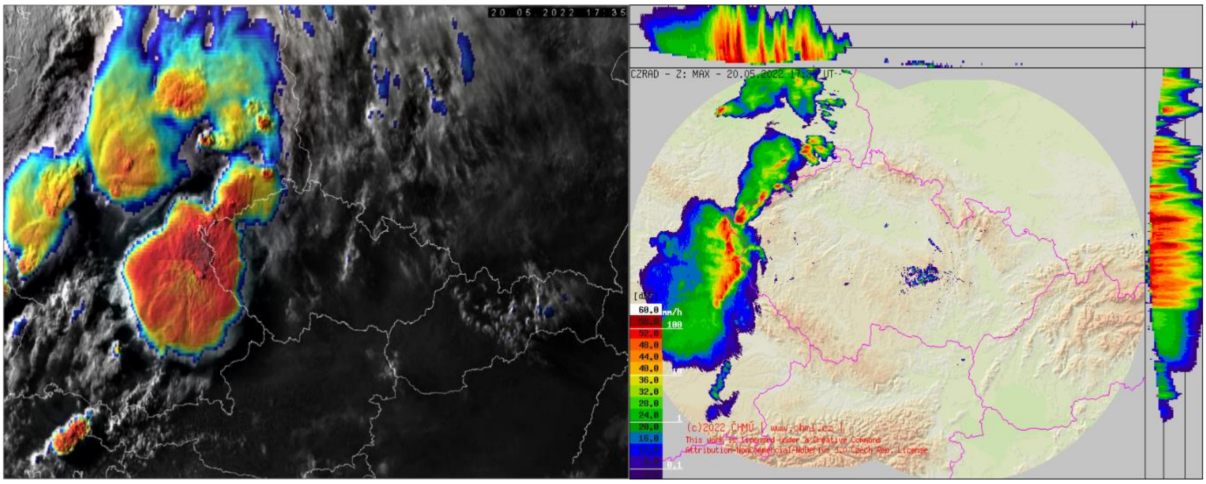

Figure 1. *MCS on 20 May 2022 at 17:35 UTC. Left panel: The Meteosat-10 (MSG3) sandwich product comprises VIS and colour-enhanced IR channels ranging from 200 K (dark red) to 240 K (blue). Source: EUMETSAT; CHMI. Right panel: CZRAD composite of maximum reflectivity (dBZ scale at bottom left) in pseudo 3D view, [Novak, 2007]. Source: CHMI.*

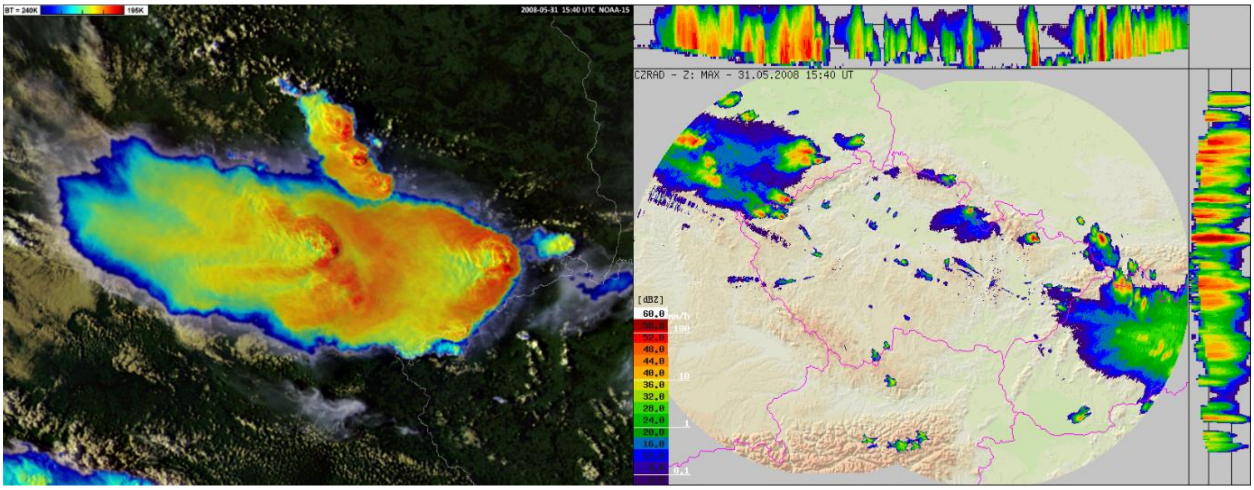

Figure 2. *Supercells on 31 May 2008 at 15:40 UTC. Left panel: NOAA-15 polar-orbiting satellite, sandwich product [Setvák et al., 2013]. Source: EUMETSAT; CHMI. Right panel: Same as the Right panel of Figure 1.*

3. Ionospheric response

Both analyzed events occurred during relatively similar conditions (low geomagnetic, stable solar forcing and season - spring before solstice) but in different Solar Cycles. Ionosphere is regularly monitored by digisonde DPS 4D with 5 and 15-minute cadence. Ionograms are manually scaled. Electron density profiles are inverted using the NHPC inversion technique. The Profilogram on Figure 3 represents the course of electron profiles for five consecutive days covering two days before and after the events. It shows variability of the entire electron density profiles. Wave-like variations in the electron concentration are well seen especially during daytime. In the case of MCS, a remarkable increase of electron concentration was seen one day before. Rather high electron concentration remains in the ionosphere during the day of the event. Afterwards, the fast depletion of the electron density is observed. The right panel on Figure 3 shows the profilogram observed during the supercell event. One can see less pronounced changes in the electron concentration compared to the MCS event. However, some depletion of electron density can still be observed during the day of the event that remains till the following day. The gaps in the profilograms are caused by the presence of a sporadic E layer, that especially in 2008 event is rather strong and is blanketing the ionosphere above. In Figure 4, the detailed analysis of the variability of critical frequency of the F2 layer (foF2) and corresponding maximum height (hmF2) reveals for both cases a slight decrease in foF2 (blue line) corresponding to the depletion seen on profilograms. While on the course of hmF2 (red lines) slight uplift is seen during the day of event followed by decrease on the consecutive days.

Our study confirms the observation of the electron concentration depletion in the whole profile shortly after the occurrence of a MCS and local scale supercell thunderstorms. Gravity waves launched by such tropospheric systems may alter the process of ionization, recombination and transport process so that it may lead to the decrease of electron concentration. Similar effects related to the organised tropospheric convection were reported in studies [Barta et al., 2025; Koucká Knížová et al., 2024; Koucká Knížová et al., 2023].

The wave-like activity in the gravity wave spectrum is well seen on the occurrence of particular types of the echo (split and spread echo) on ionograms recorded by digisonde DPS 4D (not shown here). Such types of the echo are observed when the reflection planes Spread F echo, often associated with atmospheric wave activity, occurs on several consequent ionograms before sunrise of the following day.

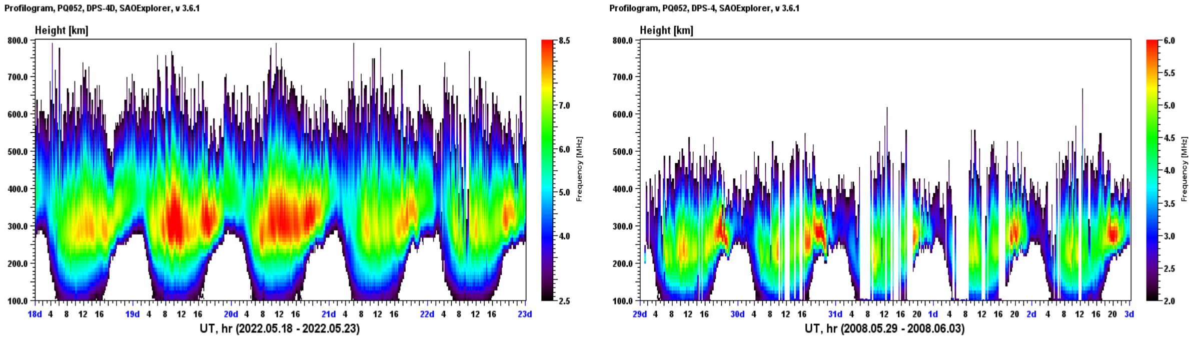

Figure 3. *Left panel: Profilogram from Průhonice observatory 18 - 22 May, 2022, displays variability of electron density profiles during five consecutive days covering day of MCS. Right panel: Same as the left panel for 29 May - 2 June, 2008 for the event of supercells.*

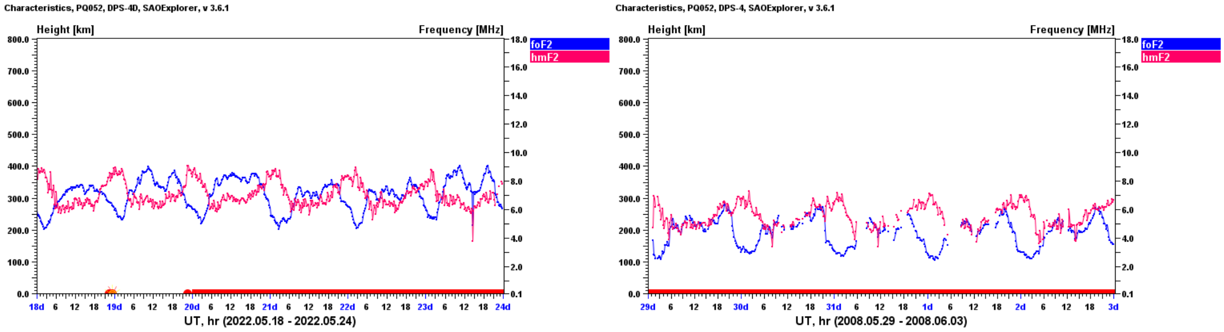

Figure 4. *Course of foF2 (blue line) and hmF2 (red line).*

4. Conclusion

This case study examined two meteorological events associated with severe convection. The first event was a MCS that developed ahead of a cold front. Based on records from meteorological surface stations and radar, this event was classified as a derecho, this event was classified as a derecho, confirming the mesosynoptic scale of the convection visible on satellite image. The second event was a severe air-mass (non-frontal) local-scale supercell thunderstorm. The vertical sounding measurement revealed similarity in the ionospheric response. The depletion of electron density was most pronounced feature. The uplift of the F2 layer maximum was registered shortly after the tropospheric situation occurrence close to sounding site. In both cases sporadic E was detected. In the derecho case, the sporadic E blanketed significantly the ionosphere above. Our preliminary results suggest that the effects of severe local-scale thunderstorms should not be overlooked in research on troposphere–ionosphere coupling.

Acknowledgment

The authors wish to acknowledge M. Setvák and P. Novák from the Czech Hydrometeorological Institute for providing data and consultations. Work has been supported by National Funding Agency No. 25-14158L Czech Science Foundation (GAČR), by HORIZON-CL4-2022-Space-01-62 T-FORS (number: 101081835), ESA project QUID-REGIS ESA Contract No. 4000143632/24/I-EB. and by the Johannes Amos Comenius Programme (OP JAC), project No. CZ.02.01.01/00/22_008/0004605, Natural and anthropogenic georisks.

References

Barta, V., Potužníková, K., Koucká Knížová, P.K., Chum, J., Mielich, J., Guerra, M., Burešová, D., Sivakandan, M., Verhulst, T.G.W., Berényi, K.A., Altadi, D., Segarra, A., Kouba, D., Mošna, Z., Buzás, A., Spogli, L., Urbár, J., de Paula, V., Ventriglia, V., Belehaki, A. (2025). Multi-instrument analysis of medium-scale travelling ionospheric disturbances generated by an intense tropospheric jet-front system with severe convection in Europe in August 2023, *Journal of Space Weather and Space Climate*, Vol. 15, 31.

Koucká Knížová, P.K., Georgieva, K., Mošna, Z., Kozubek, M., Kouba, D., Kirov, B., Potužníková, K., Boska, J. (2018). Solar signals detected within neutral atmospheric and ionospheric parameters, *Journal of Atmospheric and Solar-Terrestrial Physics*, Vol. 171, pp. 147–156.

Koucká Knížová, P.K., Potužníková, K., Podolska, K., Hannawald, P., Mošna, Z., Kouba, D., Chum, J., Wüst, S., Bittner, M., Kerum, J. (2023). Multi-instrumental observation of mesoscale tropospheric systems in July 2021 with a potential impact on ionospheric variability in mid-latitudes, *Frontiers in Astronomy and Space Sciences*, Vol. 10, 1197157.

Koucká Knížová, P.K., Potužníková, K., Podolska, K., Šindelářová, T., Bozóki, T., Pásztor, M.S., Szárnya, C., Mošna, Z., Kouba, D., Chum, J., Zacharov, P., Buzás, A., Hanzlíková, H., Kozubek, M., Burešová, D., Bozsó, I., Berényi, K.A., Barta, V. (2024). Impacts of storm "Zyprian" on middle and upper atmosphere observed from Central European stations, *Remote Sensing*, Vol. 16, 4338.

Laštovička, J. (2006). Forcing of the ionosphere by waves from below, *Journal of Atmospheric and Solar-Terrestrial Physics*, Vol. 68, pp. 479–497.

Novák, P. (2007). The Czech Hydrometeorological Institute's severe storm nowcasting system, *Atmospheric Research*, Vol. 83, pp. 450–457.

Setvák, M., Bedka, K., Sokol, A., Charvát, Z., Šťastka, J., Wang, P.K. (2013). A-train observations of deep convective storm tops, *Atmospheric Research*, Vol. 123, pp. 229–248.

Setvák, M., Lindsey, D.T., Novák, P., Wang, P.K., Radová, M., Kerkmann, J., Grasso, L., Su, S.-H., Rabin, R.M., Šťastka, J., Charvát, Z. (2010). Satellite-observed cold-ring-shaped features atop deep convective clouds, *Atmospheric Research*, Vol. 97, pp. 80–96.

Yigit, E., Koucká Knížová, P.K., Georgieva, K., Ward, W. (2016). A review of vertical coupling in the atmosphere–ionosphere system: Effects of waves, sudden stratospheric warmings, space weather, and of solar activity, *Journal of Atmospheric and Solar-Terrestrial Physics*, Vol. 141, pp. 1–12.

DOI: 10.31401/WS.2025.proc.17

Proceedings of
the Seventeenth Workshop “Solar Influences on the Magnetosphere, Ionosphere and Atmosphere”
June, 2025

Space Radiation Measurements during a Ship Round Trip from Varna, Bulgaria to Bulgarian Antarctic Base on Livingston Island

Dachev T.P.[1], Sapundjiev P.V.[2], Tomov B.T.[1], Matviichuk Y.N.[1], Mitev M.M.[1], Jordanova M.[1]

[1]Space Research and Technology Institute, Bulgarian Academy of Sciences, Sofia, Bulgaria
[2]National Institute of Geophysics, Geodesy and Geography, Bulgarian Academy of Sciences, Sofia, Bulgaria

Abstract

The spectrometer-dosimeter Liulin-AA performed radiation measurements during a round trip on board of the Bulgarian scientific research ship "St. St. Cyril and Methodius" from Varna, Bulgaria, to the Bulgarian Antarctic Base on Livingston Island. Different radiation and environment conditions were identified. The trip started with few days measurements in the Black Sea with an average dose rates of 0.0562-μGy h^{-1}, continued with recording of descending dose rates towards the magnetic equator while crossings in Atlantic Ocean and ended at the Bulgarian Antarctic Base on Livingston Island. Close to the magnetic equator on the back trip, the averaged dose is 0.0494-μGy h^{-1}. This is the smallest dose observed by Liulin-AA during the registrations performed in the Arctic and Antarctic regions in 2024 and 2025. The average detected doses on Livingston Island were considerably higher and reached 0.0806-μGy h^{-1}. They were measured during monitoring inside the Bulgarian base from 1st till 14th of February, 2025. The radiation doses measured on the way back from Livingstone Island to Varna were similar to those, already observed, during the first half of the round trip.

Keywords: Space radiation measurements; Liulin spectrometer-dosimeter

1. Introduction

Cosmic rays at sea level consist mostly of neutrons, protons, peons, muons, electrons, and photons. The particles, which cause significant soft fails in electronics, are those particles with the strong interaction: neutrons, protons, and peons. At sea level, about 95% of these particles are neutrons.

The level of exposure to cosmic radiation also increases with altitude since there is less air as altitude increases to act as a shield. Consequently, someone living at sea level will, on average, receive a lesser dose of cosmic radiation every year than an individual living in locations above 2,000 meters.

The earth's magnetic field is the main reason for the decrease in cosmic ray intensity at the equator. In the poles, the charged particles are travelling parallel to the direction of the magnetic field. Thus, they can travel to earth almost unhindered so the intensity is always maximum at the poles.

There were two expeditions with the Liulin-AA spectrometer in 2024. The First expedition was from Livingstone Island to Sofia, Bulgaria [Dachev et. al., 2024a]. The Second one from Sofia, Bulgaria to Longyearbyen town, Norway and back [Dachev et. al., 2024b].

This paper presents the analysis of the data obtained in 2025 during the third expedition with Liulin-AA. This is a round trip by ship from Varna, Bulgaria to Bulgarian Antarctic Base on Livingston Island.

2. Liulin-AA description

The design of the portable dosimeter-spectrometer Liulin-AA is not a new one. Since 1989, Space Research and Technology Institute (SRTI-BAS), in an international cooperation with scientists from Russia, Germany, Japan, Czech Republic, Italy, Norway, Switzerland, Belgium, USA and India, etc., worked at mountain peaks, flew in space and on stratospheric balloons, rockets and aircraft with more than 35 similar devices [Dachev 2009; Dachev et al, 2015, 2017, Dachev, 2021, http://www.space.bas.bg/SollarTerrestialPhysics/files/Poster-IKIT-BAN-2019%20SZF.pdf].

The last remarkable use of Liulin device in space are: the measurements outside the Japanese experimental module of International Space Station in September-October 2022 and the space radiation data during the first-ever commercial mission into suborbital space with the SpaceShipTwo spacecraft of Virgin Galactic Company (Virgin Galactic launches first commercial spaceflight (spacedaily.com)). This flight took place on 29th of June 2023 at 08:00 a.m. MT or 03:00 p.m. GMT from Spaceport America in New Mexico, USA. The preliminary results for the altitudinal profile obtained during the flight were published by Dachev et al, [2024c].

Liulin-AA spectrometer (Fig. 1) contains one silicon-PIN diode of Hamamatsu S2744-08 type (2 cm^2 area and 0.3 mm thickness), one ultra-low noise charge-sensitive preamplifier of AMPTEK A225F type and 2 microcontrollers.

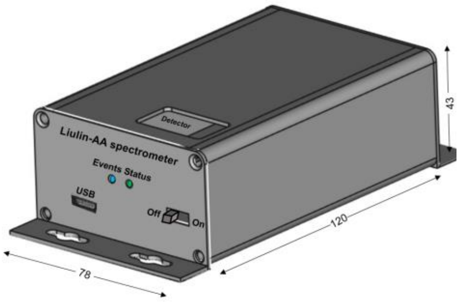

Figure 1. *Draft of Liulin-AA spectrometer.*

The doses (deposited energies in the detector) are determined by a pulse height analysis technique and then passed to a discriminator. According to AMPTEK A225 specifications, the pulse amplitudes A [V] are proportional by a factor of 240 mV/MeV to the energy loss in the detector and respectively to the dose. This is the key feature of the AMPTEK A225 preamplifier, which directly transfers the pulse amplitude, measured in volts by the spectrometer to dose and dose rate.

The amplitudes of all signals from the incoming particles and quanta are transformed into digital signals by an ADC converter and are sorted into 256 channels by a multichannel analyzer. For every exposure interval, a single 256 energy deposited spectrum (EDS) is collected.

Two microcontrollers, through specially developed firmware, manage the unit. The Liulin-AA communicates with a personal computer (PC) by a universal serial bus (USB) signal.

The following method for calculations of the dose is used [Dachev et al., 2002]: The dose D [Gy] by definition is one Joule deposited in 1kg of a mater or:

$$D = K.Sum(EL_I{*}i)_{ET}/MD, \qquad (1)$$

where MD is the mass of the detector in [kg] and EL_i is the energy loss in Joules in channel i. Energy loss in channel i is proportional to the number of events A_i in it multiplied by i. K is a coefficient.

During the construction of the Liulin-AA instrument measures have been taken to reduce the microphone effect at the detector. As a result, it can be seen that when transporting by water, land and air under general conditions, shock and jolt disturbances are not registered anywhere. A new power supply circuit for the detector [Tomchev et al., 2023] has been constructed and used. As a result, the electromagnetic interference and noises were reduced. The device has been calibrated by applying a new methodology [Mitev et al., 2023], which leads to an increase in the accuracy and convergence of the registered data.

3. Experimental Results

Figure 2. *“St. St. Cyril and Methodius” ship, performed the round trip from Varna to the Bulgarian Antarctic Base.*

The Bulgarian naval research vessel “St. Cyril and Methodius” (Fig. 2.) set sail on November 7, 2024 from Varna Marine Station on its third polar expedition to Antarctica. The crew consists of 34 people. Radko Muevski is the captain. It reached the Bulgarian Antarctic base on December 30, 2025, stay there for 45 days, set sail for the return voyage on February 15, 2025, and arrive back in Varna on 11 April 2025.

3.1.Results from the trip from Varna, Bulgaria to Bulgarian Antarctic Base on Livingston Island

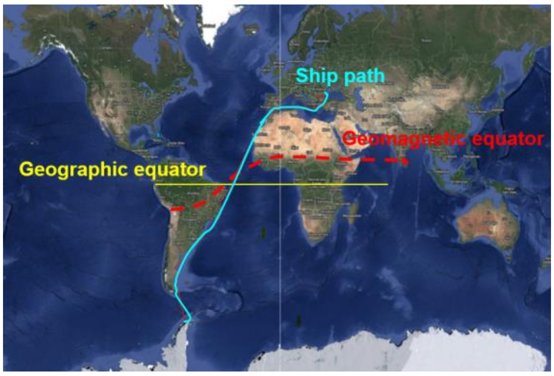

Figure 3. *Geographic map of the experiment.*

Fig. 3 presents the geographic map of the experiment. Three curves illustrate: (1) the ship path (magenta line) as monitored by the GPS receiver. The return path is not presented, as it was almost the same as the first route. (2) The geographic equator is shown with yellow line, while the (3) geomagnetic equator with a red line. It is seen that the ship first crosses the geomagnetic equator and next the geographic one.

Fig. 4 presents the results obtained during the trip from Varna to Antarctica in two panels.

The upper panel (4a) presents the measured dose rate between 24 October 10:30 UT and 30 December 11:45 UT, while the lower panel illustrates the geographic latitude of the ship, obtained by the GPS logger next to the Liulin-AA instrument. The dose rates measured by 5-minute resolution are marked with black points, while the daily averaged dose rates with red points, connected with a heavy black line. The average dose rate at the surface of the Atlantic Ocean is 0.05 μGy h^{-1}, which is 22 times less (1.1 μGy h^{-1}) than at 12 km altitude during aircraft flight.

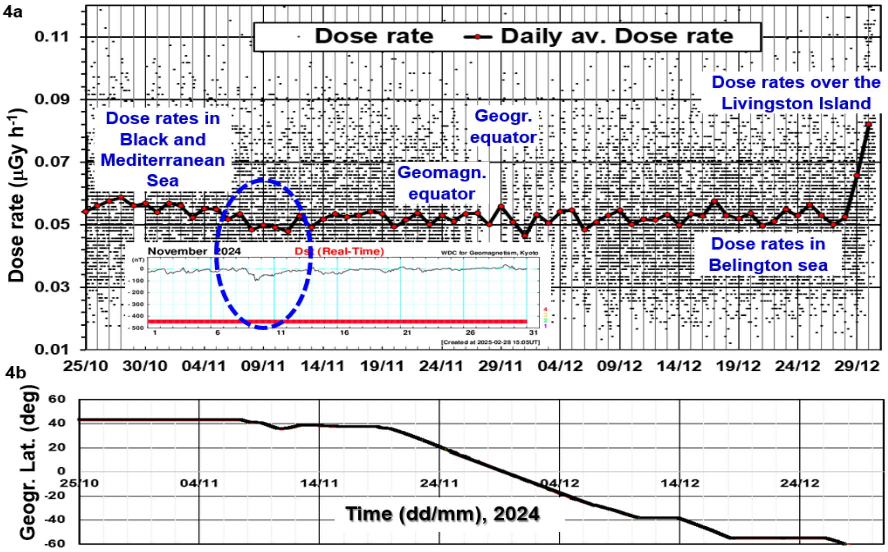

Figure 4. *Measured dose rates during the trip from Varna to Livingston Island.*

During the first part of the trip, close to 40° Northern latitude, inside Black and Mediterranean seas is observed tendency for higher dose rates. Similar tendency is seen in Belington Sea before the Livingstone Island. On the back trip, the higher doses inside the Black and Mediterranean seas is observed again. The explanation of this effect is the smaller depth, allowing Gamma radiation from the bottom to penetrate up to the sea level.

The dose rates drastically increase when the Liulin-AA instrument reaches the shore of the Livingston Island. Similar effects are observed on the back trip over the Livingston and Varna shores. The increase is explained with the absence of the shielding by the seawater. The natural Gamma radiation from the shore rocks and Radon component from the air and cosmic radiation are detected by the Liulin-AA instrument and increase the radiation level up to about 0.1 µGy h^{-1}, which is the level of the natural radiation.

The Forbush effect (Forbush, 1937) from a small magnetic storm on 9th of November 2024 decreases the dose rates. It is shown that the decrease of the dose rate, centered on 9th of November, coincides with the Disturbance Storm-Time Indices (Dst) index (Maus, and Weidelt, 2004) decrease registered on the Dst indices graphic for November 2024 (https://wdc.kugi.kyoto-u.ac.jp/dst_realtime/202411/index.html).

Results from the trip from Bulgarian Antarctic Base on Livingston Island to Varna, Bulgaria

Fig. 5, in a similar way as Fig. 4, presents the measured dose rates on the way back from Bulgarian Antarctic base on Livingston Island to Varna. Close to the magnetic equator, the averaged dose is 0.0494-µGy h^{-1}. This is the smallest dose observed by Liulin-AA during the registrations performed in the Arctic and Antarctic regions in 2024 and 2025.

3.2.Dose rate variations during a snowmobile trip on 1st of February 2025 and continues monitoring inside the Bulgarian base between 1st and 14th of February 2025

Fig 6. Presents the results of the measured spectra and dose rates during a snowmobile trip on the morning of 1st of February 2025 and the continues monitoring inside the Bulgarian base between 1st and 14th of February 2025.

Fig. 6a contains the energy-time (ET) graph showing vertically situated the color-coded 300-second spectra from 1st to 128th channels. The major amount of counts is produced by gamma rays in low energy deposited in the first five channels. The single counts up to 112th channels are produced by galactic cosmic rays primary and secondary particles as protons and muons.

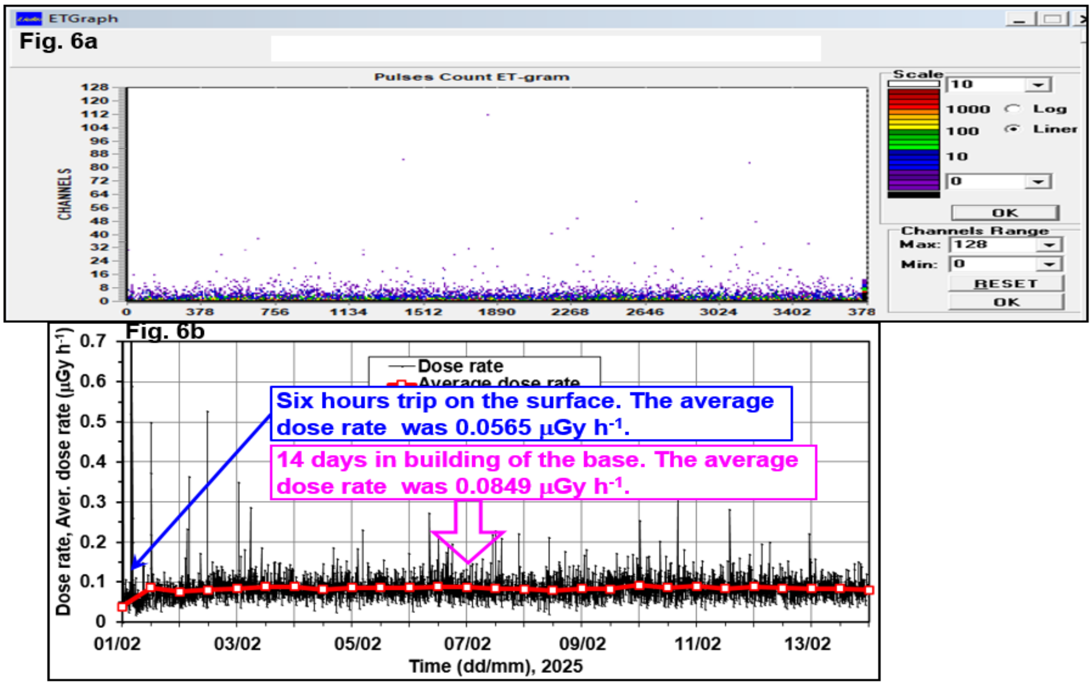

Scale: 10, 0 ○ Log ● Liner

Channels Range
Max: 128
Min: 0

Six hours trip on the surface. The average dose rate was 0.0565 µGy h⁻¹.

14 days in building of the base. The average dose rate was 0.0849 µGy h⁻¹.

***Figure 6**. Results of the measured spectra and dose rates between first and fourteenth of February 2025.*

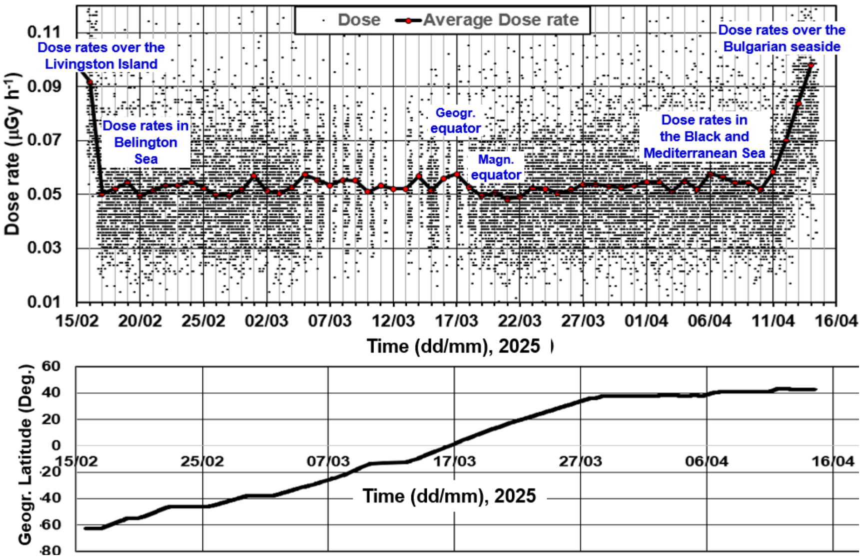

Dose rates over the Livingston Island

Dose rates in Belington Sea

Geogr. equator

Magn. equator

Dose rates in the Black and Mediterranean Sea

Dose rates over the Bulgarian seaside

***Figure 5.** Measured dose rates during the trip from Livingston Iceland to Varna.*

Fig 6b shows the variations of the measure dose rate. Because of the smaller amount of gamma rays on the open air, the average dose rate during the 6-hour snowmobile trip on the 1st of February 2025 is 0.0565-μGy h^{-1}. The average dose rate inside the building of the Antarctic base is 0.0849-μGy h^{-1}.

Conclusions

Liulin-AA measurements on ship during the round trip from Varna to Antarctica of 0.0527 μGy h^{-1} and back of 0.0528 mGy h-1 coincide with our measurements in 2024 of 0.0565 μGy h^{-1} (Dachev T. P., Sapundjiev et. al. (2024a). They are also in good correspondence the measurements performed in the Antarctic region at the surface of the sea with a portable Gamma Scout Online radiometer. The latter obtained an average dose rate of 0.0548 μGy h^{-1} (Długosz-Lisiecka et al. 2019, https://doi.org/10.18778/1427-9711.20.01).

During the six hours trip on the surface of Livingstone Island with a snowmobile the average dose rate was 0.0565 μGy h^{-1}. This small dose rate value is similar with the observed during all trips with car and bus in 2024 and 2025.

The measured average dose rate for 14 days inside the building of the Bulgarian base of 0.0849 μGy h-1 well coincides with value of 0.087, measured in February 2024 and with the measurements inside the Argentine Antarctica base in Marambio of 0.080 μGy h^{-1} with Liulin-I MDU-1 LET Spectrometer (Zanini et al. 2017, http://dx.doi.org/10.1016/j.jenvrad.2017.04.011).

As expected the Forbush effect from the small magnetic storm on 9 November 2024 decreases almost twice the dose rates.

Acknowledgements

The authors thank to all Bulgarian and foreign specialists and organizations that participated in the development of Liulin instruments.

Peter Sapundjiev is very thankful to Project/Contract No 70-25-94 from 28.04.2023, supported by National Program for Polar Studies "From Pole to Pole" 2022 – 2025.

IKIT-Antarkticheski Scientists from Bulgarian Academy of Sciences

The space radiation measurements during the round trip by from Varna, Bulgaria to Bulgarian Antarctic Base on Livingston Island was performed as part of the Memorandum of Understanding between Space Research and Technology Institute, Bulgarian Academy fo Sciences and the Bulgarian Antarctic Institute from 2024.

References

Dachev, T.P., Sapundjiev, et al. (2024a). Dose rate and flux measurements during a travel from Bulgarian Antarctic Base on Livingston Island to Sofia, Bulgaria, *Proceedings of the Seventeenth Workshop "Solar Influences on the Magnetosphere, Ionosphere and Atmosphere"*, Primorsko, Bulgaria, June, pp. 75–83, 2024. Available at: https://www.spaceclimate.bas.bg/ws-sozopol/pdf/Proceedings2024.pdf

Dachev, T.P., Sapundjiev, et al. (2024b). LIULIN-AA spectrometer measurements of the radiation dose during the travel from Bulgarian Antarctic Base on Livingston Island to Longyearbyen town, Svalbard Archipelago, Norway and back to Sofia, *Proceedings of the Seventeenth International Scientific Conference "Space, Ecology, Safety" – SES 2024*, Sofia, Bulgaria, 22–25 October 2024, pp. 33–42.

Dachev, T.P., Carlucci, et al. (2025). Space radiation measured during first-ever commercial suborbital mission on Virgin Galactic SpaceShipTwo Unity on 29 June 2023, *Life Sciences in Space Research*, Vol. 44, pp. 126–133, DOI: 10.1016/j.lssr.2024.09.003.

Forbush, S.E. (1937). On the effects in cosmic-ray intensity observed during the recent magnetic storm, *Physical Review*, Vol. 51, No. 12, p. 1108, DOI: 10.1103/PhysRev.51.1108.3.

Maus, S., Weidelt, P. (2004). Separating the magnetospheric disturbance magnetic field into external and transient internal contributions using a 1D conductivity model of the Earth, *Geophysical Research Letters*, Vol. 31, No. 12, DOI: 10.1029/2004GL020232.

Mitev, M., Tsankov, L., et al. (2023). Radiationless energy calibration of radiation survey meters, *Proceedings of the XXXII International Scientific Conference “Electronics (ET)”*, Sozopol, Bulgaria, 2023, pp. 1–4, DOI: 10.1109/ET59121.2023.10279419.

Tobiska, K., Dachev, T., et al. (2024a). Radiation field outside the ISS observed by ARMAS Flight Module 9, March–December 2022, *Proceedings of the Twenty-Seventh WRMISS Workshop*, Boulder, CO, USA, 3–5 September 2024. Available at: https://wrmiss.org/workshops/twentyseventh/Tobiska.pdf

Tobiska, K., Dachev, et al. (2024b). International Space Station radiation field measurements by Liulin-SET spectrometer of ARMAS Flight Module 9 in 2022, *Proceedings of the Twentieth International Scientific Conference “Space, Ecology, Safety” – SES 2024*, Sofia, Bulgaria, 22–25 October 2024, pp. 16–22. Available at: http://www.space.bas.bg/SES/archive/SES%202024_DOKLADI/Plenary%20Session/2_Dachev.pdf

Tomchev, N., Mitev, et al. (2023). Novel linear step-up power supply module for detector systems, *Proceedings of the 32nd International Scientific Conference “Electronics (ET)”*, Institute of Electrical and Electronics Engineers Inc., ISBN: 979-835030200-4, DOI: 10.1109/ET59121.2023.10279817.

DOI: 10.31401/WS.2025.proc.18

Proceedings of
the Seventeenth Workshop "Solar Influences on the Magnetosphere, Ionosphere and Atmosphere"
June, 2025

Space Weather Influences on Satellite Anomalies

Kirov B., Georgieva K., Asenovski S.

Space Research and Technology Institute, Bulgarian Academy of Sciences, Bl.3 Acad. G. Bonchev str. 1113 Sofia, Bulgaria
bkirov@space.bas.bg

Abstract

Space weather drives on-orbit anomalies through multiple, orbit-dependent pathways. In low Earth orbit (LEO), enhanced thermospheric drag during storms, nighttime auroral charging, and galactic-cosmic-ray (GCR) single-event effects (SEE) are prominent. In geostationary orbit (GEO), surface and deep-dielectric charging—often amplified on the nightside during substorm injections—remain leading root causes. Using consolidated anomaly catalogs (Seradata/SpaceTrak aggregates, GOES operator logs) and supplemental fleet counts from UCS snapshots, we quantify anomaly occurrence per satellite-year by orbit regime and examine dependences on magnetic local time (MLT), geomagnetic activity (daily Kpmax, GFZ/WDC), and solar-cycle phase (sunspot number v2.0). Normalization by exposure shows that the daily probability of anomaly rises sharply for $Kp \geq 5$, even though raw counts are larger under quiet conditions because quiet days dominate. The solar-cycle analysis reveals a pre-maximum enhancement consistent with outer-belt acceleration and cumulative MeV-electron fluence that governs internal charging, whereas a GCR-related SEE contribution in LEO partly anti-correlates with sunspot number. We synthesize these relationships into mitigation guidance: (i) design hardening (conductive/UV-stable surfaces and bonding, minimized floating dielectrics, rad-hard parts, current limiting, ECC/TMR with scrubbing); (ii) operational playbooks keyed to upstream solar-wind/SEP/electron monitors and geomagnetic indices; and (iii) calibrated forecasts/nowcasts and AE9/AP9/SPM-based specifications that map environment to anomaly likelihood by orbit and MLT. The framework provides actionable thresholds for fleet operations and transparent benchmarks for future anomaly reporting and model validation.

Keywords: Space weather; satellite anomalies; solar influences

1. Introduction

Space weather refers to the dynamic conditions in the near-Earth space environment, driven by solar activity and solar-terrestrial interactions. According to the U.S. National Space Weather Program, space weather is characterized by conditions in the solar wind, magnetosphere, ionosphere, and thermosphere affecting the performance and reliability of space-borne and ground-based technological systems (Seki et al., 2018). Its study is crucial due to its significant impact on satellite systems, potentially leading to operational anomalies, disruptions, or even loss of spacecraft]. Intense solar phenomena such as solar flares, coronal mass ejections, high-speed solar wind streams, and solar proton events, as well as persistent factors like cosmic rays and Earth's radiation belts, pose substantial risks to satellites in various orbits. Understanding these factors is critical for enhancing satellite resilience and ensuring the reliability of vital services provided by satellite infrastructure. This paper aims to provide an overview of the primary space weather factors responsible for satellite anomalies, explore the mechanisms behind these impacts, analyze the dependence of anomalies on orbital characteristics, and discuss mitigation strategies and forecasting capabilities.

2. Space Weather –Primary Factors

Space weather encompasses phenomena stemming from the Sun and the space environment, such as solar flares, coronal mass ejections (CMEs), high-speed solar wind streams (HSS), solar proton events (SPE), cosmic rays, and radiation belts (Seki et al., 2018; Kamide, 2013).

Solar flares. These sudden and intense bursts of X-ray and ultraviolet (UV) radiation from the Sun, accompanied by energetic particle emissions, significantly affect near-Earth space, causing ionospheric disturbances and enhancing high-energy proton fluxes. The ionospheric disturbances directly influence communication and navigation (Harrison et al., 2017) 9Phillips et al., 2016). A comprehensive understanding of solar flares is essential for predicting their potential impacts on communication and power grid systems.

Coronal mass ejections (CME). These massive eruptions of plasma and embedded magnetic fields from the Sun's corona, upon interacting with Earth's magnetosphere, can induce severe geomagnetic storms. These storms dramatically alter the radiation belts and magnetospheric environment, creating hazardous conditions such as induced currents and elevated particle fluxes, detrimental to satellite operations (Harrison et al., 2017).

High-speed solar wind streams (HSS). Originating from coronal holes on the solar surface, these streams, although weaker than typical CMEs, can cause prolonged, moderate geomagnetic disturbances (Harrison et al., 2017). HSS-induced substorms and increased fluxes of energetic particles lead to charge accumulation on satellite surfaces, increasing the risk of electrostatic discharges (Seki et al., 2018).

Solar proton events (SPE). High-energy proton and ion bursts accelerated by large solar eruptions or CME-driven shock waves arrive at Earth within hours. These particles can pose risks to astronauts in space and can disrupt satellite electronics, primarily through radiation damage (Crowley et al., 2010; Robinson, 2012).. SPEs significantly heighten the risk of electrical discharges and electronic component failures

Cosmic rays. Originating from beyond the Solar System, these highly energetic particles continuously bombard Earth's orbit. Despite fluctuations with the 11-year solar cycle, cosmic rays significantly contribute to single-event upsets (SEU) in satellite electronics, particularly during solar minima.

Radiation belts. Earth's Van Allen radiation belts trap high-energy electrons and protons, which intensify during solar storms. These belts pose continuous risks, especially for satellites in medium Earth orbits (MEO) and geostationary Earth orbits (GEO), due to cumulative radiation damage and frequent anomalies resulting from persistent exposure (Kamide, 2013; Harrison et al., 2017).

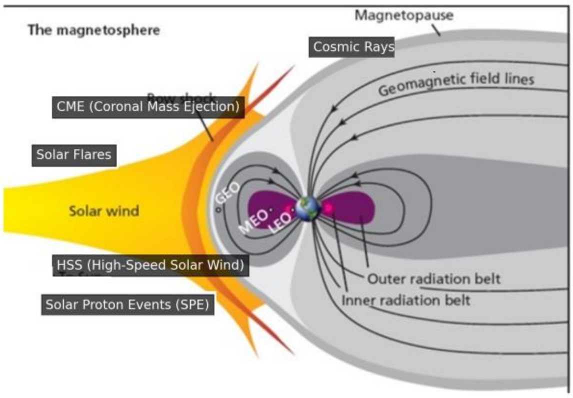

Figure 1. *Schematic of the Earth’s magnetosphere, with several regions labeled wheresatellite anomalies often occur, including the Van Allen Radiation Belts (Inner andOuter), and typical satellite orbits (GEO, MEO, and LEO) and space weather factors. Courtesy of RAND Corporation,* *www.RAND.org*.

Regime	Description	Typical hazard
Absolute charging	The whole spacecraft floats to a nearly uniform potential (±kV). Sudden environmental changes (e.g., eclipse exit) drive large potential shifts and spark *global* electrostatic discharges (ESD).	Arcing on solar-array strings, loss of star-tracker sensitivity, momentary bus resets.
Differential charging	Local material properties and view-factors create patchy potentials ($\Delta V \approx$ kV over cm). Strong local E-fields trigger *micro-arcs*.	Pitting of thermal blankets, antenna feed damage, sensor drop-outs.

Regime	Dominant hazards	Secondary
LEO	Drag surges; auroral surface charging; SAA-driven TID/SEEs	SEP-driven SEEs; atomic oxygen erosion
MEO	Trapped-proton TID; MeV-electron internal charging; SEEs	SEP-driven SEEs; eclipse SRP modeling errors (service impacts)
GEO	MeV-electron internal & surface charging; deep dielectric discharges	SEP-driven SEEs; cumulative dose

3. Mechanisms of Space-Weather–Driven Satellite Anomalies

Space-weather disturbances couple into spacecraft through several well-characterised physical pathways. The subsections below summarise the dominant mechanisms and illustrate how each can provoke functional anomalies or outright mission loss.

3.1 Surface Charging

Energetic electrons (～1 eV – 30 keV) and low-energy ions in the magnetospheric plasma current to exposed spacecraft surfaces. Two regimes are distinguished:

GEO platforms are particularly vulnerable during eclipse season when the ambient electron density collapses and stored charge can suddenly discharge (Minow et al., 2024).

3.2 Deep-Dielectric (Internal) Charging

Mega-electron-volt electrons penetrate external metal and accumulate in dielectric layers (cable insulation, PCB substrates). Charge builds until the internal electric field exceeds the breakdown strength (～200–400 kV cm^{-1}), producing a punch-through discharge that often destroys power-converter transformers, gate arrays or telemetry buses. Failures frequently cluster near equinox when GEO electron fluxes peak and when spacecraft enter/exit eclipse, rapidly altering internal temperature and resistance (Horne et al., 2025).

3.3 Single-Event Effects (SEE) in Micro-electronics

A single energetic ion, proton, or heavy GCR nucleus traversing a sensitive volume causes localised ionisation:

- Single-Event Upset (SEU) – soft-error bit flips in memory or logic.
- Latch-up (SEL) – parasitic thyristor conduction path triggers over-current and thermal runaway.
- Single-Event Burn-out/ Gate-Rupture (SEB/SEGR) – catastrophic failure of power MOSFETs and GaN HEMTs.

SEE rates scale with the integral >10 MeV proton flux for LEO and with GCR flux modulated by the heliospheric cycle for GEO. Fault-tolerant design tactics include triple-modular redundancy, error-correcting memory, periodic configuration scrubbing in FPGAs, and current-limiting circuitry (Jun et al., 2024).

3.4 Enhanced Atmospheric Drag (LEO)

During strong geomagnetic storms Joule heating and particle precipitation expand the thermosphere, increasing neutral density at 200–600 km by factors of 2–10. The resulting drag torque can:

- Decrease orbital altitude and lifespan.
- Perturb attitudes on 3-axis–stabilised microsats that lack momentum margin.
- Compromise planned phasing of constellation planes.

The loss of ~40 Starlink satellites launched on 3 February 2022—during only a moderate storm (Dst ≈ –80 nT)—is the canonical recent example (Ahmad et al., 2025).

3.5 Service-Level Impacts on Communications and Navigation

Although not always recorded as spacecraft “anomalies,” disturbed upper-atmosphere and solar radio conditions degrade space-based services:

- GNSS positioning errors (L-band code-phase scintillation, cycle slips, and TEC gradients) rise by an order of magnitude during post-sunset equatorial plasma bubbles and auroral substorms (Gómez Socola et al., 2025; Tahir et al., 2024).
- Tele-com links suffer carrier-to-noise degradations when solar radio bursts (Type II/IV) coincide with Earth-pointing ground-station geometry.

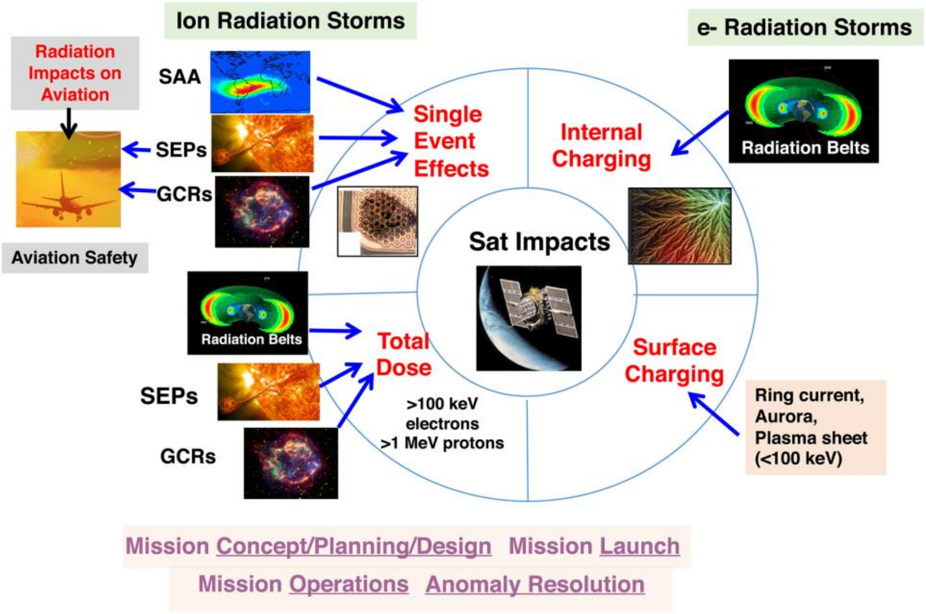

Figure 2. *Space Radiation and Plasma Effects on Satellites and Aviation (Yihua Zheng et al. 2019).*

4. Orbit Dependence

Space-weather impacts vary systematically with orbital regime and inclination because the ambient plasma, radiation, and neutral density fields change with L-shell, magnetic latitude, and local time.

4.1 Orbit type (altitude)

LEO spacecraft are most exposed to thermospheric drag enhancements during storms (Section **3**.4) and to auroral-region surface charging on high-latitude passes. Charging events >100 V negative are routinely observed during auroral crossings and correlate with geomagnetic activity. Single-event effects (SEEs) in LEO spike during SEP events; exposure is strongly inclination dependent (see §4.2). South Atlantic Anomaly (SAA) passages add trapped-proton dose and SEE risk.

MEO (GNSS ltitudes, L≈3–6). MEO platforms traverse the heart of the radiation belts and see persistent trapped protons (inner belt) and MeV electrons (outer belt), leading to higher cumulative dose and frequent SEEs relative to LEO. Dedicated monitors on Beidou/GNSS MEO spacecraft report in-situ SEUs that track the local LET/proton environment, underscoring the operational SEE hazard for navigation constellations. Extreme events can measurably degrade power subsystems and increase anomaly likelihood.

GEO (~35,786km). GEO sits on the outer-belt periphery and is continuously subject to keV–MeV electron storms; internal dielectric charging and surface charging dominate anomaly statistics. Multiple studies show strong correlations between GEO anomalies and enhancements of E>2 MeV electron fluence; classic analyses identified internal-charging signatures with 2-day fluence metrics.

Summary (by dominant risks).

Recent cross-regime statistics (2010–2022) confirm that GEO anomaly occurrence is most sensitive to relativistic-electron activity, whereas LEO anomalies align more with geomagnetic indices and local particle enhancements; MEO anomalies are tightly linked to persistent belt populations.

4.2 Inclination (magnetic latitude exposure)

Polar/high-inclination LEO. Frequent transits of the auroral oval expose spacecraft to precipitating electrons/ions and strong field-aligned currents, increasing surface-charging events and ESD risk; charging levels and anomaly counts rise with geomagnetic activity.

Equatorial/low-inclination LEO. Reduced auroral exposure but regular SAA crossings yield higher trapped-proton dose and SEEs concentrated along the SAA track.

Inclined MEO (GNSS). Typical GNSS inclinations (~55°) sweep broad magnetic latitudes, sampling both inner-belt protons and outer-belt electrons; on-board monitors show SEU occurrences that co-vary with local LET/proton spectra and storm-time electron enhancements.

GEO (near-equatorial inclination). Even with small inclinations, GEO local-time geometry matters: near-midnight to dawn sectors and eclipse seasons coincide with enhanced surface/internal charging and higher anomaly likelihood due to cold-plasma depletion and rapid environmental transitions.

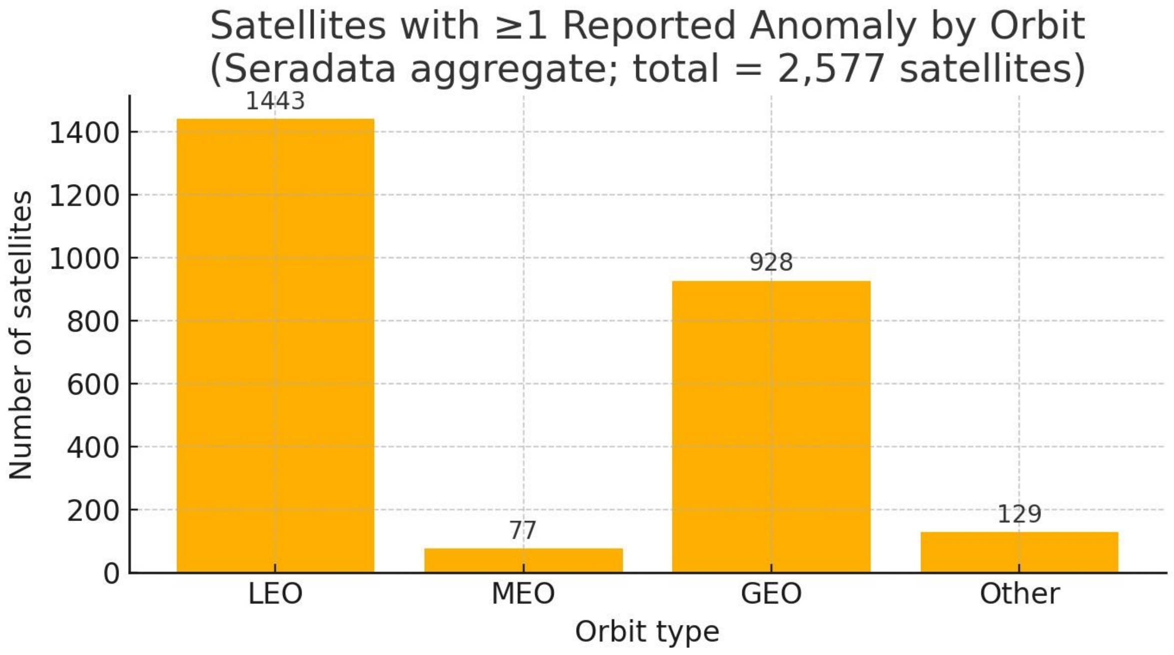

Figure 3. *Number of spacecraft with ≥1 reported on-orbit anomaly by orbit regime. Totals: LEO = 1,443, GEO = 928, MEO = 77, Other/HEO = 129 (N = 2,577). Percentages are 56%, 36%, 3%, and 5%, respectively. "Other" groups highly elliptical, transfer, and miscellaneous non-LEO/MEO/GEO orbits. Counts are per* ***spacecraft*** *(whether single or multiple events), not per* ***event****. Source: Seradata/SpaceTrak anomaly database, aggregated as in Buitrago-Leiva et al. (2024).*

It seems that MEO orbits are much more reliable than others, but this is not the case. There are several reasons why there are far fewer anomalies in databases with satellites flying on MEOs than those in other orbits.

Population effect (denominator). The global MEO fleet is tiny compared with LEO (thousands) and smaller than GEO (hundreds). Even with similar per-satellite risk, the absolute count of MEO spacecraft with ≥1 recorded anomaly will be much lower.

Reporting bias. Most MEO spacecraft are GNSS (GPS, GLONASS, Galileo, BeiDou). Their operators (often military/state) publish fewer on-orbit anomaly details. Well-known GNSS "events" (e.g., Galileo 2019, GLONASS 2014) were largely ground-segment or service issues and typically aren't logged as spacecraft anomalies in public databases.

Hardening and autonomy. GNSS platforms are built conservatively: rad-hard parts, TMR/ECC, periodic scrubbing, tight current limiting, and robust FDIR. Many radiation-induced upsets get corrected onboard and never escalate to a recorded "anomaly."

Environment vs outcome. MEO sits in a tough radiation environment (inner-belt protons + outer-belt electrons), but the design margins and operational practices keep many effects below the threshold of "reportable anomaly." So the true event rate (e.g., SEUs) can be non-trivial, while the anomaly count that reaches public logs stays small.

5. Dependence on Local Time and Geomagnetic Activity

5.1 Local time (day/night geometry and MLT sector)

GEO eclipse seasons and day–night transitions. Near the equinoxes, geostationary satellites enter Earth's shadow around local midnight. Eclipse exit brings rapid illumination changes and steep photoelectron/current gradients across surfaces and harnesses, which promote differential charging and ESD. GEO surface-charging anomalies show a marked night–pre-dawn preference (~21–06 MLT), consistent with substorm-driven injections on the nightside [Ferguson et al., 2011; Matéo-Vélez et al., 2018; Horne et al., 2013]. Clustering of anomalies around eclipse seasons has been reported in GEO anomaly catalogs [Iucci et al., 2005; Choi et al., 2011].

Substorms and nightside GEO. Many GEO anomalies concentrate on the nightside when injections of 10–100 keV electrons from the magnetotail are most frequent. Statistical studies link the local-time dependence (night-sector maxima) to these injections rather than to sunspot number [Iucci et al., 2005; Choi et al., 2011].

LEO auroral crossings (polar orbits). In LEO, large negative surface potentials and ESD risk arise predominantly during nighttime auroral traversals, where precipitating keV electrons and low photoemission drive negative charging (>100 V). Long-term DMSP statistics show thousands of such charging events with strong local-time/auroral dependence and enhanced occurrence during substorms and at lower solar activity [Anderson, 2012]. Event-based diagnosis of LEO anomalies also finds that many cases coincide with enhanced 30–100 keV electron fluxes and magnetic perturbations near the anomaly time [Ahmad et al., 2018].

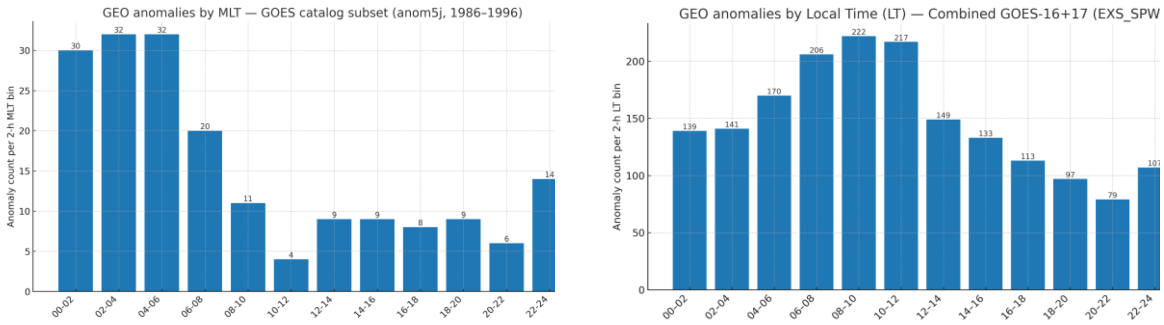

Figure 4. *GEO anomalies by Magnetic Local Time (MLT). (a) Catalog-based GEO anomalies from the legacy GOES subset (anom5j, 1986–1996): nightside/pre-dawn maximum consistent with charging/substorm injections. (b) GOES-16/17 EXIS SpaceWire (EXS_SPW) event set: instrument-specific dayside enhancement; not representative of canonical GEO charging statistics. Sources: (a) NOAA/NCEI legacy 'anom5j' GOES table; (b) GOES-16/17 EXS_SPW engineering logs.*

5.2 Geomagnetic-activity dependence (by orbit)

GEO. The strongest statistical link is with relativistic/MeV electrons that charge internal dielectrics (deep dielectric charging). GEO anomalies correlate with the integrated >2 MeV electron fluence over the preceding ~1–2 days, not with sunspot number; the relationship strengthens during storm/substorm activity and near the equinoxes [Wrenn, 1995; Choi et al., 2011; Meredith et al., 2015; Minow et al., 2024].

LEO. Anomaly occurrence increases with auroral electron precipitation and geomagnetic disturbance (e.g., elevated AE/Kp), with a pronounced nightside dependence and frequent proximity to substorms. During solar minima, GCR-related SEE can also be relatively elevated, contributing to logic upsets even under low Kp conditions [Anderson, 2012; Ahmad et al., 2018; Iucci et al., 2005].

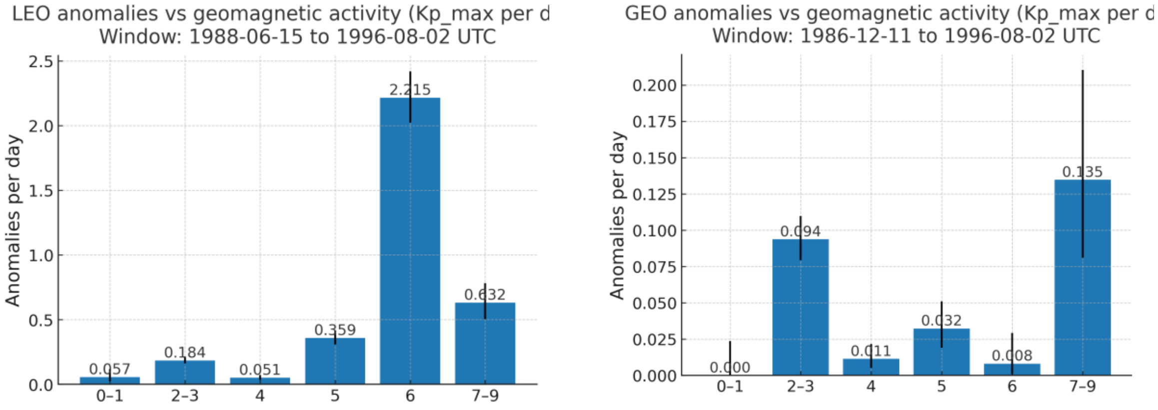

Figure 5. *Anomaly rate vs geomagnetic activity (daily Kp_max). (a) LEO anomalies (ALT ≤ 2000 km), 1988-06-15 to 1996-08-02 UTC. (b) GEO anomalies (GOES legacy list), 1986-12-11 to 1996-08-02 UTC. Bars show anomalies per day by Kp bin (0–1, 2–3, 4, 5, 6, 7–9) with 95% Poisson confidence intervals (Byar). Data sources: Daily Kp_max — GFZ/WDC (Matzka et al., 2021; doi:10.5880/Kp.0001). Anomaly catalogs — LEO from anom5j.xlsm (ALT ≤ 2000 km), GEO from GoesAnomalyTrends.xlsm.*

MEO (GNSS). MEO satellites traverse the heart of the belts; while the environment is severe, platform hardening and operations often suppress reportable anomalies. Where on-board monitors are available (e.g., BeiDou), SEE activity and LET spectra track radiation conditions, while relativistic-electron fluxes at GPS-type L-shells peak during enhanced geomagnetic activity [Meredith et al., 2016; Zhang et al., 2023; Ye et al., 2021]. Consequently, MEO anomaly rates may show mixed dependence: internal-charging/SEE components strengthening with geomagnetic disturbances and GCR-driven SEE showing anti-correlation with solar activity.

6. Dependence on solar-cycle phase (sunspot number)

Solar-cycle modulation of satellite anomalies arises from how solar activity controls the drivers of the near-Earth radiation environment. During active phases, coronal mass ejections (CMEs) and high-speed streams (HSS) trigger geomagnetic storms and substorms. These, in turn, heat and expand the thermosphere (raising LEO drag), inject and accelerate keV–MeV electrons (enhancing surface charging in LEO/GEO and deep-dielectric charging at GEO), and elevate solar energetic proton (SEP) fluxes that increase single-event effects (SEE). Hence, higher sunspot number (SSN) generally implies a higher likelihood of anomalies through these pathways—though the response is orbit-dependent and not strictly proportional to SSN [Wrenn et al., 2002; Meredith et al., 2015; Baker et al., 2018].

Crucially, the geoeffective particle environment does not peak exactly with SSN. At GEO, anomaly statistics correlate best with the integrated fluence of >2 MeV electrons over the prior 1–2 days—a quantity that often maximizes in the rising and declining phases when chorus-driven acceleration and storm-time injections are strongest, rather than at SSN peak [Wrenn et al., 2002; Meredith et al., 2015; Baker et al., 2018]. In LEO, nightside auroral charging and substorm activity can be frequent under modest to strong driving, while GCR-driven SEE anti-correlates with SSN and becomes relatively more important toward solar minima [Buitrago-Leiva et al., 2024; Baker et al., 2018].

Figure ***6*** compares the annual anomaly rate per satellite-year for LEO and GEO with the annual SSN (SILSO v2.0). The curves reveal a pre-maximum enhancement in anomalies during Solar Cycle 24. This is consistent with intense storm sequences and equinoctial coupling in 2011–2012 that produced large seed and relativistic electron populations. Note also that Solar Cycle 24 exhibited a double maximum (～2012 and ～2014); the first peak is partially obscured by annual averaging/smoothing in the SSN curve, but the anomaly rate retains a clear rise on the early-maximum flank [Reeves et al., 2013; Wrenn et al., 2002; Meredith et al., 2015].

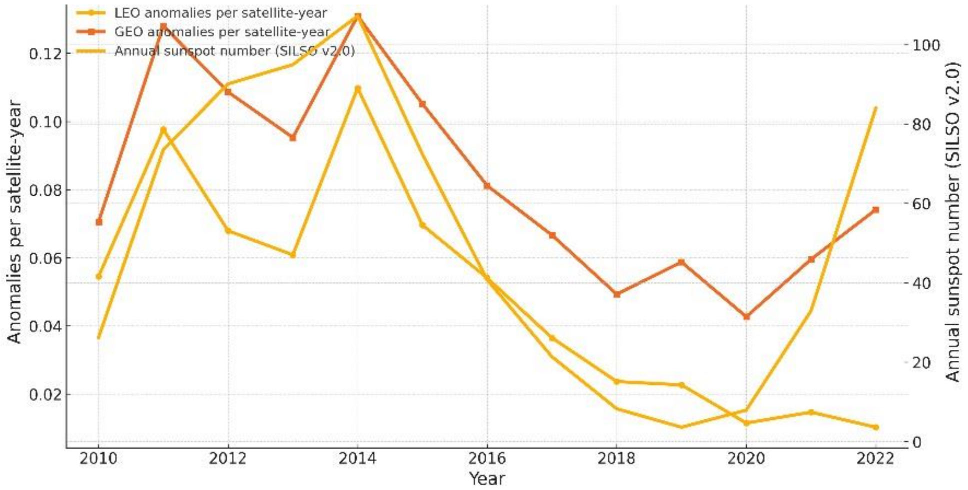

Figure 6. *LEO and GEO anomalies per satellite-year vs annual sunspot number (2010–2022). Anomaly rates (left axis) derive from the Seradata/SpaceTrak anomaly compilation aggregated in [Buitrago-Leiva et al., 2024] and normalized by annual fleet size (UCS Satellite Database, 2020–2023 snapshots, interpolated to 2010–2019). Sunspot number (right axis): WDC-SILSO v2.0 (DOI: 10.24414/qnza-ac80). Rates peak on the rising/declining flanks rather than at SSN maximum, reflecting storm-time seed/MeV electron enhancements (GEO internal charging) and mixed LEO contributions (auroral charging, SEP-related SEE, and GCR-related SEE). Cycle-dependent changes in CME and heliospheric pressures can modulate CME expansion and geoeffectiveness, providing additional context for anomaly peaks near solar maxima [Gopalswamy et al., 2024].*

7. Mitigation and Forecasting Strategies

7.1 Design hardening and materials (charging, radiation)

Design begins with making the environment non-catastrophic for the hardware. For surface and internal charging, best practice includes low-resistivity/UV-stable coatings, controlled ground paths and bonding, avoidance of isolated dielectrics, and placing sensitive harnesses behind conductive structure. For internal charging, designers allocate dielectric thickness, leakage paths, and shielding such that worst-case internal dose rates keep electric fields below breakdown margins; GEO is most demanding. Rad-hard parts, part derating, current-limiting and latch-up protection, ECC/TMR with periodic memory scrubbing, and watchdog/safe-hold logic reduce the probability that single-event effects escalate to anomalies [Minow et al., 2024; Matéo-Vélez et al., 2018; Wrenn, 1995; Wrenn et al., 2002; NASA-HDBK-4002B, 2022; NASA-STD-4005A, 2016; NASA-HDBK-4006A, 2024].

7.2 Fault management and operational playbooks

Operational risk can be cut substantially by conditioning the spacecraft state on upstream warnings and local monitors. Common measures include: pre-emptive safe-mode entry; powering down high-voltage or non-essential loads; biasing attitudes to reduce differential charging; delaying propulsion or sensitive payload operations; and raising error-correction/scrubbing cadence. Thresholds are typically tied to SEP and electron flux monitors (e.g., GOES), geomagnetic indices (Kp/AE), or solar-wind–derived coupling proxies; these actions are most effective when applied hours before the peak response [Choi et al., 2011; Iucci et al., 2005; Horne et al., 2021; Newell et al., 2007].

7.3 Environment specification and design margins

To dimension shielding and set charging/radiation margins, modern environment specifications rely on AE9/AP9/SPM for trapped particles with quantified uncertainties, replacing legacy AE8/AP8; internal-charging design should use fluence/flux percentiles from these models rather than climatological means. For LEO drag risk, thermospheric density models (e.g., NRLMSISE-00) and density climatologies inform conjunction with orbit-maintenance margins and power/thermal budgets [Ginet et al., 2013; Picone et al., 2002; Emmert, 2015].

7.4 Forecasting and nowcasting for operations

Short-lead alerts combine (i) solar-wind measurements at L1 (DSCOVR/ACE) with (ii) empirical/physics-based drivers of geomagnetic response (e.g., the Newell coupling function) to anticipate geomagnetic activity for GEO/LEO charging and MEO radiation risk. For relativistic electrons, skillful GEO nowcasts/forecasts feed into anomaly likelihood for internal charging; for LEO drag, atmospheric models driven by solar/EUV proxies are used for maneuver planning. Probabilistic forecasts with explicit uncertainty are increasingly recommended, and machine-learning methods are being fused with physics-based models to provide actionable risk metrics for operators [Horne et al., 2021; Newell et al., 2007; Emmert, 2015; Camporeale, 2019].

7.5 Fleet-level risk management

Large constellations benefit from statistically calibrated hazard-to-risk mappings: anomaly-per-satellite-day as a function of Kp/AE and local time, and orbit-class-specific thresholds for deep-dielectric charging and SEE. Rolling A/B tests (e.g., increased scrubbing or bias changes) during elevated activity quantify mitigation benefit. Combining design hardening, operational playbooks, and calibrated forecasts yields the largest reduction in anomaly rates at minimal cost [Hands et al., 2018; Horne et al., 2021]. Radiation-risk assessment that couples in-flight dosimetry with numerical transport is routinely used beyond Earth orbit and informs design/operations trade-offs [Krastev et al., 2024].

8. Conclusions

Space weather drives satellite anomalies through multiple, orbit-dependent pathways. In LEO, enhanced thermospheric drag during storms, nighttime auroral charging, and GCR-driven single-event effects (SEE) dominate. In GEO, deep-dielectric and surface charging—often amplified on the nightside during substorm injections—remain the leading root causes. MEO platforms reside in a severe radiation environment, yet public anomaly catalogs under-report spacecraft-level events relative to LEO/GEO because of hardening, autonomy, and reporting practices. Across the aggregated sample (N ≈ 2,577 spacecraft with ≥1 reported anomaly), the distribution by orbit class is strongly skewed toward LEO (≈56%) and GEO (≈36%), with far fewer MEO and HEO/other cases—reflecting both environmental exposure and population/reporting effects.

Local-time and geomagnetic-activity dependences are clear. GEO anomalies cluster on the night/pre-dawn sector, consistent with injections of 10–100 keV electrons from the magnetotail that drive surface and internal charging. LEO anomalies occur preferentially during nighttime auroral traversals, when photoemission is weak and precipitating electrons elevate charging risk. When normalized by exposure (days in each Kp bin), the probability of anomaly per day increases with geomagnetic activity—especially for Kp ≥ 5—despite raw counts appearing larger at low Kp simply because quiet days are far more common.

Solar-cycle modulation is evident in the anomaly-per-satellite-year metrics. GEO-like charging risks track the build-up of relativistic/MeV electrons, yielding peaks near (and sometimes slightly before) sunspot maxima, consistent with outer-belt acceleration and the cumulative fluence that governs deep-dielectric charging. In contrast, LEO SEE components include a GCR contribution that tends to anti-correlate with solar activity, partly offsetting storm-time increases in auroral-charging-related events. These phase differences—and the well-known "double maxima" in some solar cycles—help explain the observed pre-maximum bump in anomalies.

Implications for design and operations. The most effective risk reduction comes from combining (i) design hardening (conductive/UV-stable surfaces, managed grounds/bonds, minimized floating dielectrics, rad-hard parts, current limiting, ECC/TMR with scrubbing), (ii) operational playbooks keyed to upstream solar-wind/SEP/electron monitors and geomagnetic indices (pre-emptive safe-modes, HV stand-downs, attitude/bias adjustments, schedule deferrals), and (iii) calibrated forecasts/nowcasts that map environmental drivers to anomaly likelihood by orbit and local time. Using modern specifications (e.g., AE9/AP9/SPM percentiles for trapped particles; validated density models for LEO drag) aligns margins with true tail risks rather than climatological means.

Limitations and data needs. Catalog-based results still carry biases: incomplete or uneven reporting (notably in MEO), ambiguous time tags for some events, and the use of LT as a proxy for MLT in parts of the historical record. Standardizing anomaly taxonomies, preserving precise timing/MLT stamps, and publishing aggregated, de-identified spacecraft-level outcomes would materially improve the fidelity of hazard-to-risk relationships.

Outlook. As fleets scale, probabilistic, orbit- and MLT-conditioned risk metrics (e.g., anomalies per satellite-day vs. Kp/AE) should become standard for mission assurance and operations. Paired with targeted hardening and pre-planned responses, such metrics can reduce anomaly rates substantially at modest cost, while enabling transparent, testable performance commitments for both operators and service users.

References

Ahmad, N., Kim, H., Kim, J., Kim, S. (2018). Diagnosing low Earth orbit satellite anomalies using NOAA-15 electron data associated with geomagnetic perturbations, *Earth, Planets and Space*, Vol. 70, 161, DOI: 10.1186/s40623-018-0852-2.

Ahmad, N., Kilowasid, L.M.M., Fakhrurroja, H., et al. (2025). How geomagnetic storms affect the loss of Starlink satellites in February 2022?, *Earth, Planets and Space*, Vol. 77, 2, DOI: 10.1186/s40623-024-02124-2.

Anderson, P.C., et al. (2012). Characteristics of spacecraft charging in low Earth orbit, *Journal of Geophysical Research: Space Physics*, Vol. 117, A01214, DOI: 10.1029/2011JA016875.

Baker, D.N., Kanekal, S.G., Hoxie, V.C., et al. (2018). Space weather effects in the Earth's radiation belts, *Space Science Reviews*, Vol. 214, 17, DOI: 10.1007/s11214-017-0452-7.

Camporeale, E. (2019). The challenge of machine learning in space weather: Nowcasting and forecasting, *Space Weather*, Vol. 17, No. 8, pp. 1166–1207, DOI: 10.1029/2018SW002061.

Choi, H.-S., et al. (2011). Analysis of GEO spacecraft anomalies: Space weather relationships, *Space Weather*, Vol. 9, S06001, DOI: 10.1029/2010SW000597.

Crowley, G., Guhathakurta, M., Oh, S., Tobiska, W. (2010). Space weather gets real—on smartphones, *Space Weather*, Vol. 8, No. 10, DOI: 10.1029/2010SW000619.

Emmert, J.T. (2015). Thermospheric mass density: A review, *Advances in Space Research*, Vol. 56, No. 5, pp. 773–824, DOI: 10.1016/j.asr.2015.05.038.

Ferguson, D.C., Denig, W.F., Rodriguez, J.V. (2011). Plasma conditions during the Galaxy 15 anomaly and the possibility of ESD from subsurface charging, *AIAA 2011–1061*, DOI: 10.2514/6.2011-1061.

Ginet, G.P., O’Brien, T.P., Huston, S.L., et al. (2013). AE9, AP9 and SPM: New models for specifying the trapped energetic particle and space plasma environment, *Space Science Reviews*, Vol. 179, pp. 579–615, DOI: 10.1007/s11214-013-9964-y.

Gopalswamy, N., Akiyama, S., Yashiro, S., Mäkelä, P., Xie, H., Michalek, G. (2024). The backreaction of the reduced heliospheric pressure on CMEs and its implications for the strength of Solar Cycle 25, *Proceedings of the Sixteenth Workshop “Solar Influences on the Magnetosphere, Ionosphere and Atmosphere”*, pp. 9–17, DOI: 10.31401/WS.2024.proc.2.

Harrison, R., Davies, J., Biesecker, D., Gibbs, M. (2017). The application of heliospheric imaging to space weather operations: Lessons learned from published studies, *Space Weather*, Vol. 15, No. 8, pp. 985–1003, DOI: 10.1002/2017SW001633.

Horne, R.B., Glauert, S.A., Meredith, N.P., Boscher, D., Maget, V., Heynderickx, D., Pitchford, D. (2013). Space weather impacts on satellites and forecasting the Earth’s electron radiation belts with SPACECAST, *Space Weather*, Vol. 11, No. 4, pp. 169–186, DOI: 10.1002/swe.20023.

Horne, R.B., Meredith, N.P., Grew, R.S., et al. (2025). Satellite internal charging for a reasonable worst-case, *Space Weather*, Vol. 23, e2024SW004226, DOI: 10.1029/2024SW004226.

Iucci, N., Levitin, A.E., Belov, A.V., Eroshenko, E.A., Ptitsyna, N.G., Villoresi, G., et al. (2005). Space weather conditions and spacecraft anomalies in different orbits, *Space Weather*, Vol. 3, S01001, DOI: 10.1029/2003SW000056.

Jun, I., Garrett, H.B., Dyer, C., et al. (2024). A review on radiation environment pathways to impacts: Radiation effects, relevant empirical environment models, and future needs, *Advances in Space Research*, Vol. 80, No. 2, pp. 215–247, DOI: 10.1016/j.asr.2024.03.079.

Kamide, Y. (2013). Space weather: Japanese perspectives, in *Geophysical Monograph Series*, Vol. 125, pp. 59–64, DOI: 10.1029/gm125p0059.

Krastev, K., Semkova, J., Koleva, R., Benghin, V., Drobyshev, S. (2024). An assessment of the radiation risk in orbit around Mars, based on measurements by the Lyulin instrument and numerical simulations, *Proceedings of the Sixteenth Workshop “Solar Influences on the Magnetosphere, Ionosphere and Atmosphere”*, pp. 83–88, DOI: 10.31401/WS.2024.proc.12.

Matzka, J., Stolle, C., Yamazaki, Y., et al. (2021). The geomagnetic Kp index and derived indices, *GFZ Data Services*, DOI: 10.5880/Kp.0001.

Meredith, N.P., Horne, R.B., Anderson, R.R. (2015). Extreme relativistic electron fluxes at geosynchronous orbit: 1996–2012, *Space Weather*, Vol. 13, No. 3, pp. 170–184, DOI: 10.1002/2014SW001143.

Meredith, N.P., Horne, R.B., Isles, J.D., Ryden, K.A., Hands, A.D.P., Heynderickx, D. (2016). Extreme internal charging currents in medium Earth orbit: Analysis of SURF plate currents on Giove-A, *Space Weather*, Vol. 14, pp. 578–591, DOI: 10.1002/2016SW001404.

Minow, J.I., Jordanova, V.K., Pitchford, D., Ganushkina, N.Y., Zheng, Y., Delzanno, G.L., Jun, I., Kim, W. (2024). ISWAT spacecraft surface charging review, *Advances in Space Research*, in press, DOI: 10.1016/j.asr.2024.08.058.

NASA-HDBK-4002B. (2022). *Avoiding problems caused by spacecraft on-orbit internal charging effects*, NASA Technical Handbook. (No DOI).

NASA-HDBK-4006A. (2024). *Low Earth orbit spacecraft charging design handbook (Revalidated 2024)*, NASA Technical Handbook. (No DOI).

NASA-STD-4005A. (2016). *Low Earth orbit spacecraft charging design standard*, NASA Technical Standard. (No DOI).

Newell, P.T., Sotirelis, T., Liou, K., Meng, C.-I., Rich, F.J. (2007). A nearly universal solar wind–magnetosphere coupling function inferred from 10 magnetospheric state variables, *Journal of Geophysical Research: Space Physics*, Vol. 112, A01206, DOI: 10.1029/2006JA012015.

Picone, J.M., Hedin, A.E., Drob, D.P., Aikin, A.C. (2002). NRLMSISE-00 empirical model of the atmosphere: Statistical comparisons and scientific issues, *Journal of Geophysical Research: Space Physics*, Vol. 107, No. A12, 1468, DOI: 10.1029/2002JA009430.

Reeves, G.D., Spence, H.E., Henderson, M.G., et al. (2013). Electron acceleration in the heart of the Van Allen radiation belts, *Science*, Vol. 341, pp. 991–994, DOI: 10.1126/science.1237743.

Robinson, R. (2012). Research to operations: Space weather's valley of opportunity, *Space Weather*, Vol. 10, No. 10, DOI: 10.1029/2012SW000854.

Seki, D., Ueno, S., Isobe, H., Otsuji, K., Cabezas, D., Ichimoto, K., et al. (2018). Space weather prediction from the ground: Case of CHAIN, *Sun and Geosphere*, Vol. 13, No. 2, pp. 157–161.

Tahir, A., Zhang, Y., Li, M., et al. (2024). Multi-instrument observation of the ionospheric irregularities and disturbances during the 23–24 March 2023 geomagnetic storm, *Remote Sensing*, Vol. 16, No. 9, 1594, DOI: 10.3390/rs16091594.

UCS Satellite Database. (n.d.). *Union of Concerned Scientists Satellite Database*. Available at: https://www.ucsusa.org/resources/satellite-database.

Wrenn, G.L. (1995). Conclusive evidence for internal dielectric charging anomalies on geosynchronous communications spacecraft, *Journal of Spacecraft and Rockets*, Vol. 32, pp. 514–520, DOI: 10.2514/3.26645.

Wrenn, G.L., Rodgers, D.J., Ryden, K.A. (2002). A solar cycle of spacecraft anomalies due to internal charging, *Annales Geophysicae*, Vol. 20, pp. 953–956, DOI: 10.5194/angeo-20-953-2002.

Ye, Y.-G., Zou, H., Zong, Q.-G., Chen, H.-F., Zou, J.-Q., Shi, W.-H., et al. (2021). Energetic electron detection packages on board Chinese navigation satellites in MEO, *Earth and Planetary Physics*, Vol. 5, No. 2, pp. 158–179, DOI: 10.26464/epp2021021.

Zhang, B., Zhang, S., Shen, G., Quan, L., Tian, C., Hou, D., Zhou, P., Ji, W. (2023). Monitor of the single event upsets and linear energy transfer of space radiation on the BeiDou navigation satellites, *Open Astronomy*, Vol. 32, No. 1, pp. 206–216, DOI: 10.1515/astro-2022-0206.

Zheng, Y., Sibeck, D.G., Reeves, G.D., et al. (2019). Space radiation and plasma effects on satellites and aviation: Quantities and metrics for tracking performance of space weather environment models, *Space Weather*, Vol. 17, No. 10, pp. 1384–1403, DOI: 10.1029/2018SW002042.

DOI: 10.31401/WS.2025.proc.19

Proceedings of
the Seventeenth Workshop "Solar Influences on the Magnetosphere, Ionosphere and Atmosphere"
Primorsko, Bulgaria, June, 2025

Catalog of Solar Energetic Particles Events Registered by Liulin-MO Dosimeter at Martian Orbit during the Current Solar Cycle

Koleva R.[1], *Semkova J.*[1], *Benghin V.*[2], *Gopalswamy N.*[3], *Maltchev S.*[1], *Bankov N.*[1], *Shurshakov V.*[2], *Drobyshev S.*[2], *Mitrofanov I.*[4], *Golovin D.*[4], *Litvak M.*[4], *Sanin A.*[4], *Mokrousov M.*[4], *Lukyanov N.*[4]

[1]Space Research and Technology Institute, Bulgarian Academy of Sciences, Sofia, Bulgaria
[2] State Research Center, Institute of Biomedical Problems, Moscow, Russia
[3]NASA Goddard Space Flight Center, Greenbelt Maryland, USA
[4]Space Research Institute, Russian Academy of Sciences, Moscow, Russia
rkoleva1900@gmail.com

Abstract

During the ascending and maximum phases of the current 25th solar cycle the Liulin-MO dosimeter aboard Trace Gas Orbiter registered a considerable number of solar energetic particle events. The catalog presented here lists the 27 events observed till June 2025 summarising the main characteristic of each event – its dosimetric parameters, the relation of the event with a coronal mass ejection and a flare in the sun, Erath's effect.

Keywords: Solar energetic particles, dose rate and flux, Mars.

1. Introduction

Solar energetic particles (SEP) are injected into the heliosphere following energetic solar eruptions. While the galactic cosmic rays (GCR) represent an unceasing flux through the heliosphere, though with low intensity but with energies up to 10^{20} eV/nucleon, SEP are randomly distributed events. Two different acceleration mechanisms are believed to be most responsible for accelerating SEPs: magnetic reconnection during solar flares and shock acceleration at coronal mass ejection (CME)-driven shocks [Reames 1999; Kallenrode, 2003]. The flares themselves release impulsive events while the CME shocks produce gradual events [Cliver and Cane, 2002]. High fluxes of charged particles (mostly protons, some helium and heavier ions) with energies up to several GeV and intensity up to 10^4 $cm^{-2}s^{-1}sr^{-1}$ are emitted. The time profile of a typical SEP event starts with a rapid increase in flux, reaching a peak in minutes to hours. Although SEPs are more likely to occur around solar maximum, such events are at present unpredictable with regard to their times of occurrence and it cannot be assumed that SEPs will not occur under solar minimum.

The Liulin-MO dosimeter [Semkova et al., 2018] is a module of the Fine Resolution Epithermal Neutron Detector (FREND) instrument [Mitrofanov et al., 2018] aboard Trace Gas Orbiter (TGO). TGO was launched in March 2016; reached Mars in late September 2016 and till March 2017 orbited the planet at high elliptic orbits. After a year of aerobraking TGO was inserted into a Mars circular orbit with 400 km altitude (varying within ±25 km in every orbital pass), 74^0 inclination, ~ 2 hours orbit period.

Liulin-MO has provided and is providing in-situ measurements of the radiation environment during the TGO interplanetary travel and at Martian orbit. During the declining phase and the minimum of the 24th solar cycle, from 2016 till June 2021 only GCR were registered. With the increasing solar activity in the 25th solar cycle registration of SEP events at Martian orbit started. From July 2021 to the end of June 2025 twenty seven SEP events were observed. Different characteristics of the SEPs registered till October 2024 were discussed in [Semkova et al. 2022; Semkova et al., 2023; Semkova et al., 2024; Semkova et al., 2025].

The aim of the present work is to summarise in a manner suitable for easy perception the characteristics of all 27 SEP events registered till June 2025 at Mars orbit – their dosimetric parameters, the relation of each event with a coronal mass ejection and a flare in the sun, a possible effects on Earth.

2. Catalog of Solar Energetic Particles Events at Martian Orbit during the Current Solar Cycle

2.1. Complementary tools

To relate the observed SEPs at Martian orbit to solar phenomena, we use the information provided in the CME lists in the on-line catalogues: Solar Eruptive Event Detection System (SEEDS, http://spaceweather.gmu.edu/seeds/) and the CDAW catalog (https://cdaw.gsfc.nasa.gov/CME_list/), [Gopalswamy et al., 2009]. SEEDS uses images from the Solar and Heliospheric Observatory (SOHO) Large Angle and Spectrometric Coronagraph (LASCO) [Brueckner et al., 1995] C2 telescope and the outer coronagraph (COR2) of the Sun Earth Connection Coronal and Heliospheric Investigation (SECCHI) [Howard et al., 2002] on board the Solar Terrestrial Relations Observatory (STEREO). The CDAW catalogue uses images from SOHO/LASCO C2 and C3 telescopes.

We have used data on solar flares provided by the data center for the Spectrometer and Telescope for Imaging X-rays (STIX) on board the Solar Orbiter [Muller et al., 2020; Xiao et al,, 2023], https://datacenter.stix.i4ds.net/view/flares/list, github.com/hayesla/stix_flarelist_science.

The following data on SEP events have also been used:

- In Earth vicinity – from the NOAA Space Weather Prediction Center catalog of the Solar Proton Events Affecting the Earth Environment (https://www.ngdc.noaa.gov/stp/space-weather/interplanetary-data/solar-proton-events/SEP%20page%20code.html) and Catalogues of Solar Proton Events in the 20-25 Cycles of Solar Activity on the space weather website of the SINP MSU (https://swx.sinp.msu.ru/apps/sep_events_cat/);

To present the mutual longitudinal location of Mars and the spacecraft carrying the coronagraphs, we use the Solar-MACH on-line plotter https://solar-mach.github.io/ [Gieseler, et al., 2022]. The plots are in the Stonyhurst System of heliographic coordinates and they present the projections in the Sun equatorial plane during the discussed events. Since the propagation of high-energy charged particles in interplanetary space is controlled by the interplanetary magnetic field, we used the field lines (FL) modeled by that tool and connecting Mars and the satellites carrying the coronagraphs SOHO, STEREO A and Solar Orbiter (SolO) spacecraft to the Sun.

The GOES-18 [Kress et al., 2020] proton fluxes data used in the paper for the comparison with the Liulin-MO fluxes is downloaded from the space weather website of the Institute of Nuclear Physics of Moscow State University (section “INSTRUMENTS”) https://swx.sinp.msu.ru/tools/ida.php?gcm=1. The data on GOES proton fluxes in $cm^{-2}s^{-1}sr^{-1}$ are multiplied by 2π to compare with the Liulin-MO fluxes in $cm^{-2}s^{-1}$. In the analysis of the GOES data, the paper also uses plots from NOAA/NWS Space Weather Prediction Center at https://www.swpc.noaa.gov/products/goes-proton-flux and from Space Weather Data Portal (https://lasp.colorado.edu/space-weather-portal) of the University of Colorado Boulder and Space Weather Technology, Research, and Education Center, “SWx TREC Space Weather Data Portal”, Laboratory for Atmospheric and Space Physics, 2019, https://doi.org/10.25980/NMFX-XX89.

2.2. Description of the Catalog

The catalog is presented in Table 1 below. From left to right:

- *First column*: Start time of the observed SEP event in Liulin-MO data;
- *Second column*: Approximate duration of the SEP event;

- *Third column*: Total dose from background GCR and SEP (in Si) during the event /total dose from SEP (in Si) during the event;
- *Forth column*: Maximum dose rate from GCR and SEP measured during the event;
- *Fifth column*: Maximum flux from GCR and SEP measured during the event;
- *Sixth column*: Drawing of the mutual location of Mars (TGO) and the three spacecraft carrying the coronagraphs (the location of the SOHO/LASCO spacecraft is annotated as 'Earth');
- *Seventh column*: Time profiles of Liulin-MO and GOES flux increase during the event.
- *Eighth column*: Details of CME related to the corresponding event-type, onset time, an appropriate image of LASCO C2 or STEREO A Cor2. Annotation:
  - * *According to CDAW C2+C3 catalog*
  - ** *According to SEEDS LASCO C2 catalog*
  - *** *According to SEEDS SECCHI COR2 catalog*
- *Ninth column*: Details of X ray flare related to the corresponding event, observing satellite and approximate peak time of the flare and location. Annotation:
  - \+ *NOAA catalogue*
  - \+\+ *SINP MSU catalogue*
  - \+\+\+ *Solar Orbiter STIX catalog*

3. References

Brueckner, G.E., Howard, R.A., Koomen, M.J., et al. (1995). The Large Angle Spectroscopic Coronagraph (LASCO), Solar Physics, Vol. 162, pp. 357–402, DOI: 10.1007/BF00733434.

Cliver, E.W., Cane, H.V. (2002). Gradual and impulsive solar energetic particle events, Eos Transactions AGU, Vol. 83, pp. 61–68, DOI: 10.1029/2002EO000084.

Gieseler, J., Dresing, N., Palmroos, C., von Forstner, J.L.F., Price, D.J., Vainio, R., et al. (2022). Solar-MACH: An open-source tool to analyze solar magnetic connection configurations, Frontiers in Astronomy and Space Sciences, Vol. 9, DOI: 10.3389/fspas.2022.1058810.

Gopalswamy, N., Yashiro, S., Michalek, G., et al. (2009). The SOHO/LASCO CME catalog, Earth, Moon, and Planets, Vol. 104, pp. 295–313, DOI: 10.1007/s11038-008-9282-7.

Kallenrode, M. (2003). Current views on impulsive and gradual solar energetic particle events, Journal of Physics G: Nuclear and Particle Physics, Vol. 29, No. 5, p. 965, DOI: 10.1088/0954-3899/29/5/316.

Kress, B.T., Rodriguez, J.V., Onsager, T.G. (2020). The GOES-R Space Environment In Situ Suite (SEISS): Measurement of energetic particles in geospace, in: Goodman, S.J., Schmit, T.J., Daniels, J., Redmon, R.J. (Eds.), The GOES-R Series, Elsevier, pp. 243–250, DOI: 10.1016/B978-0-12-814327-8.00020-2.

Mitrofanov, I., Malakhov, A., Bakhtin, B., Golovin, D., Kozyrev, A., et al. (2018). Fine Resolution Epithermal Neutron Detector (FREND) onboard the ExoMars Trace Gas Orbiter, Space Science Reviews, Vol. 214, 86, DOI: 10.1007/s11214-018-0522-5.

Müller, D., St. Cyr, O.C., Zouganelis, I., et al. (2020). The Solar Orbiter mission: Science overview, Astronomy & Astrophysics, Vol. 642, A1, DOI: 10.1051/0004-6361/202038467.

Reames, D.V. (1999). Particle acceleration at the Sun and in the heliosphere, Space Science Reviews, Vol. 90, pp. 413–491.

Semkova, J., Koleva, R., Benghin, V., Dachev, T., Matviichuk, Yu., et al. (2018). Charged particles radiation measurements with Liulin-MO dosimeter of FREND instrument aboard ExoMars Trace Gas Orbiter during the transit and in high elliptic Mars orbit, Icarus, Vol. 303, pp. 53–66, DOI: 10.1016/j.icarus.2017.12.034.

Semkova, J., Koleva, R., Benghin, V., Krastev, K., Matviichuk, Yu., et al. (2022). Observation of solar energetic particle events onboard ExoMars TGO in July 2021–March 2022, Proceedings of the Fourteenth Workshop "Solar Influences on the Magnetosphere, Ionosphere and Atmosphere", June 2022, ISSN 2367-7570, pp. 55–60, DOI: 10.31401/WS.2022.proc.

Semkova, J., Koleva, R., Benghin, V., Krastev, K., Matviichuk, Yu., et al. (2023). Observation of the radiation environment and solar energetic particle events in Mars orbit in May 2018–June 2022, Life Sciences in Space Research, Vol. 39, pp. 106–118, DOI: 10.1016/j.lssr.2023.03.006.

Semkova, J., Benghin, V., Koleva, R., Krastev, K., Matviichuk, Yu., et al. (2024). New results of radiation study on board TGO ExoMars in 2018–2023, Solar System Research, Vol. 58, No. 4, pp. 367–376, DOI: 10.1134/S0038094624700291.

Semkova, J., Koleva, R., Benghin, V., Gopalswamy, N., Matviichuk, Yu., et al. (2025). Radiation environment on TGO Mars orbit during solar particle events in January–October 2024: Corresponding solar eruptions and GOES proton fluxes data, Life Sciences in Space Research, Vol. 45, pp. 117–134, DOI: 10.1016/j.lssr.2025.02.010.

Table 1: Catalog of Solar Energetic Particles Events registered by Liulin-MO at Martian Orbit during the Current Solar Cycle

Start time of SEP event [UT]	**Duration [h]**	**Total dose/ total dose from SEPs (in Si) [µGy]**	**Maximum dose rate [µGy/h]**	**Maximum flux [cm^{-2} s^{-1}]**	**Location**	**Time profiles of Liulin-MO and GOES-18 flux rates**	**CME Type onset UT**	**X ray flare class** *(GOES scale)* **flare list location**
17 July 2021, 09:06	23	444.9±44.5/ 96.2±9.6	20.3±2	4.25±0.2	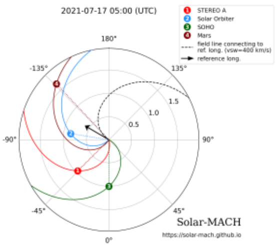	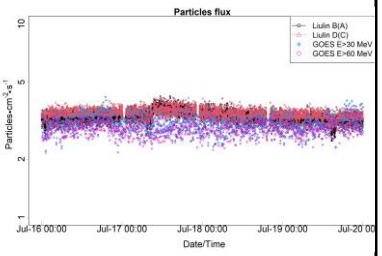	*Behind the E limb halo CME 04:55:05 - 05:04:45, 17 July 2021 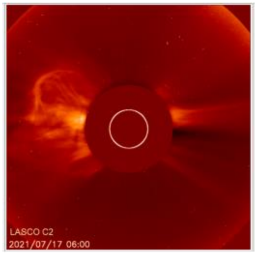	Behind limb event
17 September 2021, 07:12	37	757±76/ 185±19	25.6±2.6	4.5±0.2	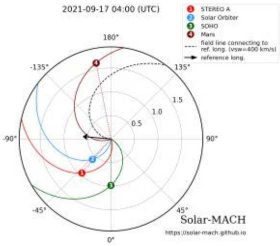	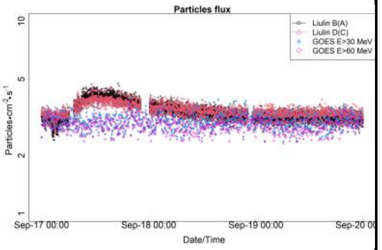	*East limb partial halo CME 04:05:17 – 04:17:47, 17 September 2021 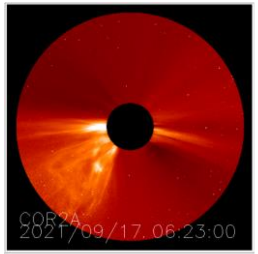	Backside event
28 October 2021, 16:55	79	7700±770/ 6500±650	402±40.2	48.5±2.43	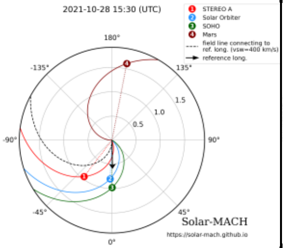	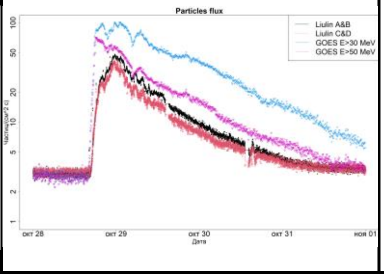	*Halo CME, 15:25:32 - 15:32:36, 28 October 2021 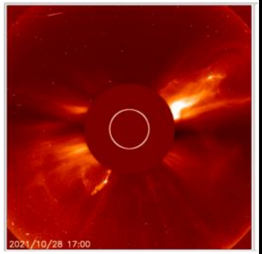	++X1.0 28 October 2021, 15:17 S26W05

15 February 2022, 23:00	76	15000±1500/ 13800±1380	1009±101	109.7±5.5	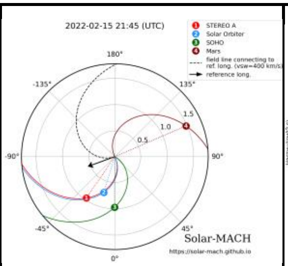	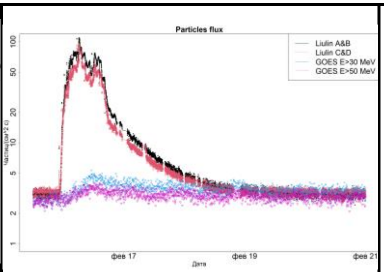	Behind the east limb halo CME # 21:25, 15 February 2022 *from STEREO A EUV images* 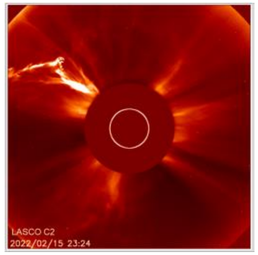	++M1.3 15 February, 18:15
14 March 2022, 17:55	17	328.1±33/ 95.2±9.5	31.2±3.1	5.13±0.26	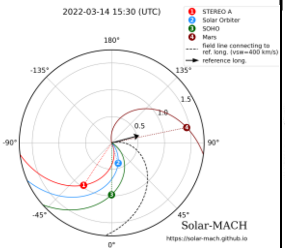	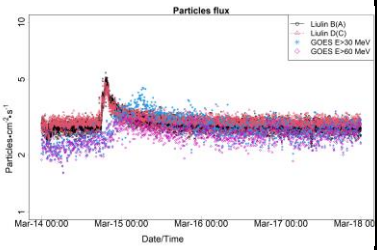	*Behind the W limb partial halo CME, 17:02:17 - 17:16:28, 14 March 2022 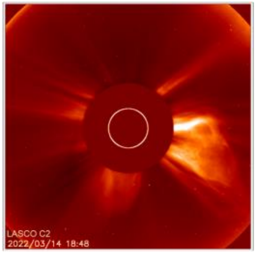	Behind limb event
24 February 2023, 21:07	24	413.4±41.3/ 194/55±19.45	58.83±5.9	5.1±0.25	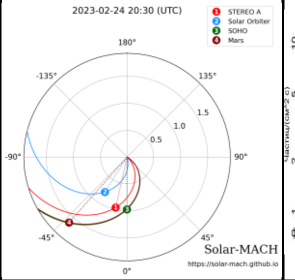	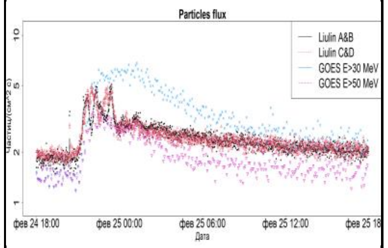	*Halo CME, 20:09:46 - 20:13:22 24 February 2023 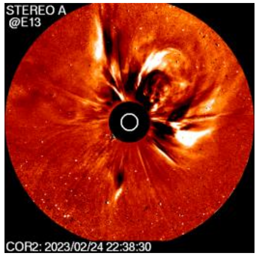	++M3.7 24 February, 20:03 N29W24
25 February 2023, 21:20	21	354.36±35.44/ 162.87±16.3	33.87±3.4	3.9±0.2	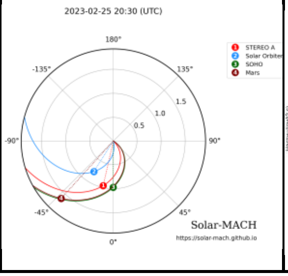	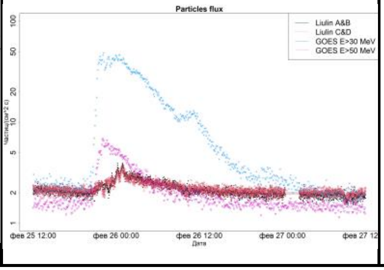	*Halo CME, 19:10:47 - 19:08:05 25 February 2023 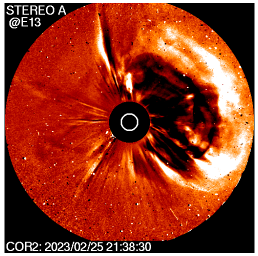	++M6.4 25 February 2023, 18:40 N24W45

13 March 2023, 05:24	39	668.9±66.9/ 270.9±27.1	41.7±4.2	4.4±0.22	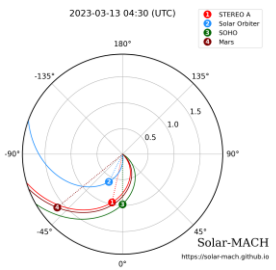	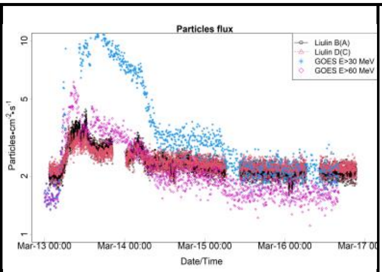	*Halo CME 03:18:20 - 03:24:29 13 March 2023	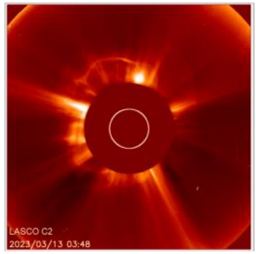	Behind limb event
01 January 2024, 00:08	81	2220±222/ 1670±167	70.5±7	7.3±0.37	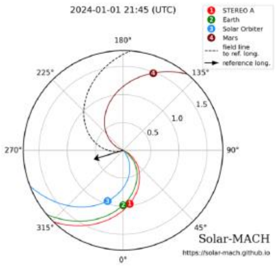	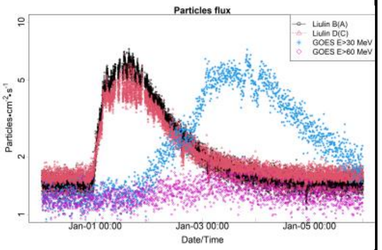	*Halo CME 21:42:57 - 21:45:45, 31 December 2023	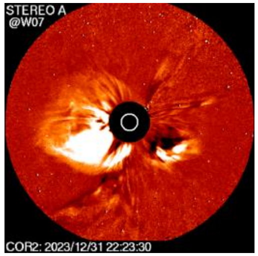	++X5.0 31 December 2023, 21:52 N04E73
06 February 2024, 13:10	40	630±63/ 350±35	24.8±2.5	3.2±0.16	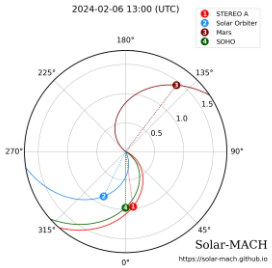	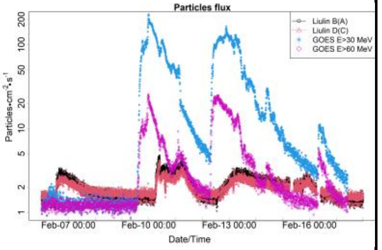	*Backside halo CME 11:23:26 - 11:28:14, 06 February 2024	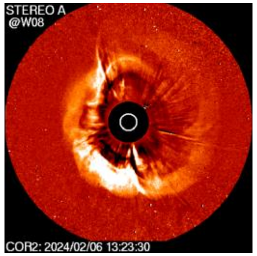	no data
10 February 2024, 06:30 merged events	39	944±94/ 647±65	36.3±3.6	4.6±0.23	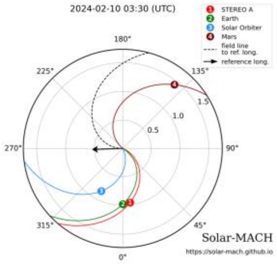	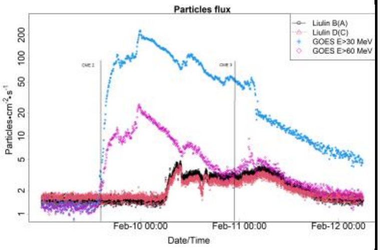	*East Limb halo CME (CME2) 03:28:41- 03:29:37, 10 February 2024	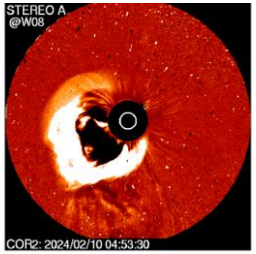	+++M3.4, 10 February 2024, 03:48 S14E88

					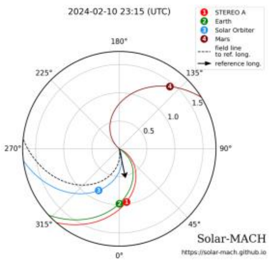		*Halo CME (CME3) 23:10:53-23:11:13, 10 February 2024	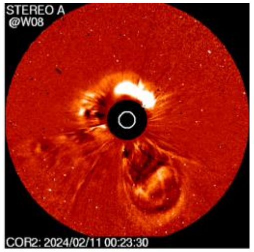	+++M9.0 10 February 2024, 23:07 S10W12
12 February 2024, 12:10 merged events	107	1945±195/ 1280±128	24.6±2.5	3.3±0.17	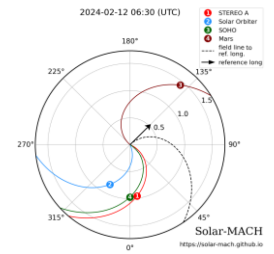	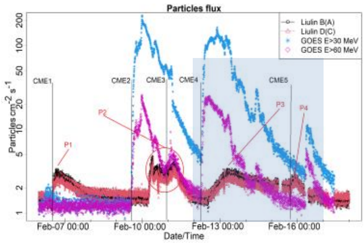	*Halo CME behind the Limb (CME 4) 06:25:45 - 06:29:05, 12 Feb 2024	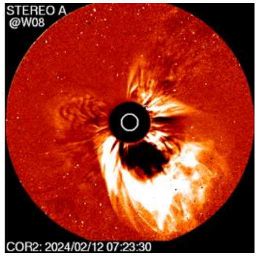	S36W135 *estimated*
					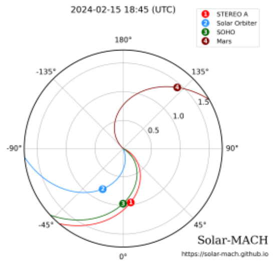		**Behind the W limb (CME 5) 18:26:14 - 18:52:59 15 February 2024	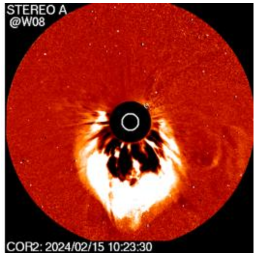	No data
20 May 2024, 05:40	64	25220±2522/2 4720±2472	2800±280	383 ± 19	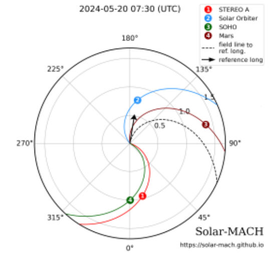	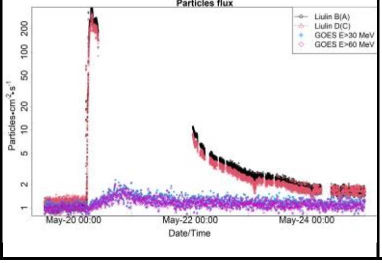	*Backside halo CME 05:06:25-05:10:26 20 May 2024	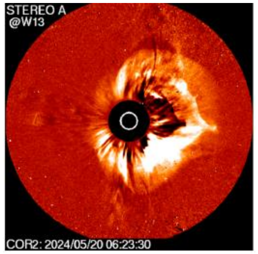	+++X12 20 May 2024 05:14:40 S18W171

11 June 2024, 23:30	52	1020±102/ 660±66	51.6±5.2	7.8±0.39	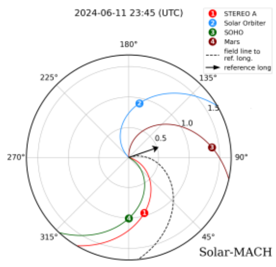	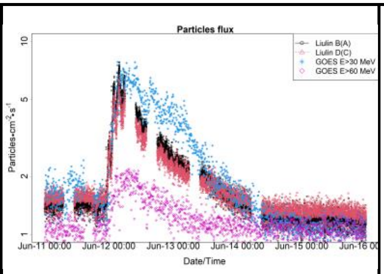	*Halo CME Behind west limb 22:27:56 , 11 June 2024	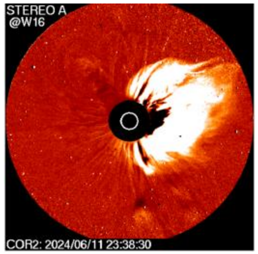	+++X3 11 June 2024 22:38:52 S16W118
23 July 2024, 01:20 Merged events	95	3200±320/ 2580±258	197±20	21.8±1.1	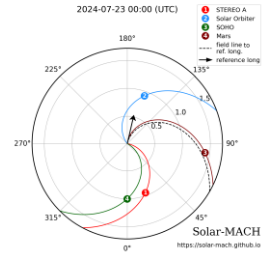	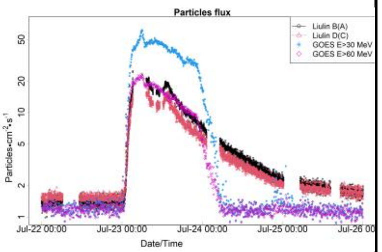	**Backside halo CME, 23:51:22, 22 July – 00:01:46, 23 July 2024	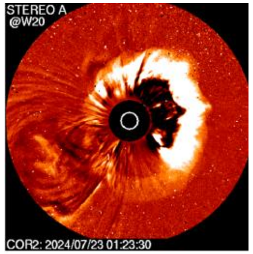	+++X14 22 July 2024 23:56:37 N15 behind the W limb
03 September 2024, 09:15	47	1817±182/ 1521±152	208.3±21	18.8±0.95	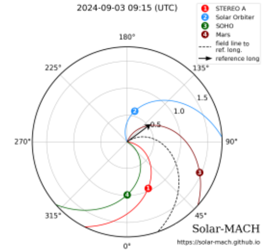	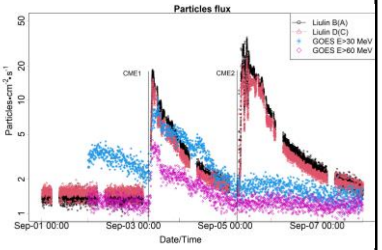	***Behind west limb partial halo CME1, 07:32:56 - 07:50:20 03 September 2024	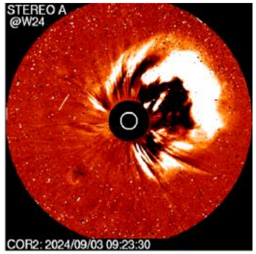	+++X2.4 03 Septem-ber 2024, 07:55:36 N21W125 (estima-ted)
05 September 2024, 07:52	59	3522±352/ 3138±314	336±34	35.9±1.8	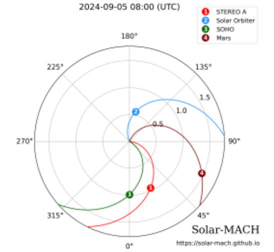	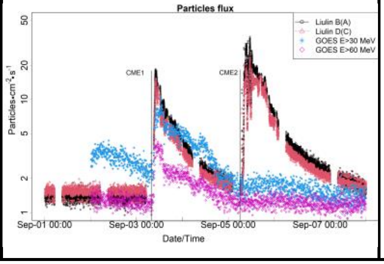	***Backside halo CME2, 05:57:25 - 06:36:17 05 September 2024	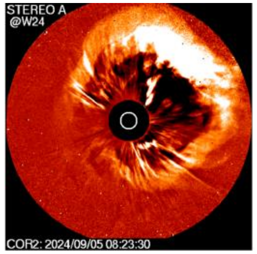	+++X2 05 Septem-ber, 06:35:16 No flare position

09 October, 2024, 06:05	52	1675±168/ 1380±138	54±5.4	5.8±0.29	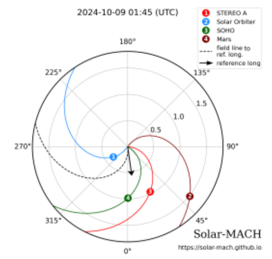	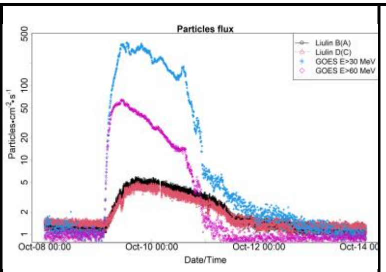	***Halo CME 01:50:45 - 01:50:41 09 October 2024 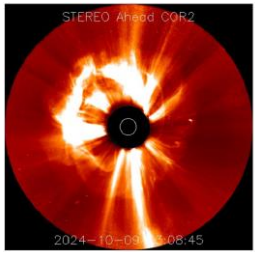	++X1.8 09 October, 01:35:23 N13W08
21 November, 2024, 18:30	40	1256±126/ 1025±103	76±7.6	8.8±0.44	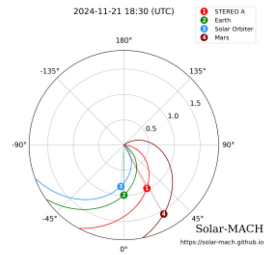	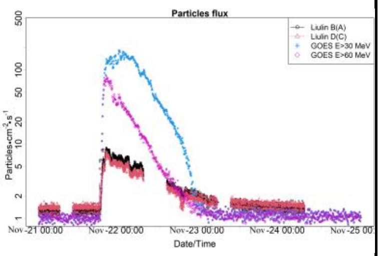	*Beyond W limb halo CME 17:43:40 - 17:55:09 21 November 2024 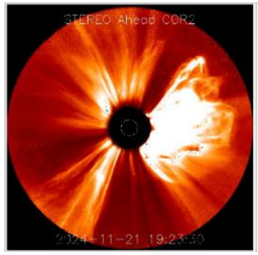	Beyond western limb S12
17 December 2024, 23:20	38	631±63/ 402±40	50±5	4.6±0.23	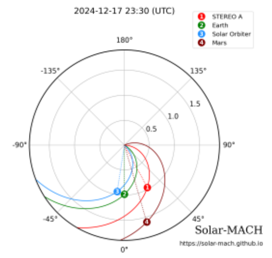	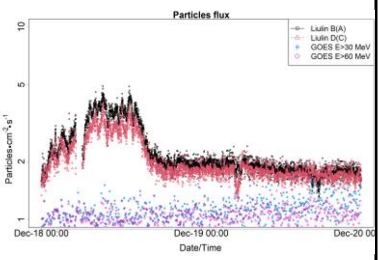	No appropriate CME found	
05 January 2025, 04:30	18	178±18/ 70±7	22±2.2	2.1±0.1	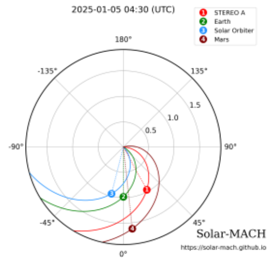	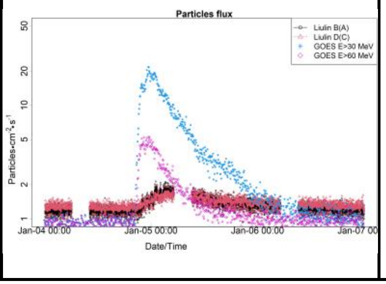	*** West limb partial halo CME 19:40:47 4 January 2025 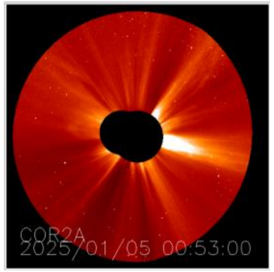	+C7.6 4 January, 19:55 S17W61

25 February 2025, 02:10	32	285±28/ 92±9.2	25±2.5	1.8±0.09	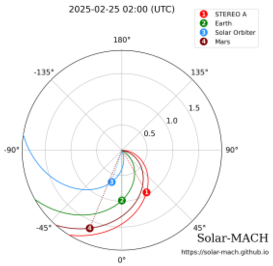	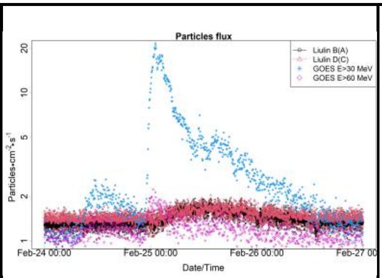	West limb semi-halo CME ** 20:53 – 21:30 ***22:02: 24 February 2025 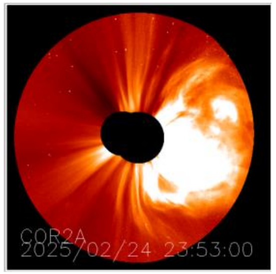	+M3.9 24 February, 23:02 around SW Lim
01 April 2025 01:10	15	147±15/ 45±4.5	17.7±1.8	2±0.1	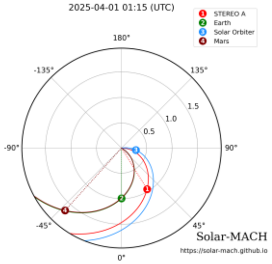	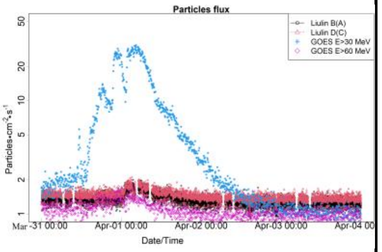	*** Behind East limb CME, 16:43 31 March 2025 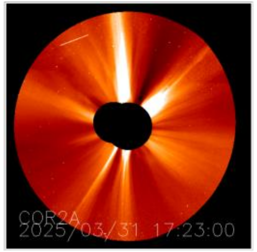	+X1.1 28 March, 15:21 N05E85
31 May 2025 01:24	48	1872±187/ 1592±159	179±18	13±0.65	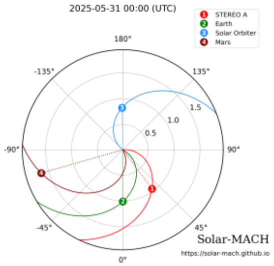	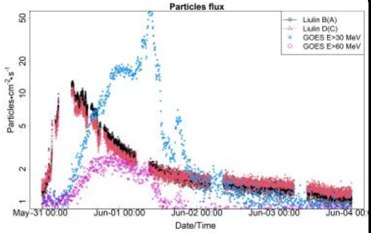	***East limb halo CME 23:03 30 May 2025 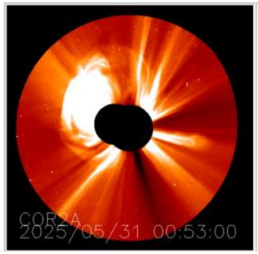	+++M8.2 30 May 23:24

DOI: 10.31401/WS.2025.proc.20

Solar Proton Events Recorded by the Lyulin Instrument - Composition Analysis Using Numerical Modeling

Krastev K.

Space Research and Technology Institute, Bulgarian Academy of Sciences

Abstract

In recent years, the Liulin instrument has recorded numerous solar proton events associated with increased solar activity. This paper focuses on several of the most significant of these events. A qualitative assessment of the energy composition and types of solar particle fluxes was carried out based on numerical modeling. The simulations were performed using a numerical model implemented in GEANT4, which reproduces the operation of the Liulin device for detecting ionizing radiation.

1. Introduction

The Liulin-MO instrument, part of the ExoMars TGO mission, has collected an extensive database of radiation field measurements over more than nine years of operation, both in interplanetary space and in orbit around Mars. Figure 1 presents the measurement data obtained by Liulin-MO for the entire period of its operation.

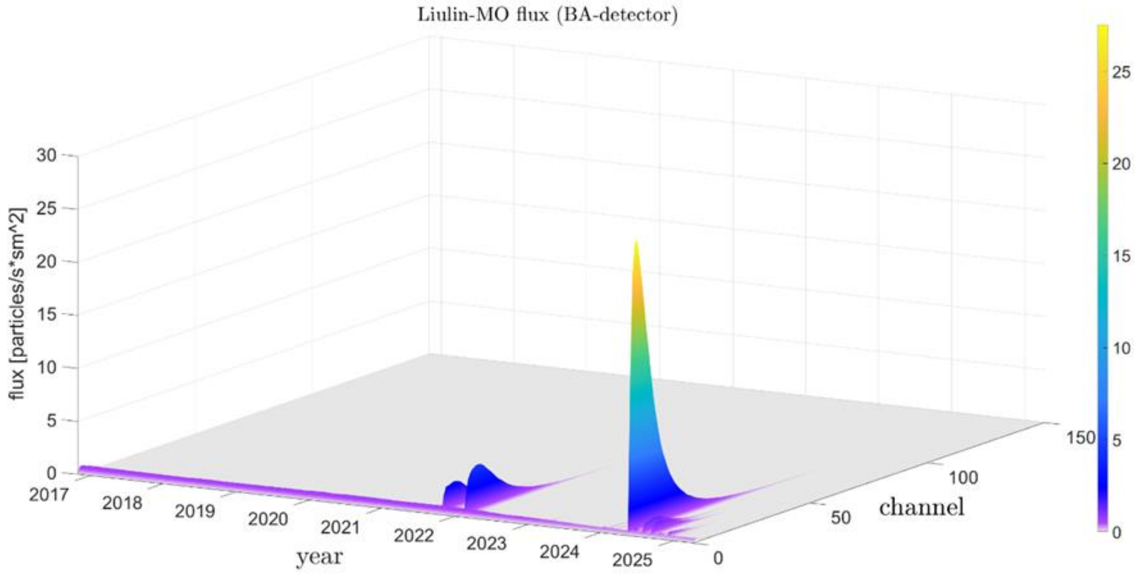

Figure 1. *The measurement data from the Liulin-MO instrument for the entire period of its operation (BA-single detector).*

In the figure, the solar proton events from 2021, 2022, and 2024, which are the subject of our study, are clearly visible.

2. Methods

The methodology of the computer simulations follows that described in [Krastev et al., 2023a]. Figure 2 shows the geometric model of the Liulin-MO detector system, which is used in the simulations. This work presents simulations of the operation of the single BA detector, whose operating logic is presented in [Semkova et al, 2018].

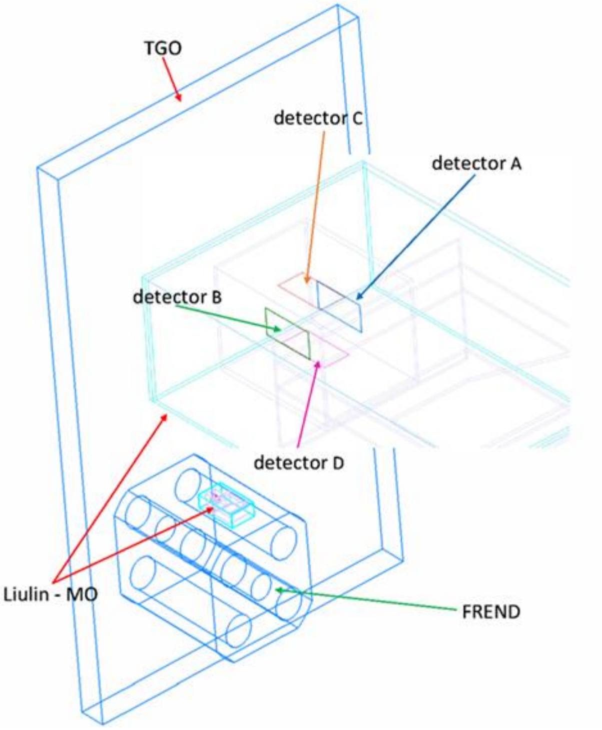

Figure 2. *Liulin-MO instrument detector system model.*

A series of simulations was performed to determine the response of the single BA detector to various types of particles with different energies. For the simulation, protons with energies ranging from 100 to 500 MeV and alpha particles with energies between 1 and 5 GeV were generated. For each proton energy, 9 billion particles were generated, while for each alpha-particle energy the corresponding number was 1 billion. The source of the generated particles is a sphere with a radius of 150 cm, with the center of the sphere coinciding with the center of the Liulin-MO detector system. The sphere also includes the entire TGO structure.

3. Results

Figures 3 and 4 show the reaction of one BA detector obtained from simulation to protons and alpha particles, respectively, at different energies.

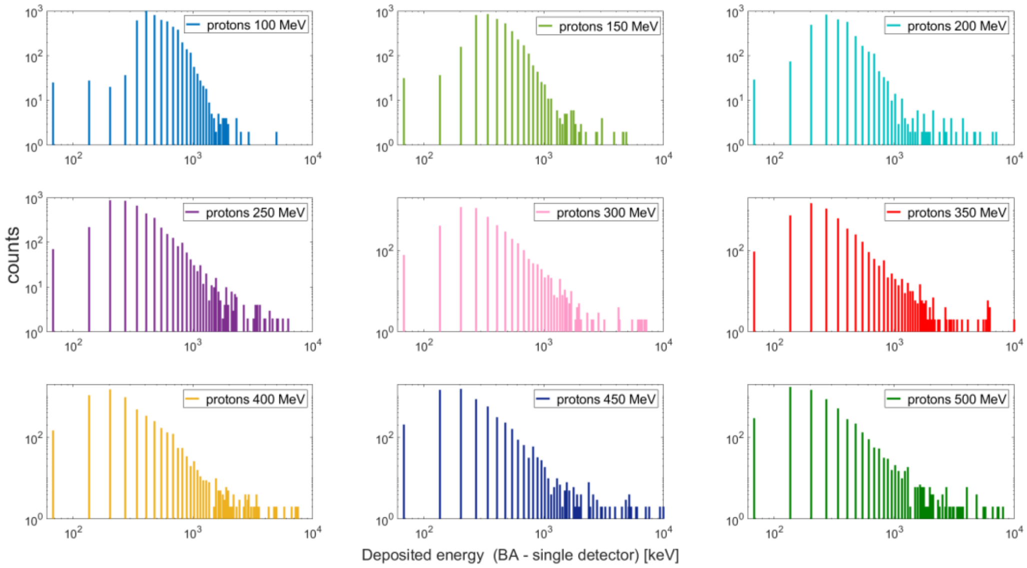

Figure 3. *The response of the single BA detector to protons at different energies.*

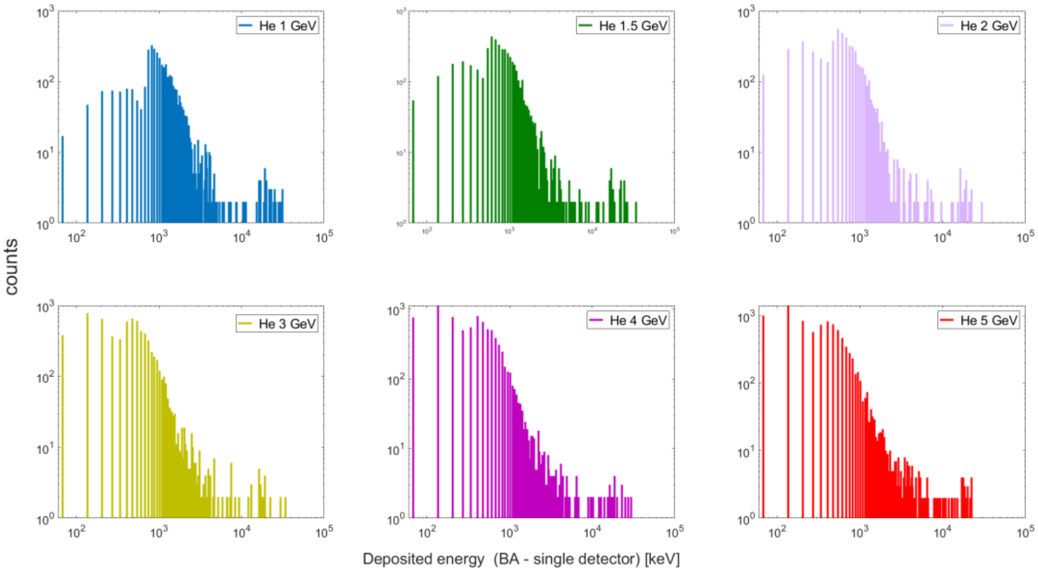

Figure 4. *The response of the single BA detector to alpha particles at different energies.*

Figure 5 allows a preliminary analysis of the contribution of protons with different energies to the formation of the events shown in the graph. For instance, the May 2024 event is primarily produced by protons with energies in the range of 300–450 MeV. The February 2022 event is formed by protons with energies between 50 and 100 MeV (the cutoff energy for the Liulin-MO design is 30 MeV), while the October 2021 event is produced by protons with energies greater than 450 MeV.

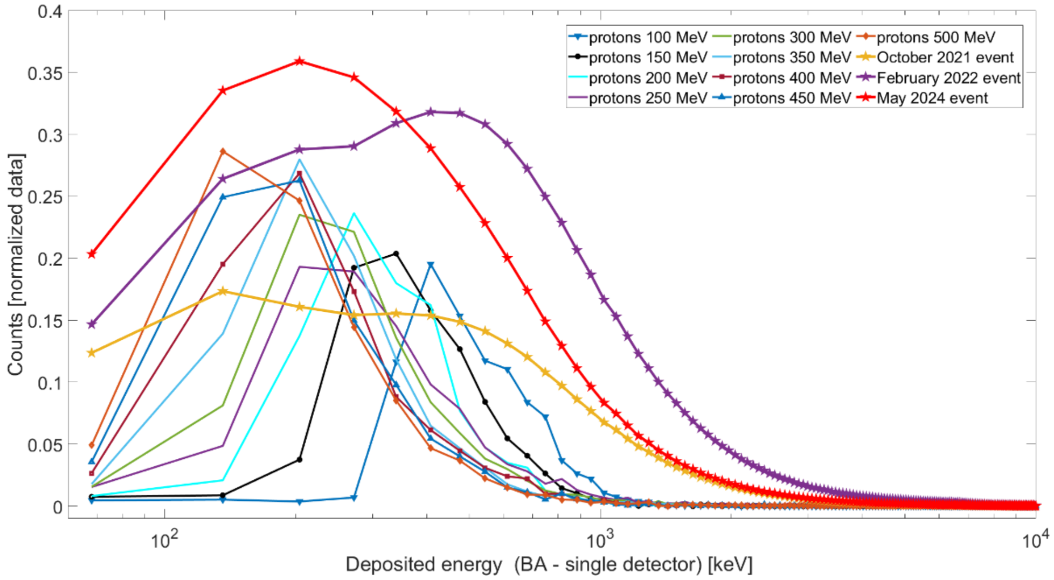

Figure 5. *Comparison between measured and simulated data.*

4. Conclusion

Instruments such as ACE-SIS are specifically designed to study the composition of solar proton events. Nevertheless, the results obtained demonstrate that numerical simulations can offer an initial approximation of the composition of solar proton events detected by instruments of the Liulin-MO type. While this task was not part of the instrument’s original scientific mission, this additional functionality is particularly valuable, as Liulin-MO currently remains the only dosimeter operating in orbit around Mars.

References

Krastev, K., Semkova, S., Koleva, R., Benghin, V., Drobyshev, S. (2023). Numerical Simulation of the LIULIN-MO Device, *Proceedings of the 15th Workshop “Solar Influences on the Magnetosphere, Ionosphere and Atmosphere”*, June 2023, ISSN 2367-7570, pp. 108–113, https://doi.org/10.31401/WS.2023.proc.19.

Semkova, J., Koleva, R., Benghin, V., Dachev, T., Matviichuk, Y., Tomov, B., Krastev, K., Maltchev, S., Dimitrov, P., Mitrofanov, I., Malakhov, A., Golovin, D., Mokrousov, M., Sanin, A., Litvak, M., Kozyrev, A., Tretyakov, V., Nikiforov, S., Vostrukhin, A., Fedosov, F., Drobyshev, S. (2018). Charged Particles Radiation Measurements with Liulin-MO Dosimeter of FREND Instrument Aboard ExoMars Trace Gas Orbiter during the Transit and in High Elliptic Mars Orbit, *Icarus*, Vol. 303, pp. 53–66, https://doi.org/10.1016/j.icarus.2017.12.034.

DOI: 10.31401/WS.2025.proc.21

Effects of Geomagnetic Storms on the Mid-Latitude D Region Ionosphere

Mustafa F.[1,2], *Bayramova E.*[1], *Dzhalilov N.*[1]

[1]Shamakhy Astrophysical Observatory named after N.Tusi, Ministry of Science and Education of the Republic of Azerbaijan
famil.mustafa@gmail.com
[2]Khazar University, Azerbaijan

Abstract

The response of D Layer Preparation Time (DLPT) depth to geomagnetic storms during 2008-2011 is studied to investigate the effect of geomagnetic storms on the D layer of the ionosphere. The Very Low Frequency (VLF) signal at 19.6 kHz transmitted from the GBZ transmitter station Anthorn, UK (54ºN, 3ºW) and recorded by the AWESOME receiver at the Shamakhy Astrophysical Observatory named after N.Tusi, Shamakhy, Azerbaijan (40ºN, 48ºE) was used for analysis. Five geomagnetically disturbed days (Ap>26) were studied. A decrease in DLPT depth was observed for the storm day on October 11, 2008, while an increase was observed for all other storms.

Keywords: D layer preparation time; VLF wave propagation; Geomagnetic storms, AWESOME receiver.

1. Introduction

Earth's ionosphere plays a significant role in radio communication by reflecting the wave owing to electrical conductivity. Radio waves first penetrate the D layer (60-90 km) when they propagate in the ionosphere and are exposed to attenuation. Therefore, fading of signals is strongly dependent on the ionization level of this layer. Space weather events, such as Solar flares and geomagnetic storms, adversely affect radio communication, radio navigation systems, and satellite communication by increasing the ionization level of the ionosphere. Substantial enhancement of electron density, particularly in the auroral zone, during geomagnetic storms, increases radio wave attenuation, which causes the disappearance of radio signals in MH/HF ranges (Lastovicka, 1996).

VLF (3-30 kHz) remote sensing method is considered the best technique to detect space weather effects on the lower ionosphere. VLF signals are transmitted from around the world to the ionosphere and received at Sudden Ionospheric Disturbances (SID) monitoring stations. They propagate with little attenuation on the cavity called the Earth-Ionosphere Waveguide (EIWG) between ionospheric D-layer and ground (Kumar, 2018). Amplitude and phase of the waves are much sensitive to changes in the electrical conductivity of the ionosphere on the propagation path (Peter et al., 2006). EIWG height is 70 km during the daytime and 85 km during the nighttime, depending on the diurnal variation of the ionosphere (Thomson et al., 1993). The impacts of solar flares on VLF signals propagation have been discussed by many investigators (Kumar et al., 2015; Selvakumaran et al., 2014; Bouderba et al., 2016; Hayes et al., 2017; Sreckovic et al., 2017; Korsakov et al., 2018; Sharma et al., 2018). They determined that enhanced X-ray radiation when a solar flare occurs increases the ionization of the D-layer, which results in a sudden anomaly in amplitude and phase of the VLF signals. Solar flares affect the entire daytime ionosphere, while geomagnetic storms primarily affect the high-latitude ionosphere; the effect extends to low and equatorial latitudes (Kumar et al., 2018).

A geomagnetic storm is a temporary disturbance of Earth’s magnetosphere in response to changes in solar wind parameters and interplanetary magnetic field (IMF) conditions. Magnetic storms lead to energetic electron precipitation into the ionosphere associated with magnetospheric substorms. In order to penetrate below the 100 km altitude, electrons must have energies exceeding 20 keV (Spjeldvik et al., 1975). Lastovicka (Lastovicka, 1996) opined that at high latitudes, enhancement in electron density and radio wave absorption is caused by energetic electron precipitation from the magnetosphere in the storm main phase. Cummer et al. (Cummer et al., 1996) mentioned that energetic precipitating electrons penetrate the lower ionosphere, where they can cause extra ionization. Consequently, as the auroral electrojet crosses a VLF signal propagation path, this electron precipitation results in variations in amplitude and phase of the signal. Observing a decrease or increase in the amplitude at the receiving station depends on the modal mixture of the signal (Rodger et al., 2007). Clilverd et al. (Clilverd et al., 2010) observed that the amplitude of the very low-frequency signal transmitted from the NAA (24.0 kHz, 44°N, 67°W, L = 2.9) received at Sodankyla increased during geomagnetic activity. They showed ground-based electron precipitation flux (>100 keV) calculated from the NAA amplitude corresponds with the variation of electron fluxes determined by the POES satellite. From the analysis of two severe geomagnetic effects on the D-layer at low-equatorial latitudes, Kumar et al. (Kumar et al., 2018) observed that for the March 2015 storm, VLF signal amplitude decreased on the primary phase and recovered one day after the storm. For June 2015 storm, they observed amplitude decreased in the storm recovery phase.

The effect of geomagnetic storms on the lower ionosphere is characterized in terms of “primary storm effect,” “after storm effect,” “post-storm effect.” “Primary storm effect” describes signal anomaly during the main phase of the storm, whereas “after storm effect” describes anomaly during the storm recovery period and subsequent days. The “Post-storm” effect, on the other hand, is observed due to excess ionization when the magnetic perturbations have abated (Araki, 1974; Larsen et al., 1976).

In this work, the influence of geomagnetic storms during 2008-2011 on the mid-latitude D region of the ionosphere via VLF signal amplitude was studied.

2. Materials and Methods

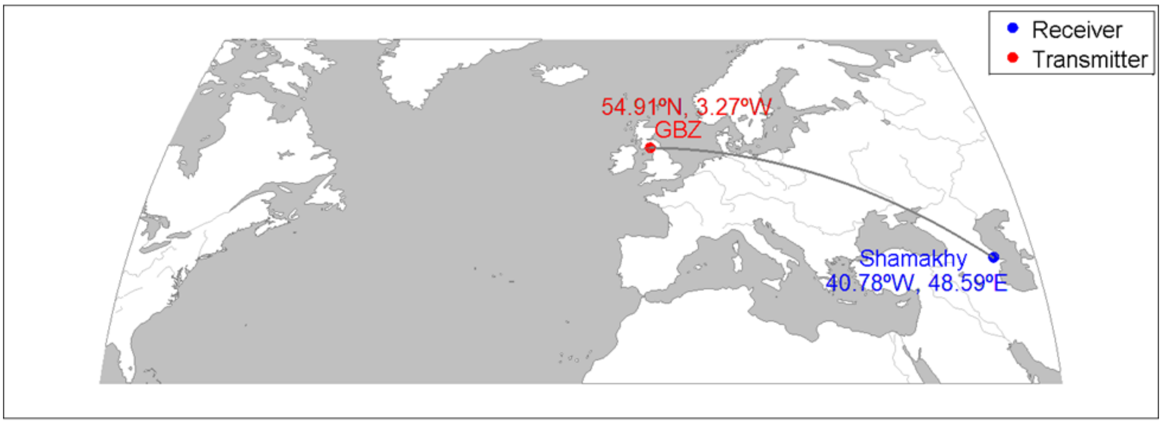

***Figure 1**. Map showing the location of transmitter and receiver stations, geographical coordinates, and VLF signal propagation path along TRGCP.*

Narrowband VLF signals transmitted from the transmitter (call sign is GBZ) located in Anthorn, UK (54ºN, 3ºW) and operating at 19.6 kHz stabilized frequency, received at

Shamakhy, Azerbaijan (40ºN, 48ºE) are used for analysis. VLF signals are recorded with AWESOME (Atmospheric Weather Electromagnetic System for Observation Modeling and Education) receiver provided by Stanford University and installed at Shamakhy Astrophysics Observatory named after Nasraddin Tusi (Figure 2). Transmitter-Receiver Great Circle Path (TRGCP) is shown in Figure 1. The distance between the GBZ transmitter and the receiver station is 5228 km.

(a) **(b)**

Figure 2. *(a) AWESOME receiver and (b) VLF antenna*

Ap index was utilized for determining geomagnetically disturbed days. A geomagnetic storm is classified as minor when the activity level is Ap<50, moderate when the storm is 50≤Ap<100, and severe when Ap≥100. Magnetic storms with Ap index above 26 were selected for analysis. Ap index data is taken from the OMNIWeb (https://omniweb.gsfc.nasa.gov/form/dx1.html). Detailed information on geomagnetic storms is given in Table 1.

The VLF DAQviewer (Data Acquisition Viewer) Matlab program was used to view VLF signal data. The DLPT depth parameter was utilized to investigate the effect of geomagnetic storms on the D-layer. A Diurnal variation of VLF signal is given in Figure 3. Sunrise Maxima, Sunrise Minima, Afternoon Maxima, Sunset Minima, and Sunset Maxima are marked with points A-E, respectively (Kumar 2018; Choudhury et al., 2015). The change in amplitude between A and B points is taken as "DLPT depth." DLPT depth was evaluated on the storm day, four days before, and four days after for each geomagnetic storm. In this way, nine days variation of DLPT depth was obtained.

Table 1. *Properties of geomagnetic storms considered in the study*

Event Date	Daily Averaged Ap index	Ap max	Start time
04 Sep 2008	31	80	04 Sep 2008 00:00 UT
11 Oct 2008	34	94	11 Oct 2008 06:00 UT
29 May 2010	28	56	29 May 2010 06:00 UT
04 Aug 2010	49	111	03 Aug 2010 18:00 UT
25 Oct 2011	38	154	24 Oct 2011 18:00 UT

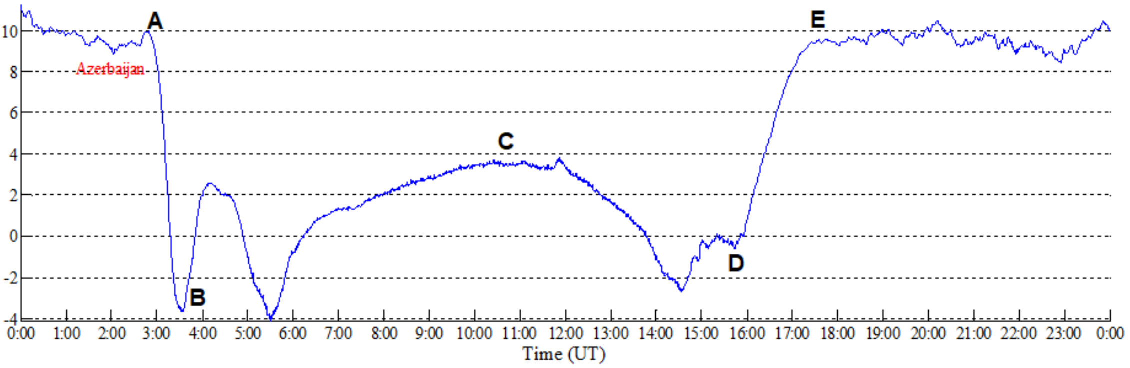

Figure 3. *A diurnal variation of GBZ signal amplitude. A-Sunrise Maxima, B-Sunrise Minima, C-Afternoon Maxima, D-Sunset Minima, E-Sunset Maxima*

3. Observational Results

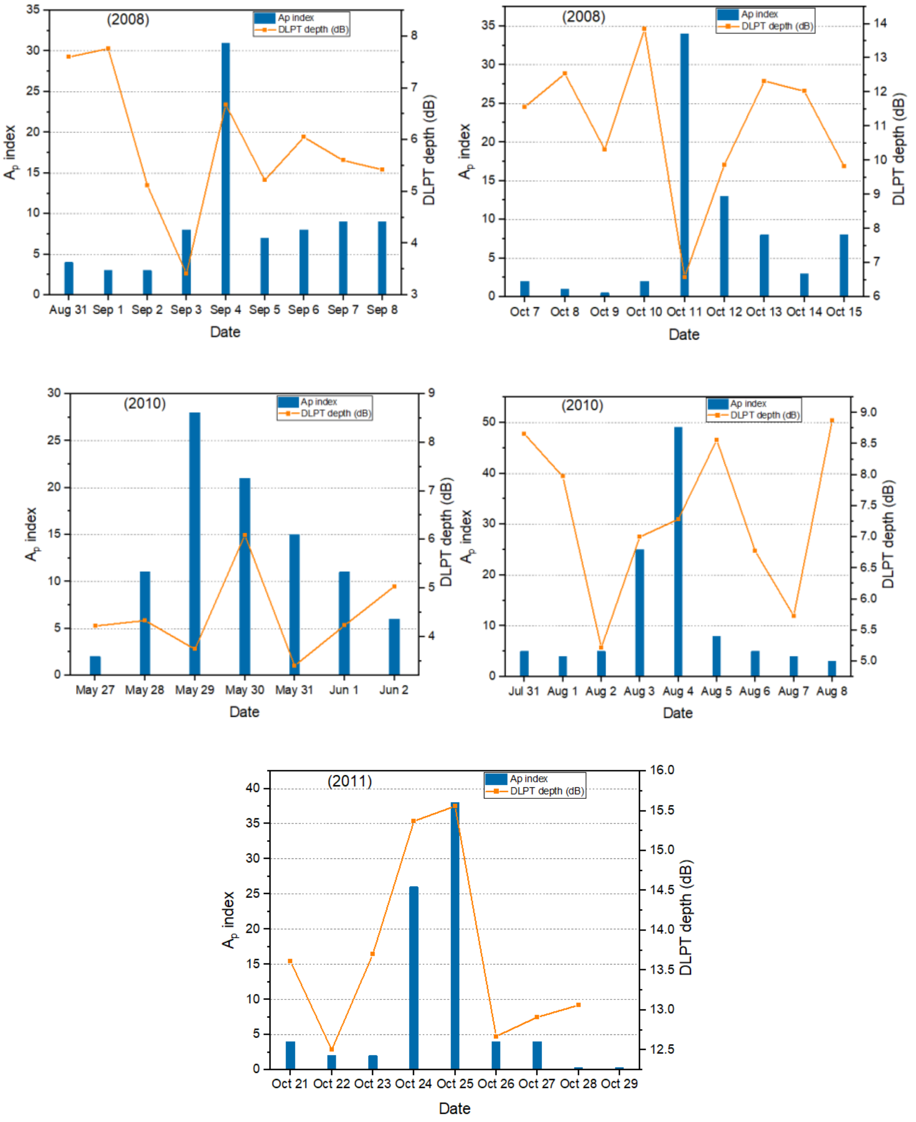

Figure 4. *Nine days variation of DLPT depth and Ap index values for all geomagnetic storms considered in the study.*

Figure 4 represents the variation of DLPT depth with bars and Ap index values with lines for all events. There was an increase in DLPT depth on the storm day for the September 2008 and October 2011 events, whereas there was an increase in the storm recovery period for the August 2010 and May 2010 events. Only for the October 11, 2008 storm, a dramatic decrease by 7dB was observed in DLPT depth

4. Discussion and Conclusions

The present paper investigated the effect of geomagnetic storms on the D layer of the ionosphere using the DLPT depth parameter of the VLF signal. The “primary storm effect” was observed on the DLPT depth parameter for three magnetic storms, but the “after-storm effect” was observed for the remaining two storms. Clilverd et al. (Clilverd 2008) found that phase advance on signal recorded at mid-latitudes is associated with magnetospheric substorms. They suggested that the phase advance is related to triggering energetic electron precipitation during the substorm, concerning electromagnetic ion cyclotron (EMIC) wave-particle interaction. Additionally, the cause of the after-storm effect at mid-latitudes is the loss of energetic electrons from Earth's radiation belt during the recovery phase of the storm (Spjeldvik et al., 1975; Larsen et al., 1976).

In this study, DLPT depth showed an increase for all geomagnetic storms, apart from one storm. An increase in DLPT depth resulted from decreased amplitude during the morning terminator with respect to the previous day. This depression of amplitude can be related to a storm-induced increase in electron concentration of the D-layer, which is to say more electron-molecule collisions and consequently leads to absorption of the signal. In the previous works, researchers discussed geomagnetic storm effects on DLPT depth. Kumar and Singh (Kumar 2018) studied a severe geomagnetic storm effect on the D region for the mid-equatorial-low path using VLF signals transmitted from GBZ and NWC transmitters. They observed that DLPT shows an increase during the recovery phase of the storm. Naidu et al. (Naidu et al., 2020) investigated the change of DLPT depth during intense magnetic storms for mid-latitude path and observed an increase in DLPT depth on the storm day, except for one event. They explained that an increase in DLPT depth could be due to a reduction in the reflection height of VLF waves resulting from the enhanced electron concentration of the D layer. Nevertheless, from the study of DLPT depth variation for low-latitude path, Choudhury et al. (Choudhury et al 2015) reported that during long-duration geomagnetic storms, DLPT depth decreases due to decreased day-night asymmetry caused by increased electron density.

Obtained results showed that the response of the D region to geomagnetic storms varies from storm to storm. We will investigate separately the influence of geomagnetic storms on the D region originating distinct solar and interplanetary sources in the near future.

Acknowledgments: We are grateful to the website of https://omniweb.gsfc.nasa.gov/form/dx1.html for Geomagnetic data.

References

Araki, T. (1974). Anomalous phase changes of transequatorial VLF radio waves during geomagnetic storms, *Journal of Geophysical Research*, Vol. 79, pp. 4811–4816.

Bouderba, Y., NaitAmor, S., Tribeche, M. (2016). Study of the solar flares effect on VLF radio signal propagating along NRK-ALG path using LWPC code, *Journal of Geophysical Research: Space Physics*, Vol. 121, pp. 6799–6807, DOI: 10.1002/2015JA022233.

Choudhury, A., De, B.K., Guha, A., Roy, R. (2015). Long-duration geomagnetic storm effects on the D region of the ionosphere: Some case studies using VLF signal, *Journal of Geophysical Research: Space Physics*, Vol. 120, pp. 778–787, DOI: 10.1002/2014JA020738.

Clilverd, M.A., Rodger, C.J., Brundell, J., Bahr, J., Cobbett, N., Moffat-Griffin, T., Kavanagh, A.J., Seppälä, A., Thomson, N.R., Friedel, R.H.W., Menk, F.W. (2008). Energetic electron precipitation during substorm injection events: High-latitude fluxes and an unexpected midlatitude signature, *Journal of Geophysical Research*, Vol. 113, A10311, DOI: 10.1029/2008JA013220.

Clilverd, M.A., Rodger, C.J., Gamble, R.J., Ulich, T., Raita, T., Seppälä, A., Green, J.C., Thomson, N.R., Sauvaud, J.A., Parrot, M. (2010). Ground-based estimates of outer radiation belt energetic electron precipitation fluxes into the atmosphere, *Journal of Geophysical Research*, Vol. 115, A12304, DOI: 10.1029/2010JA015638.

Cummer, S.A., Bell, T.F., Inan, U.S., Zanetti, L.J. (1996). VLF remote sensing of the auroral electrojet, *Journal of Geophysical Research*, Vol. 101, pp. 5381–5389, DOI: 10.1029/95JA03409.

Hayes, L.A., Gallagher, P.T., McCauley, J., Dennis, B.R., Ireland, J., Inglis, A. (2017). Pulsations in the Earth’s lower ionosphere synchronized with solar flare emission, *Journal of Geophysical Research: Space Physics*, Vol. 122, pp. 9841–9847, DOI: 10.1002/2017JA024647.

Korsakov, A.A., Kozlov, V.I., Karimov, R.R. (2018). Solar flares effects in amplitude and phase variations of VLF radio station signals during September 2017, *24th International Symposium on Atmospheric and Ocean Optics: Atmospheric Physics*, Tomsk, Russian Federation, DOI: 10.1117/12.2504428.

Kumar, A., Kumar, S. (2014). Space weather effects on the low latitude D-region ionosphere during solar minimum, *Earth, Planets and Space*, Vol. 66, 76, DOI: 10.1186/1880-5981-66-76.

Kumar, A., Singh, R. (2018). St. Patrick’s Day geomagnetic storm effect on mid-low-equatorial D-region ionosphere using very low-frequency radio waves, *Proceedings of the 2nd URSI AT-RASC*, Gran Canaria, 28 May – 1 June 2018.

Kumar, A., Venkatesham, K., Kumar, S., Singh, R., Tiwari, P., Singh, A.K. (2018). Effects of St. Patrick’s Day geomagnetic storm of March 2015 and of June 2015 on low-equatorial D region ionosphere, *Journal of Geophysical Research: Space Physics*, Vol. 123, pp. 6836–6850, DOI: 10.1029/2018JA025536.

Larsen, T.R., Reagan, J.B., Imhof, W.L., Montbriand, L.E., Belrose, J.S. (1976). A coordinated study of energetic electron precipitation and D region electron concentrations over Ottawa during disturbed conditions, *Journal of Geophysical Research*, Vol. 81, pp. 2200–2212, DOI: 10.1029/JA081i013p02200.

Lastovicka, J. (1996). Effects of geomagnetic storms in the lower ionosphere, middle atmosphere and troposphere, *Journal of Atmospheric and Terrestrial Physics*, Vol. 58, pp. 831–843, DOI: 10.1016/0021-9169(95)00106-9.

Naidu, P.P., Madhavilatha, T., Devi, M.I. (2020). Influence of geomagnetic storms on the mid latitude D and F2 regions, *Annals of Geophysics*, Vol. 63, No. 2, GM214, DOI: 10.4401/ag-8127.

OMNIWeb. (n.d.). *OMNI data interface*. Available at: https://omniweb.gsfc.nasa.gov/form/dx1.html.

Peter, W.B., Chevalier, M.W., Inan, U.S. (2006). Perturbations of midlatitude subionospheric VLF signals associated with lower ionospheric disturbances during major geomagnetic storms, *Journal of Geophysical Research*, Vol. 111, A03301, DOI: 10.1029/2005JA011346.

Rodger, C.J., Clilverd, M.A., Thomson, N.R., Gamble, R.J., Seppälä, A., Turunen, E., Meredith, N.P., Parrot, M., Sauvaud, J.-A., Berthelier, J.-J. (2007). Radiation belt electron precipitation into the atmosphere: Recovery from a geomagnetic storm, *Journal of Geophysical Research*, Vol. 112, A11307, DOI: 10.1029/2007JA012383.

Selvakumaran, R., Kumar, A., Gokani, S.A., Veenadhari, B., Kumar, S., Venkatesham, K., Phanikumar, D.V., Singh, A.K., Siingh, D., Singh, R. (2015). Solar flares induced D-region ionospheric and geomagnetic perturbations, *Journal of Atmospheric and Solar-Terrestrial Physics*, Vol. 123, pp. 102–112, DOI: 10.1016/j.jastp.2014.12.009.

Sharma, A.K., More, C.T. (2018). Effect of solar X-ray flares on VLF radio wave signal strength at 19.8 and 24 kHz received at Khatav (India) (16°46'N, 75°53'E), *Journal of Space Science & Technology*, Vol. 6, pp. 2321–2837.

Spjeldvik, W.N., Thorne, R.M. (1975). The cause of storm after effects in the middle latitude D-region, *Journal of Atmospheric and Terrestrial Physics*, Vol. 37, pp. 777–795.

Srećković, V.A., Šulić, D.M., Vujčić, V., Jevremović, D., Vyklyuk, Y. (2017). The effects of solar activity: Electrons in the terrestrial lower ionosphere, *Journal of the Geographical Institute “Jovan Cvijić” SASA*, Vol. 67, pp. 221–233, DOI: 10.2298/IJGI1703221S.

Thomson, N.R. (1993). Experimental daytime VLF ionospheric parameters, *Journal of Atmospheric and Terrestrial Physics*, Vol. 55, pp. 173–184.

DOI: 10.31401/WS.2025.proc.22

Radiation Conditions in Mars Vicinity during Different Phases of the Solar Cycle According Measurements by Liulin-MO Dosimeter aboard the Trace Gas Orbiter

Semkova J.[1], Koleva R.[1], Benghin V.[1], Krastev K.[1], Matviichuk Yu.[1], Tomov B.[1], Bankov N.[1], Maltchev St.[1], Dachev Ts.[1], Mitrofanov I.[2], Golovin D.[2], Mokrousov M.[2], Litvak M.[2], Lukyanov N.[2], Shurshakov V.[3], Drobyshev S.[3]

[1]Space Research and Technology Institute, Bulgarian Academy of Sciences, Sofia, Bulgaria;
jsemkova@stil.bas.bg
[2]Space Research Institute, Russian Academy of Sciences, Moscow, Russia
[3]State Scientific Center of Russian Federation, Institute of Biomedical Problems, Russian Academy of Sciences, Moscow, Russia

Abstract

Presented are the results for the dose rates and particle fluxes of the galactic and solar cosmic rays in the interplanetary space at about 1.5 AU and in Mars orbit at 400 km altitude, obtained during different phases of solar cycles 24 and 25, in the period April 2016 - May 2025. Data are provided by the Liulin-MO dosimeter aboard ExoMars Trace Gas Orbiter. Discussed is the selection of the best time interval in the solar cycle for a future manned trip to Mars, regarding the radiation safety. The obtained results may be used for verification and benchmarking of the galactic and solar cosmic rays models in free space and in Mars orbit.

Keywords: space radiation measurements; galactic and solar cosmic rays; Mars

1. Introduction

Mars is an ambitious target for future human exploration. The radiation environment during the transit and in Mars vicinity can be very hazardous for future human missions to the planet [Miroshnichenko and Petrov, 1985; Shafirkin and Grigoryev, 2009; Cucinotta, 2015]. In the interplanetary space and at Mars orbit the radiation field consists of two types of primary particles: galactic cosmic rays (GCR) and solar energetic particles (SEPs). GCR are a permanent source of radiation hazard in space. In the Solar system GCR flux is isotropic and their flux and spectra show a long term modulation that anti-correlates with the solar activity. The spectrum of the GCR is wide in both composition (from protons to the heaviest nuclei) and energies (from a few keV to 10^{21} eV) [Potgieter, 2013]. Radiations induced by GCR nuclei, especially those with high energy (e.g., protons above 100 MeV) and high charge ions, remain one of the major concerns in the planning of long-term deep-space human and robotic missions [Townsend et al., 1994; Cucinotta et al, 2013; Dachev et al, 2020; Guo et al, 2021]. SEP events are transient injections into the heliosphere of protons, electrons, and higher mass charged particles with a wide range of energies (tens of keVs to GeVs), spectra, compositions, and intensities. They follow energetic solar eruptions that are generally associated with flares and coronal mass ejections [Reames, 2013; Velinov et al, 2013]. SEP events take place much more frequently during the increasing phase of the solar cycle. Typical SEPs are known to pose a small health risk to astronauts and can be effectively attenuated by using relatively thin shielding materials, even though they can influence mission planning or interfere with mission activities such as extravehicular activities. Previous investigations based on calculations show that the expected doses to a future manned trip to Mars with start at the solar maximum are significantly lower than the doses to be obtained during other phases of the solar cycle [Shafirkin and Grigoryev, 2009; Cucinotta, 2015]. Nevertheless, although rare, large SEP events can be lethal [Committee for Evaluation of Space Radiation Cancer Risk Mode, 2012].

The Trace Gas Orbiter (TGO) spacecraft launched in March 2016 carries the Fine Resolution Epithermal Neutron Detector (FREND) instrument [Mitrofanov et al, 2018]. The Liulin-MO dosimeter is a FREND module which has provided and is providing in-situ measurements of the radiation environment during the TGO interplanetary travel and at Martian orbit [Semkova et al, 2018].

Liulin-MO data about the radiation environment during TGO cruise to Mars and in high elliptic Mars orbits (Mars capture orbits MCO1 with 98000 - 230 km altitude and MCO2 with 37150 - 200 km altitude) were taken in the period from April 2016 to March 2017. Since May 2018 Liulin-MO investigates the radiation conditions at Mars science orbit (MSO), which is a circular orbit with 400 km altitude (varying within ±25 km in every orbital pass), 74^0 inclination, ~ 2 hours orbit period.

Liulin-MO measurements to date cover the decreasing and minimum phases of the solar activity in solar cycle 24 and the rising phase, maximum, and decreasing phase near the maximum of cycle 25. Up to July 2021, the dosimeter measured the dosimetric parameters of GCR in the interplanetary space and at TGO Martian orbit, without registering any SEP events. The highest values of the dose rate and flux from GCR in MSO were registered from March to August 2020. Since July 2021, during the increasing phase and at the maximum of solar cycle 25, a number of SEP events have been observed at TGO MSO. Some of the investigated SEP events contribute significantly to the radiation environment at Martian orbit. The most powerful SEP event registered up to now at TGO orbit started on 20 May 2024. The maximum dose rate during this SEP event was 2800±280 μGy h^{-1} and the maximum particle flux – 383±19 cm^{-2} s^{-1}. The total dose from SEPs for this SEP event was 24.7±2.5 mGy - equal to the dose from the GCR received for about 200 days at this phase of solar cycle 25, the SEPs dose equivalent for the entire event is 43.7±8.7 mSv - approximately the dose equivalent received for 57 days from GCR [Semkova et al, 2025]. The other very strong SEP event was observed on 15 February 2022 – it is about twice weaker than the event of 20 May 2024 [Semkova et al, 2022a; Semkova et al, 2023].

One of the scientific objectives of the Liulin-MO investigations is to provide data for verification and benchmarking of the radiation environment models and assessment of the radiation risk to the crewmembers of future exploratory flights [Semkova et al, 2018].

Models of GCR describe their spectra and intensity in free space, away from any celestial body.

To use Liulin-MO data measured at MSO for verification and benchmarking of the radiation environment models and assessment of the radiation risk in free space, the effect of Mars presence on the measured fluxes and dose rates in TGO MSO has to be accounted. In MSO the planet shades single detectors’ field of view (FOV), thus reducing part of free-space GCR flux. The shaded part of FOV is an angle dependent on TGO orientation and altitude. TGO altitude varies within 50 (±25) km in every orbital pass. In previous works the shading effect of Mars for different orientation of TGO, and the contribution of albedo particles and gamma rays from Mars atmosphere and surface to the measured particle fluxes and dose rates by Liulin-MO at TGO MSO were estimated [**Krastev et al, 2019;** Semkova et al, 2022b**].**

In this paper we present and discuss the results for the charged particle fluxes and dose rates at 1.5 AU during different phases of the solar activity cycle based on measurements by the Liulin-MO dosimeter on TGO.

2. Instrumentation and method for calculation of the dose rate and particle flux of cosmic rays in free space at 1.5 AU based on measurements by Liulin-MO dosimeter on TGO at MSO

Liulin-MO contains two dosimetric telescopes –BA and DC, arranged at perpendicular directions [Semkova et al, 2018]. A schematic view of the location of the detectors inside the Liulin-MO box is presented in Figure 1a. Each pair of the dosimetric telescopes consists of two 300 µm thick, 20x10 mm area rectangular Si PIN photodiodes-– A, B, C and D. The parallel detectors A and B make up the BA telescope, detectors D and C make the DC telescope. One of the detectors in each pair of parallel detectors and its corresponding electronics measures the energy deposition spectrum in the range ~ 0.08÷18 MeV. Those are detectors B and D. The other detector in each pair of parallel detectors measures the energy deposition spectrum in the range ~ 0.3 ÷ 190 MeV. Those are detectors A and C. The energy deposition spectrum in the single detector named further B(A) is obtained by combining the energy deposition spectrum measured by B in the range of ~ 0.08 - 15.9 MeV with the energy deposition spectrum measured by A in the range of ~ 16 - 190 MeV. The same procedure is used to obtain the energy deposition spectrum in the single detector D(C). In that way, each pair of two parallel detectors and their corresponding electronics provide data in the energy deposition range of ~ 0.08 - 190 MeV.

Using the energy deposition spectrum in the detectors one can calculate the dose rate *D*, particle flux *F*, linear energy transfer, and to obtain the radiation quality factor <*Q*> and the biologically significant dose equivalent rate. We calculate the flux as the number of particles crossing a unit plane of one square centimeter during one second.

In this paper we use and discuss the parameters provided by the single detectors B(A) and D(C) in the two perpendicular directions BA and DC.

Data must be understood in the context of the shielding from the free-space radiation environment provided by the mass of materials surrounding the instrument’s detectors. The shielding distribution covers a thickness range from 0.9 to 178 g cm^{-2}. The mean shielding is about 20 g cm^{-2} [Semkova et al, 2021]. The energy threshold for the minimum shielding is 1.7 MeV for electrons, 30 MeV for protons and 6.8 GeV for iron ions.

At MSO when TGO is pointed to nadir (along – Y axis), the angles between the detector’s axes and the nadir direction are 90^0 (Figure 1b). In this ‘nominal’

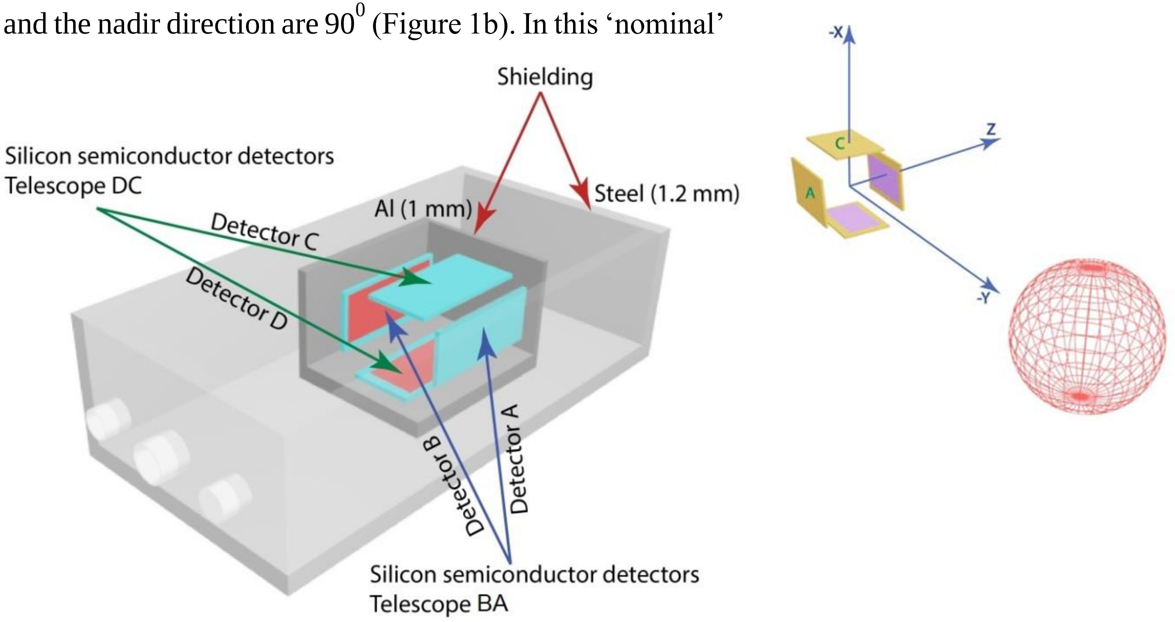

(a) (b)

Figure 1. (a) *A schematic view of Liulin-MO detectors’ location in the dosimeter box;* ***(b)*** *Dosimeter axes orientation relatively to TGO nadir (Semkova et al., 2021).*

orientation, which holds most of the time, the shading effect of Mars on the GCR flux (reduced part of free-space GCR flux) is about 23%. In first approximation the measured doses depend mainly on the distance to the planet, not on the TGO orientation [Krastev et al, 2019].

Estimation of the albedo flux from Mars surface and atmosphere, performed by Semkova et al, 2022 showed that its contribution to the total flux (GCR plus albedo) at TGO altitude in MSO is about 4-5%.

Based on these results a method was developed for calculation of the dose rate and particle flux of cosmic rays in free space at 1.5 AU from the Liulin-MO dosimeter measurements in MSO, accounting for the shading of cosmic rays fluxes from Mars and for the contribution of Mars albedo. Thus, the particle flux of cosmic rays in free space at 1.5 AU is obtained by dividing the average flux measured at TGO MSO in the single detectors B(A) and D(C) by 0.822. The dose rate of cosmic rays in free space at 1.5 AU is obtained by dividing the average dose rate measured in TGO MSO in the single detectors B(A) and D(C) by 0.766.

3. Results and discussion

The dose rate and particle flux of cosmic rays in free space at 1.5 AU based on measurements by Liulin-MO dosimeter on TGO in the period May 2016 - May 2025 are presented in Figure 2. The values from May to September 2016 were measured during the transit to Mars. The values in the period May 2018 - May 2025 were calculated from measurements at MSO as described above.

The gradual increase of the dose rates and fluxes from May 2018 to February 2020 corresponds to the increase of GCR intensity during the declining of solar cycle 24. During March–August 2020, the radiation values are maximal, corresponding to the minimum of cycle 24 and the transition to cycle 25. Since September 2020, there has been seen a decrease of the GCR dose rates and fluxes, corresponding to the increasing phase of solar cycle 25. A number

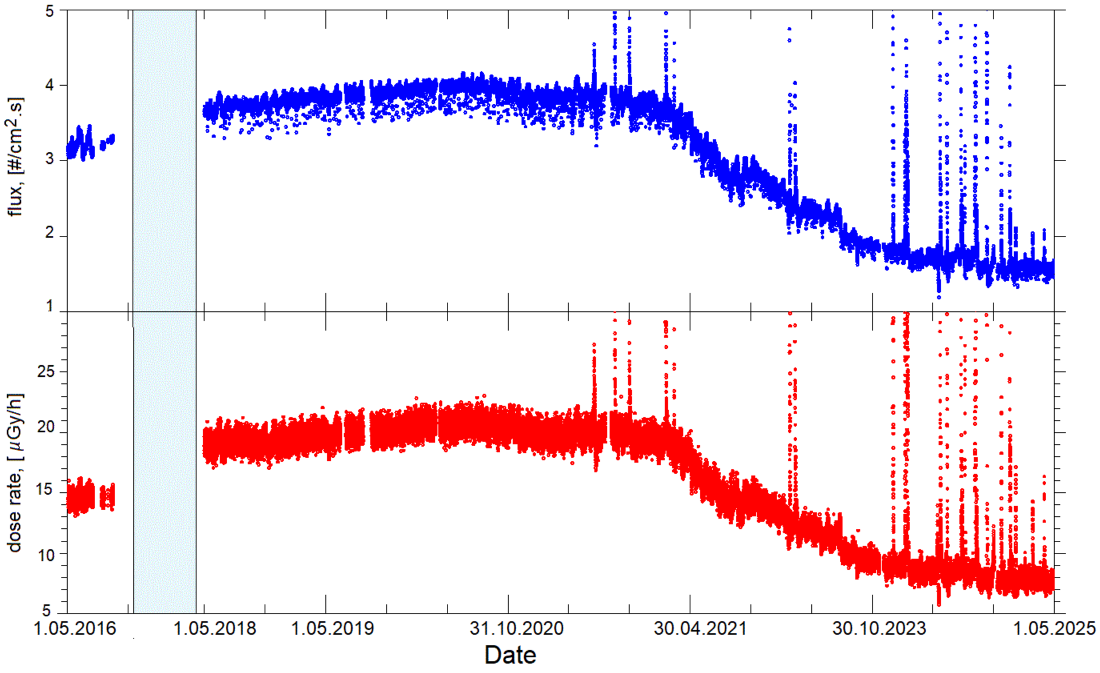

Figure 2. *Fluxes (top) and dose rates (bottom) in free space at about 1.5 AU obtained from measurements by Liulin-MO on TGO in May 2016 –May 2025. The shaded area indicates a period of missing data.*

of SEP events were observed from July 2021 to May 2025 (the spikes superposed on the GCR time profiles in Figure 2). More detailed infommation about SEP events registered at Martian orbit by Liulin-MO during 25th solar cycle may be found in Koleva et al, 2025.

Table1 summarizes the dose rate and particle flux of GCR obtained in free space and in TGO MSO during different phases of solar activity from April 2016 to May 2025.

Table1. *Dose rate D and particle flux F of GCR during different phases of the solar cycle. Superscripts* ^{a} *and* ^{b} *show correspondingly the measured and calculated values.*

Month, Year, Solar cycle phase	*D* in Si [μGy h^{-1}] (TGO MSO)	*D* in Si [μGy h^{-1}] (free space 1.5 AU)	*F* [cm^{-2} s^{-1}] (TGO MSO)	*F* [cm^{-2} s^{-1}] (free space 1.5 AU)
September, 2016, first half of decreasing phase of cycle 24	12.4±1.9^b	16.2±1.6^a	2.6±0.26^b	3.2±0.16^a
March, 2020, minimum of cycle 24	15.8±1.6^a	20.7±3.1^b	3.3±0.165^a	4±0.4^b
March 2022, first half of increasing phase of cycle 25	14.4±1.4^a	18.8 ±2.8^b	3±0.15^a	3.4±0.34^b
October, 2024, maximum of cycle 25	6±0.6^a	7.8±1.17^b	1.3±0.065^a	1.6±0.16^b
May, 2025, start of the decreasing phase close to the maximum of cycle 25	6±0.6^a	7.8±1.17^b	1.3±0.065^a	1.6±0.16^b

Table 2 presents the total dose rate from GCR and SEPs obtained in free space and in TGO MSO during different phases of the solar cycle. Chosen are 6-months periods corresponding approximately to the time necessary for a transit Earth - Mars or vice versa.

Table 2. *Total dose rate D during different phases of the solar cycle. Superscripts* ^{a} *and* ^{b} *show correspondingly the measured and calculated values.*

Months, Year, (Radiation contributors) - Solar cycle phase	*D* in Si [μGy h^{-1}] (TGO MSO)	*D* in Si [μGy h^{-1}] (free space at 1.5 AU)
April-September, 2016, (GCR, no SEPs)-first half of decreasing phase of cycle 24	12.2±1.8^b	15.9 ±1.6^a
May-October, 2018, (GCR, no SEPs)-second half of decreasing phase of cycle 24	14.6±1.5^a	19.1±2.9^b
February-July, 2020, (GCR, no SEPs)-around the minimum of cycle 24	15.8±1.6^a	20.6±3.1^b
February-July, 2022, (GCR and SEPs)-first half of increasing phase of cycle 25	16.2±1.6^a	21.2±3.2^b
May-October, 2024, (GCR and powerful SEPs)-near to and at the maximum of cycle 25	13.9±1.4^a	18.2±2.7^b
December 2024-May 2025, (GCR and weak SEPs) maximum and start of the decreasing phase of cycle 25	6.4±0.64^a	8.4±1.26^b

The calculation of the dose rates in free space shown in Table 2 is made under the presumption that the SEPs distribution at 1.5 AU is isotropic, like the distribution of GCR. This is not always the case, but the simulations conducted for some of the most powerful SEP events observed by Liulin-MO [Krastev et al, 2023] show that the modeled isotropic distribution of SEPs correlates satisfactorily with the measurement results. Besides that, as was already mentioned, the shading coefficient of the dose rate at TGO MSO does not depend significantly on the TGO orientation [Krastev et al, 2019]. Because of that we use the same coefficient 0.766 for converting the measured in TGO MSO dose rate for GCR and for mixed radiation of GCR and SEPs.

The results show that at 1.5 AU the dose rate and particle flux of GCR during the maximum of solar cycle 25 (October 2024) are about 38-39% of the corresponding values during the minimum of solar cycle 24 (March 2020).

The dose rate both from GCR and SEPs near to and at the maximum of solar cycle 25 in May-October 2024 is below, but comparable to the dose rate received from GCR near to and at the minimum of solar cycle 24 in February-July 2020. This is an important result as in the period May-October 2024 six strong SEP events were registered, including the most powerful SEP observed up to now by Liulin-MO – the event of 20 May 2024 (see Semkova et al, 2025). The dose from SEPs is larger than the dose from GCRs in this period. Taking into account that the radiation quality factor <Q> of the combined field of GCR and SEPs is lower than <Q> of the GCR [Semkova et al, 2023; Semkova et al, 2025], the biologically significant dose equivalent rate during the maximum of cycle 25 is significantly lower than the dose equivalent rate during the minimum of cycle 24.

The lowest dose rates for a 6-months time interval are registered in December 2024 - May 2025 - the period covering the maximum and start of the decreasing phase of cycle 25 – they are about 2 times less that the dose rates during the other phases of cycles 24 and 25. The relatively weak SEPs during this period contribute to the increase of the average dose rate of GCR by less than 10%.

These results are in agreement with calculations, showing that the expected doses to a future manned trip to Mars, that will start at solar maximum are lowest [Shafirkin and Grigoryev, 2009; Cucinotta, 2015]. This is also consistent with the previous experimental investigations conducted by RAD instrument onboard Curiosity rover during the transit to Mars and on Mars surface [Guo et al, 2021].

4. Data availability

The data from the Liulin-MO measurements used in this paper are part of the Unified web-based database with Liulin-type instruments available at https://esa-pro.space.bas.bg/datasources.

Conclusion

The long-term measurements of the radiation values, performed by the Liulin-MO dosimeter on Trace Gas Orbiter at MSO, behind a mean shielding of about 20 g cm^{-2}, and estimation of the dose rate and particle flux of cosmic rays in free space at 1.5 AU based on them show that:

- The dose rate and particle flux both from GCR and powerful SEP events near to and at the maximum of solar cycle 25 in May-October 2024 is below, but comparable, to the corresponding values received from GCR near to and at the minimum of solar cycle 24 in February - July 2020. The dose equivalent rate during the maximum of cycle 25 is significantly lower than the dose equivalent rate during the minimum of cycle 24.

- The lowest dose rates for a 6-months period, corresponding approximately to the time necessary for a transit to Mars or vice versa, are registered in December 2024 - May 2025 - the period that covers the maximum and the start of the decreasing phase of cycle 25. They are about 2 times less that the dose rates during the other phases of cycles 24 and 25.
- These results are important about the selection of the best time interval in the solar cycle for a future manned trip to Mars. They confirm and specify previous studies that the expected dose for a Mars mission launched during the solar maximum is significantly less than the dose for a mission taken during other phases of the solar cycle. But a trip during the solar maximum is accompanied with a potential risk of significant, unpredictable dose contributions by SEPs. A real time warning of SEP events and a radiation shelter onboard the spacecraft may reduce the radiation risk to the crew during the transit to the planet and back. The most effective countermeasure for the radiation risk would be reducing the transit time using new technological developments.

The obtained results for dose rates and particle fluxes during different phases of solar cycles 24 and 25 may be used for verification and benchmarking of cosmic rays models in free space at 1.5 AU and at Mars orbit.

References

Committee for Evaluation of Space Radiation Cancer Risk Model; Space Studies Board, National Research Council. (2012). *Technical evaluation of the NASA model for cancer risk to astronauts due to space radiation.* Washington (DC): National Academies Press (US). Available at: http://www.ncbi.nlm.nih.gov/books/NBK189542/.

Cucinotta, F.A., Kim, M.H.Y., Chappell, L.J., Hu, J.L. (2013). How safe is safe enough? Radiation risk for a human mission to Mars, *PLoS One*, Vol. 8, e74988, DOI: 10.1371/journal.pone.0074988.

Cucinotta, F.A. (2015). Review of NASA approach to space radiation risk assessments for Mars exploration, *Health Physics*, Vol. 108, No. 2, pp. 131–142, DOI: 10.1097/HP.0000000000000255.

Dachev, T.P., Tomov, B.T., Matviichuk, Y.N., Dimitrov, P.G., Semkova, J.V., et al. (2020). Solar modulation of the GCR flux and dose rate, observed in space between 1991 and 2019, *Life Sciences in Space Research*, Vol. 26, pp. 114–124, DOI: 10.1016/j.lssr.2020.06.002.

Guo, J., Zeitlin, C., Wimmer-Schweingruber, R.F., Hassler, D.M., Ehresmann, B., et al. (2021). Radiation environment for future human exploration on the surface of Mars: The current understanding based on MSL/RAD dose measurements, *Astronomy and Astrophysics Review*, Vol. 29, No. 1, pp. 1–81, DOI: 10.1007/s00159-021-00136-5.

Koleva, R., Semkova, J., Benghin, V., Gopalswamy, N., Matviichuk, Yu., et al. (2025). Catalog of solar energetic particles events registered by Liulin-MO dosimeter in Martian orbit during the current solar cycle, *Proceedings of the Seventeenth Workshop "Solar Influences on the Magnetosphere, Ionosphere and Atmosphere"*, ISSN 2367-7570 (this issue).

Krastev, K., Semkova, J., Koleva, R., Bankov, N., Benghin, V., Drobishev, S. (2019). The shading effect for doses and galactic cosmic rays fluxes measured by Liulin, *Proceedings of the Eleventh Workshop "Solar Influences on the Magnetosphere, Ionosphere and Atmosphere"*, ISSN 2367-7570, pp. 31–34, DOI: 10.31401/WS.2019.proc.

Krastev, K., Semkova, J., Koleva, R., Benghin, V., Drobishev, S. (2023). Numerical simulation of the LIULIN-MO device, *Proceedings of the Fifteenth Workshop "Solar Influences on the Magnetosphere, Ionosphere and Atmosphere"*, June 2023, ISSN 2367-7570, pp. 88–94, DOI: 10.31401/WS.2023.proc.

Miroshnichenko, L.I., Petrov, V.M. (1985). *Dynamics of the radiation conditions in space*, Energoatomizdat, 152 p. (in Russian).

Mitrofanov, I., Malakhov, A., Bakhtin, B., Golovin, D., Kozyrev, A., et al. (2018). Fine Resolution Epithermal Neutron Detector (FREND) onboard the ExoMars Trace Gas Orbiter, *Space Science Reviews*, Vol. 214, 86, DOI: 10.1007/s11214-018-0522-5.

Potgieter, M.S. (2013). Solar modulation of cosmic rays, *Living Reviews in Solar Physics*, Vol. 10, 3, DOI: 10.12942/lrsp-2013-3.

Reames, D.V. (2013). The two sources of solar energetic particles, *Space Science Reviews*, Vol. 175, pp. 53–92, DOI: 10.1007/s11214-013-9958-9.

Semkova, J., Koleva, R., Benghin, V., Dachev, T., Matviichuk, Yu., et al. (2018). Charged particles radiation measurements with Liulin-MO dosimeter of FREND instrument aboard ExoMars Trace Gas Orbiter during the transit and in high elliptic Mars orbit, *Icarus*, Vol. 303, pp. 53–66, DOI: 10.1016/j.icarus.2017.12.034.

Semkova, J., Koleva, R., Benghin, V., Dachev, T., Matviichuk, Yu., et al. (2021). Results from radiation environment measurements aboard ExoMars Trace Gas Orbiter in Mars science orbit in May 2018–December 2019, *Icarus*, Vol. 361, 114264, DOI: 10.1016/j.icarus.2020.114264.

Semkova, J., Koleva, R., Benghin, V., Krastev, K., Matviichuk, Yu., et al. (2022a). Observation of solar energetic particle events onboard ExoMars TGO in July 2021–March 2022, *Proceedings of the Fourteenth Workshop "Solar Influences on the Magnetosphere, Ionosphere and Atmosphere"*, June 2022, ISSN 2367-7570, pp. 55–60, DOI: 10.31401/WS.2022.proc.

Semkova, J., Benghin, V., Guo, J., Zhang, J., Da Pieve, F., et al. (2022b). Comparison of the flux measured by Liulin-MO dosimeter in ExoMars TGO science orbit with the calculations, *Life Sciences in Space Research*, Vol. 39, pp. 119–130, DOI: 10.1016/j.lssr.2022.08.007.

Semkova, J., Koleva, R., Benghin, V., Krastev, K., Matviichuk, Yu., et al. (2023). Observation of the radiation environment and solar energetic particle events in Mars orbit in May 2018–June 2022, *Life Sciences in Space Research*, Vol. 39, pp. 106–118, DOI: 10.1016/j.lssr.2023.03.006.

Semkova, J., Koleva, R., Benghin, V., Gopalswamy, N., Matviichuk, Yu., et al. (2025). Radiation environment on TGO Mars orbit during solar particle events in January–October 2024: Corresponding solar eruptions and GOES proton fluxes data, *Life Sciences in Space Research*, Vol. 45, pp. 117–134, DOI: 10.1016/j.lssr.2025.02.010.

Shafirkin, A.V., Grigoryev, Y.G. (2009). *Interplanetary and orbital space flights: The radiation risk to astronauts (Radiobiological basis)*, 412 p., Economica (in Russian).

Townsend, L.W., Cucinotta, C.F., Wilson, J.W., et al. (1994). Solar modulation and nuclear fragmentation effects in galactic cosmic ray transport through shielding, *Advances in Space Research*, Vol. 14, pp. 853–861, DOI: 10.1016/0273-1177(94)90550-9.

Velinov, P.I.Y., Asenovski, S., Kudela, K., Lastovicka, J., Mateev, L., et al. (2013). Impact of cosmic rays and solar energetic particles on the Earth's ionosphere and atmosphere, *Journal of Space Weather and Space Climate*, Vol. 3, A14, pp. 1–17, DOI: 10.1051/swsc/2013036.

DOI: 10.31401/WS.2025.proc.23

Proceedings of
the Seventeenth Workshop “Solar Influences on the Magnetosphere, Ionosphere and Atmosphere”
June, 2025

Research Unit for Solar Activity Monitoring, Climate Change and Light Pollution

Simić Z., Damljanović G., Samurović S., Živanović I.

Astronomical Observatory, Volgina 7, 11060 Belgrade, Serbia
zsimic@aob.rs

Abstract

The Research Unit (RU) has been performing the following activities:

i) Monitoring of solar activity both by using the resources of the Astronomical Observatory (e.g., a small refractor) and by analyzing the data available from various satellites. The obtained measurements are used to inform the public about the Sun's activity and accompanying phenomena.

ii) Study of natural causes that may contribute to climate change.

iii) Study of light pollution, one of the least understood forms of pollution on Earth using various observational instruments mounted at the Astronomical Observatory and Astronomical Station Vidojevica (ASV), operated by the Astronomical Observatory using standard astronomical techniques. These activities are performed within the three-year PRISMA project (started in January 2024) of the Urban Observatory of Belgrade, UrbObsBel (Urban Observatory of Belgrade) funded by the Science Fund of the Republic of Serbia. Astronomical Observatory coordinates the research of light pollution in Belgrade and beyond. Researchers from the Institute of Physics, the Faculty of Science, University of Novi Sad, as well as the Faculty of Medicine, University of Belgrade participate in these activities regarding the study of this problem, and all four scientific research organizations will be at the center of all future initiatives aimed to analyze and carry out activities to solve the problem of light pollution (such as, for example, the creation of dark-sky parks, the implementation of adaptive lighting systems, etc.).

iv) In addition to the above-mentioned activities, the RU also deals with the monitoring of various effects in the Earth's atmosphere using instruments installed at the Astronomical Observatory.

Keywords: Sun, climate change, light pollution

1. Introduction

In Septembar 2023 at the Astronomical Observatory of Belgrade the Research Unit (RU) for monitoring solar activity, climate change and light pollution was formed (https://www.aob.rs/en/research-en/research-units/296-research-unit-for-solar-activity-monitoring-climate-change-and-light-pollution). The RU has been performing the following activities mentioned in the abstract of this paper.

The members of the RU are: Dr. Srdjan Samurović, principal research fellow, Astronomical Observatory, RU lead, Dr. Goran Damljanović, principal research fellow, Astronomical Observatory, Belgrade, RU member, Dr. Zoran Simić, principal research fellow, Astronomical Observatory, Belgrade, RU member and Dr. Ivan Živanović, research associate, RU member. In the work of the RU the following associates also participate: Dr. Zorica Cvetković, principal research fellow, Institute of Physics, Belgrade, Dr. Rade Pavlović, principal research fellow, Institute of Physics, Belgrade, Dr. Dragan Lukić, research associate, Institute of Physics, Belgrade, Dr. Branislav Rovčanin, senior research associate, Faculty of Medicine, University of Belgrade and Dr. Dajana Bjelajac, assistant professor, Faculty of Sciences, University of Novi Sad.

1.1. Solar Activity Monitoring

The main results are in area of investigations of the different physical parameters of the sunspots and small-scale structures on the Sun. First of them is the radial distribution of the vertical component of magnetic field which is obtained using the satellite data (SDO – Solar Dynamics Observatory) [Živanović et al., 2016]. Obtained radial distribution of the vertical component of the magnetic field is presented on Fig. 1.

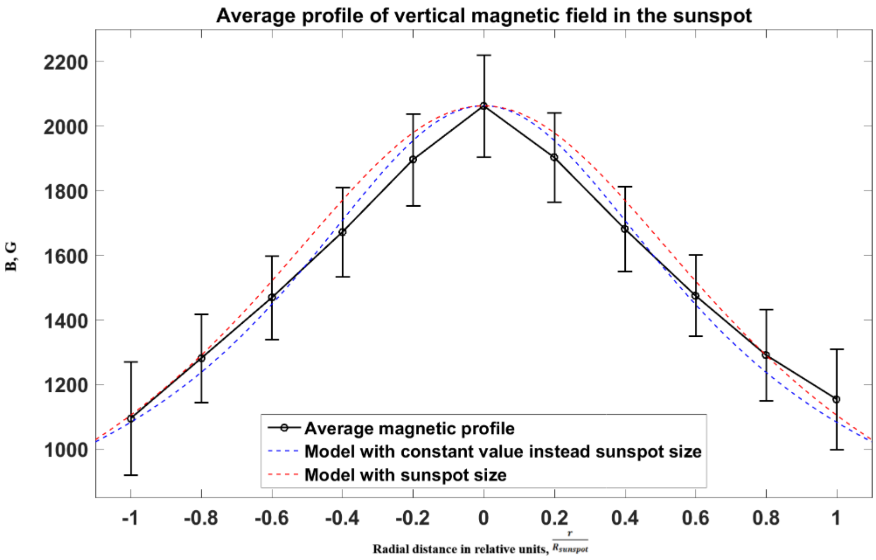

Figure 1. *The radial distribution of the vertical component of the magnetic field in sunspots obtained by the satellite (SDO – Solar Dynamics Observatory) data.*

Another important result is the evaluation of the superconvective cells depth with the analysis of the differential rotation of small-scale structures on the Sun and helioseismology data. In this research new method of the obtaining the differential rotation is used. This research is presented in work [Živanović et al., 2021]. Obtained result is presented on Fig. 2 and Fig. 3. The obtained estimation of the depth of the superconvective cells is about 30 Mm.

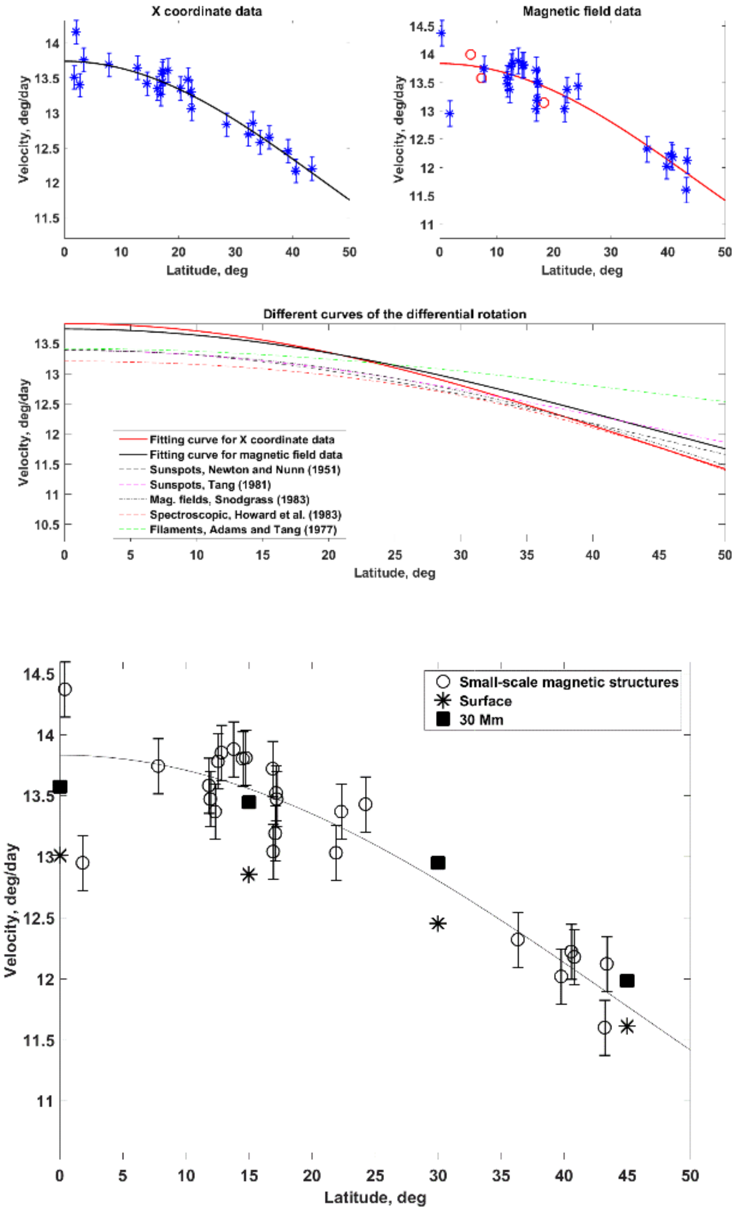

Figure 2. *Different curves of the differential rotation of the Sun are presented on the left side. These curves were obtained by different authors and different methods. Two of them are obtained by us [Živanović et al., 2021]. On the right side the curve of the differential rotation obtained by us is presented by the black line. Data from helioseismology marked by black squares presents the velocities of the differential rotation on the depth of 30 Mm, black asterisks marks the velocities of differential rotation on the surface of the Sun.*

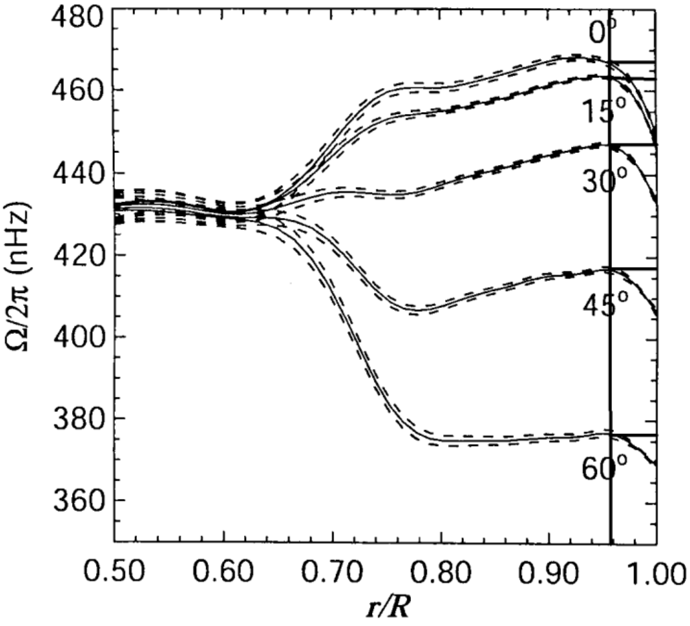

Figure 3. *Differential rotation of the different depth layers of the Sun by the helioseismology data. Our result [Živanović et al., 2021] is marked by the vertical black line.*

Other side of researches is the modeling of the magnetohydrodynamic processes on the solar atmosphere. For this research, we use the astrophysical code PLUTO, where the magnetohydrodynamic is realized for different physical situations. In our case, we simulate perturbations in the solar atmosphere and compare it with the actual models and observations [Živanović et al., 2025].

The dependency between the magnetic field strength and the brightness in the sunspots and small-scale structures is investigated using the SDO data [Živanović et al., 2020; Efremov et al., 2021]. The research includes the dependency between the time series with the brightness and magnetic field strength synchronized in time. In this timeseries the anticorrelation in the variations of this physical parameters [Efremov et al., 2021]. Another important research in this area is the research of the dependency between the magnetic field strength and brightness in case of the relations between the magnetic field and plasma convection. This is well known that in strong magnetic fields the convection of plasma is lower than in regions without strong magnetic fields. Due to this effect we can see sunspots as dark regions on the solar surface. In our research [Živanović et al., 2020] we show that this process of the suppression of the convection by the magnetic field have a point of saturation. In other words, with further growth of the magnetic field the brightness does not decrease any more. This result is presented on the Fig. 4.

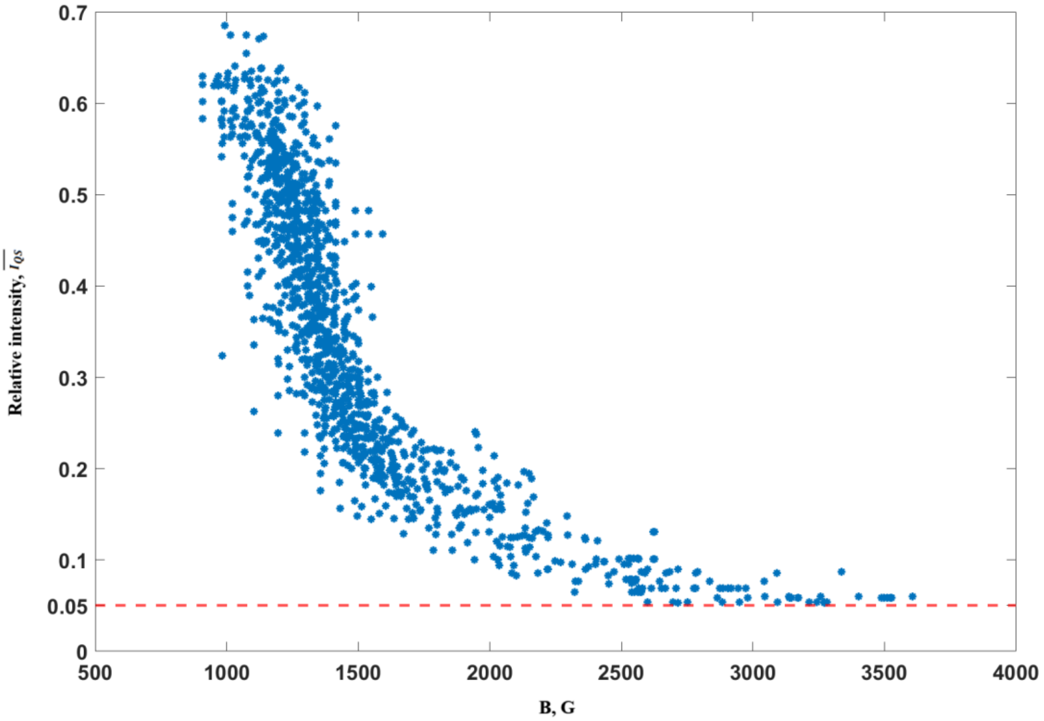

Figure 4. *Distribution of the brightness in the sunspot (vertical axis, normalized at the brightness of the Quiet Sun) and magnetic field strength at the same region of the sunspot (horizontal axis, in units of Gs).*

Another (and new) area of investigation is the relations between the solar activity and climate changes on Earth. This area of research is perspective in case of the new possibilities of observations of the markers for the reconstruction of the solar activity in the past. At the same time now we have a lot of observations of the climate markers. Hence we can find dependencies between the solar activity and climate changes on the Earth.

2.2. Climate Change

Climate change affects the physical environment and therefore poses a fundamental threat to human health. If these changes are frequent and intense, storms, extreme heat, droughts or, on the other hand, floods, erosion and loss of fertile arable land appear. Which obviously puts all life, including its inhabitants, at risk. This research area is in our unit's development plan for the next decade.

2.3. Light pollution

The main part of activities of the RU were lately dedicated to the problem of the light pollution (item iii listed above) and were performed within the UrbObsBel project and thus we describe them here in some detail. The instruments of the project are mounted at the top of the Tower of the Astronomical Observatory of Belgrade, Municipality of Zvezdara at altitude of approximately 250 meters which is the highest point of the urban part of Belgrade from which all parts of the city are perfectly visible. In Figure 5 we show the panoramic view to the West (downtown area of Belgrade).

Figure 5. *The panoramic view of the downtown area of Belgrade as seen from the top of the Tower of the Astronomical Observatory of Belgrade.*

We have the following instruments: two Sky Quality Meters (SQMs, one mounted in Belgrade and one at the ASV), two TESS-W instruments (again, one mounted at Zvezdara, and one mounted at the ASV), two FLIR A700 infrared cameras (both mounted at the Tower of the Astronomical Observatory, one pointed to the city center, see Figure 5, and one pointed to the outskirts of Belgrade), two visible and near-infrared (VNIR) hyperspectral imaging (HSI) detectors (again, one pointed to the city center and the other one pointed to the outskirts of town, see Figure 6 for FLIR and HSI detectors), the All Sky Camera Alcor OMEA 3C designed for continuous for continuous, day-and-night monitoring of the entire sky (see Figure 7) and a digital camera with a fish lens.

Figure 6. *The FLIR A700 infrared camera (on the right) and the HSI detector (on the left) mounted at the Tower of the Astronomical Observatory of Belgrade.*

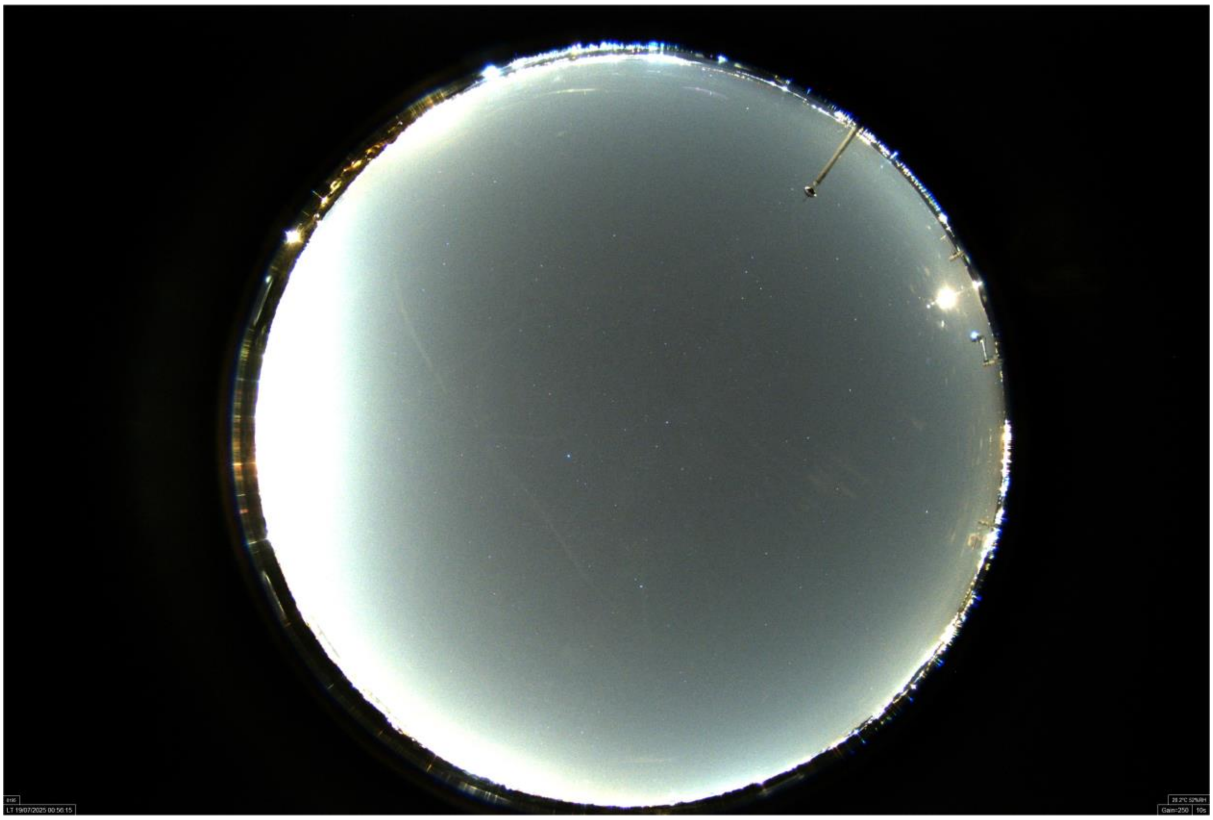

Figure 7. *The image of sky above the Tower of the Astronomical Observatory of Belgrade taken on July 19, 2025 (00:56:15 Local Time). In the upper right corner one can see a lighting rod.*

We plan to ask the citizens of Belgrade (various municipalities) to fill in our questionnaire regarding their experiences with the light pollution. Their responses, together with the results of the UrbObsBel project will be used by the Municipality of Zvezdara and the City of Belgrade because these measurements will provide elemets for making decisions in the direction of creating a better environment that will improve the health of the population of Belgrade and its surroundings.

Our preliminary results presented in Pavlović et al. (2025) suggest that at the ASV one can see fainter objects up to 4.5 mag than at the Astronomical Observatory of Belgrade due to the light pollution. Here, in Figure 8 we present another comparison, i.e., we compare two sets of ten SQM observations made on the same night at two different locations: the Tower of the Astronomical Observatory of Belgrade and the Tower of the Astronomical Society "Rudjer Bošković" in downtown Belgrade (altitude 110 m). The measurements started at 11:13 PM (Local Time) and 10 values were taken each 5 minutes (the last measurements were taken at 11:58 PM Local Time). One can see that the center of Belgrade clearly has larger light pollution (difference of the measured magnitudes is always greater than 1 mag).

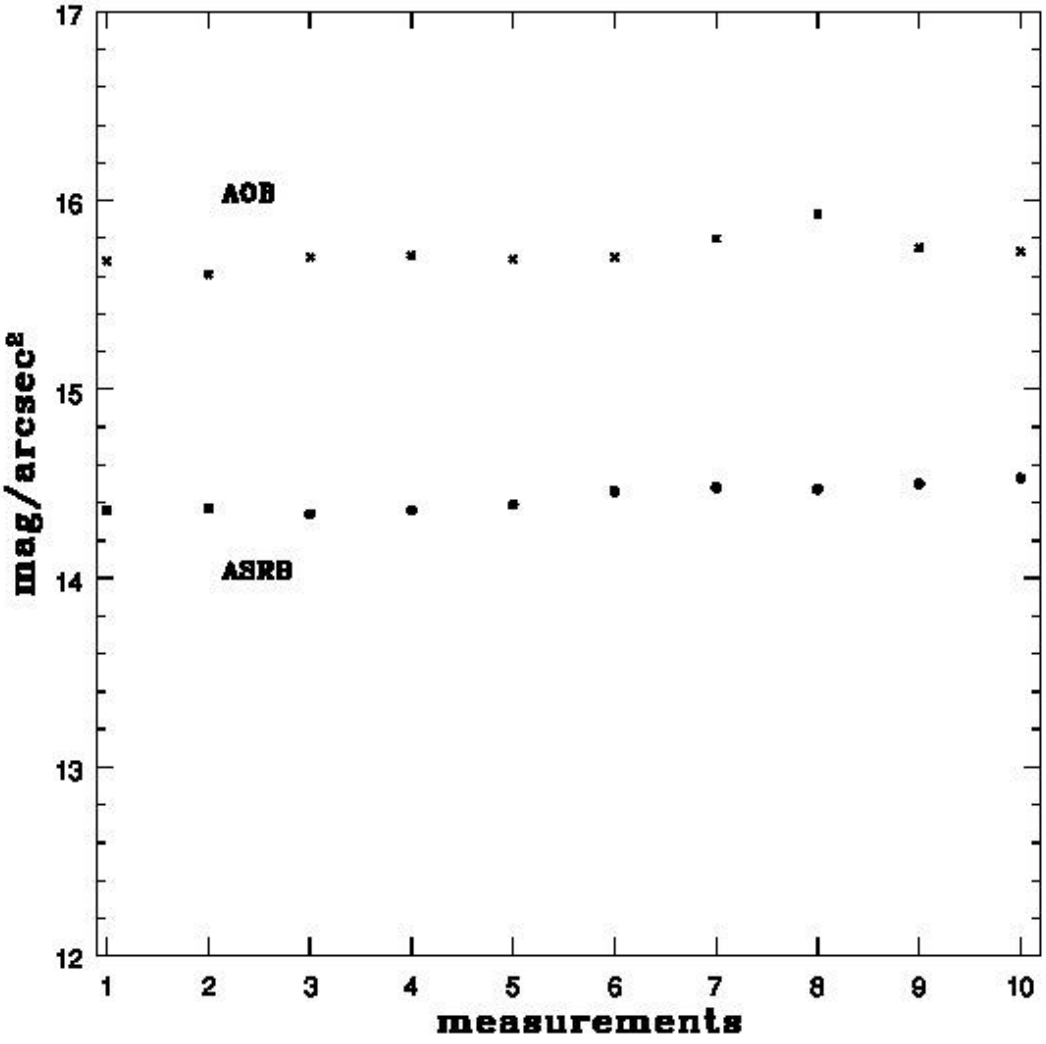

Figure 8. *Comparison of ten SQM measurements on the same night (July 27, 2025) at two different locations: the Tower of the Astronomical Observatory of Belgrade (AOB, crosses) and the Tower of the Astronomical Society "Rudjer Bošković" (ASRB, filled circles).*

The Web site of the UrbObsBel project is available at https://urbobsbel.aob.rs and contains all the relevant information about the project.

Acknowledgments

This research was supported by the Science Fund of the Republic of Serbia, no. 6775, Urban Observatory of Belgrade – UrbObsBel and by the Ministry of Science, Technological Development and Innovations of the Republic of Serbia through the Project contract No. 451-03-136/2025-03/200002. We thank the members of the UrbObsBel team for their efforts and especially Dr. Rade Pavlović and Dr. Branislav Rovčanin for providing us the data presented in Figure 8. We also thank the Director of the Astronomical Observatory of Belgrade Prof. Dr. Luka Č. Popović for establishing our Research Unit and his support of its activities.

References

Efremov, V.I., Solov’ev, A.A., Parfinenko, L.D., et al. (2021). Anticorrelation of variations of the magnetic field of a sunspot and the brightness of its umbra in long-period sunspot oscillations, *Geomagnetism and Aeronomy*, Vol. 60, pp. 1023–1027, DOI: 10.1134/S0016793220080071.

Živanović, I., Smirnova, V.V., Tsap, Yu.T., Chen, Y. (2025). Propagation of coronal large-amplitude Alfvén-type waves to the solar photosphere, *Astronomy & Astrophysics*, Vol. 697, A221, DOI: 10.1051/0004-6361/202452849.

Živanović, I., Solov’ev, A.A., Efremov, V.I. (2021). Differential rotation of the Sun, helioseismology data, and estimation of the depth of superconvection cells, *Geomagnetism and Aeronomy*, Vol. 61, pp. 940–948, DOI: 10.1134/S0016793221070264.

Živanović, I., Solov’ev, A.A., Smirnova, V.V., et al. (2016). Radial profile of sunspot magnetic field on the SDO data, *Astrophysics and Space Science*, Vol. 361, 102, DOI: 10.1007/s10509-016-2681-8.

Živanović, I., Solov’ev, A.A., Efremov, V.I., et al. (2020). Relationship of the magnetic-field strength and the brightness of the sunspot umbra and the center of a facular knot, *Geomagnetism and Aeronomy*, Vol. 60, pp. 865–871, DOI: 10.1134/S0016793220070324.

DOI: 10.31401/WS.2025.proc.24

Hale Magnetic Cycle on the Sun: Manifestations in Geophysical Characteristics and Possible Influence on the Earth’s Climate

Veretenenko S.V.[1], *Dmitriev P.B.*[1], *Obridko V.N.*[2]

[1]Ioffe Institute, Russian Academy of Sciences, St. Petersburg, Russia
s.veretenenko@mail.ioffe.ru
[2]IZMIRAN, Troitsk, Moscow, Russia

Abstract

Oscillations with periods of ~22 years close to the Hale magnetic cycle on the Sun are observed in a large number of climatic characteristics, and amplitudes of these oscillations often exceed those of 11-yr ones. In this work, we study the manifestations of the solar Hale cycle in different geophysical characteristics, which can contribute to the formation of bidecadal oscillations in the Earth’s climate. It was found that temporal variations of cosmic ray fluxes in the stratosphere, as well as geoeffective parameters of solar wind and geomagnetic activity characteristics differ significantly in even and odd solar cycles. The results obtained suggest that the solar Hale cycle can contribute to bidecadal variations in fluxes of energetic charged particles (cosmic rays and auroral electrons) affecting the ionization rate in the atmosphere of high latitudes. In turn, changes in the ionization rate affect the chemical composition and temperature regime of the high-latitudinal atmosphere, which can lead to changes in atmospheric circulation and climate characteristics.

Keywords: Hale cycle; cosmic rays; solar wind; Earth’s climate.

1. Introduction

A roughly 22-yr Hale cycle on the Sun, which consists of two consecutive 11-yr cycles, is known to manifest in the magnetic field polarity (e.g., [Hathaway, 2015]). When a new 11-yr cycle begins, the polarity distribution in sunspot groups reverses. Near the sunspot maximum, a reversal of the general magnetic field of the Sun takes place. According to the Gnevyshev-Ohl rule, there is a rather close connection between sunspot number totals per cycle for pairs of “even-succeeding odd” cycles, with the correlation coefficient exceeding 0.9, whereas for pairs of “odd-succeeding even” cycles, the correlation is noticeably weaker (~0.5) (e.g. [Nagovitsyn et al, 2009]). So, the Hale cycle is believed to start from an even 11-yr cycle.

At the same time, oscillations with a period of ~22 years close to the Hale cycle are observed in a large number of climatic parameters: occurrences of droughts in the USA [Cook et al., 1997], occurrences of hurricanes over the oceans [Mendoza and Pazos, 2009], regional temperatures in different seasons ([Pudovkin and Lubchich, 1990], Ogurtsov et al., 2020]). It is noted that a bidecadal variation in climatic characteristics is very often stronger than a decadal one [Raspopov et al., 2004]. So, a question arises whether the solar Hale cycle can influence the Earth’s climate and what solar agents may be responsible for this influence. In this work, we consider manifestations of the Hale cycle in geophysical characteristics which could be a link between processes on the Sun and in the Earth’s atmosphere.

2. Bidecadal variations of galactic cosmic ray influx in the atmosphere

Currently galactic cosmic rays (GCRs) are considered as an important link between solar activity and the lower atmosphere state due to their capability to penetrate deeply into the atmosphere and pronounced variability on a wide range of time scales. The bidecadal variation in GCR fluxes is manifested as an alternation of dome-shaped and peaked maxima at sunspot minima depending on the polarity of the general magnetic field on the Sun. GCR maxima are dome-shaped under positive polarity $A > 0$ (when magnetic field lines come out from the north pole and enter the south one) and peaked under negative polarity $A < 0$. This results in a clear ~22-yr oscillation in GCR fluxes, which can be seen in their spectra (Figure 1a) constructed on the base of the data of balloon measurements in the stratosphere of middle and high latitudes for 1957-2021 [Stozhkov et al., 2009]. Figures 1b and 1c present mean changes of cosmic ray fluxes in 3 even (20th to 24th, red line) and 3 odd (19th to 23rd, blue line) cycles obtained by the superposed epoch analysis (SPEA), using the same balloon measurement data. The year of sunspot maximum is taken as a zero year. One can see a noticeable difference between cosmic ray fluxes at the descending phase of even and odd cycles. The input of GCRs in the atmosphere in even cycles noticeably exceeds that in odd cycles, with the difference reaching its maximum (~0.3-0.5 $\mathrm{cm^{-2}\cdot s^{-1}}$) in the 3rd-4th years after the solar maximum. This allows suggesting that a roughly 22-yr variation in GCR fluxes can be one of possible factors of climate variations on the bidecadal time scale.

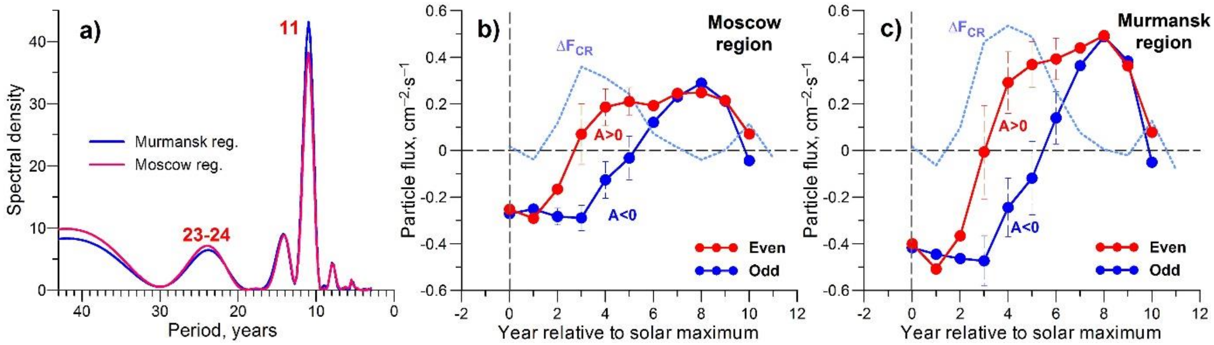

Figure 1. *a) Sampling estimates of the normalized spectral density of mean yearly fluxes of cosmic rays in the stratosphere of high latitudes (Murmansk region) and middle latitudes (Moscow region); b) mean (SPEA) changes of cosmic ray fluxes (detrended) in 3 even and 3 odd cycles (Moscow region); c) the same for Murmansk region. Dotted lines show the difference between mean yearly cosmic ray fluxes in even and odd cycles. Vertical bars show two standard errors of the mean.*

3. Bidecadal variations in geomagnetic activity and solar wind characteristics

Figure 2 (a, b) presents mean (SPEA) changes of yearly occurrences of magnetic storms with sudden (SC) and gradual (GC) commencement in 6 even (12th to 22th) and 6 odd (13th to 23rd) solar cycles, the data being taken from the stations IZMIRAN (http://www.izmiran.ru/magnetism/magobs/MagneticStormCatalog.html) and Slutsk/Pavlovsk [Kanonidi, 2012]. These kinds of storms are associated with different solar sources. Magnetic storms with sudden commencement are usually produced by coronal mass ejections and their occurrences peak at sunspot maxima. Magnetic storms with gradual commencement are usually associated with high-speed streams of solar wind from coronal holes, and their occurrences increase at the descending phase of a solar cycle. One can see that SC storms reveal a similar temporal behavior in even and odd cycles, with the maximal occurrence being observed in the year of sunspot maximum. However, in odd cycles their occurrences are somewhat higher, especially at the descending phase. As to GC magnetic storms, temporal variations in even and odd cycles differ noticeably. In odd cycles, GC storm occurrences grow rapidly and reach their maxima in the +3rd year after the solar maximum. In even cycles, they grow slowly and peak in the +5th year. The difference between SC and GC storm occurrences is most statistically significant at the descending phase of a cycle. The difference between even and odd cycles is also clearly seen in yearly values of geomagnetic *aa*-index (Figure 2c). Thus, geomagnetic activity, which reveals variations depending on the Hale cycle, may be considered as a possible factor of the formation of bidecadal variations in climatic characteristics, along with GCR variations.

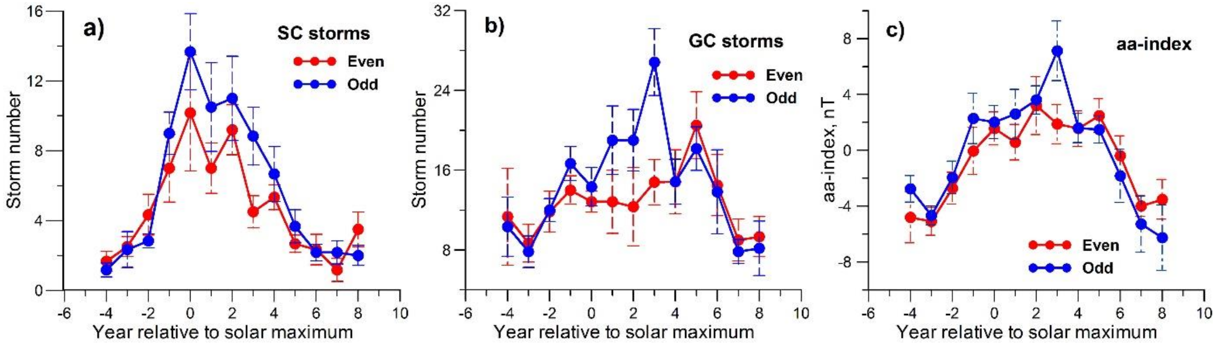

Figure 2. *a) Mean (SPEA) numbers of magnetic storms with sudden commencement (total yearly number of storms from moderate to very strong) in even (red line) and odd (blue line) solar cycles; b) the same for magnetic storms with gradual commencement; c) mean (SPEA) changes of yearly aa-indices (detrended) in even and odd cycles. Vertical bars show two standard errors of the mean.*

As geomagnetic activity is caused by the interaction of solar wind with the Earth's magnetosphere, let us consider variations in solar wind characteristics. The most important geoeffective parameter is the *Bz* component of interplanetary magnetic field (IMF) carried by solar wind, since the development of magnetic storms is closely related to the negative (southward) *Bz*. Along with the *Bz* component, the azimuthal IMF *By* component and solar wind speed are also of importance for geomagnetic disturbances. Geoefficiency of solar wind influence on the Earth's magnetosphere is determined by the "coupling function", which includes all the three indicated parameters [Troshichev, 2022].

Temporal variations of yearly values of the *Bz* component (in the GSM coordinate system) are presented in Figure 3a, the OMNI data (https://omniweb.gsfc.nasa.gov) being used. One can see a negative trend since the early 1960s, as well as a periodicity of ~20 years, which is revealed by a 5-yr smoothing (red line). The results of a spectral analysis (Figure 3b) show that the ~20-yr periodicity close to the Hale cycle is strongly dominating in the spectrum of the *Bz* component (the confidence level calculated relative to the "red noise" [Torrence and Compo, 1998] exceeds 0.98).

Figure 3c presents the results of the SPEA for yearly values of the *Bz* component (detrended), the year of sunspot maximum being taken as a zero year. The red line shows mean variations of the *Bz* component on the time interval from −10 to +12 years relative to the zero years, which are the maxima of even cycles, the blue line shows the same relative to the maxima of odd ones. One can see that temporal variations of yearly *Bz* values are opposite in even and odd cycles. The change of the *Bz* sign occurs near the sunspot maximum. Maximal absolute *Bz* values are observed in the +5th-7th years after the zero year, i.e., at sunspot minimum. At minima of even cycles (with positive polarity of the Sun's general magnetic field, $A > 0$), the *Bz* is, on average, negative (southward), whereas at minima of odd cycles ($A < 0$) it is positive (northward). Thus, the average direction of the *Bz* component at solar minima corresponds to the direction of the general magnetic field of the Sun. Indeed, the analysis of hourly values of the *Bz* component showed that at the minimum of an even cycle (1996) the occurrence of negative *Bz* values (from −1 to −7 nT) is higher by 13% compared with the minimum of an odd cycle (2008), whereas the occurrence of positive values (0–3 nT), on the contrary, is lower. The results obtained suggest that at minima of even cycles, when the southward *Bz* is more frequent, the geoefficiency of solar wind may be higher compared with odd cycles. Indeed, Figure 2b shows the maximal GC storm occurrence at minima of even cycles, which slightly exceeds the GC storm occurrence in odd ones.

A roughly 20-yr periodicity close to the Hale cycle is also well pronounced in temporal variations of the IMF *By* component (Figure 4a). According to the results of a spectral analysis in Figure 4b, this periodicity dominates in the spectrum of the *By* component along with the periodicity of 7.8 years, however, it is less significant than that in the *Bz* component. Mean (SPEA) changes in yearly *By* values (Figure 4c) are opposite in even and odd cycles similarly to *Bz* values, but the most significant differences are observed at the ascending phase and the maximum of a cycle: in odd cycles, the *By* component is, on average, positive (directed from dawn to dusk), whereas in even cycles, it is negative. At the descending phase, the differences between *By* values in even and odd cycles weaken and disappear completely at the sunspot minimum. Thus, temporal variations of geoeffective IMF components *Bz* and *By* reveal a roughly 20-yr periodicity closely related to the Hale cycle, which is manifested in the opposite character of yearly changes in even and odd cycles.

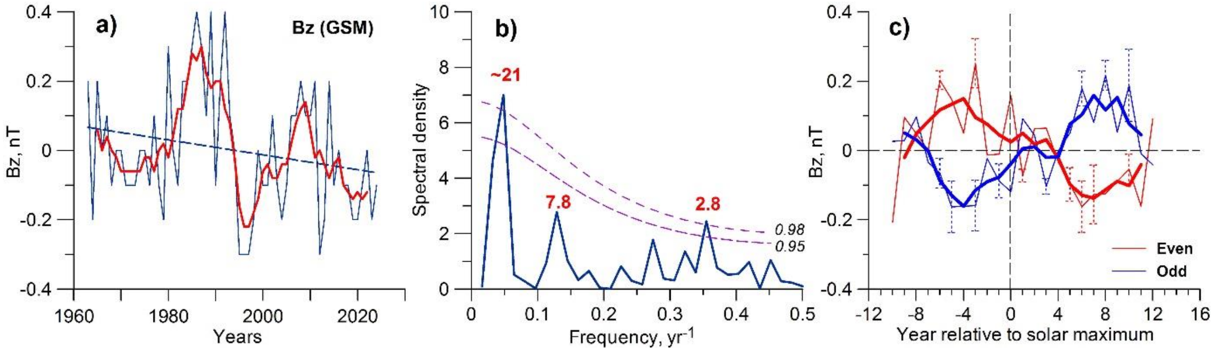

Figure 3. *a) Temporal variations of yearly values of the Bz component (GSM). Thick red line shows 5-yr running averages; b) Fourier spectrum of yearly Bz values (after the removal of the 2nd order polynomial trend). Dashed lines show the confidence levels calculated relative to the “red noise” with AR(1) = 0.3; c) mean (SPEA) changes of yearly Bz values (detrended). Red line – the zero years are maxima of even cycles; blue line – the zero years are maxima of odd cycles. Thick lines show 3-yr running averages. Vertical bars show two standard errors of the mean.*

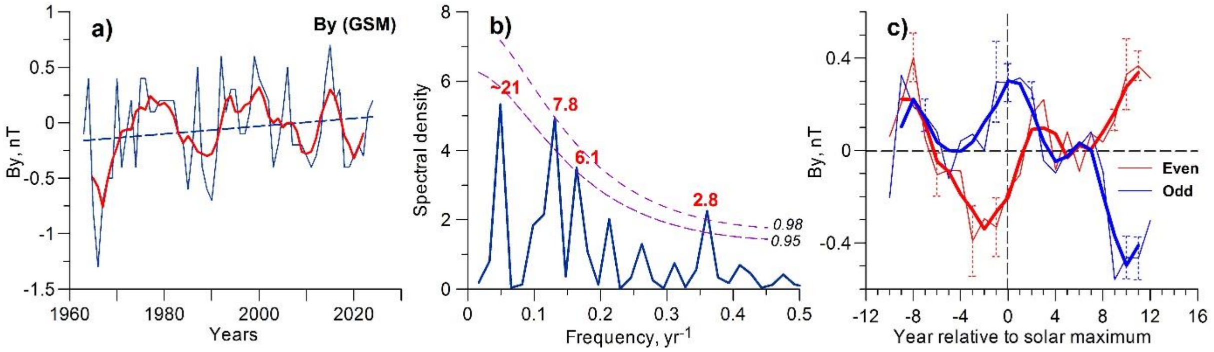

Figure 4. *The same as in Figure 3, but for the By component (GSM) and AR(1) = 0.36.*

The results of the study of variations in solar wind (SW) speed are presented in Figure 5. One can see that yearly values of SW speed do not reveal periodicities close to the Hale cycle. Both temporal variations (Figure 5a) and the Fourier spectrum of SW speed (Figure 5b) demonstrate a strongly dominating periodicity of ~10 years associated with the Schwabe cycle. The results of the superposed epoch analysis (Figure 5c) show that solar wind speed reaches maximal values at the descending phase of a solar cycle, which is due to the enhancement of coronal hole activity.

Although yearly values of SW speed did not demonstrate bidecadal variations, a noticeable difference was detected in the distribution of hourly values of SW speed at the descending phase (the 3rd year after sunspot maximum) of even and odd solar cycles. In even cycles, the occurrence of low values of SW speed (300-400 km/s) was found to be markedly higher compared with odd cycles. On the contrary, in odd cycles the occurrence of SW speed above 500 km/s is higher compared with even cycles. As SW speed is a geoeffective factor, along with the IMF *Bz* and *By* components, the enhancement of SW speed detected in hourly values at the descending phase of odd cycles seems to explain more intensive geomagnetic activity in the +3rd year after the sunspot maximum (Figure 2).

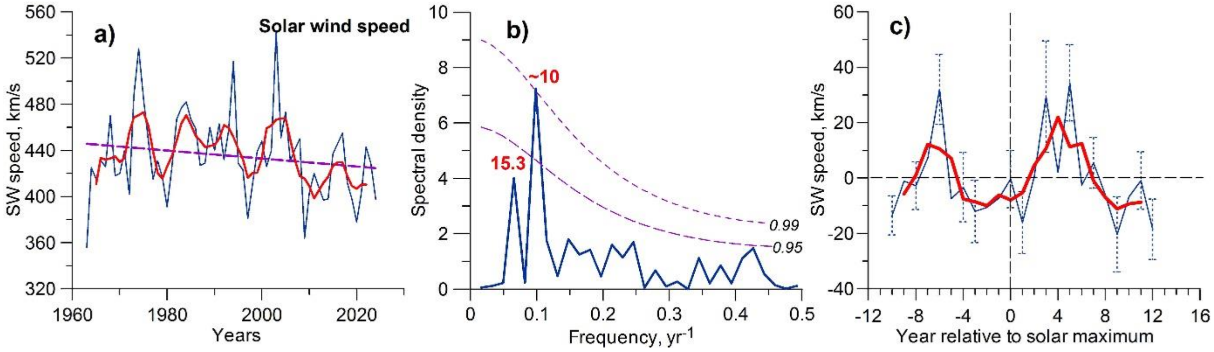

Figure 5. *a) Temporal variations of yearly values of SW speed. Thick red line shows 5-yr running averages; b) Fourier spectrum of yearly values of SW speed (after the removal of the 2nd order polynomial trend). Dashed lines show the confidence levels calculated relative to the “red noise” with AR(1) = 0.33; c) mean (SPEA) changes of yearly values of SW speed in a solar cycle. Thick red line shows 3-yr running averages. Vertical bars show two standard errors of the mean.*

4. Discussion and conclusion

As it was said above, oscillations with a period of ~22 years close to the magnetic Hale cycle are observed in a large number of climatic parameters. An important feature is that a bidecadal variation in climatic parameters is often significantly stronger than a decadal one [Raspopov et al., 2004; Pudovkin and Lubchich, 1989; Ogurtsov et al., 2020]. A pronounced ~22-yr variation was found to be a characteristic feature of storm track latitudes in different regions of the North Atlantic [Veretenenko and Dmitriev, 2024]. In even cycles, there is a noticeable shift of cyclone trajectories to the north (relative to a secular variation) from the +2nd to the 6th year after the sunspot maximum, i.e., at the descending phase and the minimum of a cycle. In odd cycles, cyclone trajectories slightly shift to the south. The effect is most pronounced in the Icelandic Low (Figure 6), which is a specific region of the North Atlantic. North Atlantic cyclones, which usually arise near the eastern coast of North America, arrive in this region, having reached the stage of their maximal development, and their occurrence is maximal. East of the Icelandic Low, cyclones usually start destroying (filling), their occurrence decreases and a roughly 22-yr variation in their trajectories weaken rapidly.

Thus, we can note that the most significant changes in latitudes of cyclone trajectories are observed at the descending phase and the minimum of a solar cycle. As was shown above, at this stage we also observe the most pronounced differences in galactic cosmic ray fluxes and geomagnetic activity in even and odd cycles. This allows suggesting that these factors may contribute to the formation of bidecadal variations in cyclone trajectories, which, in turn, result in bidecadal variations of different characteristics of regional climate at middle and high latitudes (temperature, pressure, precipitation etc.). Indeed, extratropical cyclones in the North Atlantic usually travel from the eastern coast of North America to the Barents Sea, so their paths lie in the region of low geomagnetic cutoff rigidity, which is accessible for cosmic ray particles in a wide energy range. On the other hand, paths of North Atlantic cyclones coincide rather well with the position of the auroral zone, which allows possible influence of auroral electron precipitations during geomagnetic disturbances.

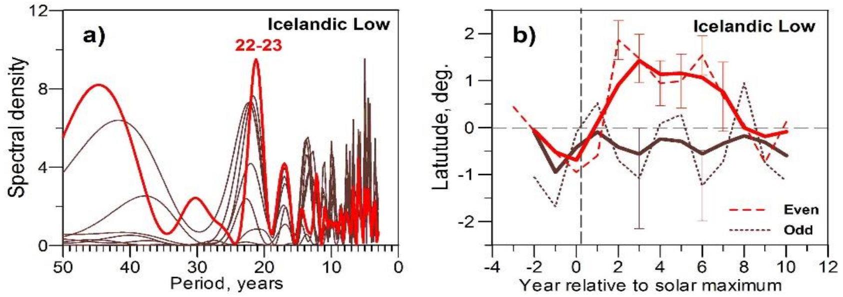

Figure 6. *a) Sampling estimates of the normalized spectral density of average storm track latitudes in the cold months (October-March) in the Icelandic Low for the initial time series (thick red line) and its high frequency components with “cut-off” parameter* $T_{cut\text{-}off}$ *=7, 11, 17, 23, 29, 37 and 43 years (thin brown lines); b) mean (SPEA) variations of storm track latitudes in 7 even (red dashed line) and 6 odd (brown dotted line) solar cycles. Thick lines show 3-yr running averages. The vertical bars show two standard errors of the mean. According to [Veretenenko and Dmitriev, 2024].*

A possible physical mechanism may involve variations in ionization rate in the high-latitudinal atmosphere associated with variations in galactic cosmic rays and auroral electrons. Increases of ionization rate contribute to changes in the chemical composition (ozone depletion), which, in turn, influence the temperature regime of the middle atmosphere and the intensity of the stratospheric polar vortex affecting cyclone trajectories [Veretenenko and Dmitriev, 2024]. Thus, the results of this study allow suggesting a possible contribution of the solar Hale cycle, which affects fluxes of energetic charged particles (cosmic rays and auroral electrons), to the formation of bidecadal variations in climatic characteristics.

References

Cook, E.R., Meko, D.M., Stockton, C.W. (1997). A new assessment of possible solar and lunar forcing of the bidecadal drought rhythm in the Western United States, *Journal of Climate*, Vol. 10, pp. 1343–1356, DOI: 10.1175/1520-0442(1997)010<1343:ANAOPS>2.0.CO;2.

Hathaway, D.H. (2015). The solar cycle, *Living Reviews in Solar Physics*, Vol. 12, Article No. 4, DOI: 10.1007/lrsp-2015-4.

Kanonidi, Kh.D. (2012). *Catalogue of Magnetic Storms*, IZMIRAN, Troitsk, DOI: 10.2205/Mag-St-052.

Mendoza, B., Pazos, M. (2009). A 22-year hurricane cycle and its relation with geomagnetic activity, *Journal of Atmospheric and Solar-Terrestrial Physics*, Vol. 71, pp. 2047–2054, DOI: 10.1016/j.jastp.2009.09.012.

Nagovitsyn, Yu.A., Nagovitsyna, E.Yu., Makarova, V.V. (2009). The Gnevyshev–Ohl rule for physical parameters of the solar magnetic field: The 400-year interval, *Astronomy Letters*, Vol. 35, No. 8, pp. 564–571, DOI: 10.1134/S1063773709080064.

Ogurtsov, M., Veretenenko, S., Helama, S., Jalkanen, R., Lindholm, M. (2020). Assessing the signals of the Hale solar cycle in temperature proxy records from Northern Fennoscandia, *Advances in Space Research*, Vol. 66, pp. 2113–2121, DOI: 10.1016/j.asr.2020.07.038.

Pudovkin, M.I., Lubchich, A.A. (1989). Manifestation of solar- and magnetic-activity cycles in air-temperature variations in Leningrad, *Geomagnetism and Aeronomy*, Vol. 29, No. 3, pp. 326–329.

Raspopov, O.M., Dergachev, V.A., Kolström, T. (2004). Hale cyclicity of solar activity and its relation to climate variability, *Solar Physics*, Vol. 224, pp. 445–463, DOI: 10.1007/s11207-005-5251-8.

Stozhkov, Y.I., Svirzhevsky, N.S., Bazilevskaya, G.A., Kvashnin, A.N., Makhmutov, V.S., Svirzhevskaya, A.K. (2009). Long-term (50 years) measurements of cosmic ray fluxes in the atmosphere, *Advances in Space Research*, Vol. 44, pp. 1124–1137, DOI: 10.1016/j.asr.2008.10.038.

Torrence, C., Compo, G.P. (1998). A practical guide to wavelet analyses, *Bulletin of the American Meteorological Society*, Vol. 79, pp. 61–78, DOI: 10.1175/1520-0477(1998)079<0061:APGTWA>2.0.CO;2.

Troshichev, O.A. (2022). PC index as a ground-based indicator of the solar wind energy incoming into the magnetosphere: (1) Relation of PC index to the solar wind electric field EKL, *Frontiers in Astronomy and Space Sciences*, Vol. 9, 1069470, DOI: 10.3389/fspas.2022.1069470.

Veretenenko, S.V., Dmitriev, P.B. (2024). Comparative analysis of solar activity influences on trajectories of extratropical cyclones in different regions of the North Atlantic, *Proceedings of the Sixteenth Workshop “Solar Influences on the Magnetosphere, Ionosphere and Atmosphere”*, pp. 100–105, DOI: 10.31401/WS.2024.proc.15.

DOI: 10.31401/WS.2025.proc.25

Proceedings of
the Seventeenth Workshop "Solar Influences on the Magnetosphere, Ionosphere and Atmosphere"
June, 2025

Applications of Chaos Theory to Astrophysical Time Series: Analysis of Blazar Light Curves from *TESS*

Bachev R., Strigachev A., Dechev M.

Institute of Astronomy and NAO, Bulgarian Academy of Sciences, 1784 Sofia, BG
(bachevr@astro.bas.bg)

Abstract

Searching for low-dimensional chaos in time series is a rarely used, but very promising approach to reveal the systems' internal dynamics, which drives the observed temporal variability. In this work we use long and intermittent optical intensity time series from *TESS* satellite to search for signatures of low-dimensional attractors. We present briefly the commonly used for chaos searches *Correlation Integral* (*CI*) method and its application. This method is applied not only in astrophysics (including Solar physics), but also in the fields of meteorology, climate, geophysics, medicine, ecology, economy, etc. As an example, we apply the *CI* method to the *TESS* light curves of a relativistic jet-dominated active galactic nucleus - the blazar S5 0716+714. Even though our first results are inconclusive, such searches are promising and encouraging.

Keywords: blazar; variability; chaos

1. Introduction

The concept of *deterministic chaos* was introduced in 1960s with the realization that relatively simple systems of ordinary differential equations can have highly unpredictable (or *chaotic*) solutions. An example of a chaotic system is the *Lorenz system* (Equation 1), developed to model the atmospheric convection (Lorenz, 1963, see also Figure 1):

$$\left|\begin{aligned}\frac{dx}{dt} &= \sigma(y-x)\\ \frac{dy}{dt} &= x(\rho-z)-y\\ \frac{dz}{dt} &= xy-\beta z\end{aligned}\right. \qquad (1)$$

Such solutions, called *strange attractors*, stay bound and never leave a sub-space of the phase space of (non-integer) dimension $d < N$, where N is the phase space dimension (the number of the variables/equations) of the system. The trajectories of a strange attractor evolve into a finite volume in the phase space, never returning to the same points. The divergence between two close trajectories increase exponentially in time and the long-term predictions are impossible. Consequently, each variable of a strange attractor system, represented as function of time, can mimic random behavior, yet still being a solution of a deterministic system.

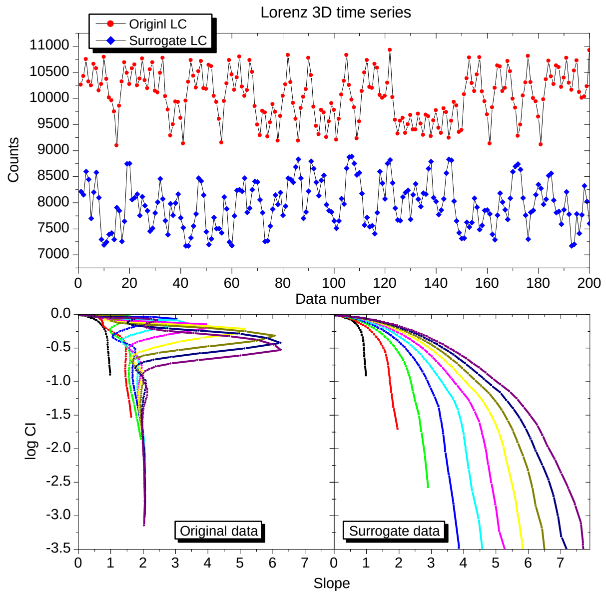

Figure 1. *Upper panel: Chaotic time evolution (the first 200 points) of the x-coordinate of the Lorenz system and the phase randomized surrogate (see the text), shifted vertically for clarity. Lower panels: Application of the CI method to the both curves (16000 points used). The original Lorenz curve (left) saturates at about* $Dc = 2.06$*, which is the correlation dimension of the Lorenz attractor, while the surrogate shows no sign of saturation and demonstrate behavior very similar to random noise (e.g. Bachev R. et al., 2015).*

Chaos theory applications include not only the field of astrophysics, including variable stars (Cannizzo et al., 1990; Bachev et al., 2011), Solar activity (Kurths & Herzel, 1987), active galactic nuclei (Lehto et al., 1993; Provenzale et al., 1994; Bachev R. et al., 2015; Bachev R. et al., 2018), X-ray binaries (Lochner et al., 1989; Misra et al., 2004), etc. but also many other disciplines as meteorology and climatology (wind directions, climate changes; Nicolis & Nicolis G., 1984; Fraedrich, 1986), geophysics (earthquakes intervals, Earth polarity reversals; Pavlos et al., 1994; Anufriev & Sokoloff, 1994), medicine (heart rhythm, epidemic outbreaks; Van der Heiden, 1991; Olsen & Schaffer, 1990), ecology (population size changes; May, 1986), economics (stock indices, exchange rates; Lorenz, 1989), etc.

In this work we will apply the *Correlation Integral* method (see the next section) to search for chaotic signatures in *TESS* light curves of a blazar (S5 0716+714). Blazars are active galactic nuclei, whose emission is almost entirely generated in a relativistic jet via non-thermal (synchrotron, Inverse-Compton) mechanisms and is additionally Doppler-boosted towards the observer (Urry & Padovani, 1995).

2. Correlation Integral method

The correlation integral method (Grassberger & Procaccia, 1983) is a relatively popular method in nonlinear dynamics. It is based on the construction of a new (empirical) phase space from the available N discrete observation points. The time series (the points of the light curve) is divided into strings of length d. Each string can be viewed as a d-dimensional vector (X_i) embedded in the d-dimensional empirical phase space. The number of pairs of vectors less than r apart as a function of r is calculated for different r and related to the total number of pairs (n_p) for that r. Thus, the correlation integral can be written as (Equation 2):

$$C_d(r) = \frac{1}{n_p} \sum_{i,j=1;\, j>i}^{N} \Theta\left(r - \left|X_i - X_j\right|\right), \tag{2}$$

where Θ is the Heaviside function. If the dimension of the attractor is D (Equation 3), then:

$$C_d(r) \propto \begin{cases} r^d, d < D \\ r^D, d > D \end{cases}, \tag{3}$$

Increasing d therefore leads to saturation at $d > D$, so the maximal *slope* of the CI can used to estimate the dimensionality of the attractor (Equation 4):

$$D_c = \lim_{r \to 0} \frac{d \ln C(r)}{d \ln r}, \tag{4}$$

where D_c is the correlation dimension of the attractor and may not be an integer. Knowing D_c allows determining the number of differential equations describing the dynamical system, N, i.e. the first integer greater than D_c. In this way, it becomes possible to draw conclusions about the physical processes leading to the variability.

The method also has some setbacks, for example, a quasi-periodic signal (with fractal dimension around one) accompanied by noise could be disguised as low-dimensional chaos of dimension 2 – 3. To prevent this possibility, it is necessary to test "surrogates" light curves obtained from the original curve by phase randomization (see e.g. Bachev R. et al., 2015). The surrogate curve preserves the frequency (Fourier) spectrum of the original, but destroys the appearance of deterministic chaos, if any. Thus, if manifestations of low-dimensional chaos are also observed in the surrogate curve, these manifestations will not be considered real (details in Bachev R. et al., 2015) and will be attributed to features in the frequency spectrum of the curve.

3. Data and results

For the purpose of this study we used light curve data from *TESS* orbital observatory (Ricker et al., 2015). *TESS* monitors continuously certain sectors from the sky for about 4 weeks with time resolution of about 2 (or 30 for some objects) min. Although primarily designed to search for extrasolar planets, *TESS* provides an additional and unique opportunity to study the variability of any type of object in the field. The resulting data cover the optical range in the red region (600 – 1000 nm) and are available as whole images or light curves (time series) for specific objects. The blazar S5 0716+714 was observed during several episodes (segments) and its light curves are used in our analysis as the objects is bright enough and rapidly variable. Each *TESS* segment contains typically a middle gap, large enough that each of the two parts to be treated separately. In addition, a few too deviating or missing points of the light curve had to be replaced via linear approximation between the adjacent points as the *CI* method works only for equidistant data series. Thus, each time series that we analysed consisted of about 8000 – 9000 equally spaced points, each measured with accuracy of < 1%. *TESS* segments 20, 26, 40 and 47, covering the field of S5 0716+714 were used for our analysis. Among the two flux calibration techniques (SAP and PDSCAP), we chose to use the SAP flux (details in Poore et al., 2024).

All tested light curves showed very similar behavior – a saturation around embedded dimension $d{\sim}1$ for both original and surrogate data. This means no detection of chaotic behaviour of the light curves, instead the light curves might be dominated by a (quasi) periodic signal (with $D = 1$ by definition). Further clues, supporting this possibility is that the surrogates demonstrate very similar behavior. In other words, the LC's of this blazar appear to be dominated by specific features of their Fourier spectra, not by deterministic chaos. Actually, similar results were obtained for another blazar, observed by *Kepler* - W2R 1926+42 (Bachev R. et al., 2015).

We show three examples (Figure 2 – 4) of *TESS* light curve (the original ones and the surrogates) of S5 0716+714 (parts from three different segments – 20, 26 and 40), all of which show strong variability and appear suitable for chaos searches. The time separation between data points is 2 min for all curves.

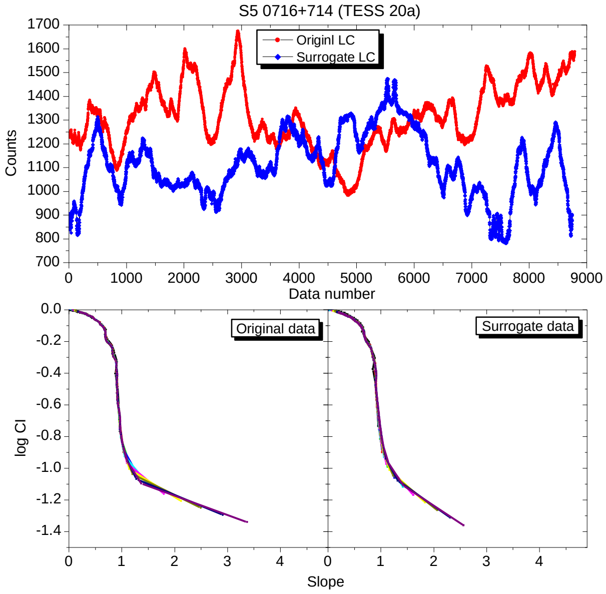

***Figure 2**. An example of the application of the CI method to real light curve of a blazar (S5 0716+714, TESS, segment 20, first part, covering the period between 25.12.2019 and 06.01.2020) and its surrogate (see the text and Figure 1).*

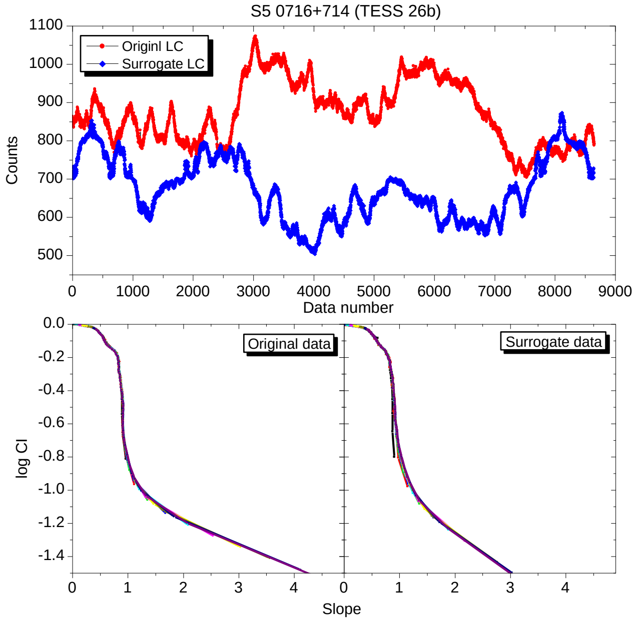

***Figure 3**. An example of the application of the CI method to real light curve of a blazar (S5 0716+714, TESS, segment 26, second part, covering the period between 22.06.2020 and 04.07.2020) and its surrogate (see the text and Figure 1).*

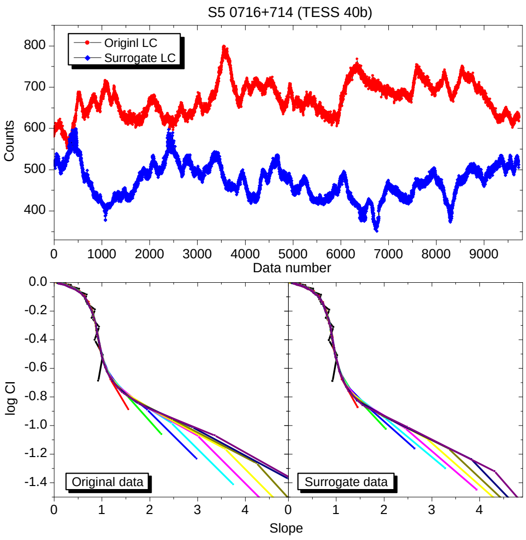

Figure 4. *An example of the application of the CI method to real light curve of a blazar (S5 0716+714, TESS, segment 40, second part, covering the period between 09.07.2021 and 23.07.2021) and its surrogate (see the text and Figure 1).*

4. Discussion

Finding low-dimensional chaos in a dynamical system (e.g. light curve) can be very important for the theoretical modelling, because it may limit the number of independent variables (or the number of equations) that governs the system entirely. In the case of blazars, such find may help to understand better the energy-producing mechanisms in a relativistic jet. The most often used is the so-called *single-zone* model to reproduce the observed blazar spectral-energy distribution (SED). In this model, the synchrotron radiation, which is responsible for the optical emission, is controlled by only a few parameters, such as electron density, electron energy distribution, magnetic field strength, Doppler factor, etc. Therefore, the single-zone models may actually produce low dimensional (say $D_c = 3 - 4$) chaotic behavior in blazar light curves.

One way to explain the apparently stochastic light curves, which would be consistent to a greater extent with our findings, is to invoke a large number of independent active zones (or emitting blobs) as an alternative to the single zone model. Another way to account for the observed variability is to invoke turbulence in the jet. In these models either turbulent flow passes through a standing shock (e.g. Marscher, 2014) leading to instant energy injection in the corresponding (shock crossing) plasma volume or the opposite: a shock wave passes through a turbulent medium (Marscher et al., 1992; Kirk et al., 1998).

5. Conclusions

We apply *chaos theory* methods to the *TESS* light curves of a relativistic jet-dominated active galactic nucleus – the blazar S5 0716+714. Although not able to detect the presence of low-dimensional chaotic behaviour in the light curves of this object, we find such studies important to restrain the emission mechanisms and the time evolution of blazars and other astrophysical objects. With the introduction of new or future ground- and space-based observational facilities, which can monitor the same objects repeatedly for very long periods of time, such studies will become even more feasible and perspective.

Acknowledgements

This research was partially supported by the Bulgarian National Science Fund of the Ministry of Education and Science under grant KP-06-H88/4 (2024).

References

Anufriev, A., Sokoloff, D. (1994). Fractal properties of geodynamo models, *Geophysical and Astrophysical Fluid Dynamics*, Vol. 74, pp. 207–223, DOI: 10.1080/03091929408203639.

Bachev, R., Boeva, S., Georgiev, Ts., Latev, G., Spassov, B., Stoyanov, K., Tsvetkova, S. (2011). On the nature of the short-term variability of the cataclysmic binary star KR Aurigae, *Bulgarian Astronomical Journal*, Vol. 16, pp. 31–40.

Bachev, R., Mukhopadhyay, B., Strigachev, A. (2015). A search for chaos in the optical light curve of a blazar: W2R 1926+42, *Astronomy and Astrophysics*, Vol. 576, A17, DOI: 10.1051/0004-6361/201425563.

Bachev, R., Strigachev, A., Mukhopadhyay, B. (2018). Searching for deterministic chaos in Kepler light curve of the Seyfert 1 AGN Zw229-015, *Bulgarian Astronomical Journal*, Vol. 29, pp. 74–79.

Cannizzo, J.K., Goodings, D.A., Mattei, J.A. (1990). A search for chaotic behavior in the light curves of three long-period variables, *The Astrophysical Journal*, Vol. 357, pp. 235–242, DOI: 10.1086/168910.

Fraedrich, K. (1986). Estimating the dimensions of weather and climate attractors, *Journal of the Atmospheric Sciences*, Vol. 43, pp. 419–432, DOI: 10.1175/1520-0469(1986)043<0419:ETDOWA>2.0.CO;2.

Grassberger, P., Procaccia, I. (1983). Characterization of strange attractors, *Physical Review Letters*, Vol. 50, pp. 346–349, DOI: 10.1103/PhysRevLett.50.346.

Kirk, J.G., Rieger, F.M., Mastichiadis, A. (1998). Particle acceleration and synchrotron emission in blazar jets, *Astronomy and Astrophysics*, Vol. 333, pp. 452–458.

Kurths, J., Herzel, H. (1987). An attractor in a solar time series, *Physica D: Nonlinear Phenomena*, Vol. 25, pp. 165–172, DOI: 10.1016/0167-2789(87)90099-6.

Lehto, H.J., Czerny, B., McHardy, I.M. (1993). AGN X-ray light curves – shot noise or low-dimensional attractor?, *Monthly Notices of the Royal Astronomical Society*, Vol. 261, No. 1, pp. 125–143, DOI: 10.1093/mnras/261.1.125.

Lochner, J.C., Swank, J.H., Szymkowiak, A.E. (1989). A search for a dynamical attractor in Cygnus X-1, *The Astrophysical Journal*, Vol. 337, pp. 823–832, DOI: 10.1086/167152.

Lorenz, E.N. (1963). Deterministic nonperiodic flow, *Journal of the Atmospheric Sciences*, Vol. 20, pp. 130–141, DOI: 10.1175/1520-0469.

Lorenz, H.-W. (1989). *Nonlinear Dynamical Economics and Chaotic Motion*, Lecture Notes in Economics and Mathematical Systems, Vol. 334, Springer, Berlin–Heidelberg, DOI: 10.1007/978-3-662-22233-1.

Marscher, A.P. (2014). Turbulent, extreme multi-zone model for simulating flux and polarization variability in blazars, *The Astrophysical Journal*, Vol. 780, 87, DOI: 10.1088/0004-637X/780/1/87.

Marscher, A.P., Gear, W.K., Travis, J.P. (1992). Variability of nonthermal continuum emission in blazars, in *Variability of Blazars* (Eds. E. Valtaoja, M. Valtonen), Cambridge University Press, Cambridge, pp. 85–101.

May, R.M. (1986). When two and two do not make four: Nonlinear phenomena in ecology, *Proceedings of the Royal Society of London B: Biological Sciences*, Vol. 228, No. 1252, pp. 241–266, DOI: 10.1098/rspb.1986.0054.

Misra, R., Harikrishnan, K.P., Mukhopadhyay, B., Ambika, G., Kembhavi, A.K. (2004). The chaotic behavior of the black hole system GRS 1915+105, *The Astrophysical Journal*, Vol. 609, pp. 313–316, DOI: 10.1086/421005.

Nicolis, C., Nicolis, G. (1984). Is there a climatic attractor?, *Nature*, Vol. 311, pp. 529–532, DOI: 10.1038/311529a0.

Olsen, L.F., Schaffer, W.M. (1990). Chaos versus noisy periodicity: Alternative hypotheses for childhood epidemics, *Science*, Vol. 249, pp. 499–504, DOI: 10.1126/science.2382131.

Pavlos, G.P., Karakatsanis, L., Latoussakis, J.B., Dialetis, D., Papaioannou, G. (1994). Chaotic analysis of a time series composed of seismic events recorded in Japan, *International Journal of Bifurcation and Chaos*, Vol. 4, No. 1, pp. 87–98, DOI: 10.1142/S0218127494000071.

Poore, E., Carini, M., Dingler, R., Wehrle, A.E., Wiita, P.J. (2024). A comparative study of TESS light-curve extraction methods applied to blazars, *The Astrophysical Journal*, Vol. 966, 158, DOI: 10.3847/1538-4357/ad2fca.

Provenzale, A., Vio, R., Cristiani, S. (1994). Luminosity variations of 3C 345: Is there any evidence of low-dimensional chaos?, *The Astrophysical Journal*, Vol. 428, pp. 591–598, DOI: 10.1086/174267.

Ricker, G.R., Winn, J.N., Vanderspek, R., Latham, D.W., Bakos, G., Bean, J.L., et al. (2015). Transiting Exoplanet Survey Satellite, *Journal of Astronomical Telescopes, Instruments, and Systems*, Vol. 1, 014003, DOI: 10.1117/1.JATIS.1.1.014003.

Urry, C.M., Padovani, P. (1995). Unified schemes for radio-loud active galactic nuclei, *Publications of the Astronomical Society of the Pacific*, Vol. 107, pp. 803–845, DOI: 10.1086/133630.

Van der Heiden, U. (1992). Chaos in health and disease—phenomenology and theory, in *Self-Organization and Clinical Psychology* (Eds. W. Tschacher, G. Schiepek, E.J. Brunner), Springer Series in Synergetics, Vol. 58, Springer, Berlin, pp. 55–87, DOI: 10.1007/978-3-642-77534-5_3.

DOI: 10.31401/WS.2025.proc.26

Proceedings of
the Seventeenth Workshop “Solar Influences on the Magnetosphere, Ionosphere and Atmosphere”
June, 2025

Solar-type Activities and Brightness Variations in Three Binary Star Systems

Boneva D.[1], Yankova K.[1], Dimitrov W.[2]

[1] Space Research and Technology Institute, Bulgarian Academy of Sciences, Sofia, Bulgaria;
danvasan@space.bas.bg
[2] Astronomical Observatory Institute, Faculty of Physics and Astronomy, Adam Mickiewicz
University, Poznan, Poland

Abstract

This survey presents our study of brightness variations exhibited by three binary star systems at various time-scales.

We use observational data obtained from the Transiting Exoplanet Survey Satellite (TESS); the 2m telescope of the National Astronomical Observatory (NAO) Rozhen and the American Association of Variable Star Observers (AAVSO) International Database. Observations cover the different periods of time in optical bands of the selected binary systems: the visual binary with a solar-type dwarf 61 Cyg (Cygnus); the spectroscopic binary YY Gem (Gemini) and the ER UMa type dwarf novae IX Dra (Draconis). The indicated types of variability in brightness are compared to some solar type of activities, including flares, seen in the optical and X-ray bands. States of outbursts are also detected during the observational periods and we explore the possibility that the studied stars could exhibit solar-type bursts. We examine the similarities in the manifestation properties between the three targets and the Sun, and discuss their feasible sources.

Keywords: Solar activity; Flares; Binary stars: K and M dwarfs.

1. Introduction

Solar activity is known to manifests in different types of phenomena as flares, coronal mass ejections, bursts, prominences, solar wind, eruptions, sun spots.

The most energetic phenomena on the Sun are Solar flares [Shibata & Magara, 2011]. Solar flares are powerful bursts of electromagnetic radiation produced from the Sun. They could last from minutes to hours, within the wavelengths’ range from radio waves to gamma rays [Hathaway, 2015].

These types of activity are found in various types of stars. In binary stars a repeated variability in the brightness, known as flares, is a common occurrence [Pearson et al., 2005]. The flares appear particularly in systems with accretion discs in time scales of hours to days, with amplitudes in a range of $1 \div 3$ magnitudes. Flaring is known to be an ordinary phenomenon among K and M dwarfs [Hartman et al., 2011].

Two typical members of these spectral classes are 61 Cyg and YY Gem.

The first object 61 Cyg is a visual binary that contains a solar-type dwarf of spectral type K5 - 61 Cyg A and a K7 dwarf 61 Cyg B [Boro Saikia et al., 2016]. The distance to the star is only 3.5 pc. 61 Cyg A has a radius of $0.665 \pm 0.005\ R_\odot$ and mass $M_A \sim 0.66\ M_\odot$ [Kervella et al., 2008; Takeda et al., 2007]. Its effective temperature is measured as $T_{eff} = 4545 \pm 40$K and the mass transfer value is $\approx 0.06 \times 10^{-12}\ M_\odot\ yr^{-1}$.

The rotation periods are: 35 ± 1.7 days for the primary A and 38 ± 1.5 days for the secondary B [Donahue et al., 1996]. The object is defined with its solar-type variability, and 61 Cyg A is also known as a strong X-ray source.

The activity cycle of 61 Cyg A is about 7.3 ± 0.1 years [Baliunas et al., 1995, Robrade et al., 2012]. In its maximum active state, the X-ray luminosity of 61 Cyg A reaches $L_X = 6 \times 10^{27}$ erg s^{-1} with released energy about 1×10^{31} erg in soft X-rays. This corresponds to activity level of $\log L_X/L_{bol} = (-5.9) - (-5.4)$.

For the K7 component 61 Cyg B only a chromospheric activity cycle of ~ 11.7 ± 0.4 yr is obtained [Hempelmann et al., 2006]. The registered flare of the B component is even with higher luminosity $L_X = 1.4 \times 10^{28}$ erg s^{-1} and releases 7×10^{31} erg. The activity level is measured as $\log L_X/L_{bol} = (-5.6)$.

Observations report that flares produced by active M-dwarfs stars are more energetic and more frequent than those of the Sun [Kajikiya, 2025].

The second object YY Gem (Gemini) is a spectroscopic eclipsing binary system. It consists of two M-dwarf components of dM1e spectral type with almost equal parameters, considered as: the masses are $M_1 = M_2 = 0.57 \pm 0.005\ M_\odot$; radii of the components: $R_1 = R_2 = 0.61 \pm 0.005\ R_\odot$, and the separation of the two components: $a = 3.83\ R_\odot$ [Brancewicz & Dworak, 1980; Torres & Ribas, 2002]. The mean value of the effective temperature is 3820±100 K [Torres & Ribas 2002]. The orbital period of the system is determined as Porb ~ 0.814 days [van Gent, 1931].

Flare activity of YY Gem was observed photometrically [Doyle et al., 1990], spectroscopically in UV [Saar & Bookbinder, 2003] and X-ray [Stelzer et al., 2002], and also using radio data [Jackson et al., 1989].

YY Gem is one of the M-stars which flaring activity in UV and X-ray are more powerful than those on the Sun [Haisch et al., 1990].

The X-ray luminosity in the soft band during the observed flares was estimated to be in a range: $(2 - 8) \times 10^{29} - 10^{33}$ erg s^{-1} [Tsikoudi & Kellett, 2000].

The optical light curves of the flare give the flux values in the maximum of $\approx 7.4 \times 10^{30}$ erg s^{-1} in U and $\approx 5.9 \times 10^{30}\ erg\ s^{-1}$ in B, with the total energy in optical bands 5×10^{33} erg [Butler, 2015].

For comparison, in average registered solar X-class flare emits roughly 1×10^{27} erg s^{-1} in the 0.2−5.0 keV band [Robrade et al., 2012].

The third object is of different type, IX Dra (Draconis) is a binary system, a dwarf nova of ER UMa-type. The orbital period of IX Dra is estimated as Porb ~ 0.066 days [Kato et al., 2017].

IX Dra manifests superoutbursts with a supercycle length of 53 days and outbursts amplitude of 2.5 mag [Ishioka et al., 2001]. Photometrically obtained magnitude range of the objects is 14.7 - 18.2 in V band [Otulakowska-Hypka et al., 2013].

Superhumps during the supercycle length were also detected with a period of 0.067 days. They are known as periodic variations in brightness, which periodicity is a few percent longer than the orbital period. Then the mass ratio of the two binary components is obtained, using the average superhump period Porb=0.0672 days and q=0.101 [Liu, 2023].

In this paper, we present observational results both from Transiting Exoplanet Survey Satellite (TESS) and the 2 m telescope of the National Astronomical Observatory (NAO) Rozhen for 61 Cyg A, YY Gem and IX Dra (Section 3). A comparison of the solar-type activities between the three stars and with those of the Sun is given in Section 4.

2. Observational data and results for the three binary star systems

In this section, we apply data from TESS (The Transiting Exoplanet Survey Satellite) observations of the northern sky. The TESS is designed mainly to search for and observe the transiting Earth-sized exo-planets [Günther et al., 2020]. Its field of view is divided into 26 sectors, which gives the opportunity to observe more than 200 000 selected objects, including bright stars. The light curves of the objects are analyzing with a 2- minute cadence [Ricker et al., 2015].

Here we present observational data taken from sectors 75, 72 and 15, for the three binary stars: 61 Cyg, YY Gem, IX Dra. The time intervals of the obtained data are different for the three objects, as follows: for 61 Cyg it is January 29 - February 26, 2024 (59796.602 -

59823.767 MJD); for YY Gem it is November 11 - December 6, 2023 (60259.684 - 60285.086 MJD); for IX Dra we have: August 15 - November 2, 2019 (58710.863 - 58736.909 MJD). Where MJD in the squares means the corresponded Modified Julian Date.

The details for the TESS observations and data are seen in Table 1 below.

Table 1. *TESS observational details for the three binary stars.*

TESS data details / Object	**61 Cyg A**	**YY Gem**	**IX Dra**
Exposure Time [sec]	20	120	120
Observation Time [MJD]:	59796.602 - 59823.767	60259.684 - 60285.086	58710.863 - 58736.909
Sector Number:	75	72	15
Period, defined at zeropoint t0:	24.693	14.91	9.491
Period derivative:	0.15	0.15	0.0002
Wrapping phase:	0.5	0.5	0.5
Algorithm/Method:	Lomb-Scargle	Lomb-Scargle	Lomb-Scargle
Number of bins N:	400	300	300

The resulting light curves and power-period diagrams were created from the Simple Aperture Photometry (SAP) Flux data. They show the activity in these objects during the observational time-intervals (see Figures 1, 2, 3). The light curves were constructed as Flux-rate [e-/s] (electrons per second) vs. time in [days]. The appearance of flares is detected in two of the objects 61 Cyg A and YY Gem, seen both at the flux vs. time curve and in the frequency analysis diagrams. The maximum amplitudes of these light variations are $3.5 \pm 0.0003 \times 10^9\ e/s$ for 61 Cyg A and $0.21 \pm 0.0002 \times 10^9\ e/s$ for YY Gem.

The observed variations in the flux-rate of IX Dra are less powerful and with a lower amplitude 8.31 ± 0.0005 x 10 e/s. They could be identified as regular outbursts that prolong for 2 -- 5 days, which is in agreement with the object dwarf nova nature and its registered so far bursts activity [Ishioka et al., 2001].

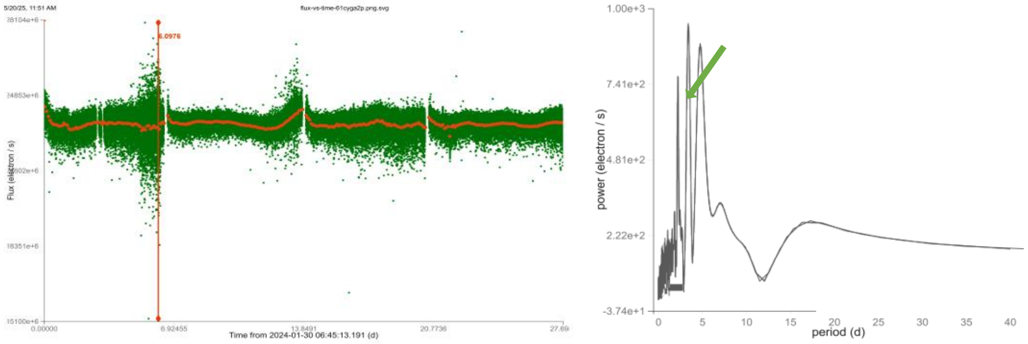

Figure 1. *Light curve of 61Cyg A, created with data obtained from TESS for the observational time interval (January 29 - February 26, 2024) (left panel). Two flares are indicated during this period. The more intensive one is marked with a red vertical line. The dotted red line denotes the binned curve with number of bins 400 for the optimal fit. (Right panel): Frequency analysis, power-period diagram of 61Cyg A with the TESS data for the same observational time. The stronger flare is marked with a green arrow.*

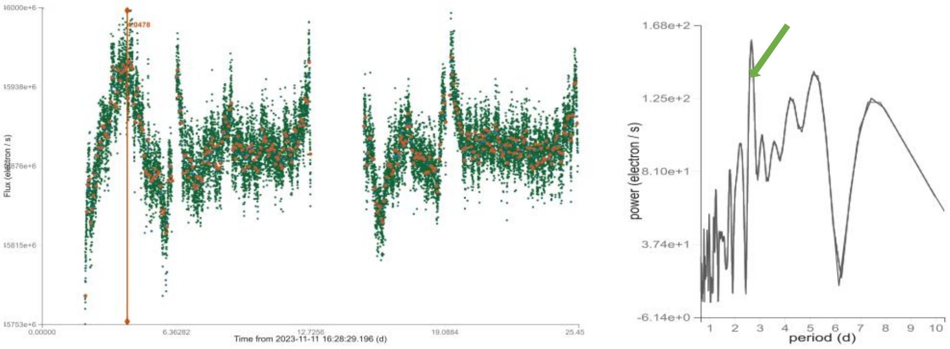

Figure 2. *Light curve of YY Gem, created with data obtained from TESS for the observational time (November 11 - December 6, 2023) (left panel). Two flares are indicated during this period. The more intensive one is marked with a red vertical line. The dotted red line denotes the binned curve with number of bins 300 for the optimal fit. (Right panel): Frequency analysis, power-period diagram of YY Gem, obtained with the TESS data for the same observational time. The flare is marked with a green arrow.*

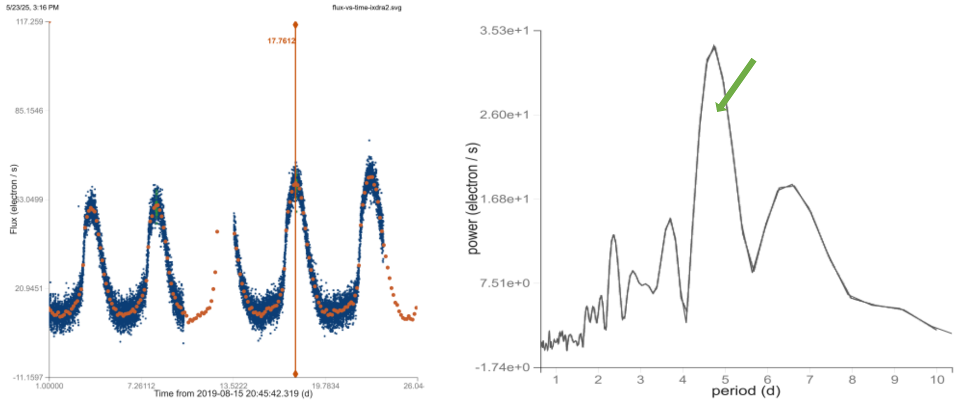

Figure 3. *Light curve of IX Dra, created with data obtained from TESS - observational time (August 15 - November 2, 2019) (left panel). Several outbursts are indicated during this period. The more intensive one is marked with a red vertical line. The dotted red line denotes the binned curve with number of bins 300 for the optimal fit. (Right panel): Frequency analysis, power-period diagram of IX Dra, obtained with TESS data for the same observational time-interval. The green arrow marks the outburst.*

For the third object IX Dra, we perform photometric observations with the 2 m telescope of the National Astronomical Observatory (NAO) Rozhen. The two-channel focal reductor FoReRo2 and two identical CCD cameras Andor iKON-L were used to obtain the observational data. Data reduction was performed with standard tools and aperture photometry. On the night of October 15 2023, the maximum brightness of the star was 16.5 ± 0.02 magnitude in V band and 18.2 ± 0.04 mag in B. The estimated amplitude of variations in V was 0.71 mag and 0.85 mag in the B band. During this time, according to the AAVSO data the object was in a cycle of an outburst’s state, with a maximum magnitude of 15.87 ± 0.021 in V. Then, the observed from us curve’s shape is most likely an orbital hump that appear during the outburst period (see Figure 4).

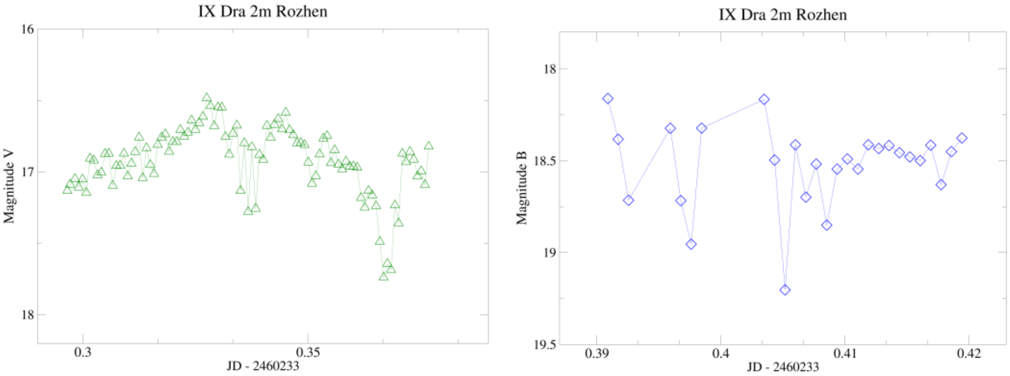

Figure 4. *Light curves obtained by photometric observations of IX Dra in V (left) and B (right) bands, using the 2m telescope Rozhen. Observational data for 2460233 JD (2023-10-15 UTC date). Small-scale brightness variations are detected, identified as orbital humps with amplitude of ~0.7 mag.*

3. Comparison of flares types and their possible sources

The obtained observational results for the three binary stars, 61 Cyg A, YY Gem and IX Dra, show different behavior in their states of flares' or burst' activity. It is coming from the physical nature of the objects' structure, and as we have described in the Introduction, they are members of different classes.

The maximum values of the flare emission obtained from the TESS data during the pointed time-interval (Section 3) of 61 Cyg A is $2.65\ \pm 0.0002\ \times 10^{10}\ e/s$ (see previous Section). This flux rate is a bit lower than the registered large flares of the Sun, which is 10^{36} $\mathrm{e/s}$, as an example of the solar event during October 2003 [Warmuth et al., 2007, Mann et al., 2009].

Comparing the results to the second star YY Gem, the flux-rate value in its maximum during the interval with a flare activity is $2.46\ \pm 0.0002\ \times 10^{11}\ e/s$, which is higher than the 61 Cyg A with a factor of ~ 10.

Although, it is already found [Robrade et al., 2012] the source of the observed activity in 61 Cyg A is coming from the variations in its chromosphere (or coronal properties), which is similar to the properties of the solar corona fluctuations. They also found in their results that the amplitude of the star's X-ray cycle is ~ 3 times lower than that of the Sun. The coronal cycles are typical for the G and K dwarfs, but with a smoother activity.

In both type of stars, the flares are produced in the result of the so-called magnetic reconnection, the same as considered for the Sun [Gao et al., 2008].

That's why we could compare the power of flares of our objects to those on the Sun. From the amplitude in the electron distributions, we could estimate the velocity of the particles spreading under the magnetic arc, which precedes the rising of flares.

After comparing these velocity values with the energy released during the flare, we can roughly estimate the order of magnitude of the increase in luminosity (in erg s^{-1}), compared to the average value emitted by the objects. We obtain for these orders of magnitude for both objects and it is 10^3 for 61 Cyg A and 10^4 for YY Gem, respectively. These values are larger compared to those of the Sun $(10 - 10^2)$. This result was expected, as one of the possible reasons being the smaller radii of K and M dwarfs. Therefore, the dynamo is located closer to the surface of the star. Due to the lower masses and, accordingly, the weaker gravity is more difficult to resist the effects of the dynamo. For this reason, the K- and M- dwarfs components of our two objects have a higher brightness, in terms of the activity, than that of the Sun.

The dwarf-nova nature of IX Dra exhibits in its regular outbursts' activity, seen in the TESS light curve. The outbursts are similar to those of the Sun, but less powerful. The source of bursts in IX Dra is most likely thermonuclear processes in its white dwarf companion or instability in the surrounded accretion disc. The flux-rate maximum value is $1.02 \pm 0.002 \times 10^2\ e/s$, which is a bit lower than the flux coming from flares. We did not observe any flares activity in this object.

4. Conclusion

In this paper we studied the appearance of solar-like activity, such as flares and bursts, in three selected binary stars by using observations of TESS and the 2m telescope of the National Astronomical Observatory Rozhen.

We presented results on the brightness variations in these three binary stars that are members of different classes: 61 Cyg; YY Gem and IX Dra. In the obtained observational data from TESS, we found manifestation of flares in the objects that contain a solar-type K - dwarf (61 Cyg A) and M - dwarfs (YY Gem) companions. During the time-intervals of the detected flares in the 61 Cyg A and YY Gem light curves, we found that the second object has more powerful emission than the first one. Comparing to the solar flares, both stars manifest higher increase in brightness than that of the Sun.

A conformation of an outburst’s activity in a cycle of 2-5 days are identified in the TESS light curve of the ER UMa star IX Dra. During the outburst time, the photometric results show an appearance of orbital like hump with a period a few percent less than the orbital period of the object.

Acknowledgements

This paper includes data collected with the TESS mission, obtained from the MAST data archive at the Space Telescope Science Institute (STScI). Funding for the TESS mission is provided by the NASA Explorer Program. STScI is operated by the Association of Universities for Research in Astronomy, Inc., under NASA contract NAS 5–26555. The research infrastructure is supported by the National Roadmap for Scientific Infrastructure, financially coordinated by the Ministry of Education and Science of the Republic of Bulgaria. The authors thank the AAVSO (American Association of Variable Star Observers) for providing the data of Light Curve Generator, contributed by observers worldwide and used in this research.

References

Baliunas, S.L., Donahue, R.A., Soon, W.H., et al. (1995). Chromospheric variations in main-sequence stars, *The Astrophysical Journal*, Vol. 438, No. 1, pp. 269–287.

Boro Saikia, S., Jeffers, S.V., Morin, J., et al. (2016). A solar-like magnetic cycle on the mature K-dwarf 61 Cygni A (HD 201091), *Astronomy and Astrophysics*, Vol. 594, A29, DOI: 10.1051/0004-6361/201628262.

Brancewicz, H.K., Dworak, T.Z. (1980). A catalogue of parameters for eclipsing binaries, *Acta Astronomica*, Vol. 30, No. 4, pp. 501–524.

Donahue, R.A., Saar, S.H., Baliunas, S.L. (1996). A relationship between mean rotation period in lower main-sequence stars and its observed range, *The Astrophysical Journal*, Vol. 466, pp. 384–391.

Doyle, J.G., Butler, C.J., Van den Oord, G.H.J., Kiang, T. (1990). A periodicity in the flaring rate on the eclipsing binary YY Geminorum, *Astronomy and Astrophysics*, Vol. 232, pp. 83–86.

Günther, M.N., Zhan, Z., Seager, S., et al. (2020). Stellar flares from the first TESS data release: Exploring a new sample of M dwarfs, *The Astronomical Journal*, Vol. 159, 60, DOI: 10.3847/1538-3881/ab5d3a.

Hartman, J.D., Bakos, G.Á., Noyes, R.W. (2011). A photometric variability survey of field K and M dwarf stars with HATNet, *The Astronomical Journal*, Vol. 141, No. 5, 166, DOI: 10.1088/0004-6256/141/5/166.

Hathaway, D.H. (2015). The solar cycle, *Living Reviews in Solar Physics*, Vol. 12, Article No. 4, DOI: 10.1007/lrsp-2015-4.

Hempelmann, A., Robrade, J., Schmitt, J.H.M.M., et al. (2006). Coronal activity cycles in 61 Cygni, *Astronomy and Astrophysics*, Vol. 460, No. 1, pp. 261–267, DOI: 10.1051/0004-6361:20065459.

Ishioka, R., Kato, T., Uemura, M., Iwamatsu, H., Matsumoto, K., Martin, B.E., Billings, G.W., Novak, R. (2001). Optical observations of cataclysmic variables, *Publications of the Astronomical Society of Japan*, Vol. 53, Issue 6, L51–L54, DOI: 10.1093/pasj/53.6.L51.

Jackson, P.D., Kundu, M.R., White, S.M. (1989). Quiescent and flaring radio emission from the flare stars AD Leonis, EQ Pegasi, UV Ceti, Wolf 630, YY Geminorum and YZ Canis Minoris, *Astronomy and Astrophysics*, Vol. 210, pp. 284–294.

Kajikiya, Y., Namekata, K., Notsu, Y., Ikuta, K., Maehara, H., Sato, B., Nogami, D. (2025). High-time-cadence spectroscopy and photometry of stellar flares on M-dwarf YZ Canis Minoris with Seimei Telescope and TESS. II. Statistical properties of blue/red asymmetries in the Hα line, *The Astrophysical Journal*, Vol. 985, 136, DOI: 10.3847/1538-4357/adce7d.

Kato, T., Isogai, K., Hambsch, Fr.J., et al. (2017). Survey of period variations of superhumps in SU UMa-type dwarf novae. IX. The ninth year (2016–2017), *Publications of the Astronomical Society of Japan*, Vol. 69, Issue 5, 75, DOI: 10.1093/pasj/psx058.

Kervella, P., Mérand, A., Pichon, B., et al. (2008). The radii of the nearby K5V and K7V stars 61 Cygni A and B, *Astronomy and Astrophysics*, Vol. 488, No. 2, pp. 667–674.

Mallama, A.D. (1980). Photometry and period study of YY Gem, *Publications of the Astronomical Society of the Pacific*, Vol. 92, pp. 468–471, DOI: 10.1086/130694.

Mann, G., Warmuth, A., Aurass, H. (2009). Generation of highly energetic electrons at reconnection outflow shocks during solar flares, *Astronomy and Astrophysics*, Vol. 494, Issue 2, pp. 669–675, DOI: 10.1051/0004-6361:200810099.

Otulakowska-Hypka, M., Olech, A., de Miguel, E., Rutkowski, A., Koff, R., Bąkowska, K. (2013). IX Draconis – a curious ER UMa-type dwarf nova, *Monthly Notices of the Royal Astronomical Society*, Vol. 429, Issue 1, pp. 868–880, DOI: 10.1093/mnras/sts385.

Pearson, K.J., Horne, K., Skidmore, W. (2005). Fireballs, flares, and flickering: A semi-analytic LTE explosive model from accretion disks to supernovae, *The Astrophysical Journal*, Vol. 619, No. 2, p. 999, DOI: 10.1086/426582.

Ricker, G.R., Winn, J.N., Vanderspek, R., et al. (2015). Transiting Exoplanet Survey Satellite (TESS), *Journal of Astronomical Telescopes, Instruments, and Systems*, Vol. 1, 014003, DOI: 10.1117/1.JATIS.1.1.014003.

Robrade, J., Schmitt, J.H.M.M., Favata, F. (2012). Coronal activity cycles in nearby G and K stars, *Astronomy and Astrophysics*, Vol. 543, A84, DOI: 10.1051/0004-6361/201219046.

Saar, S.H., Bookbinder, J.A. (2003). STIS far-UV studies of spatial and temporal activity variations in YY Gem, in *The Future of Cool-Star Astrophysics: 12th Cambridge Workshop on Cool Stars, Stellar Systems, and the Sun*, pp. 1020–1023.

See, V., Jardine, M., Vidotto, A.A., Donati, J.F., Folsom, C.P., Boro Saikia, S., et al. (2015). The energy budget of stellar magnetic fields, *Monthly Notices of the Royal Astronomical Society*, Vol. 453, Issue 4, pp. 4301–4310, DOI: 10.1093/mnras/stv1925.

Shibata, K., Magara, T. (2011). Solar flares: Magnetohydrodynamic processes, *Living Reviews in Solar Physics*, Vol. 8, Article No. 6, DOI: 10.12942/lrsp-2011-6.

Takeda, G., Ford, E.B., Sills, A., et al. (2007). Structure and evolution of nearby stars with planets. II. Physical properties of ~1000 cool stars from the SPOCS catalog, *The Astrophysical Journal Supplement Series*, Vol. 168, No. 2, pp. 297–318, DOI: 10.1086/509763.

Torres, G., Ribas, I. (2002). Absolute dimensions of the M-type eclipsing binary YY Geminorum (Castor C): A challenge to evolutionary models in the lower main sequence, *The Astrophysical Journal*, Vol. 567, pp. 1140–1165, DOI: 10.1086/338587.

Tsikoudi, V., Kellett, B.J. (2000). ROSAT all-sky survey X-ray and EUV observations of YY Gem and AU Mic, *Monthly Notices of the Royal Astronomical Society*, Vol. 319, Issue 4, pp. 1147–1153, DOI: 10.1046/j.1365-8711.2000.03905.x.

Van Gent, H. (1931). Photographic observations of the eclipsing variable Castor C = YY Geminorum from 1926 Oct. 2 to 1928 Jan. 13, *Bulletin of the Astronomical Institutes of the Netherlands*, Vol. 6, No. 215, p. 99.

Vidotto, A.A., Gregory, S.G., Jardine, M., Donati, J.F., Petit, P., Morin, J., et al. (2014). Stellar magnetism: Empirical trends with age and rotation, *Monthly Notices of the Royal Astronomical Society*, Vol. 441, Issue 3, pp. 2361–2374, DOI: 10.1093/mnras/stu728.

Warmuth, A., Mann, G., Aurass, H. (2007). Constraining electron acceleration at a standing shock with HXR and radio observations, *Central European Astrophysical Bulletin*, Vol. 31, pp. 135–153.

DOI: 10.31401/WS.2025.proc.27

Proceedings of
the Seventeenth Workshop “Solar Influences on the Magnetosphere, Ionosphere and Atmosphere”
June, 2025

Accuracy Analysis of the Analytical Approximation Model for Electrons Resonant Acceleration in Space Plasma

Shkevov R.[1], *Zolnikova N.N.*[2, 3], *Mikhailovskaya L.A.*[2], *Metodiev K.*[1]

[1]Space Research and Technology Institute, Bulgarian Academy of Sciences, Acad. Georgy Bonchev str., bl. 1, Sofia, Bulgaria
Corresponding author: shkevov@space.bas.bg
[2]Space Research Institute, Russian Academy of Sciences, Profsoyusnaya str., 84/32, Moscow, Russia
[3]Russian University of Transport, Obraztsova str., 9-9, Moscow, Russia

Abstract

An electrons resonant acceleration analytical model is investigated. The model describes the process of the strong particle acceleration by the electromagnetic waves packet propagating across the weak constant magnetic field in space plasmas by an analytical formula. The particle strong acceleration is carried out under strict compliance with the Cherenkov resonance conditions. Based on the exact solutions of the second order nonlinear nonstationary differential equation for the wave phase on the charged particle trajectory the initial numerical results are obtained. The calculations using the analytical model are also made. Compering the numerical results, the accuracy of the analytical model was accessed. The model accuracy results are presented in graphical forms. Conclusions on the analytical model applicability of charged particles resonant acceleration studies in space plasma are drawn.

Keywords: Resonant wave-particle interactions, analytical approximation, particle relativistic factor, nonlinear equations, electrons capture, space plasma.

1. Introduction

Investigation of the relativistic particles fluxes generation processes is one of the actual tasks of space plasma physics. It is of considerable interest for the problem of cosmic rays (CR) generation in astrophysics. This is due to the fact that the charged particles surfing on the electromagnetic waves, which was discussed earlier, for example in (Bulanov and Sakharov 1986), (Chernikov et al. 1992), (Dieckmann and Shukla 2006), (Erokhin et al. 1987, 1989, 2007, 2010), (Gribov et al. 1985), (Itin et al. 2000), (Joshi 1984), (Katsouleas and Dawson 1983). This is one of the most effective mechanisms for generating fluxes of ultrarelativistic particles. The correct estimation of the accelerated particles number, their energy spectra, acceleration region characteristic dimensions, require a detailed analysis of charged particles capture conditions in the surfatron acceleration mode. The favorable capture conditions determination of the charged particle and study of the efficiency of particle acceleration under the influence of finite amplitude space localized waves packet is a difficult task. There exists a possibility of multiple charge acceleration by wave packets. In addition, it must be taking into consideration the cyclotron rotation of the particles in an external magnetic field. However, the problem is multiparametric, and to identify patterns of charged particles surfing on the wave packets in space plasma a very large number of numerical calculations needed. In this paper, based on nonlinear numerical calculations, the capture of weakly relativistic charged particles, in surfatron acceleration mode by electromagnetic wave packet, propagating in plasma across a weak external magnetic field H_0 is considered. It should be noted that surfing is possible also for inclined wave propagation, where wave field threshold level is low. Acceleration variant of weakly relativistic particles is discussed, when the period of charges cyclotron rotation is relatively small. For wave amplitude above the threshold on the available time intervals of numerical calculations outside the numerical range favorable for surfing on the waves initial phases on the particle trajectory, charge rotation in the external magnetic field occurs. After several periods of cyclotron rotation (tens, hundreds or more), the condition of Cherenkov resonance occurs and the wave phase on the particle trajectory becomes favorable for the charge capture. Consequently, particle capture by waves packet occurs and ultrarelativistic acceleration begins. Therefore, in the particle pulse area the space capture by the electromagnetic wave turns out to be large enough. These results are helpful for the interpretation of experimental data of relativistic particles fluxes in space conditions. Surfing on the electromagnetic waves (Katsouleas and Dawson 1983), (Kichigin 1995, 2001), (Neishtadt et al. 2009), (Shkevov et al. 2013, 2016, 2017), (Sitnov 1988), (Vasiliev et al. 2011), can be a local source (Loznikov and Erokhin 2010) generates fuxes of ultrarelativistic particles in the near space of relatively quiet stars, such as solar heliosphere. In result of this phenomenon, local deviations of the recorded spectrum of CR from the standard power scaling may be observed.

2. Theoretical background

The starting point is the relativistic equations describing the motion of a charged particle, interacting with an electromagnetic wave, with phase velocity, which in the plasma must be less than the speed of light in vacuum. Taking into account the constant of motion, a nonlinear second-order equation for the wave phase on the accelerated charged particle trajectory is obtained. The numerical calculations are carried out for various values of initial parameters.

The surfatron acceleration mechanism is associated with the realization in a magnetoactive plasma of the Cerenkov resonance with the wave-particle interaction, is possible for p-polarized waves with refractive index $N^2 = \varepsilon\perp - (\varepsilon_c^2 / \varepsilon\perp) = 1 - [v (1 - v)] / (1 - u^2 - v)$. An external magnetic field is directed along the z axis $H_0 = H_0 e_z$. Capture in surfing mode occurs for wave amplitudes above the threshold $\sigma = e E / m c$, $\omega > \sigma_c \equiv u \gamma p = u / (1 - \beta p^2) 1 / 2$, $\beta p = \omega / k c$. Consider a wave spectrum with a carrier frequency $\omega_0 = \omega(k_0)$. The parameters are: $u = \omega He / \omega$, $v = (\omega_{pe} / \omega)^2$. Where ω_{He} - is cyclotron frequency of nonrelativistic electrons in plasma, ω_{pe}- is plasma Langmuir frequency $\omega_{pe} = (4 \pi e^2 n_0 / m)^{1/2}$. In perpendicular wave propagation with p-polarization, the wave field's components are E_x, E_y, H_z.

For the phase of the wave packet on the caring frequency $\Psi_0(\tau) = (\omega_0 t - k_0 x)$ can be used nonlinear equation (Erokhin et al. 1987, 1989, 2007, 2010), (Neishtadt et al. 2009), (Shkevov et al. 2013, 2016, 2017), (Sitnov 1988):

$$\gamma\beta_p d^2\Psi_0 / d\tau^2 - (1 - \beta x^2) \cdot (e E_x / m c \omega) - u \beta_y = 0 \tag{1}$$

Where E_x (x, t) is defined above, $\beta_{p0} = \omega_0 / ck_0$, $\gamma = (1 + h^2 + r_0^2)^{0.5} / (1 - \beta_x^2)^{0.5}$, $r_0 = \gamma\beta_y$ is the initial particle pulse along wave front and the integral of motion $J = \gamma\beta_y + u_0 \beta_{p0} (\Psi_0 - \tau)$ should be taken into account. There exists second integral $\gamma\beta_z = const \equiv h$. Charge velocity component β_x in (1) is given by term $\beta_x = \beta_{p0} [1 - (d\Psi_0/d\tau)]$.

3. Task Formulation

In this work accuracy analysis of the electron surfatron acceleration analytical approximation introduced in earlier works is presented. The electron surfatron resonance interactions can be analyticaly expressed by (Erokhin et al. 1987, 1989, 2007, 2010), (Shkevov et al. 2013, 2016, 2017):

$$M (\tau) = \gamma (0) + u \cdot \gamma \cdot \beta (\tau - \tau_c) \tag{2}$$

Where γ (0) is the particle relativistic factor at the $\tau = 0$, u is defined above, $\beta_p = \beta$ (define by Cherenkov resonance) is wave packet phase velocity, τ_c – moment of the particle capturing; τ_{out} – moment when the particle escapes from the potential well, end of the acceleration period.

Additionally in the Table 3 the following notations is used: $M(\tau)\gamma_{Aini}$ – is the initial value of $\gamma(\tau)$ at the τ_c calculated by analytical approximation; $M(\tau)\gamma_{Aout}$ – is the value of $\gamma(\tau)$ at the τ_{out} calculated by analytical approximation method; DEENS γ_{Eini}– is the initial value of $\gamma(\tau)$ at the τ_c calculated by Differential Equation Exact Numerical Solution method; DEENS γ_{Eout} – is the initial value of $\gamma(\tau)$ at the τ_{out} calculated by Differential Equation Exact Numerical Solution method.

The analysis is carried out by parallel collating of the computing results, both on the proposed model and the numerical solution of second order nonlinear nonstationary differential equations for the wave phase on the charged particle's trajectory. The parallel calculations are made for the 15 cases of different initial phases in range of $\delta\Psi(0) = -3.1 \div 3.1$.

4. Calculation results

The calculations results with initial parameters, shown in the Table 1, are presented in the Table 2 for 70 different cases. Analysis of the Table 2 shows that in two cases no particle trapping (marked with > 70k), in thirty five cases electron initially performs cyclotron rotation with next strong acceleration and in thirty three cases charged particle is trapped immediately (marked with 0). The approximate value of total particle capturing probability is 97%. Further analysis of Table 2 showed that there are two cases with no electrons trapping - marked with (> 70k) ≈ 3 % (in grey); in thirty two cases electrons are trapped immediately ≈ 47 % of calculated cases (dark blue) and thirty six cases (light blue) with initial particle cyclotron rotation and next strong surfatron acceleration ≈ 50 %.

In earlier works (Erokhin et al. 1987, 1989, 2007, 2010), (Neishtadt et al. 2009), (Shkevov et al. 2013, 2016, 2017), (Sitnov 1988), was shown that the most effective particle acceleration takes place in the case when particle capture occurs on the left side of the wave packet. From the other hand, the capture probability is higher when the charged particle is situated in the center of the wave packet structure, similar to the problem discussed in current paper.

For the correct estimation of the particle energy growth, it needed to calculate the relativistic factor value before and after surfatron acceleration period. As it was mentioned above, electron initial relativistic factor is $\gamma(0) = 1.076$ from where $E_{INI} \cong 0.55$ MeV resulting electron initial energy is received. For all cases the dynamics of the relativistic factor $\gamma(\tau)$ analysis showed that for $\delta\Psi_0 = 3.1$ particle is accelerated and energy growth is $\gamma(54830) = 2.83.10^3$, $E_{OUT} \cong 1.45$ GeV. The higher efficiency occurs in case with $\delta\Psi_0 = +1.4$; $\gamma(57280) = 2.957.10^4$ from where E_{OUT} max $\cong 1.51$ GeV.

The dynamics of the particle relativistic factors and its analytical approximation for $\delta\Psi_0 = +3.1$ is presented on the Figure 1. In this case the capture hapens at $\tau_c = 0$ and charged particle is accelerated up to the living the potential well at $\tau_d = 54830$. For this acceleration period the electron reaches the value of the relativistic factor $\gamma(54830) = 2.83.10^3$, $E_{OUT} \cong 1.45$ GeV and the coincidence between proposed function of analytical approximation $M(\tau)$ is accurate up to the third sign - $M(54830) = 2830$ at the acceleration period.

In this paper our calculations were performed for the following set of initial parameters of the charged particle: $u = 0.20$; $\beta = 0.25$; $h = 0.20$; $g = 0.21$; $a = 0$; $\rho = 70000$, $\sigma = u\,\gamma_p = 1.65\,\sigma_c$; $\Psi_0 = \Psi(0) = 0$ shown in Table 1. Such parameters set corresponds to a low relativistic initial energy of the electron with initial relativistic factor $\gamma(0) = 1.08$ and the resulting electron initial energy is estimated as $E_{INI} \cong 0.55$ MeV. The calculations results are presented in Table 2, where the number written in the cell indicates the time period. The $\delta\Psi_0$ is the value of the wave packet phase and the first point ($\delta\Psi_0 = \Psi(0) = 0$) corresponds to the particle central position in the wave packet, as it was mentioned above. The wave packet electric field amplitude must be above σ_c - $\sigma \geq \sigma_c$, because the surfatron acceleration below the line $\sigma < \sigma_c$ is impossible (Katsouleas and Dawson 1983).

Table 1. *Initial parameters set for the second order nonlinear nonstationary differential equation (1) for the wave phase on the particle trajectory used in the calculations performed. Presented set corresponds to the low relativistic electron energy.*

τ_{max}	φ	u	β_p	h	$g_y(0)$	a	ρ	σ/σ_c	τ_c	τ_d
70k	0	0.20	0.25	0.20	0.21	0	70000	1.65	0 ÷ 33662	> 50k ÷ 70k

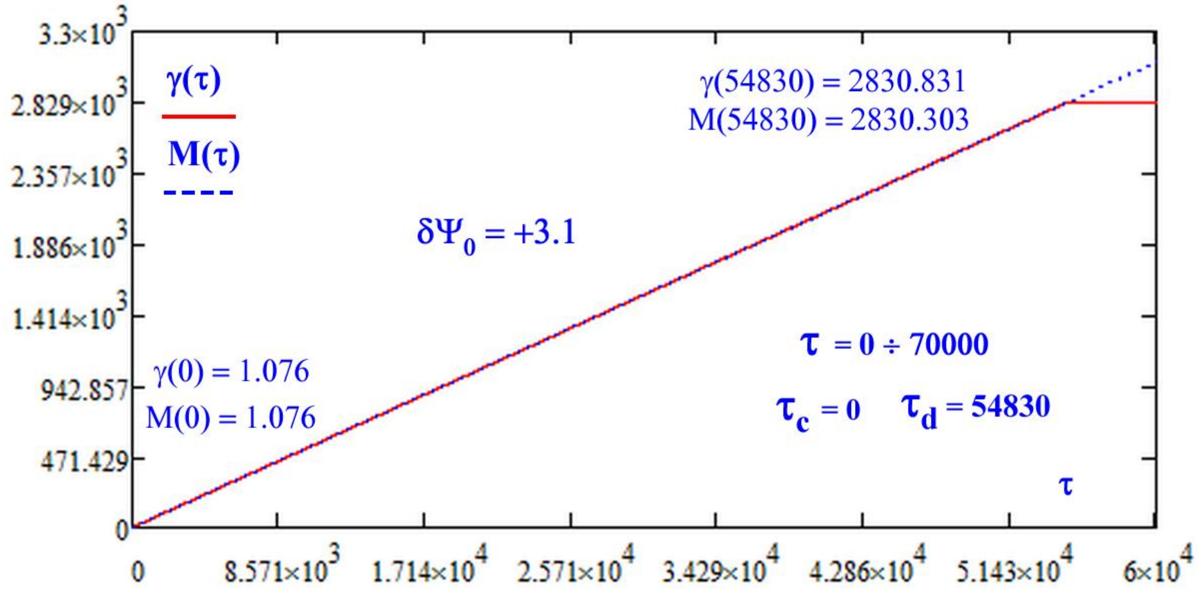

Figure 1. *Plot of charged particle relativistic factor $\gamma(\tau)$ and its analytical approximation $M(\tau)$ for $\delta\Psi(0) = +3.1$ in the range of $\tau = 0 \div 70\,000$ where $\tau_c = 0$ and $\tau_d = 54\,800$.*

Table 2. *The calculations results of 70 cases for the initial phases $\Psi(0) = \phi - \delta\Psi(0)$, where $\phi = 0$ are presented. There exist 68 cases of the particle capturing and strong surfatron acceleration. Capture times τ_c are pointed below the phases values. The green cells correspond to the cases were particle acceleration in surfatron mode takes place. The probability for the surfatron acceleration in this case is about ≈ 97%.*

$\delta\Psi_0$	-3.1	-3.0	-2.9	-2.8	-2.7	-2.6	-2.5	-2.4	-2.3	-2.2
τ_c	0	0	0	19741	15732	6181	9417	27895	3535	16573
$\delta\Psi_0$	-2.1	-2.0	-1.9	-1.8	-1.7	-1.6	-1.5	-1.4	-1.3	-1.2
τ_c	3003	11578	17924	33662	3221	10447	13343	27706	19198	3403
$\delta\Psi_0$	-1.1	-1.0	-0.9	-0.8	-0.7	-0.6	-0.5	-0.4	-0.3	-0.2
τ_c	5011	8693	20675	20212	21529	3653	11614	> 70k	23938	10238
$\delta\Psi_0$	-0.1	-0.05	-0.02	-0.01	0	0.01	0.02	0.03	0.05	0.1
τ_c	1058	2836	10684	25605	3451	21183	1491	> 70k	20636	12235
$\delta\Psi_0$	0.2	0.3	0.4	0.5	0.6	0.7	0.8	0.9	1.0	1.1
τ_c	0	0	0	0	0	0	0	0	0	0
$\delta\Psi_0$	1.2	1.3	1.4	1.5	1.6	1.7	1.8	1.9	2.0	2.1
τ_c	0	0	0	0	0	0	0	0	0	0
$\delta\Psi_0$	2.2	2.3	2.4	2.5	2.6	2.7	2.8	2.9	3.0	3.1
τ_c	0	0	0	0	0	0	0	0	0	0

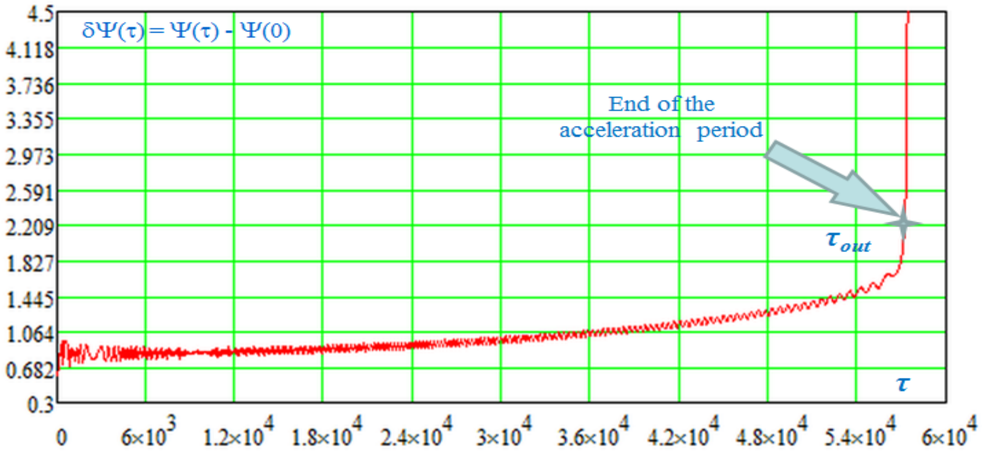

Figure 2. *Acceleration period in the plane of $\Phi(\tau) = d\Psi / d\tau$ and τ is presented. The end of this period is marked as τ_{out}. In this moment particle escape from the potential well and becomes free from the resonance interactions and returns to cyclotron rotation.*

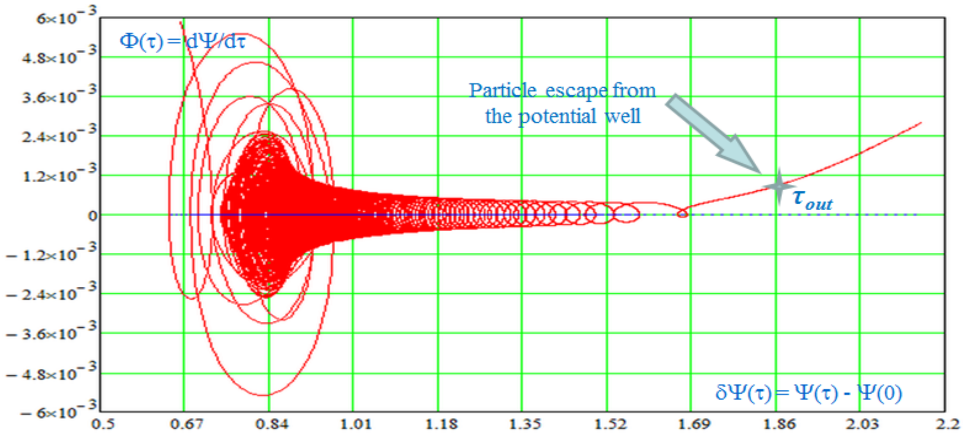

Figure 3. *Phase plane of accelerated particle $\Phi(\tau) = d\Psi / d\tau$ vs $\delta\Psi(\tau) = \Psi(\tau) - \Psi(0)$ in time interval $\tau = 60 \div 5.7\ 10^4$. The end of acceleration period is marked as τ_{out}. The structure of the phase plane resembles the nonlinear oscillators. This kind of trajectories and similar ones proposed in (Shkevov et al. 2017) is called surfatron resonant trajectory.*

Table 3. Part one. *The results of parallel collating of the computing of $\gamma(\tau)$ for the tasks of exact equation solutions and analytic approximation ones. The calculations are carried out for the 15 cases of different initial phases of $\delta\Psi(0) = -3.1 \div 3.1$. The columns ε and ε^2 present the differences in particle relativistic factor $\gamma(\tau)$ by simultainious calculations using two methods.*

$\delta\Psi_0$	τ_c	τ_{out}	M $(\tau)\gamma_{Aini}$	M (τ)	DEENS γ_{Eini}	DEENS γ_{Eout}	ε	ε^2
3.1	0	54830	1.0756	2830.303	1.0756	2830.831	0.528	0.279
2.5	0	56210	1.0756	2901.512	1.0756	2901.942	0.431	0.186
2.0	0	56850	1.0756	2934.536	1.0749	2935.617	1.081	1.169
1.5	0	57000	1.0756	2942.276	1.0745	2943.307	1.032	1.065
1.0	0	56930	1.0747	2938.664	1.0745	2939.286	0.622	0.387
0.5	0	55150	1.0726	2846.813	1.0726	2847.264	0.452	0.204

Table 3. Part two.

$\delta\Psi_0$	τ_c	τ_{out}	M $(\tau)\gamma_{Aini}$	M (τ)	DEENS γ_{Eini}	DEENS γ_{Eout}	ε	ε^2

0.1	12235	66250	1.0608	2788.235	1.0608	2788.823	0.589	0.347
0	3451	57850	2.1637	2809.152	2.1637	2808.777	-0.38	0.141
- 0.1	1058	55220	1.0576	2795.817	1.0576	2796.492	0.675	0.456
- 0.5	11614	65250	4.5475	2772.165	4.5475	2769.513	-2.65	7.033
- 1.0	8693	63550	1.4961	2832.117	1.4961	2832.298	0.181	0.033
- 1.5	13343	66300	6.9934	2742.155	6.9934	2736.672	-5.15	26.481
- 2.0	11578	65500	2.1167	2784.492	2.1167	2784.346	-0.38	0.147
- 2.5	9417	63370	1.4888	2785.464	1.4888	2785.808	0.345	0.119
- 3.1	0	54580	1.078	2818.284	1.078	2817.406	0.878	0.771

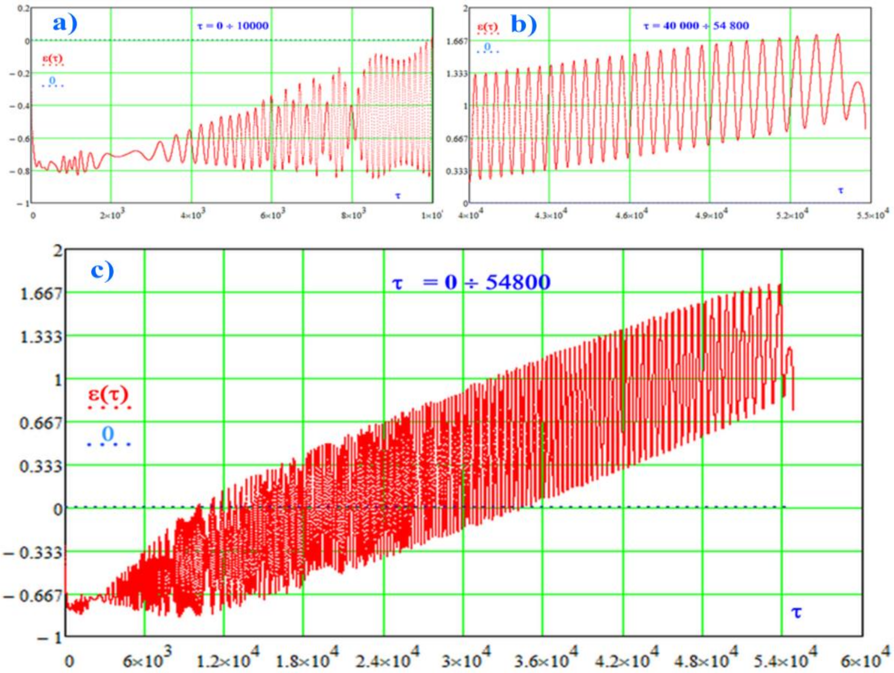

Figure 4. *Function of the absolute difference ε(τ) = γ(τ) - M(τ) at the range of: a) τ = 0 ÷ 10k - the beginning of the acceleration stage; b) τ = 40k ÷ 54.8k - end of the acceleration stage; c) τ = 0 ÷ 54.8k - full length of the acceleration stage for δΨ(0) = 3.1. The maximum in difference value between two calculations methods for τ = 54 800 is 0.018 %.*

5. Conclusions

- ➢ Resonant wave-particle interactions of the electrons and electromagnetic wave packet with Lorenz envelope is studied numericaly.
- ➢ 70 calculation tasks based on 70 different values for the wave packet phase around $\Psi(0) = 0$ in range from - 3.1 to +3.1, with maximal calculation length of $\tau_{max} = 7.10^4$ are formed.
- ➢ The results presented in Table 2 show cumulative particle capturing probability estimated to approximately ≈ 97%.
- ➢ In ≈ 47% of cases, the wave packet traps particle immediately $\delta\Psi_0 = 0$ and in about ≈ 50% electron is trapped after periods with different length of cyclotron rotation.
- ➢ The differences in the parallel collating of the computing for the tasks of exact equation solutions and analytic approximation are presented in Table 3.

- The maximum in difference value between two calculations methods for ε (τ) in % calculated by (DEENS $\gamma_{Eout} - M(\tau)\gamma_{Aout}$) / (DEENS γ_{Eout})*100 is in range of 0.0064% (for $\delta\Psi(0) = -1.0$) and 0.97% (for $\delta\Psi(0) = -1.5$).

Acknowledgement

This work is realized in the framework of the bilateral connections between IKI-RAS and SRTI-BAS established by the “Surfatron” project.

References

Bulanov, S.V., Sakharov, A.S. (1986). Acceleration of particles captured by a strong electrostatic wave with curved wave front in a magnetic field, *JETP Letters*, Vol. 44, No. 9, p. 543.

Chernikov, A.A., Schmidt, G., Neishtadt, A.I. (1992). Unlimited particle acceleration by waves in a magnetic field, *Physical Review Letters*, Vol. 68, No. 10, pp. 1507–1510.

Dieckmann, M.E., Shukla, P.K. (2006). Electron surfing acceleration by the electron two-stream instability in a weak magnetic field, *Plasma Physics and Controlled Fusion*, Vol. 48, p. 1515.

Erokhin, N.S., Moiseev, S.S., Sagdeev, R.Z. (1987). The fascination and following acceleration of the charged particles by slow wave in non-uniform plasma, *Doklady of the Russian Academy of Sciences*, Vol. 295, No. 4, pp. 849–852.

Erokhin, N.S., Moiseev, S.S., Sagdeev, R.Z. (1989). Relativistic surfing in non-uniform plasma and cosmic rays generation, *Astronomy Letters*, Vol. 15, No. 1, pp. 3–10.

Erokhin, N.S., Zolnikova, N.N., Shkevov, R., Mikhailovskaya, L.A., Trenchev, P. (2007). On the charged particles surfatron acceleration in space plasmas, *Proceedings of the Bulgarian Academy of Sciences (Comptes Rendus de l’Académie Bulgare des Sciences)*, Vol. 60, p. 967.

Erokhin, N.S., Zolnikova, N.N., Kuznetsov, E.A., Mikhailovskaya, L.A. (2010). Dynamics of the relativistic acceleration of charged particles in space plasma at the surfing at packet of electromagnetic waves, *Problems of Atomic Science and Technology (PAST), Plasma Electronics and New Methods of Acceleration*, Vol. 4 (68), pp. 116–120.

Gribov, B.E., Sagdeev, R.Z., Shapiro, V.D., Shevchenko, V.I. (1985). Damping of plasma waves and acceleration of resonant electrons in a transverse magnetic field, *JETP Letters*, Vol. 42, No. 2, p. 63.

Itin, A.P., Neishtadt, A.I., Vasiliev, A.A. (2000). Captures into resonance and scattering on resonance in dynamics of a charged relativistic particle in magnetic field and electrostatic wave, *Physica D: Nonlinear Phenomena*, Vol. 141, pp. 281–296.

Joshi, C. (1984). The surfatron laser–plasma accelerators: Prospects and limitations, *Radiation in Plasma*, Vol. 1, No. 4, p. 527.

Katsouleas, N., Dawson, J.M. (1983). Unlimited electron acceleration in laser-driven plasma wave, *Physical Review Letters*, Vol. 51, No. 5, pp. 392–395.

Kichigin, G.N. (1995). The features of electrons surfatron acceleration, *JETP*, Vol. 81, No. 4, p. 736.

Kichigin, G.N. (2001). The surfatron acceleration of cosmic rays in the galactic plasma, *JETP*, Vol. 92, No. 6, p. 895.

Loznikov, V.M., Erokhin, N.S. (2010). The variable source of space electrons excess in the heliosphere, *Problems of Atomic Science and Technology (PAST), Plasma Electronics and New Methods of Acceleration*, Vol. 4 (68), pp. 121–124.

Neishtadt, A.I., Artemyev, A.V., Zelenyi, L.M., Vainshtein, D.L. (2009). Surfatron acceleration in electromagnetic waves with a low phase velocity, *JETP Letters*, Vol. 89, pp. 441–447.

Shkevov, R., Erokhin, N.S., Mikhailovskaya, L.A., Zolnikova, N.N. (2013). Numerical investigation of the surfatron acceleration efficiency of charged particles by wave packets in space plasma, *Journal of Atmospheric and Solar–Terrestrial Physics*, Vol. 99, pp. 73–77.

Shkevov, R., Erokhin, N., Zolnikova, N., Mikhailovskaya, L. (2016). Protons surfatron acceleration by electromagnetic wave in space plasma, *Comptes Rendus de l’Académie Bulgare des Sciences*, Vol. 69, No. 2, pp. 177–182.

Shkevov, R., Erokhin, N.S., Loznikov, V.M., Zolnikova, N.N., Mikhailovskaya, L.A. (2018). Surfatron acceleration of weakly relativistic electrons by electromagnetic wave packet in space plasma, *Journal of Atmospheric and Solar–Terrestrial Physics*, Vol. 177, pp. 266–273.

Sitnov, M.I. (1988). Maximal particles energy in surfatron “unlimited” acceleration mode, *Technical Physics Letters*, Vol. 14, No. 1, pp. 89–92.

Vasiliev, A.A., Neishtadt, A.I., Artemyev, A.V. (2011). Nonlinear dynamics of charged particles in an oblique electromagnetic wave, *Physics Letters A*, Vol. 375, pp. 3075–3079.

DOI: 10.31401/WS.2025.proc.28

Proceedings of
the Seventeenth Workshop “Solar Influences on the Magnetosphere, Ionosphere and Atmosphere”
June, 2025

Basic Statistical Properties of the 10-years Ozone Daily Time Series from Stara Zagora

Werner R.[1], Petkov B.[2], Guineva V.[1], Bojilova R.[3], Raykova L.[1], Valev D.[1], Kirillov A.S.[4]

[1] Space Research and Technology Institute (SRTI) – Bulgarian Academy of Sciences, Stara Zagora Department, Bulgaria,

rolwer52@yahoo.co.uk
[2] Institute of Polar Sciences, National Research Council, Bologna, Italy
[3] National Institute of Geophysics, Geodesy and Geography (NIGGG) - Bulgarian Academy of Sciences, Sofia, Bulgaria
[4] Polar Geophysical Institute (PGI), Apatity, Russia

Abstract

In order to examine some important statistical parameters, the ozone series were detrended and seasonally adjusted. Then we determined the central moments as well as the skewness and kurtosis of the series. The distributions were analysed using histograms and Q-Q plots for different seasons. We divided the series into two groups with high and low ozone variations. The group with high variations includes the months from December to March (DJFM), while the group with lower variations includes the months from May to October (MJJAASO) with standard deviations of 36 DU and 19 DU, respectively. The reason for the high ozone variations is the frequent exchange of ozone-rich polar air masses with pure ozone air masses from the mid-latitudes and the tropics. The Q-Q plots show that the distributions for the two groups are close to normal distribution. On short time scales of a few days, the ozone residuals can be described by an AR (1) model. Long-term persistence was investigated using detrended fluctuation analysis (DFA). On scales ranging from a few days to a crossover of about 20 days, a Hurst coefficient of 0.93 was found, which characterises the series on these scales by strong persistence, far from chaotic behaviour but close to 1/f noise. From the crossover onwards, a Hurst coefficient of around 0.7 characterises the long-range correlation. The crossover achieved in the DFA of the seasonally adjusted and detrended total column ozone (TCO) indicates a change in the dominant processes on different time scales.

Keywords: statistic distribution, short-range correlation, Detrended Fluctuation Analysis

1. Introduction

Since the discovery of the Antarctic ozone hole, the mechanisms that cause ozone depletion have been intensively studied and the number of related publications is enormous. Here we will only refer to the reviews by Solomon [1999], Grewe [2007] and Chipperfield [2017]. Over the Antarctic, the lowest average ozone levels are reached in October. The October values decreased from the level 360 DU before 1980 by 120 DU in 1998-2000. The entry into force of the Montreal Protocol banning ozone depletion substances led to a decrease in the effective stratospheric chlorine loading (EESC) since the end of the 1990s. Since then, Antarctic ozone has not decreased any further. The same applies to ozone above the Arctic, although the decrease in ozone there is not as strong as in the Antarctic and the observed ozone depletion in March is only about 54 DU during 1998-2000 [Andersen and Knudsen, 2002]. At the Northern mid-latitudes (between latitudes of 30°N and 60°N) for the interval from 1979 up to the middle of 1990 the ozone decrease was about 5.5% [Harris et al., 2008]. That means the ozone loss was about 25 DU related to an averaged mean March total column ozone before 1979 of about 460 DU. Weber et al. [2022], using a multiple regression model based on different ozone annual satellite data sets, has found a significant downward trend of ozone depletion (from 1979 and

1995) for the latitude band 35°N – 60°N. But the observed trend of 0.5% per decade from 1995 up to 2020 is at the significance limit of 2σ. Fountoulakis et al. [2016] based on measurements with a Brewer spectralphotometer has been reported a TCO trend of 0.8%/decade for the time interval of 1994-2014 at Thessaloniki, a location near to Stara Zagora at a distance of only about 300 km in south-west direction. Werner et al. [2023a] did not find a significant trend in the ozone series from 1981 to 2022 based on the Sofia overpass data TM3DAM-MSR2. The increase in ozone following the observed trend reversal between 1995 and 1998 I s very slow and depends on latitude. The significance of the trends found is influenced by the correlation properties of the residuals of the ozone time series models. AR(1) models are generally used. However, the residuals also exhibit long-rang correlations, whereby the decline in the correlation function with increasing time delay can be described by a power law. Probability distributions and correlation properties are therefore among the fundamental characteristics of time series. They are essential, for example, when performing hypothesis tests. Significance tests of parameters in linear regressions, including trend parameters, are based on the assumption of a normal distribution of the residuals. The comparison of variances using the F-test also assumes a normal distribution. Skewness and kurtosis are used to assess whether the distribution of daily ozone values can be described by a normal distribution.

2. Data

This work is based on ground-based measurements of ultraviolet radiation intensity using a GUV 2511 global ultraviolet radiometer developed by Biospherical Instruments Inc. (BSI). Light, both direct sunlight and light scattered from the sky, falls on a Teflon entrance window and enters a hollow cylinder. This cavity contains seven photodiodes with filters in the UV range at wavelengths of 305, 313, 320, 340, 380, and 390 nm, each with an FWHM of approximately 10 nm, and a channel for detecting photosynthetically active radiation (PAR) in the visible range from 400 nm to 700 nm. The measurement process is controlled by a controller. The data files for each day are stored using a computer. Our device is stabilized at 50 °C. Further details about the device can be found in the brochure [BSI, 2008]. Biospheric Instruments subjects all GUV devices to radiation calibration in its optical laboratories.

To determine the total ozone in the atmosphere (TCO), we used the ratio of UV radiation at 340 nm, which is not affected by ozone, to radiation at 313 nm, which belongs to the absorption bands of ozone. In addition, the optical depth was determined using the ratio of the actual measured radiation at 380 nm and the radiation on a corresponding clear day. Look-up tables (LUT) (Stamnes et al., 1991) were created using the Madronich radiation transfer model for UV, known as the TUV model, which models the irradiance ratios and optical depths as a function of the zenith angle for different TCOs. The details of the algorithm, including the preprocessing procedures for TCO determination based on GUV UV irradiance measurements, are described in the publications [Werner et al., 2017 and 2018].

The stability of the results obtained with the GUV instrument and the developed algorithm was investigated by comparing them with the ozone values of the OMI instrument on the Aura satellite. It was found that, firstly, the absolute deviation of the successive four-year intervals 2015 –2018 and 2019–2022 using the OMI-Aura TCO as a reference increases slightly by 1.8 DU, and secondly, that the parameters of the linear regressions of both 4-year time series are not statistically different and do not differ from the pooled series. It was concluded that the temporal stability is acceptable [Werner et al., 2023b].

For the period from (February) 2015 to (March) 2025, we observed 3666 daily TCO values, which corresponds to 87% of the possible number. We only have no TCO data for about 13% of the days, partly for technical reasons and partly because of insufficient daylight due to heavy cloud cover. We used the ozone data from the OMI Aura satellite to complete our data series to about 97 %.

3. Ozone time series

The sequence of daily, monthly, seasonal, or annual ozone values for a location or average values for specific regions represent time series. Their components basically consist of a trend, a seasonal component, and a residual component. The trend T and the seasonal component S are often combined as a dynamically determined component. Time series models can be described by regression equations with time-dependent (possibly delayed) factors (predictors) x_t and delayed variables $y_{t-\tau}$ that describe their own history [Maddala, 1992]. For the trend, the factors X_t represent time itself, quadratic or higher exponents of time. By introducing dummy variables that describe a ramp function, a piecewise regression can be performed to detect structural breaks. Seasonality can be represented by sinusoidal factors. The statistical model for the time interval studied here (after the turning point, where a change in trend was observed) can therefore be represented as follows:

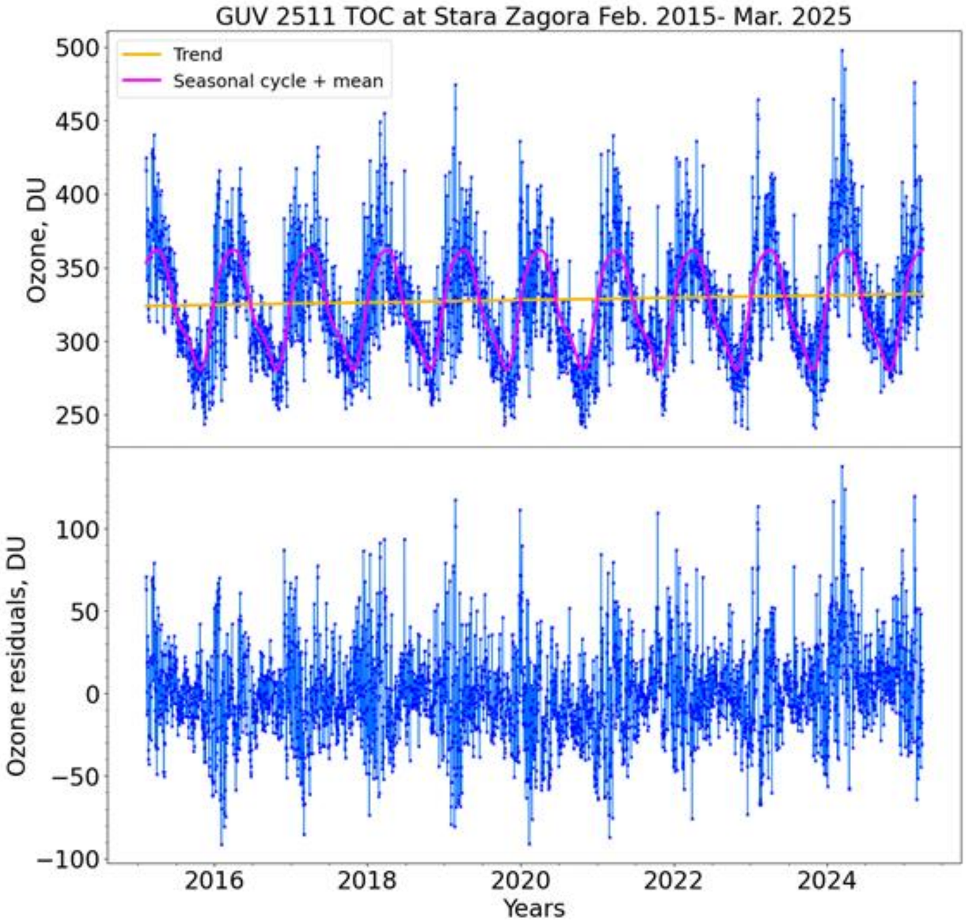

Figure 1. *The original TCO series (blue line and dots for measured values) in Stara Zagora for the period from February 2015 to March 2025, together with the annual seasonal cycle (magenta line) and the trend together with the mean value-(orange line), are shown in the upper field. The lower field shows the residuals. (The trend shown here was determined in a first step, and the seasonal cycle was calculated in a second step.)*

$$T_t = \mu + \alpha t + \sum_{i=1}^{k} \left[\beta_{2i-1} \sin\left(\frac{2\pi i t}{T_{per}}\right) + \beta_{2i} \cos\left(\frac{2\pi i t}{T_{per}}\right)\right] + \sum_{j=1}^{m} \gamma_j \ X_j + \varepsilon_t, \qquad (1)$$

where Xj are predictors as indices for solar activity and QBO and ε represent the residuals. However, the effects of QBO and solar flux on ozone in the mid-latitudes are very small (of the order of a few DU). For this reason, we limit our analysis of the ozone series to the seasonal component and the trend [see also Reinsel et al., 2002], whereby the mean value can be attributed to the trend component. We use three pairs of sinusoids for the seasonal component. The residuals ε_t must be stationary and normally distributed in order to perform tests, e.g., to perform the 2-sigma significance test of the regression coefficients in equation (1). Figure 1 shows the original TCO-Stara-Zagora series together with the seasonal and trend components in the upper panel and the residuals ε_t in the lower panel. The residual series shows clear non-stationarity. During the winter season, variability is much higher than during the rest of the year. This is caused by the frequent change of polar air masses with higher ozone content and air masses of tropical origin with lower TCO. In an earlier study, we showed through piecewise regression that the standard deviation in the winter months is about twice as high as in the other seasons [Werner, 2021]. The transition from the period with higher standard deviation to the period with lower standard deviation is related to the collapse of the vortex due to a sequence of minor and/or major sudden stratospheric warmings.

4. Standard deviation, skewness and kurtosis of the TCO residuals

The standard deviation, skewness, and kurtosis are non-Gaussian statistics that can be used to characterize time series. They are defined based on central moments of second, third, and fourth order. The skewness of single-peaked (unimodal) probability distributions describes the deviation from symmetry, and the kurtosis describes the sharpness of the peak.

To estimate the values of the standard deviation *std*, skewness *sk*, and kurtosis *k*, as well as their standard errors (*SE*), we use the traditional equations. Alternatively, the traditional statistics for skewness and kurtosis are multiplied by a function of the number of observations [Wright and Herrington, 2011]. These functions converge to 1 with *n* → ∞. (In our work, *n* is of the order of 1000). The traditional equations are as follows [ibid.]:

$=$

1

$$sk = \frac{\frac{1}{n}\sum_{i=1}^{n}(x_i-\bar{x})^3}{\sqrt{\left(\frac{1}{n}\sum_{i=1}^{n}(x_i-\bar{x})^2\right)^3}}\ , \qquad SE(sk)=\sqrt{\frac{6(n-2)}{(n+1)(n+3)}}\ , \qquad for\ \ n » 1: \qquad SE(sk)=\sqrt{\frac{6}{n}}, \qquad (2)$$

$-$

1

i=1nxi−x2, Confidence interval of SE (std): ixi−x2χn;1−α/22;ixi−x2χn;α/22 ,

$$k = \frac{\frac{1}{n}\sum_{i=1}^{n}(x_i-\bar{x})^4}{\sqrt{\left(\frac{1}{n}\sum_{i=1}(x_i-\bar{x})^2\right)^4}}, \qquad SE(k)=\sqrt{\frac{24\,n\,(n-2)(n-3)}{(n+1)^2(n+3)(n+5)}}, \qquad for\ \ n » 1: \qquad SE(k)=\sqrt{\frac{24}{n}},$$

$=$

1

where $\bar{x}$ is the mean of the observed values x_i. Because the values of the χ_n^2 distribution for the confidence levels 1-α/2 and α/2 are different, the confidences interval for the standard error of the standard deviation is not symmetrical and its lower and upper limits are given. In the statistic literature, the abbreviation g_1 and g_2 are often used for *sk* and *k*. An approximation of the standard errors of *sk* and *k* is given for observation numbers that are much larger than one. It can be seen, that for $n \gg 1$, *SE*(*k*) is twice as large as *SE*(*sk*). Instead of *k*, the excess kurtosis $k_e = k - 3$ is often given. In the case of a normal distribution, *sk* and k_e are equal to zero, which means that the distribution is symmetrical and not peaked. For sk values between -0.5 and 0.5, a normal distribution is assumed; if k_e is between -1 and 1, the distribution is well normally distributed [Hatem et al., 2022].

Bashenov et al. [2019] analysed the TCO series from 1994 to 2017 for the Tomsk station (56.50°N, 84.97°E). The authors found minimal relative standard deviations in July and August. Standard deviation, skewness, and kurtosis were used to classify the long-term TCO series from Arosa (1927–2000, 46.8N, 9.7E), Lerwick (1957–1999, 60.1°N, 1.2°W), and Camborn (1957–1999, 50.2°N, 5.3°W) [Tuomi et al., 2001]. The standard deviations at all three stations show greater variability during the winter-spring season. In order to compare the seasonal character of *std, sk* and k_e, we calculated these measures together with their standard error *SE*. The results are summarised in Table 1. The standard deviation in winter is approximately twice as high as in summer and autumn. This is in good agreement with the results obtained from the investigation of ozone variance in the Sofia overpass data TM3DAM-MSR2 from 1981 to 2018 based on the iterative method of cumulative sums of squares. It was found that the structure of the TCO series has two breakpoints each year, one near the development of the vortex and one related to the vortex break, and it was concluded that the Sofia overpass ozone series is highly heteroscedastic [Werner et al., 2021]. As it can be seen from Table 1, *sk* = 0.409 and k_e = -0.047 for the winter season, so the distribution is almost normal. In the JJA and SON seasons, the kurtosis is significantly greater than zero, but the characteristics are very similar, and the assumption that they come from the same population is obvious.

Table 1: *The number of observations n, the standard deviation std, the skewness sk, the excess kurtosis k_e and their standard errors calculated for the winter DJF, the spring MAM, the summer JJA and fall SON seasons and the same for the winter/early spring, here called vortex season, DJFM and for late spring to the autumn season, here called non-vortex season, MJJASO for all observations with and without outliers.*

	DJF	MAM	JJA	SON	DJFM	MJJASO	MJJASO outl. del.
n	887	923	879	867	1216	1765	1758
std in DU	36.5	29.8	17.2	19.2	36.5	18.5	17.9
1σ-error in DU	-1.6/1.8	-1.3/1.4	-0.8/0.8	-0.9/0.9	-1.4/1.5	-0.6/0.6	-0.6/0.6
sk	0.409	0.506	0.602	0.718	0.425	0.488	0.185
1σ-error	0.082	0.080	0.082	0.083	0.070	0.058	0.058
k_e	-0,047	0.726	1.666	1.942	0.046	1.707	0.435
1σ-error	0.163	0.160	0.164	0.165	0.140	0.116	0.116

We have divided the GUV-TCO series into two parts. One part in which the polar vortex (vortex season, DJFM) develops, and another part in which no vortex is observed (non-vortex season, MJJASO). The extended winter season DJFM has almost the same characteristics as the winter season DJF, and the characteristics of the non-vortex season, which combines the seasons JJA and SON, are comparable to those of the individual seasons. The high values of *sk* and k_e for the summer and autumn seasons as well as for the non-vortex season indicate a non-Gaussian distribution of the TCO residuals for these time intervals. The months of April and November are considered transition months from one season to the next one.

5. Histogramms and Q-Q plots

Numerous statistical tests have been developed to verify normal distribution. They include the Kolmogorov-Smirnov test, the Liliefors test, the Shapiro-Wilk test and the Anderson-Darling test. With large sample sizes, even a small deviation from normal distribution would yield significant results [Öztuna et a.l, 2006, Ghasemi and Zahediasl, 2012]. To clarify our conclusions about the distributions – non-Gaussian or Gaussian – we have created histograms and Q-Q plots for the ozone residuals distributions and all seasons examined here. In Q-Q plots, the empirical or observed sample quantiles are plotted above the theoretical quantiles.

In an ideal Gaussian distribution, the Q-Q plot is identical to the bisecting line. The theoretical probabilities were estimated here with $p = i/(n+1)$, where $i = 1\ldots n$. The graphs of the resulting histograms and Q-Q plots are shown in Figure 2. The histogram for the winter season shows a slight tail on the right side, which corresponds to the positive skewness. The tails of the distributions for the other seasons are somewhat heavier, which is caused by outliers, as documented in the Q-Q plots for sample quantiles greater than about three. The middle parts of the Q-Q plots are very close to the bisecting line. As expected, the kurtosis changes significantly to smaller values after the outliers are removed. The characteristics s_k and k_e for the vortex season DJFM and for the no vortex season MJJASO, for which outliers have been removed, indicate that a Gaussian distribution can be considered as acceptable. This impression is confirmed by examining the corresponding Q-Q plots (see Figure 3). The advantage of using combined seasonal ozone values lies in the larger number of observations. Of course, outliers must be taken into account when analysing extreme ozone value distributions.

6. ACF – short-range correlation

Residual regre-ssion equations, such as [1], are often autocorrelated. This means that in the case of first-order autoregression, the residuals can be written as follows:

$$\varepsilon_t = \varphi_1 \varepsilon_{t-1} + u_t, \tag{3}$$

where u_t is normally distributed. Whether the residuals can be described by a first-order or higher-order autoregression model or by a more general autoregression model can be investigated using the autocorrelation and partial autocorrelation functions of the residuals. Our colleagues in the Geophysical department of the National Institute of Geophysics, Geodesy and Geography have used combined satellite data from 1998 to 2008 for the Sofia location to create the autocorrelation function of the ozone residuals and have determined an exponential decay with a time constant of approximately 2.5 days [Total_ozone]. Furthermore, the PCAF have only one coefficient r_{11}, which is equal to φ_1. Here we go one step further. In addition to the autocorrelation function, we analyse also the partial autocorrelation function (PCAF). In an ideal AR(1) process, the autocorrelation coefficients ρ_k to a lag k are related to the autoregression coefficient φ_1 with the equation $\rho_k = \varphi_1^k$ being valid. The estimated ACF for k=1 yields an autoregression coefficient of 0.61. The identity $\varphi_1^k = \exp(k * \ln \varphi_1)$ shows the exponential decay of the autocorrelation function for an AR(1) process. The estimated $\widehat{ACF}$ and $\widehat{PCF}$ of the ozone residuals are presented in Figure 4. The $\widehat{ACF}$ shows the exponential decay for the first four lags τ, which are determined

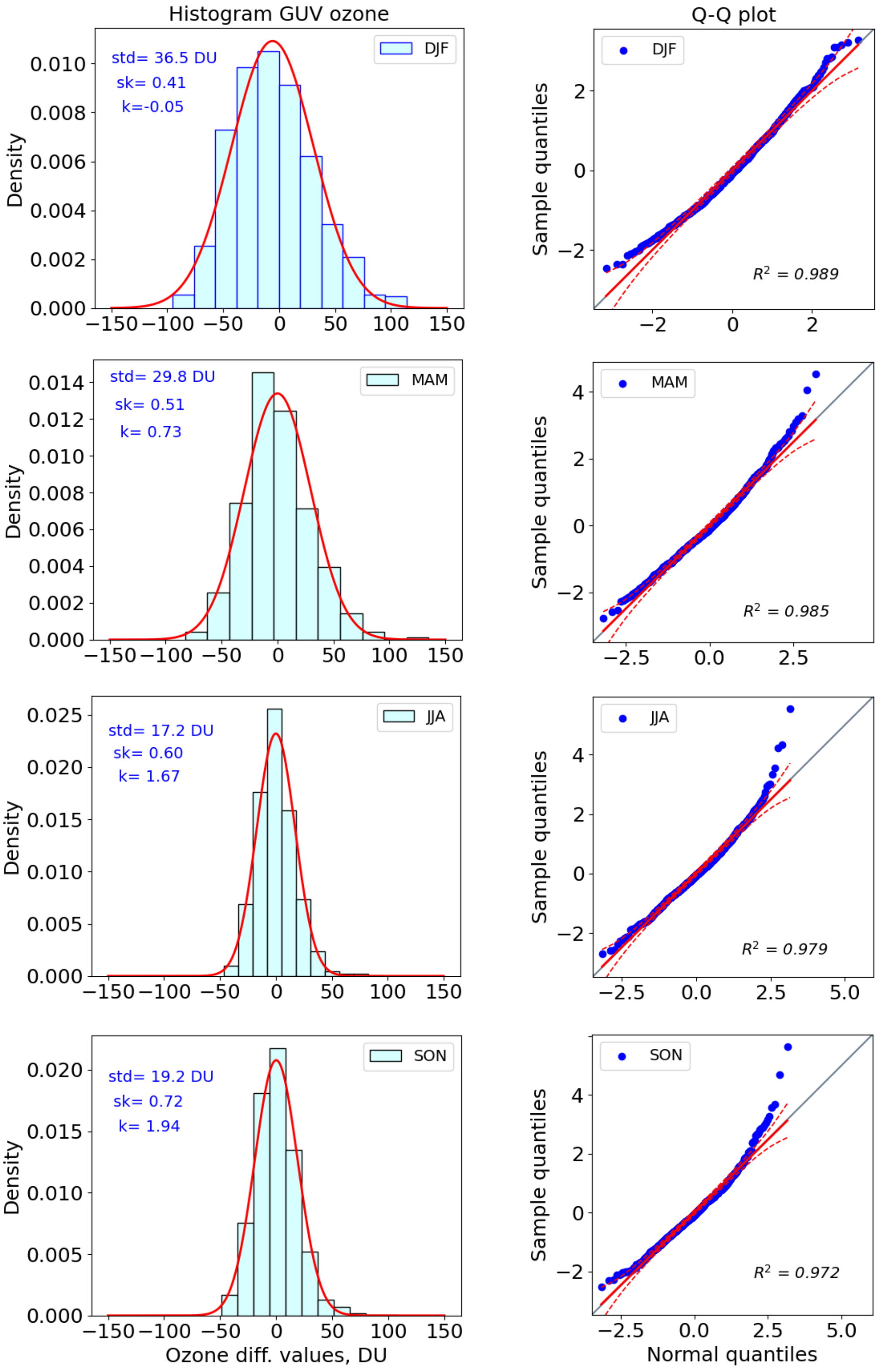

Figure 2. *Seasonal histograms of the ozone residuals together with their approximated Gausian distributions (red lines) are shown at left side and the corresponding Q-Q plots are presented at the right side of the panel. The red dashed lines are the upper and lower limits of the 0.95 confidence intervals. The graphics are displayed respectively for the DJF, MAM, JJA and SON from top to bottom.*

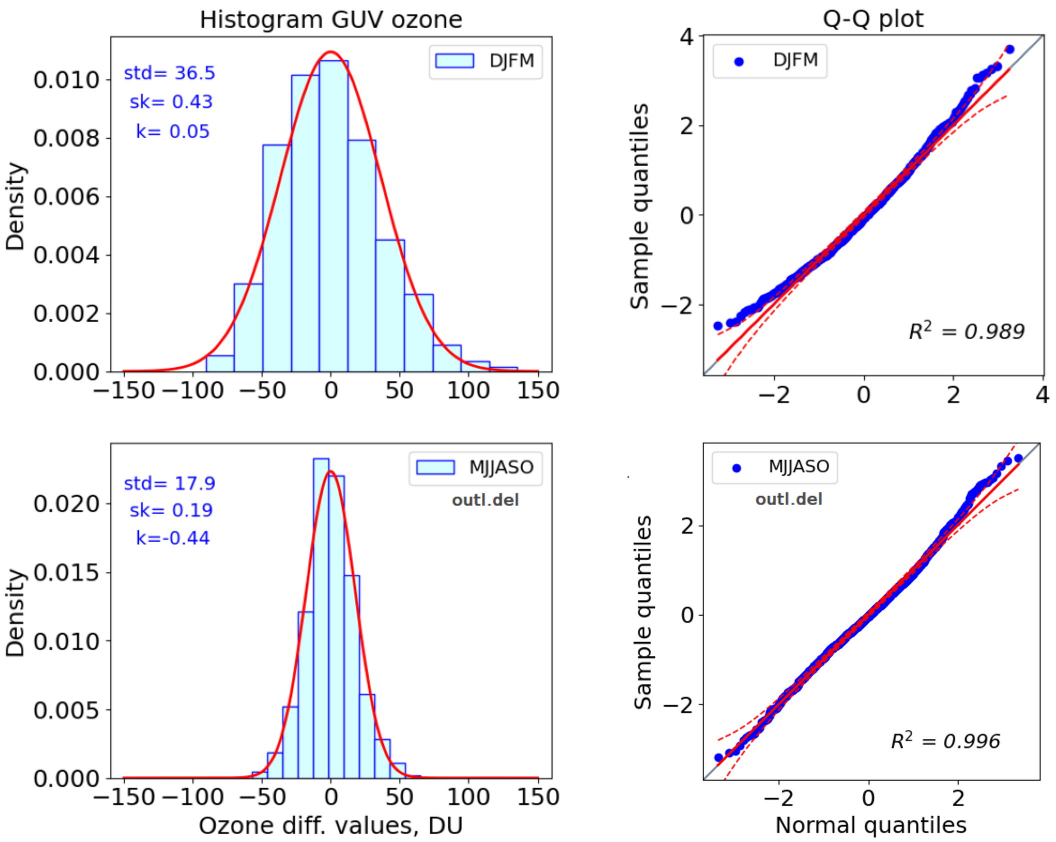

Figure 3. *The figure corresponds to Figure 2, but for the vortex season DJFM and for the non-vortex season MJJASO, where seven outliers were deleted for MJJASO (see Table 1).*

by a two-parameter approximation $\widehat{ACF} = c * exp\left(-\frac{\tau}{\tau_0}\right)$, drawn as red line in the inner figure at the left side of Figure 4. The time constant τ_0 was determined to be 2.70 days.

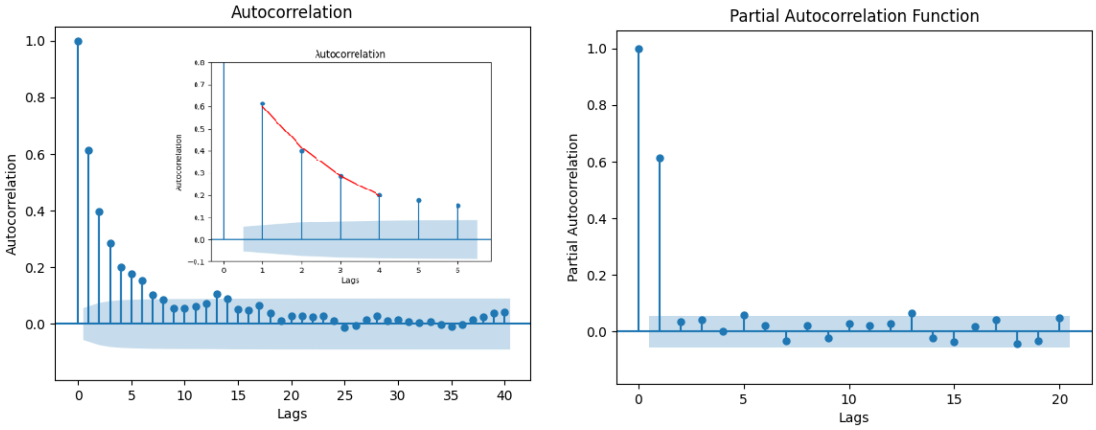

Figure 4. *The estimated autocorrelations* r_k *(left) and estimated partial autocorrelation function for the ozone residuals (right). The standard errors calculated by the Barlett equations, implemented in the Pythons ACF and PCF functions, for the corresponding lags are presented as shadowed regions.*

The estimated $\widehat{PCF}$ shows only one clear maximum at the lag 1, which characterises the order of the AR process. From this, we conclude that the ozone residual values can be describe by an AR(1) process. Ideally, an AR(1) process can be interpreted as a process with infinite memory. In practice, however, the ACF drops quickly and the memory is limited to only a few time steps. For the TCO series, this means that if the ozone has increased/decreased in the recent days, it can be assumed that it will continue to increase/decrease the next day. At greater lags, from four up to eight the autocorrelation coefficients decline more slowly and subsequently fall below the one-sigma error.

7. Detrended Fluctuation Analysis – Long persistence

The variation of correlation over time allows for interferences about the dynamics of complex physical processes. The direct calculation of autocorrelation for large lags is limited by the noise as demonstrated in the previous paragraph. A tool that is commonly used to investigate long persistence or long memory process is the Detrended Fluctuation Analysis (DFA) developed by Peng et al. [1994]. This method was further developed by Kantelhardt et al. [2002] into Multifractal Detrended Fluctuation Analysis (MF-DFA) to study multifractal processes. The results of the DFA enable the indirect determination of the decay of the autocorrelation function for large lags.

The DFA is determined in successive steps, starting with the calculation of the cumulative sum of the members of the time series, referred to as the profile or integrated anomaly. The series is then divided into N_s non-overlapping segment intervals of length s and the (local) linear trend is determined for each of these segments. (In the MF-DFA, polynomials of degree m are also permitted for this purpose). The squared values of the fluctuations in each segment are calculated by the sum of the mean square deviations of the detrended profile values.

The quadratic values of the fluctuations over all segments N_s are totalled and averaged. As not all values in the series are recorded during segmentation, the procedure is repeated from the end of the time series and the quadratic fluctuations are determined again. This results in a total of 2 N_s segments. The fluctuations as a function of the scales s result from their square root of the mean value of all 2 N_s fluctuations. If the data have a power law:

$$C(s) \sim s^{-\gamma}\,,\ where\ \ 0 < \gamma < 1 \tag{4}$$

the fluctuation function also increases by a power law [Koscielny-Bunde et al., 1998]

$F(s)\ \sim\ s^{\alpha}$. The exponent α is referred to as scaling exponent or correlation exponent and can be found as the slope of the F(s) in double logarithmic representation of F(s) over s. The relationship between α and γ is given by $\alpha\ =\ 1 - \frac{\gamma}{2}$. The correlation exponent is an estimate of the Hurst coefficient and determines the correlation properties of the series. For H = 0.5, the time series is not correlated and represents white noise. For scale intervals with H > 0.5, the series is broadly positive, the trends continue, and for H < 0.5 it is broadly negatively correlated, the trends reverse. The power spectrum function decays as: [see e.g. Varotsos, 2005]

$$S(f) \sim f^{-\beta} \text{ with } \beta = 2\alpha - 1. \tag{5}$$

[see e.g. Varotsos, 2005]. For α = 1 we obtain the power spectrum exponent β = 1 and *S(f)* ~ 1/f, corresponds to the so called *1/f* noise.

The mathematical equations of the DFA method are described in detail in Kantelhardt et al. [2002]. In recent decades, DFA and MF-DFA have been used to analyse time series in fields such as hydrology, biology, neuroscience and geophysics. Koscienlny-Bunde et al. [1998] analysed the long-term records of daily maximum temperatures (typically longer than 100 years) from 14 randomly selected surface stations around the world and determined a scaling exponent of 0.65.

Using DFA, Király found a latitudinal dependence of the scaling exponent for the daily mean temperature series [see citation in Kiss et al. 2007]. The exponents are of the order of 0.6 to 0.98, with the maximum near the equator and the minima in mid-latitudes in both hemispheres. Kiss et al. [2007] performed a DFA analysis for filtered and merged daily

Nimbus7 Earth Sample records (for each grid point between 65°S and 65°N latitudes in the Total Ozone Mapping Spectrometers (TOMS) and found a similar latitude dependence of the ozone scaling exponent as for the mean temperatures mentioned above with a maximum of 0.96 and a minimum of about 0.66. The authors conclude that the source of the long-range correlation lies in the atmospheric dynamics for both total ozone and temperature.

We applied DFA to analyse the long-range correlation of our total column ozone time series. As it is well known, non-stationarities such as cycles and trends can influence the resulting correlation.

The QBO effect on the TCO is important in the tropics and very small in mid-latitudes. Solar activity during the period of interest (2015-2024) is relatively low. At the beginning of 2015, the solar activity is in the decline phase after the maximum of 24th solar day. The F10.7 cm index averaged over 27 days decreases from about 131 solar flux units (sfu) to a minimum of 67 sfu after 2017 and starts to increase again after 2021, reaching its maximum of 252 sfu (OMNIWeb Results) in the second half of 2024.

The corresponding ozone response to solar activity is about 3.7 DU/100 sfu [Stolarski et al., 1991]. Reinsel et al. [2002] found a latitudinal dependence of the ozone response to solar variability of 6 to -2 DU/100 sfu. A response of 2 DU/100 sfu is given for the latitude band at 40°N. Calisesi and Matthes [2006] give an average value of 1-2 % total ozone change in the mid-latitudes from solar minimum to maximum. In the Ozone Assessment Report 2018, a response of -1 to 2 % of the total ozone anomaly is given for the latitude range 35° - 60°N. Knibbe et al. [2014] found no significant solar effect on the total ozone over the eastern Balkans with a confidence level of 99 %. Thus, we expect a mean ozone response of less than 3 DU over Stara Zagora for the period analysed here, and we do not include solar activity in our regression equation (1). This corresponds to the obtained results in Werner et al. [2023a], where a change from solar minimum to maximum of -2.5 DU to 5 DU for the time interval 1979 – 2022, which include the very strong solar cycles 21 and 22 was found. We only consider the linear trend (including the mean) and the seasonal cycle in the form of three sinusoids together in one equation. In this way, we obtain a linear trend of about 2.7 DU/decade. (We emphasis that this is not a long-term trend, as our ozone series is too short for such an analysis).

The DFA shows artificial deviations on small scales [Kantelhardt et al., 2001]. Therefore, we have to calculate the DFA for random series that have approximately the same length as our ozone series. DFA for such a random series is shown in Figure 5. As it was expected, the linear slope is 0.5. The shorter the scale length, i.e. shorter than 7-8 days, the more pronounced the deviation from the linear slope. Instead of correcting this effect with the correction factor function given in Kantelhardt et al., [2001], we do not interpret the DFA results for scales shorter than 7-8 days. The calculated DFA of our deseasonalised and detrended TCO is shown in Fig. 6. In our case, detrending has no influence on the resulting DFA, therefore no higher order DFA was calculated. The overall slope of the fluctuation function is 0.76 (see Figure 6). This is in good agreement with the investigated DFA of the daily deseasonalised ozone series from Arosa (1926-1970, 46.8°N, 9.7°E), from Camborn (1957-1999, 50.2°N, 5.3°W) and from Lerwick (1957-1999, 60.1°N, 1.2°W), where the Hurst coefficients obtained are 0.76, 0.76 and 0.77, respectively, with the rescaled range analysis [Tuomi et al., 2001]. For the entire Arosa series (1927-2000), H=0.80 was determined. The DFA of our TCO shows a crossover on a scale of about 20 days and a slope of 0.93 before and 0.67 after. Kiss et al. [2007] show the DFA of Arosa with better graphical resolution. We have derived a transition on a scale of about 30 days from this graph, with a slope of 0.90 before and 0.68 after it. This result agrees

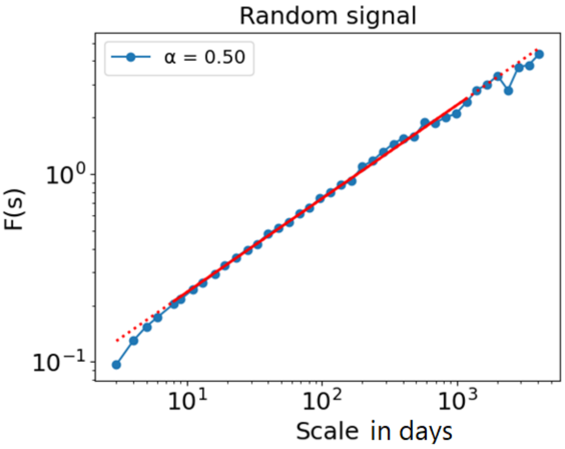

Figure 5*. DFA of a random signal. The slope of 0.5 is drawn by a continuous red line for the interval where a linear trend is observed. The dashed line extension is shown to outline the artificial deviations for small scales.*

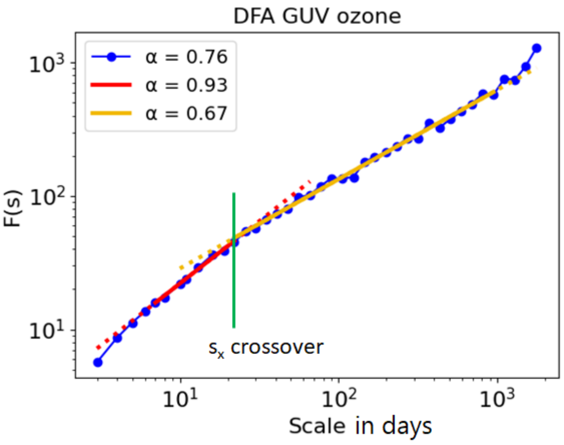

Figure 6*. DFA of the deseasonalized and detrended TCO at Stara Zagora. The location of the crossover is marked by a green vertical line. The slopes are drawn by continuous lines, which are extended to show their differences more clearly.*

very well with our findings. Kantelhardt et al. [2006] observed a transition on a scale of a few weeks in river discharge fluctuations and found that the time scale of the transition is similar to the period of planetary waves with typical periods of 2 to 30 days. Varotsos investigated the power-law correlations in the ozone column over Antarctica. He found an overlap in the DFA on a scale of about 10 days and concluded that this overlap illustrates the crucial role of planetary waves in the scaling characteristics of the spatio-temporal variability of the Antarctic ozone hole [Varotsos, 2005]. Kalamaras et al. [2017] found memory characteristics by H of 0.69, 0.67 and 0.69 for the daily mean, maximum and minimum temperature in Thessaloniki, respectively, and H=0.69 for the wind speed. It is well known that weather phenomena associated with tropospheric high or low pressure systems, which are reversible in the lower stratosphere, influence the TCO mainly through dynamical processes. Eicher et al. [2003] analyzed daily temperature records and determined a transition time of the order of 10 days, which is typical for a Großwetterlage (large-scale weather pattern) in the fluctuation function.

To test whether the non-stationarity caused by the different standard deviations during the vortex season (December–March) and non-vortex season (May–October) generated an artificial crossover at about 20 days, we calculated the DFA separately for the two seasons. The calculations were performed in two ways. Firstly, the DFA was determined individually for each segment and each year, and then the annual average was calculated. Secondly, the DFA was determined by concatenating (called "cut and stitching together", see Chen et al. [2002]) the seasonal parts, i.e. all Dec.-Mar. segments and all May-Oct. segments, correspondingly. The non-vortex season May-Oct. comprises 50% of a year and according to Cheng et al [2002] the scaling behaviour of the remaining part must be the same as for the full part. In fact, both series - the full series (Fig. 6) and of the stitching together series segments from May to October (Figure 7) - show a crossover s_x on approximately the same scale, and the slopes before and after the crossover are not noticeably different. For the series consistent of the sequences Dec. – Mar., stiching together, s_x is about 30 days and the correlation up to the crossover is also the same as for the full series. The long-range correlation after the crossover is somewhat lower. The comparison of the slopes after the crossover shows, that the

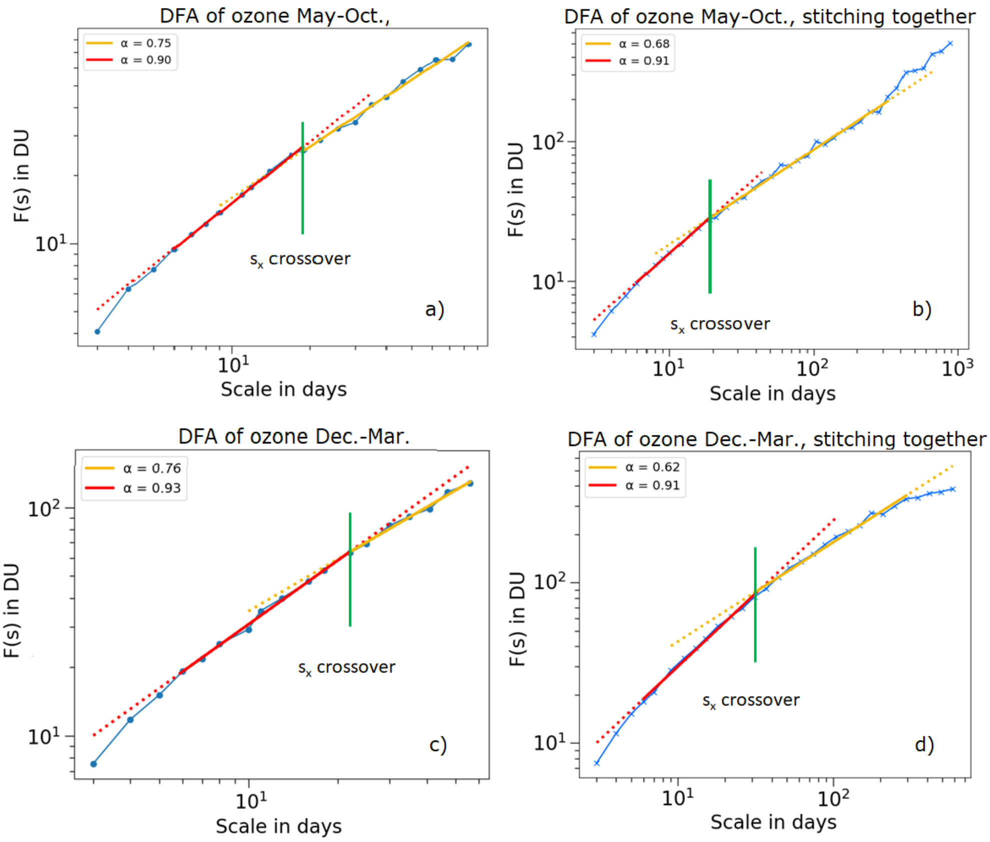

Figure 7. *Results of the DFA calculation. The left side shows the calculation of the DFA for each segment separately for each year with subsequent averaging (a and c) and the right side shows the DFA obtained by „cut and stitching together“(b and d). The upper panels show the DFA for the segments May-Oct. and the lower panels the DFA for the segments Dec.-March.*

slopes for the series from December to March and for the series from May to October, calculated by annual averaging, are significantly greater than the slope for the complete series. The reason for this may lie in the shortness of the remaining interval for determining the long-range correlation. To summarise, it can be said that the overlap occurred independently of the method used to calculate the DFA, so we conclude that the crossover is not an artificial effect.

The entire non-stationary TCO series consists of segments with two different standard deviations. These are the segments that cover the months from December to March and from May to October. The series part formed by stitching together the segments from December to March and the one formed by stitching together segments from March to October are stationary in themselves. The scaling behaviour of the non-vortex series of the segments from March to October (Figure 7) does not differ from that of the non-stationary TCO series (Figure 6). This corresponds very well to the results of Chen's simulations for non-stationary correlated signals ($\alpha > 0.5$) with segments characterised by two different standard deviations [Cheng et al., 2002].

8. Summary

The values for skewness and kurtosis as well as the Q-Q diagram confirm the normality of the ozone residuals for the winter season DJF. The characteristics standard deviation, skewness and excess of kurtosis of the summer season JJA and the autumn season SON are similar, and it is reasonable to assume that the ozone residuals originate from the same statistical sample.

The entire deseasonalised and detrended TCO series is non-stationary (heteroscedastic). We compiled samples from only two subsamples of the residuals. Namely, one for the season

December to March, when ozone in Stara Zagora is influenced by the alternation of polar air masses with tropical air, and the other for May to October. The absolute values of skewness and excess of kurtosis of the combined samples are less than 0.5 and their distributions can be considered as normal.

The DFA of the annual GUV ozone residuals shows that the series have a long time memory. A crossover was observed at scale s_x of about 20 days. Before s_x a Hurst coefficient of about 0.93 and after s_x a Hurst coefficient of about 0.68 was observed. The crossover is caused by various atmospheric processes. The fluctuations before the crossover are probably related to planetary waves and weather phenomena, while after the crossover the source of the long-range correlation is related to large-scale atmospheric dynamical processes.

Reference

Andersen, S.B., Knudsen, B.M. (2002). The influence of vortex ozone depletion on Arctic ozone trends, *Geophysical Research Letters*, Vol. 29, No. 21, pp. 9-1–9-4, DOI: 10.1029/2001GL014595.

Bazhenov, O.E., Elnikov, A.V., Sysoev, S.M. (2019). Total ozone content over Tomsk in 1994–2017: Results of statistical analysis, *Atmospheric and Oceanic Optics*, Vol. 32, No. 6, pp. 680–685, DOI: 10.1134/S1024856019060034.

Biospherical Instruments Inc. (2008). *Model GUV-2511 — Ground-Based UV / PAR Radiometer* (brochure).

Calisesi, Y., Matthes, K. (2006). The middle atmospheric ozone response to the 11-year solar cycle, *Space Science Reviews*, Vol. 125, pp. 273–286, DOI: 10.1007/s11214-006-9063-4.

Chen, Z., Ivanov, P.Ch., Hu, K., Stanley, H.E. (2002). Effect of nonstationarities on detrended fluctuation analysis, *Physical Review E*, Vol. 65, 041107, DOI: 10.1103/PhysRevE.65.041107.

Chipperfield, M.P. (2015). Global atmosphere – the Antarctic ozone hole, in: Harrison, R.M., Hester, R.E. (eds.) *Still Only One Earth: Progress in the 40 Years Since the First UN Conference on the Environment*, pp. 1–33, DOI: 10.1039/9781782622178-00001.

Eichner, J.F., Koscielny-Bunde, E., Bunde, A., Havlin, S., Schellnhuber, H.-J. (2003). Power-law persistence and trends in the atmosphere: A detailed study of long temperature records, *Physical Review E*, Vol. 68, 046133, DOI: 10.1103/PhysRevE.68.046133.

Fountoulakis, A., Bais, A., Fragkos, K., Meleti, C., Tourpali, K., Zempila, M.M. (2016). Short- and long-term variability of spectral solar UV irradiance at Thessaloniki, Greece: Effects of changes in aerosols, total ozone and clouds, *Atmospheric Chemistry and Physics*, Vol. 16, pp. 2493–2505, DOI: 10.5194/acp-16-2493-2016.

Ghasemi, A., Zahediasl, S. (2012). Normality tests for statistical analysis: A guide for non-statisticians, *International Journal of Endocrinology and Metabolism*, Vol. 10, No. 2, pp. 486–489, DOI: 10.5812/ijem.350.

Grewe, V. (2007). Impact of climate variability on tropospheric ozone, *Science of the Total Environment*, Vol. 374, pp. 167–181, DOI: 10.1016/j.scitotenv.2007.01.032.

Harris, N.R.P., Kyrö, E., Staehelin, J., Brunner, D., Andersen, S.-B., Godin-Beekmann, S., Dhomse, S., Hadjinicolaou, P., Hansen, G., Isaksen, I., Jrrar, A., Karpetchko, A., Kivi, R., Knudsen, B., Križan, P., Lastovicka, J., Maeder, J., Orsolini, Y., Pyle, J.A., Rex, M., Vaníček, K., Weber, M., Wohltmann, I., Zanis, P., Zerefos, C. (2008). Ozone trends at northern mid- and high latitudes – a European perspective, *Annales Geophysicae*, Vol. 26, pp. 1207–1220, DOI: 10.5194/angeo-26-1207-2008.

Hatem, G., Zeidan, J., Goossens, M.M., Moreira, C. (2022). Normality testing methods and the importance of skewness and kurtosis in statistical analysis, *BAU Journal – Science and Technology,* Vol. 3, No. 2, Article 7, DOI: 10.54729/KTPE9512.

Kalamaras, N., Philippopoulos, K., Deligiorgi, D. (2017). Scaling properties of meteorological time series using detrended fluctuation analysis, in: Karacostas, T., Bais, A., Nastos, P. (eds.) *Perspectives on Atmospheric Sciences*, Springer Atmospheric Sciences, Springer, Cham, DOI: 10.1007/978-3-319-35095-0_78.

Kantelhardt, J.W., Koscielny-Bunde, E., Rego, H.H.A., Havlin, S., Bunde, A. (2001). Detecting long-range correlation with detrended fluctuation analysis, *Physica A: Statistical Mechanics and its Applications*, Vol. 295, pp. 441–454, DOI: 10.1016/S0378-4371(01)00144-3.

Kantelhardt, J.W., Zschiegner, S.A., Koscielny-Bunde, E., Havlin, S., Bunde, A., Stanley, H.E. (2002). Multifractal detrended fluctuation analysis of nonstationary time series, *Physica A: Statistical Mechanics and its Applications*, Vol. 316, pp. 87–114, DOI: 10.1016/S0378-4371(02)01383-3.

Kantelhardt, J.W., Koscielny-Bunde, E., Rybski, D., Braun, P., Bunde, A., Havlin, S. (2006). Long-term persistence and multifractality of precipitation and river runoff records, *Journal of Geophysical Research: Atmospheres*, Vol. 111, D01106, DOI: 10.1029/2005JD005881.

Kiss, P., Müller, R., Jánosi, I.M. (2007). Long-range correlations of TOMS total ozone, *Nonlinear Processes in Geophysics*, Vol. 14, pp. 435–442, DOI: 10.5194/npg-14-435-2007.

Knibbe, J.S., van der A, R.J., de Laat, A.T.J. (2014). Spatial regression analysis on 32 years total column ozone data, *Atmospheric Chemistry and Physics Discussions*, Vol. 14, pp. 5323–5373, DOI: 10.5194/acpd-14-5323-2014.

Koscielny-Bunde, E., Bunde, A., Havlin, S., Roman, H.E., Goldreich, Y., Schellnhuber, H.-J. (1998). Indication of a universal persistence law governing atmospheric variability, *Physical Review Letters*, Vol. 81, No. 3, pp. 729–732, DOI: 10.1103/PhysRevLett.81.729.

Maddala, G.S. (1992). *Introduction to Econometrics* (2nd ed.). Macmillan Publishing.

Öztuna, D., Elhan, A.H., Tüccar, E. (2006). Investigation of four different normality tests in terms of type I error rate and power under different distributions, *Turkish Journal of Medical Sciences*, Vol. 36, No. 3, pp. 171–176.

Peng, C.K., Buldyrev, S.V., Havlin, S., Simons, M., Stanley, H.E., Goldberger, A.L. (1994). Mosaic organization of DNA nucleotides, *Physical Review E*, Vol. 49, pp. 1685–1689, DOI: 10.1103/PhysRevE.49.1685.

Reinsel, G.C., Weatherhead, E., Tiao, G.C., Miller, A.J., Nagatani, R.M., Wuebbles, D.J., Flynn, L.E. (2002). On detection of turnaround and recovery in trend for ozone, *Journal of Geophysical Research: Atmospheres*, Vol. 107, DOI: 10.1029/2001JD000500.

Solomon, S. (1999). Stratospheric ozone depletion: A review of concepts and history, *Reviews of Geophysics*, Vol. 37, No. 3, pp. 275–316, DOI: 10.1029/1999RG900008.

Stamnes, K., Slusser, J., Bowen, M. (1991). Derivation of total ozone abundance and cloud effects from spectral irradiance measurements, *Applied Optics*, Vol. 30, No. 30, p. 4418, DOI: 10.1364/AO.30.004418.

Stolarski, R.S., Bloomfield, P., McPeters, R.D., Herman, J.R. (1991). Total ozone trends deduced from Nimbus-7 TOMS data, *Geophysical Research Letters*, Vol. 18, No. 6, pp. 1015–1018, DOI: 10.1029/91GL01302.

Tuomi, R., Syroka, J., Barnes, C., Lewis, P. (2001). Robust non-Gaussian and long-range correlation of total ozone, *Atmospheric Science Letters*, Vol. 2, Nos. 1–4, pp. 94–103, DOI: 10.1006/asle.2001.0042.

Varotsos, C. (2005). Power-law correlations in column ozone of Antarctica, *International Journal of Remote Sensing*, Vol. 26, No. 16, pp. 3333–3342, DOI: 10.1080/01431160500076111.

Weber, M., Arosio, C., Coldewey-Egbers, M., Fioletov, V.E., Frith, S.M., Wild, J.D., Tourpali, K., Burrows, J.P., Loyola, D. (2022). Global total ozone recovery trends attributed to ozone-depleting substance changes derived from five merged ozone datasets, *Atmospheric Chemistry and Physics*, Vol. 22, pp. 6843–6859, DOI: 10.5194/acp-22-6843-2022.

Werner, R., Guineva, V., Valev, D., Bojilova, R., Kirillov, A. (2023a). Long-time trend in total ozone column by MRS2 overpass data for Sofia for 1979–2022 based on ordinary and weighted linear regression, *15th Workshop “Solar Influences on the Magnetosphere, Ionosphere, and Atmosphere”* (PowerPoint presentation).

Werner, R., Petkov, B., Guineva, V., Kirillov, A., Atanassov, A., Bojilova, R., Valev, D., Raykova, L. (2023b). Verification of the long-term stability of ozone measurements with the GUV-2511 instrument in Stara Zagora, *Proceedings of the Nineteenth International Scientific Conference “SPACE, ECOLOGY, SAFETY”*, 24–26 October, Sofia, Bulgaria, pp. 58–62, p-ISSN 2603-3313.

Werner, R., Petkov, B., Valev, D., Guineva, V., Atanassov, A., Danov, D., Bojilova, R., Kirillov, A. (2021). Study of the Sofia total ozone content time series variance, available at: https://spaceclimate.bas.bg/SW/assets/pdf/Primorsko_Werner_1.pdf

Werner, R., Valev, D., Guineva, V., Kirillov, A., Petkov, B. (2018). Determination of the UV-index using measurements performed by the GUV-2511 instrument at Stara Zagora, *Proceedings of the Fourteenth International Scientific Conference “SPACE, ECOLOGY, SAFETY”*, 7–9 November, Sofia, Bulgaria, pp. 101–105, p-ISSN 2603-3313.

Wright, D.B., Herrington, J.A. (2011). Problematic standard errors and confidence intervals for skewness and kurtosis, *Behavior Research Methods*, Vol. 43, pp. 8–17, DOI: 10.3758/s13428-010-0044-x.

DOI: 10.31401/WS.2025.proc.29

Proceedings of
the Seventeenth Workshop “Solar Influences on the Magnetosphere, Ionosphere and Atmosphere”
June, 2025

Study of the Relationship between Solar Radiation and the Level of Geological Hazard

Jelev G.N.

Space Research and Technology Institute, Bulgarian academy of Sciences
gjelev@space.bas.bg

Abstract

The amount of solar radiation (WH/m^2) is an important element in considering all processes on the Earth's surface. The study of the distribution of solar radiation allows mapping and analyzing the effects of the sun and sunlight on a given geographical area for a certain period of time. The modeling of solar radiation is based on the digital elevation model (DEM). It depends on many factors, such as the influence of the atmosphere, latitude and altitude, steepness (slope) and direction of inclination (exposure) of the slope, daily and seasonal changes in the angle of the sun, etc. Mapping the spatial distribution of the amount of solar radiation is useful in a number of fields, such as agriculture, resource management, meteorology, civil engineering, environmental studies, tourism, etc.

This study examines the relationship between the amount of solar radiation, its spatial distribution and geological hazard. The study was conducted on the coastal zone of the Republic of Bulgaria. Bulgaria with a width of 20 km, as an important section of the country's critical infrastructure. A connection has been established between the amount of solar radiation, the relief and the areas with increased geological hazard.

Keywords: solar radiation, geological hazard, digital elevation model, GIS, Remote sensing

1. Introduction

Solar radiation is the primary energy source that drives many of the physical and biological processes on Earth. Understanding its importance for the landscape at different scales is key to understanding a wide range of natural processes and human activities [Choi, et. al. 2019; Dubayah, & Rich, 1995; Fu, & Rich, 2002; Dancheva & Asenovski, 2018; Potužníková et. al. 2023].

When studying different landscapes, topography is a key factor that determines spatial variations in insolation (the amount of direct or total solar radiation reaching the Earth's surface). Differences in elevation, slope orientation (inclination and exposure), and shadows cast by topographic features affect the amount of solar radiation received by different geographic areas. Solar radiation also varies depending on the time of day and year. It contributes to changes in many components of the environment and microclimate, including factors such as: air and soil temperature, evapotranspiration, snowmelt patterns, soil moisture, light available for photosynthesis, photovoltaic parks for energy production, and, last but not least, geological hazard.

Geological hazard summarises natural disasters caused by geodynamic activity or abnormal changes in the geological environment, which usually include internal earth processes such as earthquakes and active faults, and external exogenous geophysical processes such as erosion, abrasion, landslides, debris flows, rockfalls, sinkholes, etc.

The Black Sea coast of Bulgaria is an important part of the country's critical infrastructure, and many of the processes listed above that represent geological hazard occur in this area. This makes it an interesting subject for the present study.

2. Purpose and objectives

The aim of this study is to determine the impact of solar radiation on geological hazard in the country's Black Sea coastal region. The following steps have been outlined to achieve this aim:

- Defining the study area;
- Obtaining basic data and processing it in ArcGIS;
- Analyzing the results.

3. Materials and Methods

An area 20 km inland from the coast was selected as more representative in terms of the processes determining geological hazard and the topographical expression of the relief – DEM for determining solar radiation (Figure 1). It falls entirely within the Black Sea climate region.

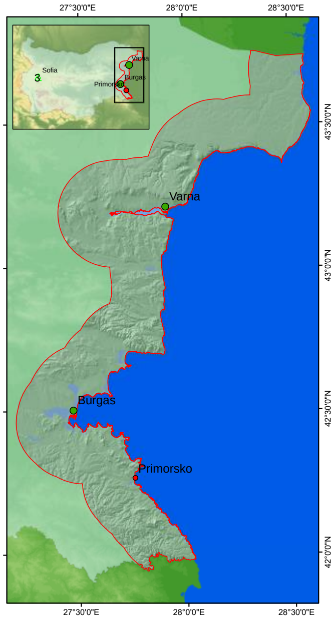

Figure 1. *Study area: Black Sea coastal strip with a width of 20 km from the territory of the Republic of Bulgaria with DEM, Source: [USGS, EarthExplorer, 2025]*

The following basic data were obtained for the analysis: a digital elevation model, coastline and a 20 km buffer inland, a geological hazard map provided by the Ministry of Regional Development and Public Works and compiled by a team from the Geological Institute of the Bulgarian Academy of Sciences [Stage II of ..., 2017, Geological hazard Map ..., 2017] (Figure 2a.). The digital elevation model (DEM) was obtained from the Endeavour space shuttle, the shuttle's radar topography mission (SRTM). The data from this mission is openly available from The U.S. Geological Survey (USGS) [USGS, EarthExplorer, 2025], with elevation information having a spatial resolution of 1 arc second or 30 m. [USGS EROS Archive, 2025].

The coastline was obtained from images from the Sentinel 2 satellite [Sentinel Hub, 2025] under Europe's Copernicus programme. A buffer zone 20 km wide was created inland from the coastline.

The data was processed and analyzed in a GIS database using a number of tools from the ArcGIS software product. The amount of reflected global solar radiation was calculated using the solar radiation analysis tools in ArcGIS, Spatial Analyst - Solar Radiation. Global radiation is calculated as the sum of direct and diffuse solar radiation for each raster cell of the digital elevation model DEM [Dubayah & Rich, 1995; Rich, et. al. 1994; ESRI. ArcGIS Desktop, 2025]. The calculation is repeated for the entire selected area to obtain a map of the insolation of the area (Figure 2b.).

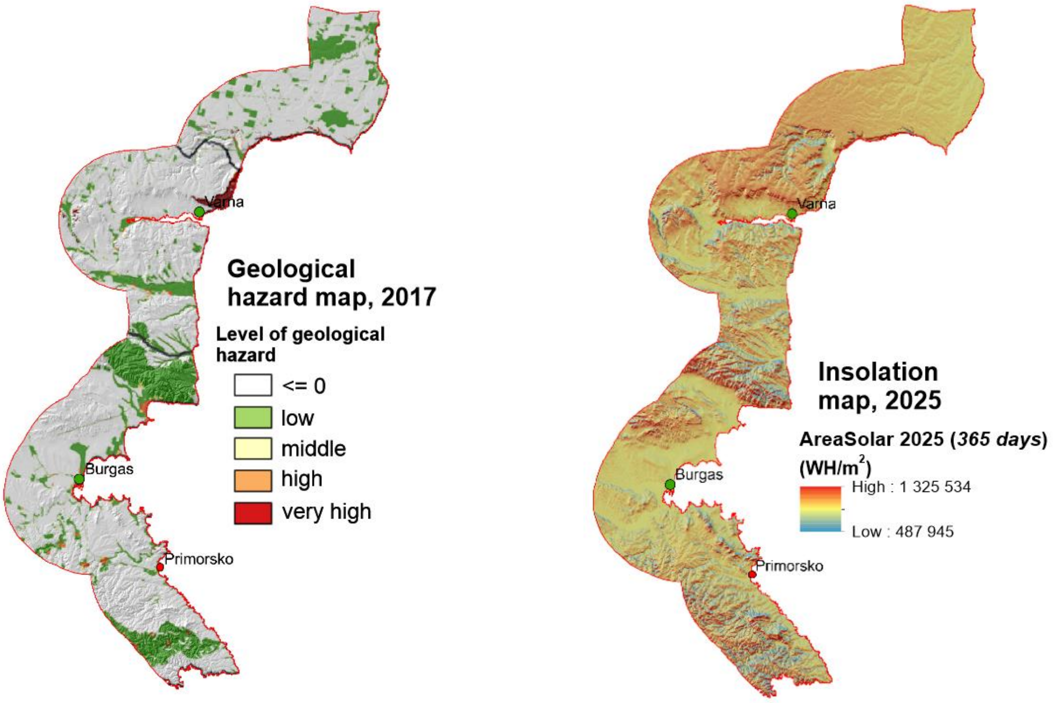

a) *b)*

Figure 2. *a) Geological hazard map, 2017; b) Insolation map, 2025*

4. Results

The global solar radiation analysis feature allows you to map and analyze the effects of the sun on a geographical area for specific periods of time. In this study, the selected period is 365 days (1 year – 2025). The calculations take into account atmospheric effects, the geographical latitude and altitude of the site, the steepness (slope) and geographical direction (aspect), daily and seasonal changes in the angle of the sun, and the effects of shadows cast by the surrounding topography. The output raster represents the global radiation (WH/m^2) or the total amount of incoming solar insolation (direct + diffuse) calculated for each DEM location [ESRI. ArcGIS Desktop, 2025] and is shown in (Figure 2b.).

The Bulgarian Black Sea coast is slightly indented with a fractal dimension of 1.11 and a curvature of 2.41 [Jelev, 2023]. The geological base of the Earth's surface has a diverse rock composition. The relief has developed mainly under the influence of internal Earth forces. This determines the presence of various abrasive and accumulative forms on the Earth's surface – cliffs, beaches, etc.

Four more characteristic areas have been selected. The northern part of the studied territory is the *Dobruja* coastal zone [Dimitrov, 2023] (Figure 3.1). There, the relief is flat and the amount of solar radiation is very high. In this section, the geological hazard is zero or very low. An exception is the coastal zone in the southern part of the section, where cliffs prevail.

In the next area (Figure 3.2), the terrain is rugged and part of the *Frangenska* coastal zone. The section is subject to the strong influence of a number of hazardous geological processes and, in combination with high anthropogenic pressure, local areas with high and very high geological hazard are formed. Global solar radiation is differentially distributed. It is high in the flat and hilly areas and low in the deep valleys and north-facing slopes.

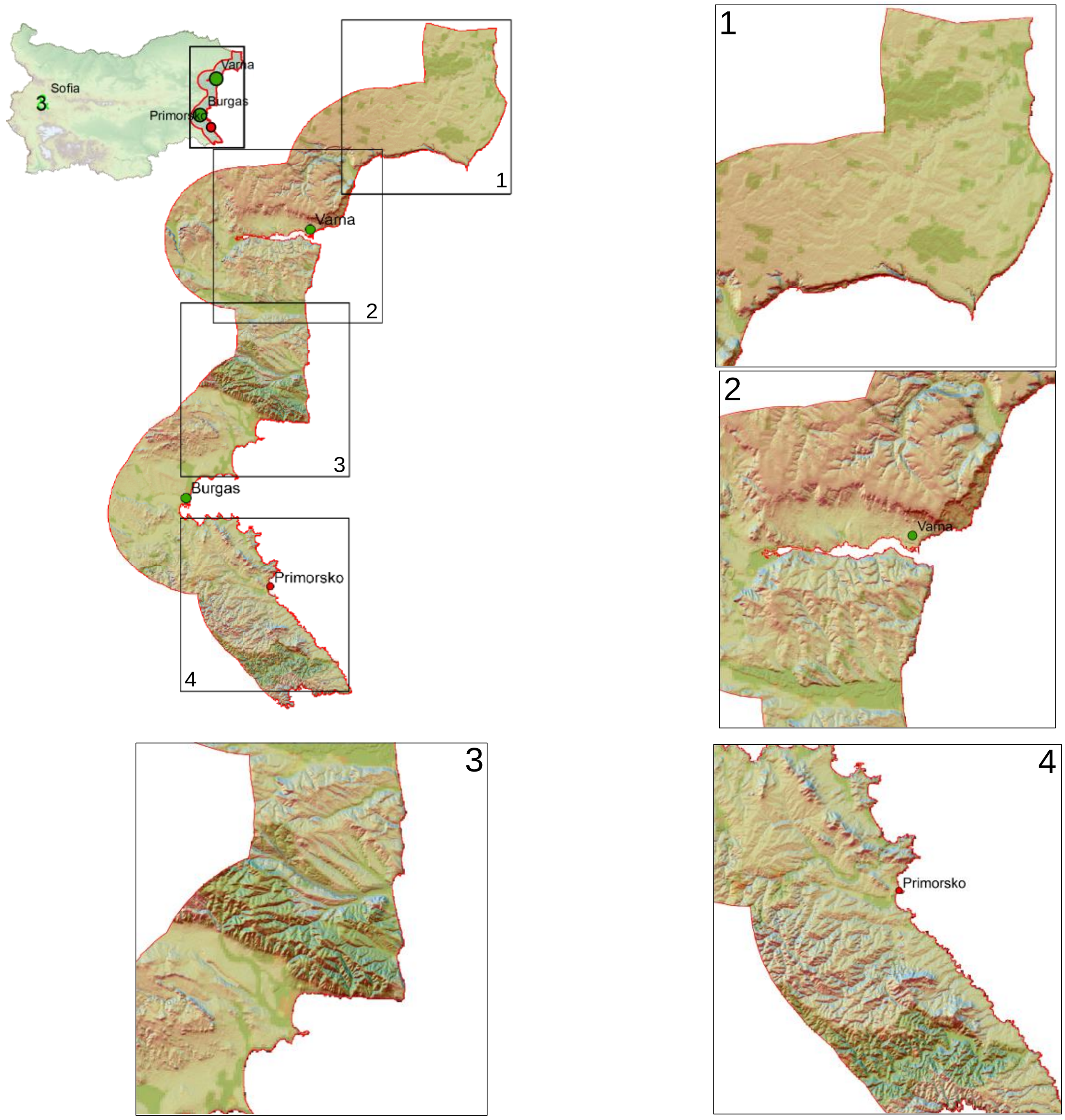

Figure 3. *Composite map of correlation between global solar radiation and geological hazard in the studied area*

Section 3 (Figure 3.3) covers the *Stara Planina* coastline. Morphologically, clearly defined accumulation forms (sand strips) have been formed along the coastline at the foot of the prevailing cliffs. In this section, the geological hazard is low to medium and is most widespread. Global solar radiation is directly related to the east-west oriented relief forms. High values prevail in the flat areas and southern slopes, while low values prevail in the northern slopes and deeper valleys. The southern part of the section falls within the Burgas coastal zone, where areas with accumulative landforms prevail. In this area, the geological hazard is locally distributed. Global solar radiation is very high, with the exception of some northern slopes.

The fourth section (Figure 3.4) is characterized by a highly indented coastline with numerous bays and peninsulas. This section falls within the *Strandzha* coastal strip. Abrasion processes prevail, shaping the characteristic type of coastline. They are the result of the strong impact of internal and external geological forces on erosion-resistant rock complexes. The geological hazard is represented in the southern part of the section as being low. In some areas, it is moderate to high. The rugged terrain determines the uneven distribution of global solar radiation. Its distribution is patchy, with rapid alternation between low and high values.

5. Conclusion

The calculation of global solar radiation and some of the factors influencing the determination of geological hazard is based on the use of a digital terrain model and its derivatives – slope, exposure, curvature, etc. This also determines the relationship between geological risk and global solar radiation.

Acknowledgments

This work was supported by the NSP DS program, which has received funding from the Ministry of Education and Science of the Republic of Bulgaria under the grant agreement no. Д01-74/19.05.2022.

References

Choi, Y., Suh, J., Kim, S.-M. (2019). GIS-based solar radiation mapping, site evaluation, and potential assessment: A review, *Applied Sciences*, Vol. 9, 1960, DOI: 10.3390/app9091960.

Dancheva, A., Asenovski, S. (2018). Study of waste disposal thermal radiation using satellite data and considering solar influence, *Aerospace Research in Bulgaria*, Vol. 30, pp. 16–25, DOI: 10.3897/arb.v30.e02.

Dimitrov, L. (2023). *Morski prostranstven plan na Republika Bulgaria 2021–2035*, Tom 2: Geologiya i geomorfologiya. Available at: https://www.mrrb.bg/bg/morski-prostranstven-plan-na-republika-bulgariya-2021-2035-g/ (in Bulgarian).

Dubayah, R., Rich, P.M. (1995). Topographic solar radiation models for GIS, *International Journal of Geographical Information Systems*, Vol. 9, No. 4, pp. 405–419, DOI: 10.1080/02693799508902046.

Ďuračiová, R., Pružinec, F. (2022). Effects of terrain parameters and spatial resolution of a digital elevation model on the calculation of potential solar radiation in the mountain environment: A case study of the Tatra Mountains, *ISPRS International Journal of Geo-Information*, Vol. 11, No. 7, 389, DOI: 10.3390/ijgi11070389.

ESRI. *ArcGIS Desktop – An overview of the Solar Radiation toolset*. Available at: https://desktop.arcgis.com/en/arcmap/latest/tools/spatial-analyst-toolbox/an-overview-of-the-solar-radiation-tools.htm (accessed 2025).

ESRI. *ArcGIS Desktop – Area Solar Radiation*. Available at: https://desktop.arcgis.com/en/arcmap/latest/tools/spatial-analyst-toolbox/area-solar-radiation.htm (accessed 2025).

ESRI. *ArcGIS Pro – How solar radiation is calculated* (Documentation). Available at: https://pro.arcgis.com/en/pro-app/latest/tool-reference/spatial-analyst/how-solar-radiation-is-calculated.htm (accessed 2025).

Fu, P., Rich, P.M. (2002). A geometric solar radiation model with applications in agriculture and forestry, *Computers and Electronics in Agriculture*, Vol. 37, pp. 25–35.

Jelev, G. (2023). Using remote sensing data and GIS in research of morphometric characteristics of the coastal area in Bulgaria, *Aerospace Research in Bulgaria*, Vol. 35, pp. 16–27, DOI: 10.3897/arb.v35.e02.

Karta na geolozhkiya risk v Bulgaria, scale 1:1,300,000 (2017). Available at: http://gis.mrrb.government.bg/KGR/02%20maps/Risk.pdf (accessed 2025) (in Bulgarian).

Kausika, B.B., van Sark, W.G.J.H.M. (2021). Calibration and validation of ArcGIS solar radiation tool for photovoltaic potential determination in the Netherlands, *Energies*, Vol. 14, 1865, DOI: 10.3390/en14071865.

Potužníková, K., Koucká Knížová, P., Chum, J., Podolská, K., Kouba, D., Mošna, Z., Georgieva, K., Bojilova, R., Kirov, B., Asenovski, S. (2023). Summer tropospheric mesoscale situations with impact on the ionospheric plasma, *Proceedings of the Fifteenth Workshop "Solar Influences on the Magnetosphere, Ionosphere and Atmosphere"*, ISSN 2367-7570, pp. 89–97, DOI: 10.31401/WS.2023.proc.

Rich, P.M., Dubayah, R., Hetrick, W.A., Saving, S.C. (1994). Using viewshed models to calculate intercepted solar radiation: Applications in ecology, in: *American Society for Photogrammetry and Remote Sensing Technical Papers*, pp. 524–529.

Sentinel Hub by Planet Labs. *EO Browser*. Available at: https://www.sentinel-hub.com/eo-browser/ (accessed 2025).

USGS EROS. *Shuttle Radar Topography Mission (SRTM) 1 Arc-Second Global* (Digital Elevation). Available at: https://www.usgs.gov/centers/eros/science/usgs-eros-archive-digital-elevation-shuttle-radar-topography-mission-srtm-1.